UNIVERSITY OF CALGARY

Traveltime Tomography in Isotropic and Transversely Isotropic Media

by

Marco Perez

A THESIS
SUBMITTED TO THE FACULTY OF GRADUATE STUDIES
IN PARTIAL FULFILMENT OF THE REQUIREMENTS FOR THE
DEGREE OF MASTERS OF SCIENCE

DEPARTMENT OF GEOLOGY AND GEOPHYSICS

CALGARY, ALBERTA

MARCH, 2004

UNIVERSITY OF CALGARY

FACULTY OF GRADUATE STUDIES

The undersigned certify that they have read, and recommend to the Faculty of Graduate Studies for acceptance, a thesis entitled “Traveltime Tomography in Isotropic and Transversely Isotropic Media” submitted by Marco Perez in partial fulfillment of the requirements for the degree of Masters of Science.

Supervisor, Dr. John C. Bancroft, Dept. of Geology and Geophysics

Dr. Larry Lines, Dept. of Geology and Geophysics

Dr. Ed Krebes, Dept. of Geology and Geophysics

Dr. J. A. Rod Blais, Dept. of Geomatics Engineering

Date

ABSTRACT

This thesis builds two types of velocity models through crosswell and surface experiments using traveltime tomography. One is isotropic, consisting of estimating P-wave velocities, and the other is transversely isotropic, estimating Thomsen's weak anisotropy parameters of α, ε and δ.

Traveltimes are modelled using a finite-difference scheme in simple isotropic and transversely isotropic models and used to determine tomographic resolution capabilities for crosswell and surface geometries. Results show that crosswell tomography can accurately detect vertical velocity variations as well as provide a reasonable estimate for ε while surface tomography can accurately detect horizontal velocity variations and provide a reasonable estimate for δ.

Two different quasi-null space inversion stabilization techniques are also introduced in this thesis. The first stabilizes the inversion result by smoothing unreliable results while the second integrates two different seismic experiments based on their relative reliability. Results show that tomogram accuracy is improved when using these two techniques.

ACKNOWLEDGEMENTS

This thesis could not have been written without the support of many people. Specifically, I would like to thank my supervisor, Dr. John Bancroft for giving me the freedom to pursue my interests in geophysics. I would also like to thank Dr. Pat Daley for invaluable insight into the complex topic of anisotropy. I would also like to thank the faculty of the University of Calgary's department of Geology and Geophysics for teaching me the fundamentals of geophysics and making themselves available for questions and discussions. Thanks also go to CREWES, who without their financial support this research could not have been accomplished. Many thanks also go to my fellow grad students. They have made my time at the university one I will never forget. Lastly, but most importantly, I would like to thank my parents and my two brothers for their support and their belief in me.

TABLE OF CONTENTS

LIST OF FIGURES

CHAPTER 1: INTRODUCTION

The fundamental challenge for exploration seismologists involves generating accurate images of subsurface geologic structures. Images are constructed by applying specialized processes to recorded reflection seismic signals. The processes work to reduce random noise and map coherent signals into correct geologic locations. In order to reposition or migrate the data into the proper geologic positions, a velocity model must be estimated. It is imperative that the model accurately represents subsurface properties because the migration quality is dependent on the accuracy of the velocity model.

Several methods have been used to determine velocity models. For data containing a minimal amount of geologic structure, velocities estimated from normal moveout correction (stacking velocities) are usually sufficient to produce a migrated section. Prestack depth migration is required to position events for more structured data. Such an imaging technique is highly dependent on the validity of the velocity model. In such cases well-log information can be useful but due to the minimal number of wells it is typically insufficient for determining an appropriate velocity model for the entire data range. The process of prestack migration itself has been used as an iterative velocity tool with the output image used as a diagnostic tool to determine the validity of the model. The process used in this work utilizes the tomography process to determine an appropriate velocity model. Simply put, tomography attempts to construct a traveltime model that will best fit the traveltimes for the recorded data.

The objective of this work focuses on using tomography to obtain an accurate model of migration velocities for isotropic and transversely isotropic media (Transversely isotropic media is symmetric upon rotation about one axis). The technique implements a quasi-null space through which conventional tomographic methods are stabilized by ascertaining a measure of reliability for each output model and modifying the result accordingly. Two different quasi-null space stabilization methods are proposed. The first is a dynamic smoothing method that attempts to limit the contribution of the unreliable values, and the second integrates two different experiments retaining the more reliable solutions in the output tomogram. These proposed stabilizing techniques, in conjunction with the iterative tomographic process of modelling and solving a least squares problem, serve as a tool for developing accurate velocity models for depth migration.

The work presented consists of three main components: developing the theory for isotropic and anisotropic traveltime modelling, developing the theory for isotropic and anisotropic traveltime tomography and the testing of the techniques put forth. Specifically, chapter two details the methods used to model the seismic response from inhomogeneous isotropic and transversely isotropic media. Chapter three describes how tomography is implemented. The fourth chapter outlines the methods used to solve the tomographic equations by construction of a pseudo-inverse. The algorithms are tested for accuracy and limitations in chapter five. Chapter six includes a discussion of results and makes concluding remarks of the methods presented. What follows in this chapter is a brief introduction to the unknowns to be estimated, the methods used to determine them and practical considerations for implementing the technique.

1.1 Geophysical Model

The traveltime inversion process begins with the construction of a model containing an estimate of the earth's seismic velocities. In this work, the unknown velocity model is represented as a two-dimensional grid of square cells, each containing unknown parameters. The cells contain constant model parameters that describe isotropic or transversely isotropic media. For isotropic media one only requires the velocity for each cell while for transversely isotropic media one must add Thomsen's (1986) parameters. The locations of the reflecting interfaces are defined at cell nodes. The model is assumed to have flat topography on the surface, an unlimited number of velocity layers, and a variable subsurface structure. Compressional or P-wave propagation will be assumed throughout this thesis though modifications can be made to include shear wave propagation. The traveltimes corresponding to first arrivals are computed using a finite-difference plane-wave approximation to the eikonal equation.

1.2 Tomography

Tomography is a statistical method that is used to update a geologic velocity model such that a modelled traveltime response converges towards recorded traveltimes in seismic experiments. The technique utilizes the difference between the estimated and actual traveltimes in an iterative approach to update the model space.

The tomographic methods presented in thesis can be categorized by the traveltimes used for inversion. Transmission tomography employs traveltimes representing direct rays between sources and receivers, while surface tomography utilizes traveltimes of rays reflected from a seismic impedance contrast. In this thesis, they will be referred to as crosswell and surface tomography based on the acquisition geometry used for transmitted and reflected rays respectively. Bording et al. (1987), distinguished between the concepts of transmission and surface tomography by comparing the unknown values to be determined. Transmission tomography has unknown values of velocity, while surface tomography has unknowns of velocity as well as the unknown location of the interfaces. The position of the reflecting interfaces can be determined through a variety of techniques. One such method involves inverting for velocity while assuming fixed reflector positions as shown by Williamson (1984). Whitmore and Lines (1986) and Stork and Clayton (1985) use each updated slowness (reciprocal of velocity) model as the input for a depth migration which in turn defines the reflecting interfaces. The method used in this thesis will assume that reflecting interfaces are known and they will not be included within the inversion process.

The transmission and surface tomographic methods can be further subdivided into isotropic and anisotropic cases. In typical seismic surveys, it is assumed that each subsurface formation is isotropic. However, it has been shown by Backus (1962) and Postma (1955), that there can be a significant amount of anisotropy present. To properly image data acquired over anisotropic regions of the earth, the appropriate elastic parameters that describe the media are required. Chapman and Pratt (1992) have done extensive work in anisotropic tomography by determining the elastic constants that correspond to such media. An alternative to determining elastic parameters is presented in this thesis where Thomsen's parameters (1986) of α_0, δ and ε are estimated for transversely isotropic (TI) media.

Bishop et al (1986) presented a classic explanation of isotropic surface tomography used in this thesis. The authors numerically simulated the seismic response from an initial model and compared the results to the actual recorded data. The method of least-squares was used to calculate the estimated model and the geologic properties. The process was repeated until the difference between the recorded and modelled data reached an acceptable threshold. The research done by Bording et al (1986) emphasized the two key elements in tomography as modelling (following traveltime picking) and solving the traveltime equations by use of a least-squares solution.

In this thesis, the first major tomographic component consists of estimating traveltimes through a grid of isotropic or anisotropic media by using a finite-difference solution to the eikonal equation. These traveltimes are computed for all grid points from a starting location within the grid. Grid points surrounding the starting location are computed using a finite-difference equation. The computed traveltime grid is referred to as a traveltime map. The starting point can be either a source or receive location, where the times on a source traveltime map represent the traveltimes from a source to any subsurface location. The times on a receiver traveltime map represent the times from any subsurface point to the receiver. Consequently the total traveltimes between any source or, receiver, to any subsurface point, can be formed by simply adding the traveltimes at the scatterpoint of the corresponding source and receiver traveltime maps. The second major component in tomography involves solving a set of overdetermined or underdetermined equations. In this thesis, solutions are found by using the method of Singular Value Decomposition (SVD). Iterating through these two major components, a final tomogram is created that accurately represents the acquired data.

1.2.1 Modelling

Modelling consists of estimating the traveltimes and raypaths through a homogeneous or heterogeneous, isotropic or anisotropic medium. Modelling is an important component in tomography in that an inaccurate modelling algorithm will lead to poor inversion results. Modelling accuracy is therefore the backbone of traveltime inversion. Knowing the limitations of the modelling routine will determine the accuracy and identify method limitations.

The modelling method used in this thesis is based on a finite-difference solution to the eikonal equation. This method was first introduced by Vidale (1988), in which a two-dimensional grid defines the velocity of the medium. Starting from an initial source corresponding to a single grid node, traveltimes are calculated along adjacent nodes as an expanding square. The method is fast and accurate for smooth velocities, but breaks down when harsh velocity contrasts are encountered. The velocity or slowness field is usually smoothed to overcome such contrasts. It should be noted that the high frequency approximation solutions to the wave equation, as produced by the eikonal equation. are of interest. This is because a consequence of the high frequency approximation is rays and it will be the rays that will play an important role in tomography.

Other methods have since been proposed that attempt to increase the accuracy and avoid the limitations of the Vidale method. Such methods include those by Van Trier and Symes (1991) and Qin et al (1992), the latter of which is employed in this work. The method proposed by Qin et al (1992) mimics expanding wavefronts thus circumventing the problems encountered by the expanding squares of Vidale's method. Anisotropic solutions to the eikonal equation have also been formulated as an adaptation to the existing isotropic solutions. Dellinger (1991) proposed an upwind scheme similar to the isotropic solution of Van Trier and Symes, while Eaton (1993) proposed a solution similar to Qin et al. using a triangular mesh. The work in this thesis is similar to Eaton's however a square mesh is used to compute traveltimes for transversely isotropic media.

In addition to traveltimes, raypaths must also be computed. As noted earlier, these raypaths are of vital importance as they will dictate the final output velocities. Raypaths, in this thesis, are those that satisfy Fermat's principle. From a geophysical perspective, Fermat's principle states that "a seismic raypath between two points is that for which the first order variation of traveltime with respect to all neighbouring paths is zero." (Sheriff, 1999) This translates into a traveltime which is usually a local minimum but can sometimes be a local maximum. In this thesis only the minimum traveltime will be considered. Raypaths in this work are calculated from a simple routine based on methods introduced by Asakawa and Kawanaka (1993). The principle of reciprocity and Fermat's principle of least time provides the basis for the method. The principle of reciprocity states that the path of wave propagation from source to receiver is the same as from receiver to source. In isotropic media, the minimum traveltime corresponds to raypaths that are orthogonal to the wavefronts. In anisotropic media the raypath direction is not orthogonal to the wavefront so equations relating the wavefront normal to the raypath must be used. Following the principle of reciprocity and the appropriate direction in each cell, the raypath from a surface point can be traced back to the source or receiver.

1.2.2 Least-squares solutions

Once the model has had traveltimes and raypaths computed, equations relating traveltimes to the velocity of the medium are formed. Recall that to simulate the response of the model, the media was divided into cells and that a velocity was assigned to each cell. The distance travelled by a ray through each cell, d_i was computed and using the reciprocal of cell velocity s_i the cell traveltime was defined as $t_i=d_is_i$. Summing the traveltime through all cells gave the total traveltime T for the ray, $T=\sum_{i=1}^{n} v_i s_i$ where n is the total number or cells traversed by the ray. Thus, each ray, for a given source-receiver pair, has a total traveltime equation as function of the assigned velocity and the distance travelled through each cell. The discrepancy between the simulated traveltimes and the recorded traveltimes is associated with the error between the velocity model used and the actual seismic velocity of the earth. The unknown quantities to be determined are the velocity perturbations required to minimize the traveltime errors. This is expressed as a linear set of equations whose solution, is used to update the velocity model.

After the set of linear equations has been designed, there are numerous methods available to invert the matrix required to obtain a solution. The technique chosen in this thesis, to solve the set of overdetermined *linear* equations is Singular Value Decomposition (SVD). SVD attempts to construct a pseudo-inverse by decomposing the elements of the data into model and data eigenfunctions and inverting each separately. However, the seismic response is a *nonlinear* function of the model parameters. The nonlinear approach to geophysical inversion iteratively updates the parameters for a given geophysical model. The nonlinear expression is recast as a linear approximation and the parameters are estimated by iteratively solving an updated set of linear equations. In this way the discrepancy between the observations and the modeled traveltimes is minimized. Chapter 3 discusses this in detail.

1.2.3 Accuracy and limitations

The limitations of the method are related to the assumptions that have been made. Such assumptions consist of the manner in which modelling was performed, the inversion process and the inherent sampling of the data acquired. These limitations affect the resolution, stability, and uniqueness of the solution.

1.2.3.1 Resolution

Tomographic resolution depends on two variables. The first variable is the cell size used, and it can be varied by the user. Determining the appropriate cell size is important since it can affect runtime and inversion quality. A small cell size is advantageous in that it minimizes the errors that arise when attempting to discretize a continuous function. It also is able to resolve smaller velocity anomalies that would normally be masked if the cell size were too large. However, making the cell size too small does have its disadvantages of larger memory requirements and longer run times. Choosing a cell size becomes a compromise between the quality of the model and the computational cost.

The second variable of tomographic resolution is the quality of source to receiver ray distribution within the survey area. Ray distribution refers to the number of linearly independent rays that traverse each cell. It follows that a uniform ray distribution contains an equal number of linearly independent rays traversing each cell. Such a ray distribution leads to a more accurate representation of the unknown velocity model. This in practice is never achieved since ray distribution depends on acquisition geometry and subsurface velocity. For a given acquisition geometry, there will always be areas containing a shortage in ray density relative to other areas of the model. In general cells near the edges of the experiment will suffer from poor ray coverage. If an experiment could be devised such that a uniform ray distribution was possible, the subsurface velocity anomalies would bend rays according to Snell's law to prevent such a distribution. High velocity zones tend to act as ray attractors (thereby minimizing traveltimes) while low velocity zones tend to repel rays. As a result cells in a high-velocity zone include more ray data than lower velocity cells.

Both these factors contribute in limiting the inversion resolution since velocity estimates are made for each cell by relating the modelled ray distances and traveltimes of the survey. Cells containing many rays will contribute heavily to the solution. In contrast, velocity anomalies corresponding to cells with no ray coverage will not be detected lowering the resolution of the inversion process. Increasing cell size will reduce zero ray density cells, however as discussed previously, it will lower resolution.

1.2.3.2 Stability

There are two basic problems affecting stability in seismic tomography: the lack of data required to properly constrain the inversion and the nonlinearity of Snell's Law. The acquired data inherently consist of an angle-limited distribution of rays: a consequence of acquisition geometry and the velocity structure present within the earth. The nonlinearity present within the problem is expressed by the non-uniform ray distribution translating into some areas of the subsurface receiving minimal or no ray coverage. This nonlinearity makes the convergence unstable, while the nonuniqueness does not guarantee that a solution will be the correct one. Because of these issues it may be extremely difficult to converge to the correct solution. Therefore solution accuracy depends heavily on the inversion technique implemented and the constraints applied.

A number of different techniques have been developed with the goal of improving the resulting velocity model by limiting the effects of the unconstrained parameters. Phillips and Fehler (1991) have given a review of popular regularization methods that emphasise the suppression of small singular values. Carrion (1991) developed a dual method in which the inversion uses both the data and imposed constraints which compensates for the lack of data. Bohm and Versnaver (1999) developed an iterative adaptive grid scheme based on null space identification and the resolution of the resultant velocity model. By modifying the cell size, based on the reliability of the inversion, the cell size is increased or decreased so as to maximize both the reliability and resolution of the solution.

This thesis presents alternative methods that attempt to overcome the limitations of statistical inversion. Both methods use SVD allowing for solution analysis, which in turn is used to determine solution reliability. The quasi-null space is used as the diagnostic tool, influential in separating reliable solutions from unreliable ones.

1.2.3.3 Uniqueness

The uniqueness of a solution depends on the number of degrees of freedom in the problem. In a typical survey there are many more recorded traveltimes than there are unknown velocity grid points indicating an overdetermined problem. Attempting to fit values to the unknowns becomes an exercise in choosing an optimal starting point and converging to a best-fit solution. However, there can be many velocity functions that can reproduce the same traveltimes. In such cases, previous knowledge in the area, such as well log data or geological information, are used to constrain the solution.

The method presented in this thesis helps to converge to the correct solution. The quasi-null space is used such that a formulation can be expressed indicating the uniqueness of the solution. Interpreting the quasi-null space tends towards a solution which suitably represents the subsurface velocities.

1.3 Innovations

In this work, a number of different algorithms have been implemented. Most of these algorithms have been developed with modifications to the original method presented. The major components of the thesis, which include significant contributions to existing methods, are summarized below.

1. Isotropic traveltime estimator: This first-arrival algorithm is based on a method first proposed by Qin et al (1992). It has been implemented using the finite-difference expressions developed by Vidale (1988). A geometrical reconstruction of the finite-difference solution gives a new perspective on the plane-wave solution and the implications of the approximations made.

2. Transversely isotropic traveltime estimator: This first-arrival algorithm is based on the finite-difference method proposed by Eaton (1993) which includes work done by

Qin et al (1992) and Vidale (1988). Eaton’s method works on a hexagonal grid as opposed to the method used in this thesis which uses a square grid. First arrivals are assured by accounting for refracted waves along cell boundaries. This is not explicitly stated in the methods proposed by Vidale, Qin or Eaton.

3. Isotropic raytracer: The isotropic raytracer is implemented based on algorithms put forth by Asakawa and Kawanaka (1993). These authors use the principal of reciprocity and Fermat’s Theorem of least time to determine raypaths. The technique used in this thesis is based on the same concepts and the traveltime maps computed by the traveltime estimator. However, it is implemented by identifying the reflection point and subsequently tracing back to the respective source and receiver. This method also considers refracted waves that can occur at cell boundaries.

4. Transversely isotropic raytracer: The transversely isotropic raytracer is similar to the isotropic raytracer but it also includes the capability to produce group and phase rays. This is done using the transformation from group to phase put forth by Brown et al (1991). In this manner one can view the differences between group and phase rays.

5. Quasi-null space stabilization: The quasi-null space was first introduced by Bohm and Vesnaver (1998) and was used to produce solution reliability grids which they used to determine how cell sizes should be changed. The same concept of the quasi-null space is used in this thesis, however the information derived from the quasi-null space is used in two new ways.

a. Dynamic smoothing: Using the quasi-null space, a solution reliability grid is constructed. A reliability threshold is defined and unreliable cells are smoothed while the reliable cells are unchanged. This smoothing is data dependent leaving the cell size constant (therefore not reducing resolution) while not compromising solution stability with unreliable cell values. The threshold value can be controlled in such a way that allows the user to interpret real velocities from false ones.

b. Integration: This technique is a new method that integrates two different seismic experiments, based on the quasi-null space. A reliability grid is constructed for each of the experiments tomographic solutions and a cell by cell comparison is made. The more reliable cell of each solution is chosen as the output for the final velocity model.

6. Isotropic traveltime tomography: The traveltime tomography method uses the algorithms outlined above and implements the two quasi-null space stabalization techniques: dynamic smoothing and integration. The algorithm has been implemented using both transmission and reflection tomography. The algorithm can be easily adapted to use mode converted waves.

7. Transversely isotropic traveltime tomography: The transversely isotropic tomography method is very similar to the isotropic case except that it inverts for the weakly anisotropic parameters of α, ε, and δ as defined by Thomsen (1986).

1.4 Summary

The tomographic method presented in this thesis inverts for isotropic velocities or the appropriate anisotropic velocity parameters. It is based on an iterative workflow consisting of modelling isotropic and anisotropic traveltimes and rays and solving a set of linearized equation. Modelling and the use of Singular Value Decomposition plays an important role in the tomographic inversion. The reliability of each process governs the accuracy of the resulting solution. Additional constraints are applied to converge to a unique solution and stabilize the inversion process.

Tomography has problems with solution nonuniqueness and inversion stability. The uncertainty exists because of the number of different parameter value combinations that can reproduce the recorded observations. It follows that the ambiguity of the solution is amplified with an increase in the number of unknown parameters, as is the case with anisotropy. The large amount of data available makes the problem difficult to solve uniquely since there can be a number of models which can reproduce the measured data. Inversion instability is a function of ray distribution of the experiment. Methods were introduced that attempt to reduce the instability and nonuniqueness and each with varying amounts of success. The final velocity models are accurate functions to be used for imaging purposes.

Tomography provides an iterative technique that is used to build a velocity model. The iterative nature of the process allows the user freedom in directing the final outcome of the model. After each iteration the solution either converges towards a reasonable result, or diverges, at which point another initial velocity estimate is required. Ultimately, the resulting models should display the geologic parameter information required for prestack depth migration.

CHAPTER 2: MODELLING – THEORETICAL CONSIDERATIONS

The objective of tomography is to create a model that reproduces recorded observations. The discrepancy between modelled and recorded data gives a measure of correctness for the proposed model. In seismic tomography there are two basic variables vital in determining the output model: the assumptions made regarding seismic wave propagation and the recorded seismic data of interest which the model is to replicate.

In conventional processing the assumption of isotropic heterogeneity is made for seismic wave propagation. However, work has shown that anisotropy is present within the earth either by depositional preferential alignment or as a consequence of many thin isotropic layers acting as an effective anisotropic medium. This thesis will consider earth models of isotropic media as well as a specific case of anisotropy known as Transverse Isotropy.

Recorded seismic responses consist of two basic variables: time and amplitude. This thesis is concerned with traveltime tomography and, as such, is only interested in traveltimes. As a result, modelling performed focuses on estimating the raypath and traveltimes taken from source to receiver. Methods have been developed to model amplitudes as well though it is not a topic of interest in this thesis.

The modelling performed encompasses the two assumptions made; propagation is modelled through plane-waves and only the first arrivals are of interest. Traveltimes are estimated for both heterogenous isotropic and anisotropic media using a finite-difference solution to the eikonal equation. A classic paper by Vidale (1988) first proposed the finite-difference solution to estimate traveltimes and a number of techniques have since been devised that build upon Vidale's initial solution. The method used in this thesis is based on a finite-difference wavefront expansion scheme presented by Qin et al (1992).

Modifications have been made by Eaton (1993) to include anisotropy to this isotropic solution. Raypaths are determined after the traveltimes have been calculated. Using the principle of reciprocity, as discussed by Asakawa and Kawanaka (1993), the raypath is traced from a scatterpoint to a source or receiver.

The modelling algorithm is based on the principles of elastic wave propagation through isotropic and anisotropic media. The principles are derived from the eikonal equation. Before proceeding from the finite-difference solution to the eikonal equation, a review of elastic wave propagation in isotropic and transversely isotropic media is presented, following the work of Slawinski (2002).

2.1 Elastic Wave Propagation

Seismic tomography attempts to acquire knowledge of the earth's interior. The properties that can be determined vary from density to the elastic parameters of the medium. Since the objective is to obtain accurate subsurface images through migration, it follows that the properties to be identified are related to the migration velocity. Determining the expressions for velocity in isotropic and transversely isotropic media begins with the principles of Hooke's Law, relating stress to strain and the equation of motion.

2.1.1 Hooke's law

2.1.1.1 Strain

An elastic medium can be defined by its deformation when a force has been applied. This deformation or strain is defined as a change in relative position of two points in a material. Consider two material points defined by $[x, y, z]$ and $[x+dx, y+dy, z+dz]$. After deformation, defined by a vector function $u = \lfloor u_x, u_y, u_z \rfloor$, the coordinates of the points are now given by

$$\lfloor x + u_x(x, y, z), y + u_y(x, y, z), z + u_z(x, y, z) \rfloor \tag{2.1}$$

and

$$\begin{bmatrix} x + dx + u_x(x + dx, y + dy, z + dz) \\ y + dy + u_y(x + dx, y + dy, z + dz) \\ z + dz + u_z(x + dx, y + dy, z + dz) \end{bmatrix}. \tag{2.2}$$

Taking the difference between these deformed points and approximating by using the first two terms of a Taylor series expansion results in the following linear expression for the vector separation of the two points after deformation

$$\begin{bmatrix} dx + \left.\frac{\partial u_x}{\partial x}\right|_{x,y,z} dx + \left.\frac{\partial u_x}{\partial y}\right|_{x,y,z} dy + \left.\frac{\partial u_x}{\partial z}\right|_{x,y,z} dz \\ dy + \left.\frac{\partial u_y}{\partial x}\right|_{x,y,z} dx + \left.\frac{\partial u_y}{\partial y}\right|_{x,y,z} dy + \left.\frac{\partial u_y}{\partial z}\right|_{x,y,z} dz \\ dz + \left.\frac{\partial u_z}{\partial x}\right|_{x,y,z} dx + \left.\frac{\partial u_z}{\partial y}\right|_{x,y,z} dy + \left.\frac{\partial u_z}{\partial z}\right|_{x,y,z} dz \end{bmatrix}. \tag{2.3}$$

The Pythagorean theorem approximates the squared distance between two points after deformation, by ignoring the higher order terms, as

$$(d\tilde{s})^2 \approx dx^2 + dy^2 + dz^2 + 2\left(\left.\frac{\partial u_x}{\partial x}\right|_{x,y,z} dx^2 + \left.\frac{\partial u_y}{\partial y}\right|_{x,y,z} dy^2 + \left.\frac{\partial u_z}{\partial z}\right|_{x,y,z} dz^2 + \right.$$
$$\left.\frac{\partial u_x}{\partial y}\right|_{x,y,z} dxdy + \left.\frac{\partial u_x}{\partial z}\right|_{x,y,z} dxdz + \left.\frac{\partial u_y}{\partial x}\right|_{x,y,z} dxdy + \quad . \quad (2.4)$$
$$\left. \left.\frac{\partial u_y}{\partial z}\right|_{x,y,z} dydz + \left.\frac{\partial u_z}{\partial x}\right|_{x,y,z} dxdz + \left.\frac{\partial u_z}{\partial y}\right|_{x,y,z} dydz \right)$$

The difference in squared distance between the original point, $ds^2 = dx^2 + dy^2 + dz^2$, and the deformed point, is

$$(d\tilde{s})^2 - ds^2 \approx 2\left[\left.\frac{\partial u_x}{\partial x}\right|_{x,y,z} dx^2 + \left.\frac{\partial u_y}{\partial y}\right|_{x,y,z} dy^2 + \left.\frac{\partial u_z}{\partial z}\right|_{x,y,z} dz^2 \right.$$
$$+ \left(\left.\frac{\partial u_x}{\partial y}\right|_{x,y,z} + \left.\frac{\partial u_y}{\partial x}\right|_{x,y,z} \right) dxdy + \left(\left.\frac{\partial u_y}{\partial z}\right|_{x,y,z} + \left.\frac{\partial u_z}{\partial y}\right|_{x,y,z} \right) dydz \quad . \quad (2.5)$$
$$\left. + \left(\left.\frac{\partial u_x}{\partial z}\right|_{x,y,z} + \left.\frac{\partial u_z}{\partial x}\right|_{x,y,z} \right) dxdz \right]$$

This is written in a more compact form as

$$(d\tilde{s})^2 - ds^2 \approx \sum_{i=1}^{3}\sum_{j=1}^{3} \left(\left.\frac{\partial u_{x_i}}{\partial x_j}\right|_{x,y,z} + \left.\frac{\partial u_{x_j}}{\partial x_i}\right|_{x,y,z} \right) dx_i dx_j \,. \quad (2.6)$$

From the above expression strain is defined mathematically as a second rank tensor

$$\varepsilon_{ij} = \frac{1}{2}\left(\frac{\partial u_i}{\partial x_j} + \frac{\partial u_j}{\partial x_i} \right) \quad i, j = 1,2,3 \quad (2.7)$$

where u_i is the displacement and x_i is the coordinate vector (Slawinski, 2002). The strain tensor describes the change in displacement as a function of the change in position (derivative of displacement with respect to position). It describes the change in shape or dimension of a material.

2.1.1.2 Stress

Stress is defined in continuum mechanics to express the interaction of a material with surrounding material in terms of contact forces. Stress is related to strain in that it is a function of the distribution of stress applied. Traction is defined as contact forces placed on a material from surrounding material, mathematically expressed as

$$\mathbf{T}_i^n = \frac{d\mathbf{F}_i}{d\mathbf{S}} \tag{2.8}$$

where $\mathbf{F}_i$ are the individual force components on the surface $\boldsymbol{S}$ defined by its normal n. To describe the stress at a given point traction is written as

$$\begin{bmatrix} T^{(x)} \\ T^{(y)} \\ T^{(z)} \end{bmatrix} = \begin{bmatrix} T_1^x & T_2^x & T_3^x \\ T_1^y & T_2^y & T_3^y \\ T_1^z & T_2^z & T_3^z \end{bmatrix} \begin{bmatrix} n_x \\ n_y \\ n_z \end{bmatrix}. \tag{2.9}$$

The matrix above is represented as the second rank stress tensor, σ_{ij},

$$\boldsymbol{\sigma} = \begin{bmatrix} \sigma_{11} & \sigma_{12} & \sigma_{13} \\ \sigma_{21} & \sigma_{22} & \sigma_{23} \\ \sigma_{31} & \sigma_{32} & \sigma_{33} \end{bmatrix} \tag{2.10}$$

which represents the jth component of the surface force acting on the surface given by the normal with the ith coordinate axis. Equation 2.9 is expressed neatly as

$$T_i = \sum_{j=1}^{3} \sigma_{ji} n_j \, . \tag{2.11}$$

2.1.1.3 Hooke's Law

It has been shown that second rank tensors describe both stress and strain. These quantities are linearly related to each other for sufficiently small strains. Linearly elastic media follow the static linear stress-strain relation of Hooke's Law,

$$\sigma_{ij} = C_{ijkl}\varepsilon_{kl} \qquad i, j, k, l = 1,2,3 \tag{2.12}$$

where C_{ijkl} is the fourth rank tensor with 81 coefficients characterizing the stiffness of the medium, σ_{ij} is the stress applied, ε_{ij} is the resulting strain and the values of *i*, *j*, *k*, and *l*, represent the *x*, *y* and *z* coordinates (Nye, 1960). The inherent symmetry of the second rank tensors reduces the number of independent C_{ijkl} coefficients. Equation 2.7 can show that $\varepsilon_{ij} = \varepsilon_{ji}$ and the symmetry within ε_{kl} implies that there are only 6 independent choices. It also follows that since Hooke's Law is a static expression then angular momentum is conserved and as such $\sigma_{ij} = \sigma_{ji}$. These two symmetries leave 36 independent coefficients of out of the original 81 in the C_{ijkl} stiffness tensor (Musgrave, 1970). Further symmetry reductions come from the principle of conservation of energy. The energy placed when a material is under stress is stored as potential energy. In an elastic material the deformation or strain returns the material to its original form once the stress is removed. In view of the stress-strain equations and the definition of work, work is defined as

$$\begin{aligned} W = \int F dxdydz &= \int \sum_{i=1}^{3}\sum_{j=1}^{3} \sigma_{ij} d\varepsilon_{ij} \\ &= \int \sum_{i=1}^{3}\sum_{j=1}^{3}\sum_{k=1}^{3}\sum_{l=1}^{3} C_{ijkl}\varepsilon_{kl} d\varepsilon_{ij} \\ &= \frac{1}{2}\sum_{i=1}^{3}\sum_{j=1}^{3} C_{ijkl}\varepsilon_{kl}\varepsilon_{ij} \end{aligned} \tag{2.13}$$

integrated over a unit volume. Note that this summation is independent of the order in which it is carried out in terms of strain. Equivalently equation 2.13 can be expressed in its differential form as either

$$dW = \sum_{i=1}^{3}\sum_{j=1}^{3} \sigma_{ij} d\varepsilon_{ij} = \sum_{i=1}^{3}\sum_{j=1}^{3}\sum_{k=1}^{3}\sum_{l=1}^{3} C_{ijkl}\varepsilon_{kl} d\varepsilon_{ij} \tag{2.14}$$

or

$$\frac{\partial W}{\partial \varepsilon_{ij}} = \sum_{k=1}^{3}\sum_{l=1}^{3} C_{ijkl}\varepsilon_{kl} . \tag{2.15}$$

Taking another derivative with respect to the strain tensor

$$\frac{\partial}{\partial \varepsilon_{kl}}\left(\frac{\partial W}{\partial \varepsilon_{ij}}\right) = C_{ijkl} \tag{2.16}$$

and by the equality of mixed partials, it follows that

$$\frac{\partial^2 W}{\partial \varepsilon_{ij}\partial \varepsilon_{kl}} = C_{ijkl} = C_{klij} = \frac{\partial^2 W}{\partial \varepsilon_{kl}\partial \varepsilon_{ij}} . \tag{2.17}$$

This shows that because of the conservation of energy the elastic stiffness tensor has the property of

$$C_{ijkl} = C_{klij} . \tag{2.18}$$

and as a result the stiffness tensor can have at most 21 independent coefficients known as the elasticity constants.

The Voigt recipe is introduced changing the 3×3×3×3 fourth rank tensor into a compact 6×6 matrix. Transforming *ij* and *kl* into *α* and *β* is as follows:

$$\begin{aligned} &11 \rightarrow 1 \\ &22 \rightarrow 2 \\ &33 \rightarrow 3 \\ &23 = 32 \rightarrow 4 \\ &13 = 31 \rightarrow 5 \\ &12 = 21 \rightarrow 6 \end{aligned} \tag{2.19}$$

so that C_{ijkl} becomes $C_{\alpha\beta}$. Both nomenclatures are used throughout the thesis. When dealing with matrices explicitly, $C_{\alpha\beta}$, will be used more often than not.

2.1.2 Equation of motion

The total force on a material is the sum of the volume, ***V***, and contact forces, ***S***, acting on a material

$$\mathbf{F} = \int_S \mathbf{T} dS + \int_V \mathbf{f} dV \tag{2.20}$$

where ***T*** is the traction applied on the surface ***S*** and ***f*** is the volume force applied on the volume ***V***. In view of Newton's second law of motion this total force is written as

$$\int_{\mathbf{V}} \rho(\mathbf{x}) \frac{\partial^2 u_i}{\partial t^2} dV = \int_{\mathbf{S}} \sum_{j=1}^{3} \sigma_{ij} n_j dS + \int_{\mathbf{V}} f_i dV \ . \tag{2.21}$$

With no volume forces applied and invoking the divergence theorem to the surface force expression the result is

$$\int_{\mathbf{V}} \left(\sum_{j=1}^{3} \frac{\partial \sigma_{ij}}{\partial x_j} - \rho(\mathbf{x}) \frac{\partial^2 u_i}{\partial t^2} \right) = 0 \ . \tag{2.22}$$

This integral is only equal to zero when

$$\rho(\mathbf{x}) \left(\frac{d^2 u_i}{dt^2} \right) = \sum_{j=1}^{3} \frac{\partial \sigma_{ij}}{\partial x_j} , \quad i = 1,2,3 \quad . \tag{2.23}$$

The result is the equation of motion for a 3-dimensional inhomogeneous elastic medium where $\rho(\boldsymbol{x})$ is density as a function of position, $\boldsymbol{u}$ is the displacement vector, x_j is the spatial coordinate and σ_{ij} is the stress tensor. This equation relates the force applied, $\frac{\partial \sigma_{ij}}{\partial x_j}$, to the rate of change of momentum. Combining equations 2.7 and 2.12 gives

$$\sigma_{ij} = \frac{1}{2} \sum_{k=1}^{3} \sum_{l=1}^{3} C_{ijkl}(x) \left(\frac{\partial u_k}{\partial x_l} + \frac{\partial u_l}{\partial x_k} \right) \tag{2.24}$$

and inserted into the equation of motion yields

$$\rho(\mathbf{x})\left(\frac{d^2u_i}{dt^2}\right)=\frac{1}{2}\sum_{j=1}^{3}\sum_{k=1}^{3}\sum_{l=1}^{3}\frac{\partial C_{ijkl}}{\partial x_j}\left(\frac{\partial u_k}{\partial x_l}+\frac{\partial u_l}{\partial x_k}\right)$$
$$+\frac{1}{2}\sum_{j=1}^{3}\sum_{k=1}^{3}\sum_{l=1}^{3}C_{ijkl}(\mathbf{x})\left(\frac{\partial^2u_k}{\partial x_j\partial x_l}+\frac{\partial^2u_l}{\partial x_j\partial x_k}\right) \tag{2.25}$$

where $i, j, k, l = 1,2,3$. It is written in this manner so that the displacement vector ***u*** is on both sides of the equation. To solve this equation a solution of the form

$$\mathbf{u}(\mathbf{x},t)=\mathbf{A}(\mathbf{x})f(\boldsymbol{\eta}) \tag{2.26}$$

is assumed where ***A*** is the amplitude of the displacement and $f(\eta)$ is defined as

$$\boldsymbol{\eta}=v_0[\psi(\mathbf{x})-t] \tag{2.27}$$

where v_0 is a reference velocity, ψ is a wavefront at a given time t_i and t is time. Using expressions 2.26 and 2.27 in equation 2.25 results in an expression of the form

$$af+bf'+cf''=0\,. \tag{2.28}$$

For this equation to hold, each coefficient of the polynomial in f must each equal zero. This results in the following sets of equations:

$$\sum_{j=1}^{3}\sum_{k=1}^{3}\sum_{l=1}^{3}C_{ijkl}(\mathbf{x})A_k\frac{\partial\psi}{\partial x_j}\frac{\partial\psi}{\partial x_l}-\rho(\mathbf{x})A_i=0 \tag{2.29}$$

$$\sum_{j=1}^{3}\sum_{k=1}^{3}\sum_{l=1}^{3}\left[\frac{\partial}{\partial x_j}\left(C_{ijkl}(\mathbf{x})A_l\left(\frac{\partial\psi}{\partial x_k}\right)+C_{ijkl}(\mathbf{x})\frac{\partial A_k}{\partial x_l}\frac{\partial\psi}{\partial x_j}\right)\right]=0 \tag{2.30}$$

$$\sum_{j=1}^{3}\sum_{k=1}^{3}\sum_{l==1}^{3}\left(\frac{\partial C_{ijkl}(\mathbf{x})}{\partial x_j}\frac{\partial A_k}{\partial x_l}+C_{ijkl}(\mathbf{x})\frac{\partial^2A_k}{\partial x_j\partial x_l}\right)=0\,. \tag{2.31}$$

Expression 2.29 is the eikonal equation for an inhomogeneous, anisotropic medium and is the basis for all the modelling performed. For the purpose of this thesis equation 2.30 and 2.31 are not of interest.

2.1.2.1 Eikonal equation

Equation 2.29 can be rewritten as

$$\mathbf{p}^2\sum_{k=1}^{3}\left(\sum_{j=1}^{3}\sum_{l=1}^{3}C_{ijkl}(\mathbf{x})n_j n_l-\rho(\mathbf{x})\mathbf{v}^2\delta_{ik}\right)A_k=0\,, \tag{2.32}$$

where ***p*** is the phase-slowness vector $\frac{\partial\psi}{\partial x_j}$, and ***n*** is the unit vector normal to the wavefront (directional cosine) of ***p***. The velocity, ***v***, is inserted allowing for the slowness ***p*** to come out of the summation. The Dirac delta function factors out the components of ***A***. This expression contains three distinct equations called the Christoffel equations:

$$\mathbf{p}^2\left[\mathbf{\Gamma}-\rho(\mathbf{x})\mathbf{v}^2\mathbf{I}\right]\begin{bmatrix}A_1\\A_2\\A_3\end{bmatrix}=\begin{bmatrix}0\\0\\0\end{bmatrix} \tag{2.33}$$

where

$$\Gamma_{ik}=C_{ijkl}n_j n_l\,. \tag{2.34}$$

From linear algebra it is known that the nontrivial solutions to this equation corresponds to velocities that satisfy

$$\left(\mathbf{p}^2\right)^3\det\left|\Gamma_{ik}-\rho(\mathbf{x})\mathbf{v}(\mathbf{x})^2\delta_{ik}\right|=0\,. \tag{2.35}$$

It follows that the solution to this equation defines three velocities at a given point $\boldsymbol{x=x_0}$ as a function of density and the stiffness tensor. The equation is a third degree polynomial in $\boldsymbol{p}^2$ which can be factored out. Thus, expression 2.35 can be rewritten as

$$\left[\mathbf{p}^2-\frac{1}{\mathbf{v}_1^2(\mathbf{x},\hat{\mathbf{n}})}\right]\left[\mathbf{p}^2-\frac{1}{\mathbf{v}_2^2(\mathbf{x},\hat{\mathbf{n}})}\right]\left[\mathbf{p}^2-\frac{1}{\mathbf{v}_3^2(\mathbf{x},\hat{\mathbf{n}})}\right]=0 \tag{2.36}$$

where $\mathbf{v}_i^2$ are the roots to the polynomial. Since ***p*** is the phase slowness, equation 2.36 is written succinctly as

$$[\nabla \psi(\mathbf{x})]^2 = \frac{1}{\mathbf{v}^2(\mathbf{x},\hat{\mathbf{n}})}. \tag{2.37}$$

2.1.3 Isotropy

Isotropic media has the simplest pattern of nonzero independent components in $C_{\alpha\beta}$, reducing to 2 independent variables, C_{11} and C_{44}.

$$C_{\alpha\beta} = \begin{bmatrix} C_{11} & (C_{11}-2C_{44}) & (C_{11}-2C_{44}) & 0 & 0 & 0 \\ (C_{11}-2C_{44}) & C_{11} & (C_{11}-2C_{44}) & 0 & 0 & 0 \\ (C_{11}-2C_{44}) & (C_{11}-2C_{44}) & C_{11} & 0 & 0 & 0 \\ 0 & 0 & 0 & C_{44} & 0 & 0 \\ 0 & 0 & 0 & 0 & C_{44} & 0 \\ 0 & 0 & 0 & 0 & 0 & C_{44} \end{bmatrix} \tag{2.38}$$

Using the isotropic stiffness tensor in equation 2.35 yields the different velocities of wave propagation. When α and β are equal and less than 4 the result is

$$\frac{\omega^2}{k^2} = v_p^2 = \frac{C_{11}}{\rho} \tag{2.39}$$

corresponding to the P-wave velocity. When α and β are equal and greater than 3 equation 2.35 yields

$$\frac{\omega^2}{k^2} = v_s^2 = \frac{C_{44}}{\rho} \tag{2.40}$$

corresponding to the S-wave velocity. Any other combination of α and β yield trivial solutions.

2.1.4 Transverse isotropy

One of the simplest forms of anisotropic symmetry is called transverse isotropy (TI). This symmetry has one distinct direction, usually *z*, and the elastic properties are invariant to any azimuthal rotation in the *x-y* plane. This symmetry is often used for the anisotropy typically found in sedimentary basins. In this case the elastic tensor has the form

$$C_{\alpha\beta} = \begin{bmatrix} C_{11} & (C_{11} - 2C_{66}) & C_{13} & 0 & 0 & 0 \\ (C_{11} - 2C_{66}) & C_{11} & C_{13} & 0 & 0 & 0 \\ C_{13} & C_{13} & C_{33} & 0 & 0 & 0 \\ 0 & 0 & 0 & C_{44} & 0 & 0 \\ 0 & 0 & 0 & 0 & C_{44} & 0 \\ 0 & 0 & 0 & 0 & 0 & C_{66} \end{bmatrix}. \tag{2.41}$$

Notice that transverse isotropy includes three additional independent elastic parameters over that of isotropy, C_{13}, C_{33} and C_{66}. It can be shown that isotropy is a special case of TI and occurs when $C_{11}=C_{33}$, $C_{66}=C_{44}$ and $C_{13}=C_{33}-2C_{44}$.

In order to determine velocity, the transversely isotropic $C_{\alpha\beta}$ is used in equation 2.35. Adopting the Voigt recipe, the determinant becomes

$$\det\begin{pmatrix} n_1^2 C_{11} + n_2^2 C_{66} + n_3^2 C_{44} - \rho v^2 & n_1 n_2 \left(C_{11} - C_{66}\right) & n_1 n_3 \left(C_{13} + C_{44}\right) \\ n_1 n_2 \left(C_{11} - C_{66}\right) & n_1^2 C_{66} + n_2^2 C_{11} + n_3^2 C_{44} - \rho v^2 & n_2 n_3 \left(C_{13} + C_{44}\right) \\ n_1 n_3 \left(C_{13} + C_{44}\right) & n_2 n_3 \left(C_{13} + C_{44}\right) & \left(n_1^2 + n_2^2\right) C_{44} + n_3^2 C_{33} - \rho v^2 \end{pmatrix} = 0 \tag{2.42}$$

Solving the cubic equation in ρv^2 yields the P-wave, SV-wave and SH-wave velocities. The velocity whose polarization is normal to the direction of propagation is

$$\rho V_p^2 = \frac{1}{2}\left[C_{33} + C_{44} + \left(C_{11} - C_{33}\right)\sin^2\theta + D(\theta)\right] \tag{2.43}$$

where

$$D(\theta)=\{(C_{33}-C_{44})^2+2[2(C_{13}+C_{44})^2-(C_{33}-C_{44})(C_{11}+C_{33}-2C_{44})]\sin^2\theta$$

$$+[(C_{11}+C_{33}-2C_{44})^2-4(C_{13}+C_{44})^2]\sin^2\theta\}^{1/2} . \qquad (2.44)$$

Equation 2.43 corresponds to the P-wave velocity, which is the only mode of interest in this work.

2.2 Weak Anisotropy

In 1986, Thomsen introduced his parameters of α, β, γ, δ, and ε, formulating the cumbersome P-wave velocity equation into a more succinct formulation. The first two parameters describe the vertical P and S wave velocity

$$\alpha_0=\sqrt{C_{33}/\rho} \qquad (2.45)$$

$$\beta_0=\sqrt{C_{44}/\rho} , \qquad (2.46)$$

while ε and γ are a linear combination of the elastic constants.

$$\varepsilon\equiv\frac{C_{11}-C_{33}}{2C_{33}} \qquad (2.47)$$

$$\gamma\equiv\frac{C_{66}-C_{44}}{2C_{44}} \qquad (2.48)$$

Using Thomsen's parameters, the P wave velocity is defined as

$$V_p^2(\theta)=\alpha_0^2[1+\varepsilon\sin^2\theta+D^*(\theta)] \qquad (2.49)$$

where

$$D^*(\theta) \equiv \frac{1}{2}\left(1-\frac{\beta_0^2}{\alpha_0^2}\right)\left\{\left[1+\frac{4\delta^*}{\left(1-\beta_0^2/\alpha_0^2\right)}\sin^2\theta\cos^2\theta + \frac{4\left(1-\beta_0^2/\alpha_0^2+\varepsilon\right)\varepsilon}{\left(1-\beta_0^2/\alpha_0^2\right)}\sin^4\theta\right]^{1/2} - 1\right\} \tag{2.50}$$

and

$$\delta^* \equiv \frac{1}{2C_{33}}\left[2(C_{13}+C_{44})^2-(C_{33}-C_{44})(C_{11}+C_{33}-2C_{44})\right]. \tag{2.51}$$

Making a weak anisotropic assumption and taking a first order Taylor series expansion in the small parameters of δ and ε at a fixed angle the P-wave velocity is simplified to

$$V_p(\theta)=\alpha_0\left(1+\delta\sin^2\theta\cos^2\theta+\varepsilon\sin^4\theta\right) \tag{2.52}$$

where δ is now defined as

$$\delta \equiv \frac{1}{2}\left[\varepsilon+\frac{\delta^*}{\left(1-\beta_0^2/\alpha_0^2\right)}\right]=\frac{(C_{13}+C_{44})^2-(C_{33}-C_{44})^2}{2C_{33}(C_{33}-C_{44})}. \tag{2.53}$$

After making a Taylor series expansion the parameters of δ and ε take on physical significance. In the case of weak anisotropy, the parameter ε is the fractional difference between vertical and horizontal P-wave velocities while the parameter δ controls the near vertical anisotropy. When $\delta = \varepsilon$, the special case of elliptical anisotropy occurs.

For modelling purposes and considering the relative amount of anisotropy present within the earth for most cases, a weak anisotropic assumption will be made. On the basis of this assumption, it is useful to use Thomsen's parameters in this thesis.

2.3 Raypaths in Inhomogeneous Media

Raypaths are a mathematical construct whose trajectory is defined as the direction of energy transport. In homogeneous media, raypaths connect a source point to another given point with a straight line. The time it takes that distance relates to the ray velocity. Rays are not real but they are helpful in understanding the notion of wave propagation. In contrast to the ray velocity, measuring the ratio of distance to time on planes normal to the wavefront is known as the phase velocity. In a general homogeneous anisotropic medium, the normal to a point on the wavefront is not parallel to the ray direction. In isotropic media the ray and phase velocities are equal. Both the ray and phase velocities are useful quantities: Snell's Law and the equation of motion is formulated in terms of phase velocities while the ray quantities follow Fermat's principle of least time defining the path of energy transport.

2.3.1 Isotropy

For homogeneous isotropic media the wave fronts are spheres. As a result the ray and phase velocities unit vectors are parallel. In such cases there is no need to distinguish between these two quantities. For inhomogeneous media the raypath follows the direction dictated by Fermat's principle. This principle states that the raypath taken between two points will be such that the traveltime is minimized. In a homogeneous medium this corresponds to a straight raypath. For the heterogeneous case the raypath bends with changes in property of the media. Snell's Law, a consequence of Fermat's principle, describes this bending. Consider Figure 2.1 shown below.

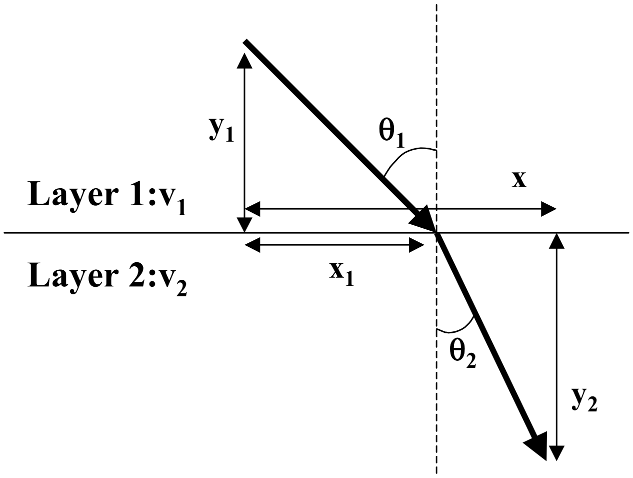

Figure 2.1. Snell's Law and Fermat's Principle of Least Time.

The total time of the ray shown is

$$t = \frac{\sqrt{x_1^2 + y_1^2}}{v_1} + \frac{\sqrt{(x - x_1)^2 + y_2^2}}{v_2} . \tag{2.54}$$

Fermat's principle states that the raypath taken will be that of least time. Taking the derivative of t with respect to x_1 yields

$$\frac{dt}{dx_1} = \frac{x_1}{v_1\left(x_1^2 + y_1^2\right)^{1/2}} - \frac{(x - x_1)}{v_2\left(x_2^2 + y_2^2\right)^{1/2}} \tag{2.55}$$

and equating the derivative to zero yields

$$\begin{aligned} 0 &= \frac{x_1}{v_1\left(x_1^2 + y_1^2\right)^{1/2}} = \frac{(x - x_1)}{v_2\left(x_2^2 + y_2^2\right)^{1/2}} \\ 0 &= \frac{\sin\theta_1}{v_1} = \frac{\sin\theta_2}{v_2} \end{aligned} \tag{2.56}$$

which is Snell's law. Thus, by tracing rays that yield the minimum traveltime, Snell's law will be honoured. In this isotropic case the normal to the wavefront, defined as the phase angle is equivalent to the ray angle and thus determines the raypath in heterogeneous isotropic media (Robinson and Clark, 1986).

2.3.2 Anisotropy

Velocities for an anisotropic media may be expressed as a function of the wavefront normal direction, θ. One of the biggest differences between isotropic and anisotropic media is distinguishing between the group and phase angles. Within isotropic media, the group and phase angle are equivalent since the raypath taken and the wavefront normal are coincident. In general this is not the case for anisotropic media, since the wavefront normal is not coincident with the path of energy transport.

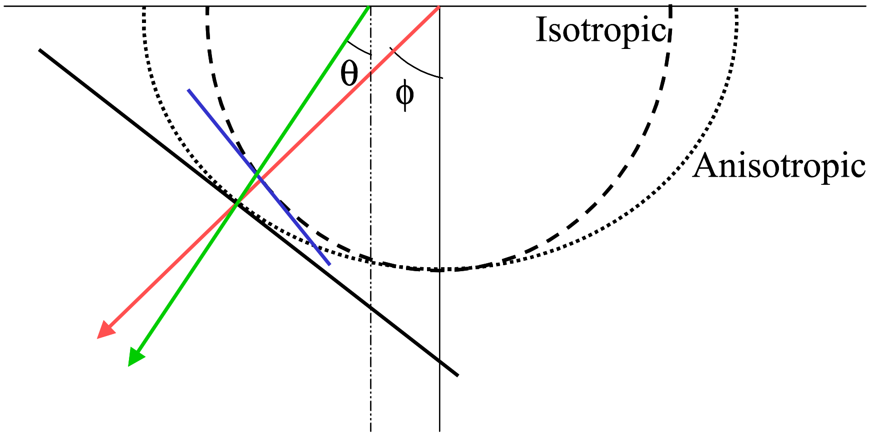

Figure 2.2 Anisotropic and isotropic wavefronts in relation to the group (ϕ) and phase (θ) angle.

Transverse isotropy is illustrated in Figure 2.2 where the wavefront normal is denoted by the phase angle θ, and the ray or group angle by ϕ. Both angles define the same point on the elliptical surface each from a different origin leading to two definitions of velocity. One corresponds to the group angle and the other to the phase angle. In inhomogeneous transversely isotropic media, the phase velocity is used to determine the ray angle that the raypath will travel (Slawinski et al, 2000).

Relations have been derived (Brown et al, 1991) which convert phase angle to group angle. In transversely isotropic media, these relations take on manageable analytic forms. The group velocity, $\boldsymbol{V}$, can be determined from the phase velocity, $\boldsymbol{v}$, using the expression

$$\mathbf{V}^2[\phi(\theta)] = \mathbf{v}^2(\theta) + \left(\frac{d\mathbf{v}}{d\theta}\right)^2 . \qquad (2.57)$$

The group angle is determined from the phase angle by using

$$\phi = \theta + \tan^{-1}\left[\frac{1}{\mathbf{v}}\left(\frac{d\mathbf{v}}{d\theta}\right)\right]. \qquad (2.58)$$

Applying equation 2.49 to equation 2.57 leads to the expression of group velocity expressed using Thomsen's parameters

$$\mathbf{V}_p^2[\phi(\theta)] = \mathbf{v}_p^2(\theta)\left\{1 + \left[\frac{\varepsilon \sin 2\theta + \left(dD^*/d\theta\right)}{2\left[1 + \varepsilon \sin^2\theta + D^*(\theta)\right]}\right]^2\right\}, \qquad (2.59)$$

where the subscript p is used to identify P-wave velocity. Similarly, applying equation 2.49 to 2.58 yields the expression for the group angle

$$\phi_p = \theta_p + \tan^{-1}\left[\frac{\varepsilon \sin 2\theta + \left(dD^*/d\theta_p\right)}{2\left(1 + \varepsilon \sin^2\theta_p + D^*\left(\theta_p\right)\right)}\right]. \qquad (2.60)$$

Thus to determine the path of energy transport from the wavefront normal, the ray velocity and direction are determined using expression 2.59 and 2.60 respectively.

2.4 Finite-Difference Solution to the Eikonal Equation

Vidale (1988) proposed an isotropic solution to the eikonal equation that used a first order finite-difference approximation. The traveltime computation scheme is straightforward and computationally efficient. The solution assumes that the velocity field is divided into a grid comprised of square cells. Within the cells the properties of the medium are constant and propagation occurs as a plane wave.

There are two basic extrapolation stencils used and both make plane wave assumptions. The derivation for the stencils for a two-dimensional model begins with the eikonal equation, seen in equation 2.37 and now expressed as:

$$\left(\frac{\partial t}{\partial x}\right)^2 + \left(\frac{\partial t}{\partial z}\right)^2 = s(x,z)^2, \qquad (2.61)$$

where $s(x,z)$ denotes slowness, the inverse of velocity. Given that the slowness model contains cells whose dimensions are equal, the two differential terms of equation 2.61 are approximated as:

$$\frac{\partial t}{\partial z} = \frac{1}{2h}(t_0 + t_2 - t_1 - t_3) \qquad (2.62)$$

and

$$\frac{\partial t}{\partial x} = \frac{1}{2h}(t_0 + t_1 - t_2 - t_3), \qquad (2.63)$$

where t_0, t_1, t_2 and t_3 are the traveltime values at the corners of a cell and h is the spacing between the points depicted in Figure 2.3. Combining equations 2.62 and 2.63 into equation 2.61 and solving for t_3 yields:

$$t_3 = t_0 + \sqrt{2(hs)^2 - (t_2 - t_1)^2}\,. \qquad (2.64)$$

Given three known traveltimes of a cell, this equation solves for the fourth unknown traveltime. Equation 2.64 is represented pictorially in Figure 2.3.

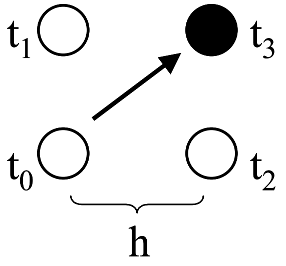

Figure 2.3 Finite difference illustration of equation (2.63), the first extrapolation equation.

This equation will be referred to in this discussion as the first extrapolation equation (EE1).

The first extrapolation equation can also be derived from simple geometry. Consider Figure 2.4 where the traveltimes of t_0, t_1, t_2, and t_3 define the direction of planewave propagation denoted by the dashed lines. Two triangles are formed, each with hypotenuses defined by diagonal points (t_1, t_2) and (t_0, t_3) seen as the finely dotted lines.

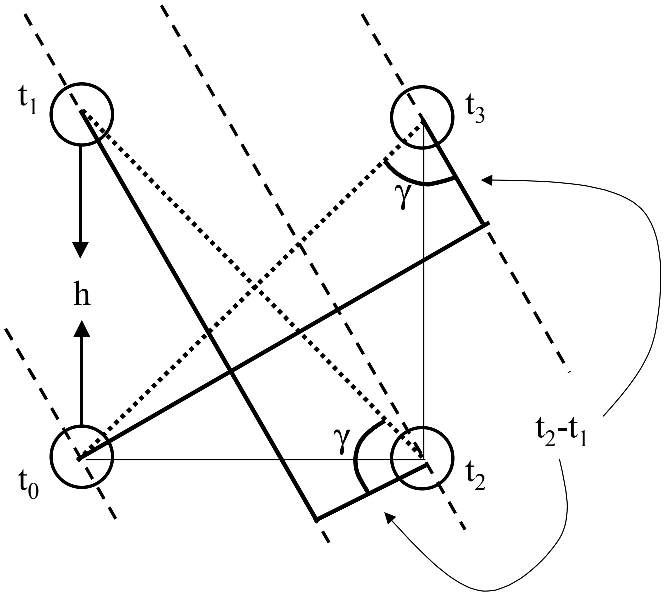

Figure 2.4 Plane-wave approximation to compute traveltimes for first extrapolation equation.

It can be shown that the triangles formed by the identical diagonals also contain a right angle and the common angle γ and therefore are congruent. The hypotenuses of both triangles have a length of $\sqrt{2}h$ with a raypath traveltime of $\sqrt{2}hs$. The triangle that includes the timed points t_2 and t_1 contains a side with the time difference t_2-t_1. It follows from congruency that the time difference between t_3 and the ray perpendicular to the wavefront that passes through the point t_0 is also t_2-t_1. The third side of the triangle is defined by t_3-t_0. Using the Pythagorean theorem, the third side of the triangle can be determined.

$$2h^2 = \left(\frac{t_2 - t_1}{s}\right)^2 + \left(\frac{t_3 - t_0}{s}\right)^2 . \tag{2.65}$$

Solving for t_3 yields EE1.

The second extrapolation equation (EE2) uses a non-centered finite difference scheme. This formula also determines the traveltime to a point using 3 points. However, these points are located at the positions illustrated in Figure 2.5.

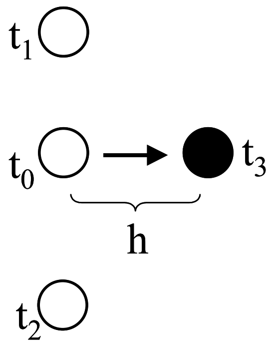

Figure 2.5 Finite-difference illustration of equation 2.67, the second extrapolation equation.

A geometric construction is made in Figure 2.6 where the two identical triangles have been constructed from three inline grid points.

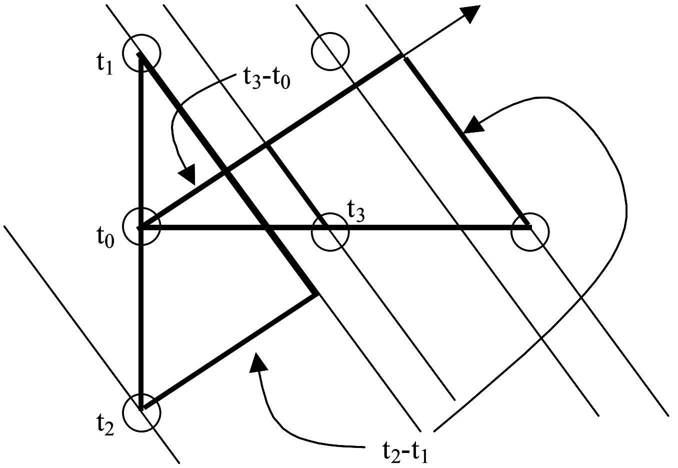

Figure 2.6 Plane-wave approximations to compute traveltimes for the second extrapolation equation.

Each triangle has one side with a time difference of t_2-t_1. The triangle of interest is half the size of the two identical triangles. Thus, instead of using the quantity t_2-t_1, only half the time difference is used. Using the Pythagorean theorem we have

$$\left(\frac{t_3 - t_0}{s}\right)^2 + \left(\frac{\frac{1}{2}(t_2 - t_1)}{s}\right)^2 = h^2 . \tag{2.66}$$

Solving for t_3 yields equation 2.67, the second extrapolation equation,

$$t_3 = t_0 + \sqrt{(hs)^2 - 0.25(t_2 - t_1)^2} \quad . \tag{2.67}$$

The final formula, which is used infrequently, has the form:

$$t = t_0 + h \cdot s \tag{2.68}$$

where t is time, h is the distance travelled and s, is the slowness. In this case the raypath is coincident with the cell boundary and the value of s chosen from the bounding cells is that which produces the smallest traveltime.

The geometrical solutions found which assume plane waves are included to illustrate that the finite-difference approximation made to the eikonal equation is a plane wave solution. It will also provide a foundation for the scheme used in transversely isotropic media.

2.5 Isotropic Finite-Difference Traveltime Approximation Schemes

Vidale's (1988) early attempts at creating traveltime maps expanded traveltimes along a square. When traveltimes of the square was completed, the traveltimes on the next outer shell of the square was computed. This was accomplished by first using EE2 at the minimum traveltime on each side of the square and then using EE1 to compute the remainder of the points on each side. This method lead to problems with maintaining minimum traveltimes at harsh velocity contrasts. The computational scheme used to determine traveltimes in this thesis follows the method proposed by Qin et al. (1992). The calculation of traveltimes proceeds in a causal fashion attempting to mimic an expanding wavefront. To accomplish this, the two same basic approximations are made: the velocity within each cell is constant and propagation through the cell occurs as a plane wave. The following presents a summary of the original expanding wavefront algorithm using the EE1 and EE2 finite-difference approximations.

2.5.1 Expanding wavefront algorithm

The method proposed by Qin et al. (1992) attempted to approximate an expanding wavefront and provided a significant improvement to the method introduced by Vidale (1988). In the wavefront expansion scheme, a surrounding traveltime shell, each containing potential new traveltimes, was estimated. However, only the minimum time of the estimation zone was updated as an accepted traveltime. New estimation points were then calculated in the area of the accepted points to update the estimation zone. The process is repeated until all points in the model become accepted. By updating the minimum in the estimation zone, the accepted points tend to mimic an expanding wavefront. This method is able to maintain the minimum traveltime or first arrivals when compared to Vidale's expanding square algorithm. In the following diagrams the estimation zone is shown as open circles and the accepted traveltimes are shown as solid black circles. The minimum of the estimation zone is identified by a grey circle while new estimation zone points are identified by striped circles.

Beginning from a single source point designating zero time and using equation 2.68, the vertical and horizontal points surrounding the source point are calculated.

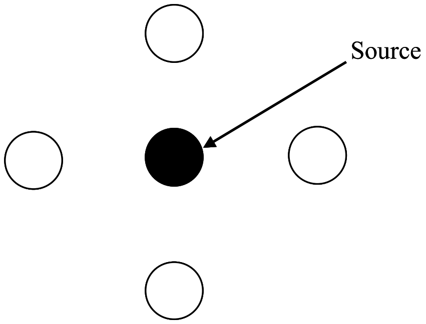

Figure 2.7 Points vertical and horizontal to the source are computed using equation 2.68

The corner points are then calculated using the first stencil, EE1.

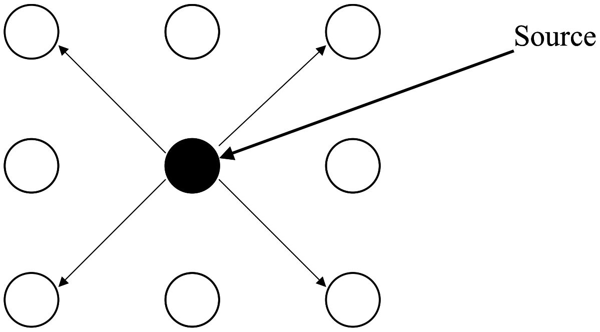

Figure 2.8 Corner points are calculated using the first extrapolation equation.

These 8 points surrounding the source point compose the first estimation zone. The minimum of this estimation zone is removed and added to the accepted points as demonstrated in Figure 2.9. All points surrounding the accepted points are estimated or re-estimated to construct a new estimation zone. The following figures illustrate this process.

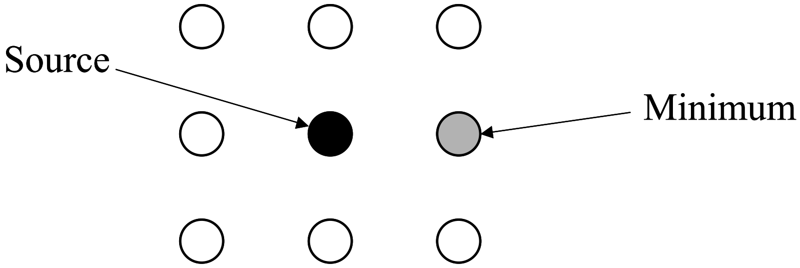

Figure 2.9 Source point surrounded by the first estimation zone. The first minimum of the estimation zone is the black point.

In determining the new estimation zone, a specific order of computation must be followed. First all previously un-estimated horizontal and vertical points are computed via EE2 seen in Figure 2.10.

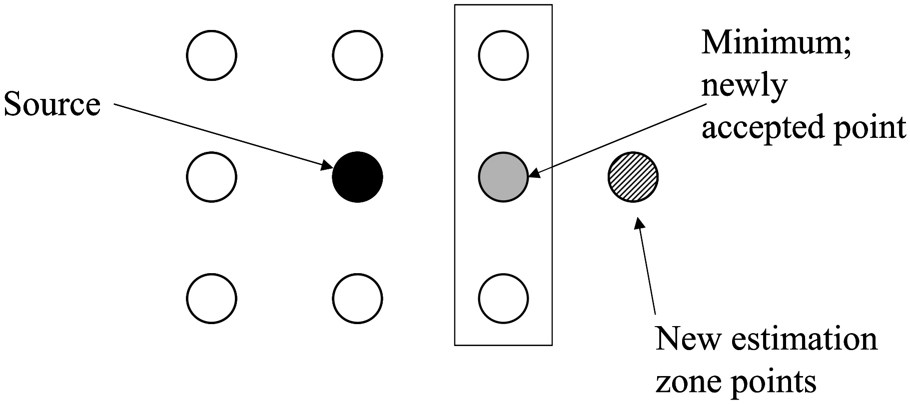

Figure 2.10 Points used to calculate (outlined by the rectangle) the first new point of the new estimation zone via the second extrapolation equation.

The remaining horizontal and vertical points are re-estimated, using both the first and the second stencil as illustrated in Figure 2.11.

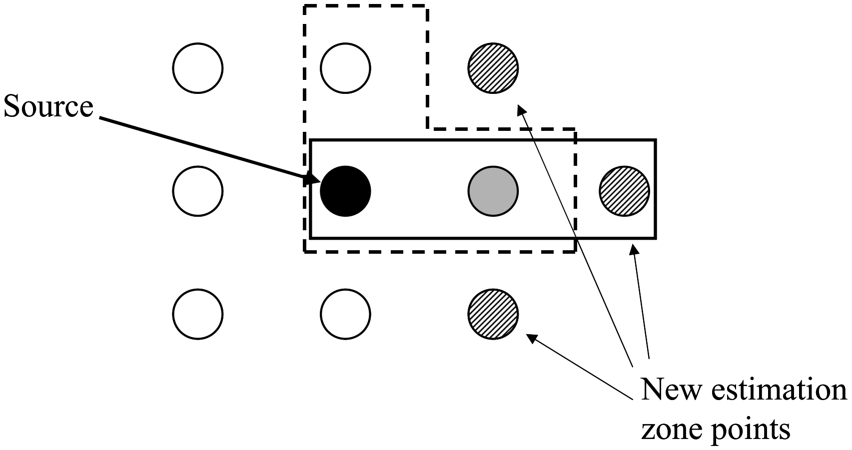

Figure 2.11 Re-estimation of points using the first stencil (dashed box) or the second stencil (solid box).

After calculating the re-estimates, the minimum of the estimates is kept within the new estimation zone. This is done for all non-accepted horizontal and vertical points. Notice that the new estimates must be computed before the re-estimated points to facilitate the use of the second extrapolation equation. This is the reason a specific order of calculation was followed. Finally, as shown in Figure 2.12, the diagonal points are then estimated or re-estimated using EE1.

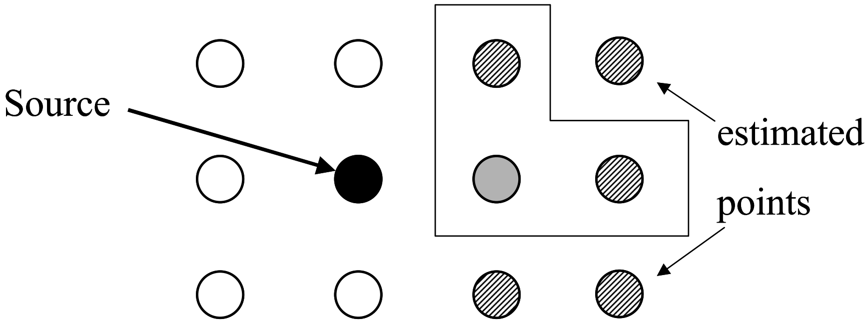

Figure 2.12 All corner points are estimated or re-estimated using the first extrapolation equation.

Notice that if the horizontal and vertical points are not calculated first, the first stencil cannot be used to estimate the corner points. The use of the simple formula is kept to a minimum when following this causal wavefront expansion method. Testing has shown that the simple formula is primarily used along the boundaries of the model where an insufficient number of points are available to use other stencils. After one sequence, there are two accepted points and ten estimated points as seen in Figure 2.13.

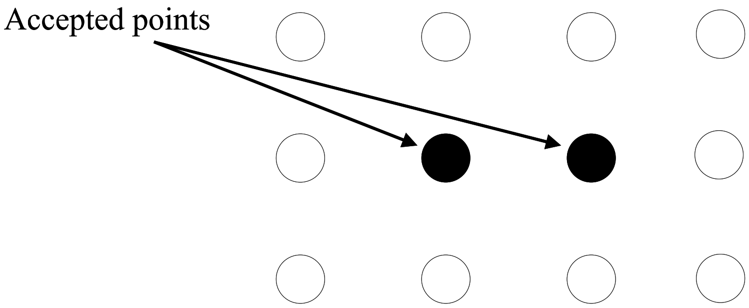

Figure 2.13 View of the estimation zone.

In the manner described above, the pattern of choosing the minimum from an estimation zone, denoting it as accepted and creating a new estimation zone is repeated until all points of the model grid become accepted traveltime points.

2.6 Anisotropic Finite-Difference Traveltime Approximation Scheme

The method proposed by Qin et al was originally was designed for isotropic media. Modifications have been made to the expanding wavefront algorithm to approximate anisotropy. The method proposed here uses cell sizes of equal dimensions and Thomsen's anisotropic parameters to define the medium. Adapting the expanding wavefront algorithm to include anisotropy, the assumed velocity within each cell is no longer constant. Instead, the anisotropic constants within the cell, namely, α_0, β_0, δ, and ε are constant, and if the direction of plane wave propagation is known, the phase velocity through a cell can be determined.

2.6.1 Anisotropic stencils

Since the finite-difference solution to the eikonal equation assumes plane wave propagation, the phase velocity will be used in determining traveltimes. The anisotropic modifications consist of determining the wavefront normal propagation direction. To determine the propagation direction, the schematic diagram seen in Figure 2.14 is used.

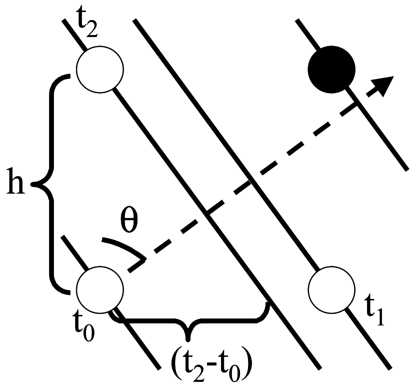

Figure 2.14 Schematic demonstrating the derivation of the phase angle *θ*.

The slope of the line normal to the plane waves is

$$\tan\theta = slope = \frac{\Delta z}{\Delta x} = \frac{h}{h\left(\dfrac{t_2 - t_0}{t_1 - t_0}\right)} = \left(\frac{t_1 - t_0}{t_2 - t_0}\right) \tag{2.69}$$

The arctangent of the slope is the propagation angle that establishes the slowness. This slowness is then used in the first extrapolation equation to calculate the traveltime to the unknown point.

The second extrapolation equation is not used in the anisotropic case. Instead a scheme based on Huygen's principle is used. To determine the traveltime to the unknown point shown in Figure 2.14 traveltimes are linearly interpolated between t_1 and t_2.

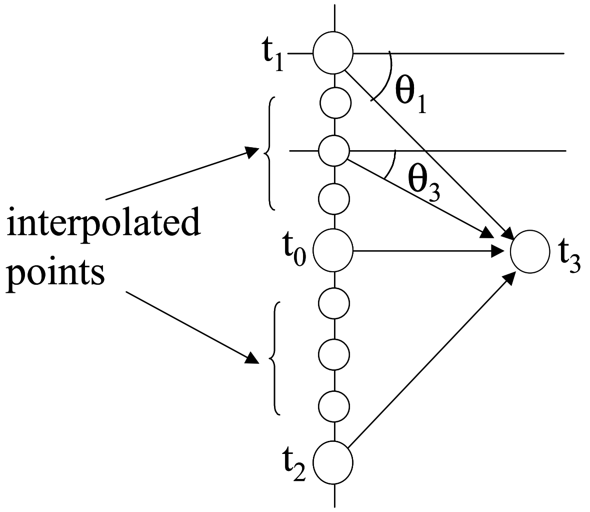

Figure 2.15 Second anisotropic stencil used for traveltime determination.

The phase angle of the plane wave is calculated using the positions of the known and interpolated traveltime points. The time to the unknown point is calculated using

$$t_{3i} = t_i + {h_i}/{V_p(\theta_i)} \tag{2.70}$$

where h_i is the distance from the ith interpolated point to the unknown point and V_i is the angle dependent velocity from the ith known point to the unknown point t_3. The minimum traveltime is chosen as the first arrival.

2.6.2 Anisotropic wavefront expansion scheme

The anisotropic wavefront expansion scheme is similar to that of the isotropic case. The exceptions are in the extrapolation equations used and the determination of the velocity used to propagate the waves. Corner points are calculated using equation 2.69 to get the phase angle, equation 2.52 to get the phase velocity and equation 2.64 to compute the traveltime. The traveltime to the unknown point is computed using the first extrapolation equation. For instances when EE2 would be used, the first anisotropic stencil shown in Figure 2.14 is used instead.

The anisotropic scheme starts with an initial estimation zone from which a minimum is reassigned as an accepted point. The estimation zone is then reconstructed and the process is repeated. The algorithm stops when all grid points in the model become accepted points. Besides the angle dependent velocity and the first anisotropic stencil, the wavefront expansion scheme is identical to that of the isotropic case.

2.7 Raypath Determination

The tomography workflow requires not only the time taken to pass through a cell but also the distance traversed by a ray through each cell. Modelling these two quantities is important in updating the velocity in each cell since both quantities are needed in formulating the traveltime equations. The modelled rays should bend at velocity contrasts according to Snell’s law and it is important to do this accurately as the time-distance relationship will dictate the output tomograms accuracy.

The principle of reciprocity, as described in Asakawa and Kawanaka (1993), states that the summation of a traveltime map with the origin at a source location and a traveltime map with the origin at a receiver location has a minimum corresponding to the path taken from the source to the receiver. Based on Fermat’s principle of least time, the raypath taken will be that of minimum time. The method used to determine raypaths is founded on both these principles.

Using a traveltime map of a source location and starting from a scatterpoint the ray is propagated back to the source following the path of least time. The principal of reciprocity states, that this also corresponds to the ray from the source to the scatterpoint. By summing the source and receiver traveltime maps, the minimum traveltime along the reflector of interest is the scatterpoint from which rays can be “back-traced” to the source or receiver. In this manner both source and receiver raypaths can be determined from a traveltime map of a source or receiver to any scatterpoint.

2.7.1 Isotropic raytracing

A raypath trajectory is determined from the traveltime map of a source or receiver. For each cell the direction of the plane wave is determined using equation 2.69, and the computed traveltimes of the cell nodes, t_1, t_2, t_3 and t_4. Assuming that the reflection point or the receiver is at t_1, a path along the normal to the plane wave is extrapolated from t_1 until it intersects the cell boundary. The time taken to traverse the cell is added to interpolated traveltime at the intersection point, t_a. This time is compared to the time it would take to travel along the boundaries of the cell, $t_{2\mathrm{int}} = hs\cos\theta$ and $t_{3\mathrm{int}} = hs\sin\theta$, where θ is the normal to the wavefront, and added to the traveltimes at t_2 and t_3 respectively. The paths along the cell boundaries represent head waves. The minimum of these three times identifies the minimum time travel path taken. If the starting point in a cell is in between known traveltime points, the starting time is determined through linear interpolation. Figure 2.15 diagrams the three possible trajectories within a cell.

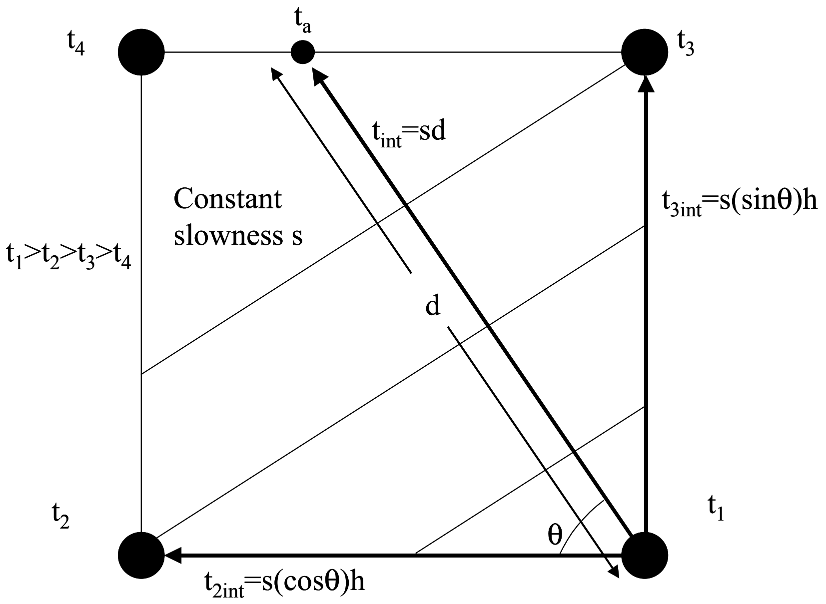

Figure 2.16 Comparison of three traveltimes to determine the raypath taken. One ray corresponds to the wavefront normal while the other two correspond to head waves. The minimum traveltime of t_a+t_{int}, $t_2+ t_{2int}$, and $t_3 + t_{3int}$ is the correct raypath.

The process is repeated with the minimum point used as the new starting point for the next cell and stops once the ray has been traced back to the source.

In a transmission experiment only a traveltime map of the source location is required. The ray is traced from the receiver location back to the source. For reflecting raypaths, two traveltime maps are required as well as the reflector position. The first traveltime map is of the source and the second is of the receiver. The two traveltime maps are summed and the minimum traveltime along the reflector is the reflection point of the ray. The problem is then divided into two transmission problems. The raypath from the reflection point to the source is determined using the source traveltime map and the raypath from the reflection point to the receiver is determined using the receiver traveltime map. The combination of the two rays defines the path for a ray emanating from a source, reflected at an impedance contrast, and detected at a receiver. In cases where the location of the receiver is coincident with the source location, only one traveltime map is required.

2.7.2 Anisotropic raytracing

As in the isotropic case, the raypath in TI media is determined using the principles of reciprocity and Fermat. For anisotropic propagation, the raypath does not follow the wavefront normal. Instead, energy propagation is in the direction of the group angle. Given the appropriate anisotropic parameters and the phase angle (θ), the group angle (ϕ) can be determined as using equation 2.60.

Phase velocities were used to compute traveltimes. Following Fermat's principle of least time, the ray will follow the path of least time. The traveltimes computed either using the group or phase velocities are equal. As such one can move freely from phase to group velocities and angles via equation 2.59 and 2.60. Figure 2.17 demonstrates that with plane wave propagation, group and phase velocities result in the same traveltime.

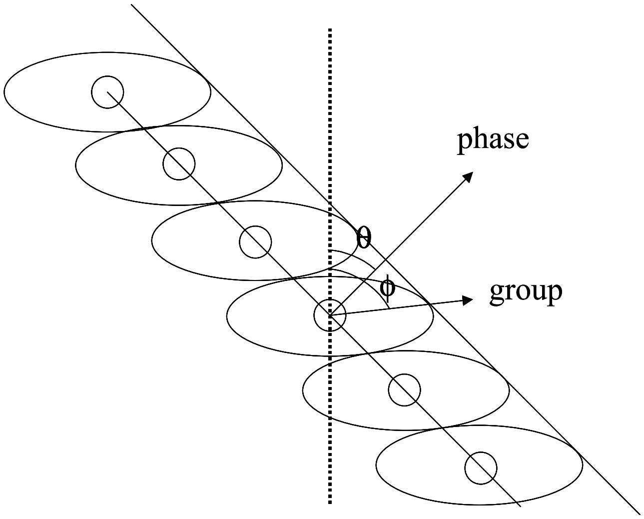

Figure 2.17 Illustration demonstrating that group and phase velocities yield the same traveltime for plane wave propagation.

Each circle represents a Huygen secondary point source of the wavefront. Each secondary source emits a wave that constructively interferes along the next plane wave shown. The intersection of the second plane wave and the secondary source wavelets show that the time required to reach the second plane wave can be computed by either using the group or phase velocity. Thus, for any plane wave, the traveltime can be computed using the wavefront normal or the path along which energy propagates.

Raytracing in transversely isotropic media requires a modification to the isotropic case. Instead of propagating the ray along the wavefront normal, using the anisotropic parameters of the cell, the phase angle is converted to a group angle. Using the group velocity, the time taken to traverse the cell is computed and added to the interpolated time where the extrapolated ray intersects the cell boundary, t_a. This time is compared to the refracted times of $t_{2\text{int}} = s(\varphi)(\cos\varphi)h$ and $t_{3\text{int}} = s(\varphi)(\sin\varphi)h$, each a function of group angle and velocity, added to the times of t_2 and t_3 respectively. This is illustrated schematically in Figure 2.18.

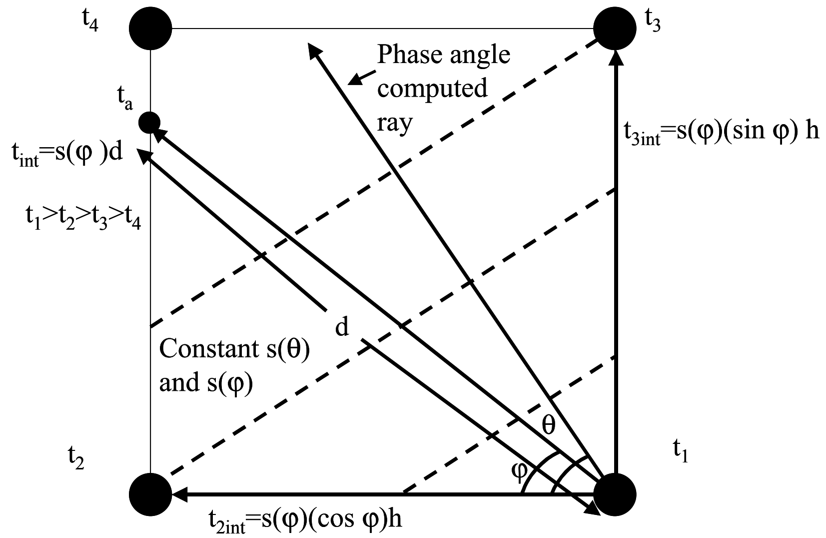

Figure 2.18 Comparison of three traveltimes to determine the raypath taken. One ray corresponds to the group angle determined from the wavefront normal while the other two correspond to head waves. The minimum traveltime of t_a+t_{int}, $t_2+ t_{2int}$, and $t_3 + t_{3int}$ is the correct raypath. Note that velocities used are group velocities.

In transversely isotropic media the conversion between phase and group angles is given by Brown et al (1991) and shown in this thesis as equations 2.57 and 2.59. Aside from the direction taken and the velocity used, the algorithm followed is identical to the isotropic case and finishes once the ray has been traced back to the source.

2.7.3 Errors in raytracing

A wavefront approximates a plane wave if observing it at a sufficient distance away from the source. As the observation distance decreases, the plane wave approximation breaks down. Approaching the source, plane waves can no longer approximate the curvature of a wavefront. As a result, the error in raypaths will increase as the distance to the source decreases. Conversely, moving away from the source makes the plane wave approximation a better one leading to more accurate raypaths. In homogeneous and isotropic media, using a plane wave approximation will result in good raypath estimates at large distances from the source and give poorer raypath estimates as it approaches the source. Figure 2.19 illustrates the inaccuracies that occur when approximating a curved wavefront using plane waves.

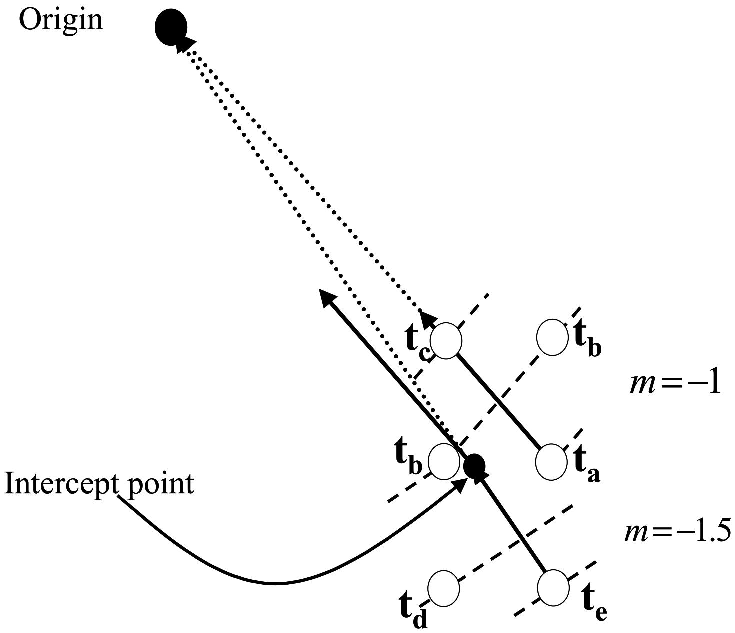

Figure 2.19 Diagram illustrating inherent errors in the plane wave approximation to a curved wavefront. Finely dotted lines show true raypath while the solid lines show deviation from true raypath when using a plane wave assumption within cells.

Figure 2.19 illustrates the inherent errors in making plane wave approximations of a smooth, curved wavefront. Two cells are shown, one defined by computed traveltime nodes of t_a, t_b, and t_c while the other is defined by traveltime nodes, t_a, t_b, t_d, and t_e. It is determined that the upper cell has a wavefront normal slope of m=-1 using equation 2.69. The lower cell has a wavefront normal slope of m=-1.5 also computed using equation 2.69. Assuming that this is a homogeneous medium, it is known that the raypath should be a straight line. The raypath connecting traveltime node t_e to the origin should have one constant slope, yet different from the slope connecting traveltime node t_a to the origin. This figure shows how each cell has a slope associated with it and that rays that travel through a cell will adopt the slope determined by the cell. As such the ray will not be straight as neighbouring cells will not have the same slope. Further away from the source, neighbouring cells will have a more smoothly varying slope value leaving a straighter raypath. Closer to the source, neighbouring cells will have a larger variation in slope values resulting in less straight raypaths. As a consequence of the inherent errors in assuming a plane wave solution to the eikonal equation, the limitations of the raytracing algorithm used should be considered when evaluating results.

2.8 Traveltime and Raytracing Testing

Simple testing is done to determine the level of accuracy for the isotropic and anisotropic traveltime and raytracing methods described previously. Testing involves two homogeneous media, one isotropic and the other transversely isotropic. Traveltimes are compared against the analytical solutions and raypaths are compared against the line connecting the source and receiver (equivalent to the raypath in a homogeneous medium). Both test models have a lateral and vertical extent of 500 meters with a 10 by 10 cell size and the source is placed at the surface (0 meters depth) and 0 meters of distance. In the isotropic model, the P-wave velocity used is 3000 m/s. In the transversely isotropic model, the P-wave velocity used is 3000 m/s, the S-wave velocity used is 1732 m/s and $\varepsilon=\delta=0.2$.

2.8.1 Isotropic traveltime testing

Figure 2.19 shows the traveltimes contours for the isotropic model while Figure 2.20 shows the errors between the estimated an analytically computed traveltimes.

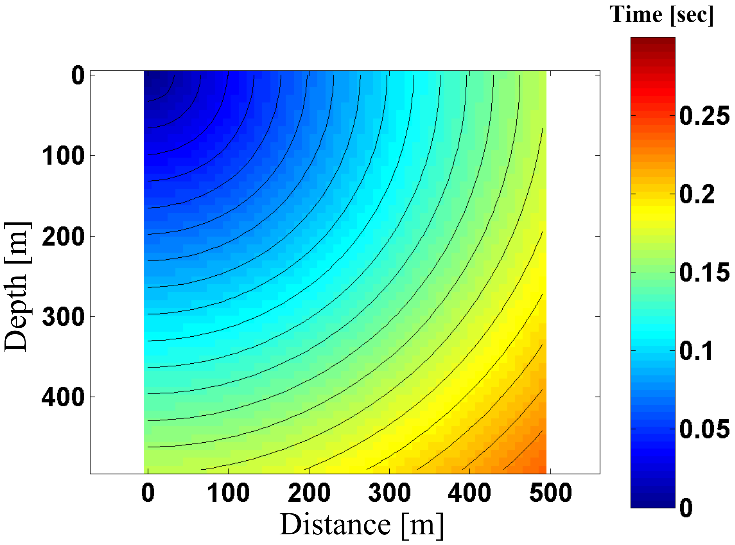

Figure 2.20. Isotropic traveltime contours in a constant velocity medium of 3000 m/s.

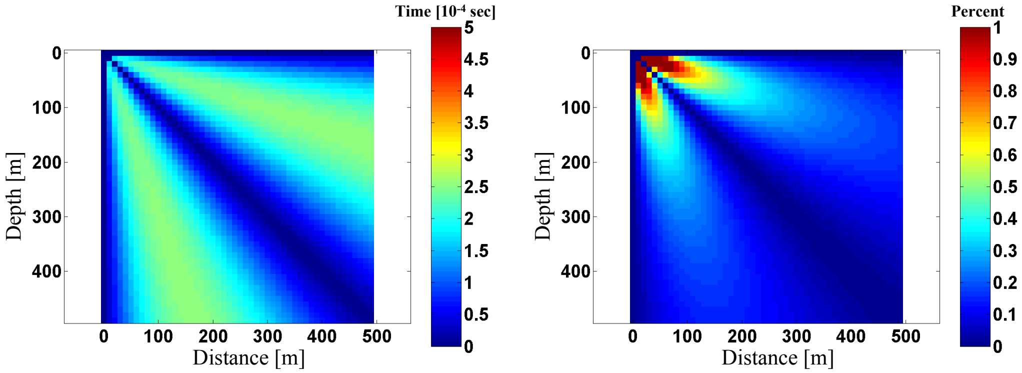

a) b)

Figure 2.21. Isotropic traveltime error between estimated and analytically computed traveltimes for a constant velocity medium: a) traveltime error and b) percent error.

The largest amounts of errors are in areas where the largest amount of curvature would exist between grid nodes. Notice that as the distance from the source increases the total amount of error decreases as indicated in Figure 2.21a. From the percent error perspective, after a distance of 10 cells from the source the error decreases drastically, from

1% error to 0.1% error. Figure 2.22 shows the visual comparison between the estimated raypath and the theoretically correct one.

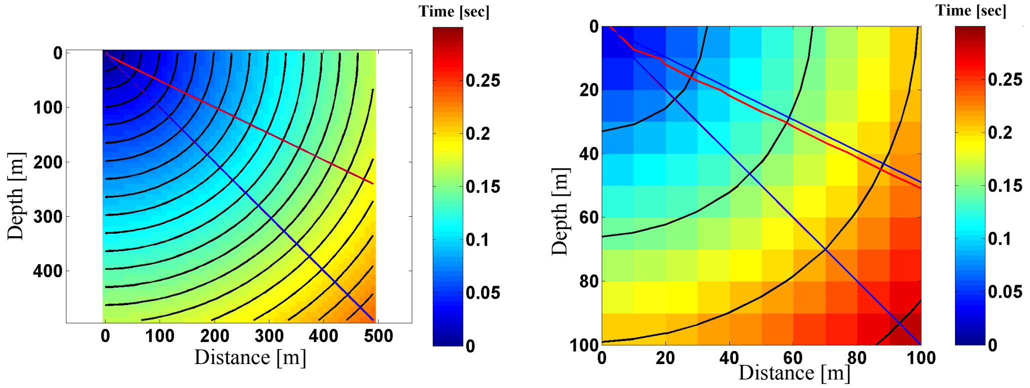

a) b)

Figure 2.22. Isotropic raypath plots showing raypath error for a constant velocity medium: a) receiver at 490 and 240 meters depth and b) close up view of raypath error near the source.

Note in the above figures that there are two receivers; one placed at a node where the traveltime has been determined very accurately, and at another node whether the traveltime estimation error is at its highest. Figure 2.22b shows the relationship between traveltime estimation error and raypath error. The accurate traveltime path with a receiver located at 490 meters depth is very accurate. The less accurate traveltime path, with a receiver located at 240 meters depth, is less accurate and increasingly so as one approaches the source. This is a result of the plane-wave approximation made and as a result both the traveltimes and raypaths will be predictably less accurate between nodes where a large amount of curvature exists.

2.8.2 Transverse isotropy traveltime testing

Figure 2.23 shows the traveltimes and contours for the transversely isotropic model.

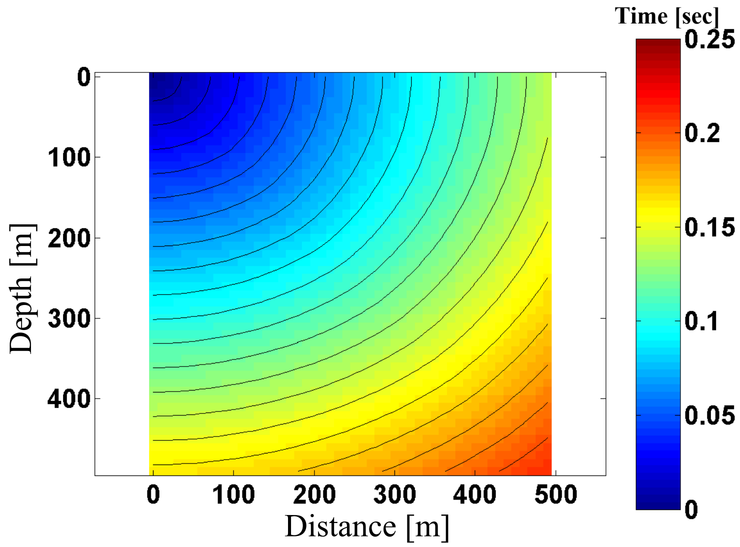

Figure 2.23. Transverse isotropy traveltime contours for homogeneous anisotropic media with α_0=3000 m/s, β=1732 m/s and ε=δ=0.2.

Figure 2.24 below, shows the absolute and percentage error between the estimated and analytically computed traveltimes. Notice the relative increase in error compared to that of the isotropic estimates. This is function of the difference in wavefront curvature for anisotropic and isotropic media.

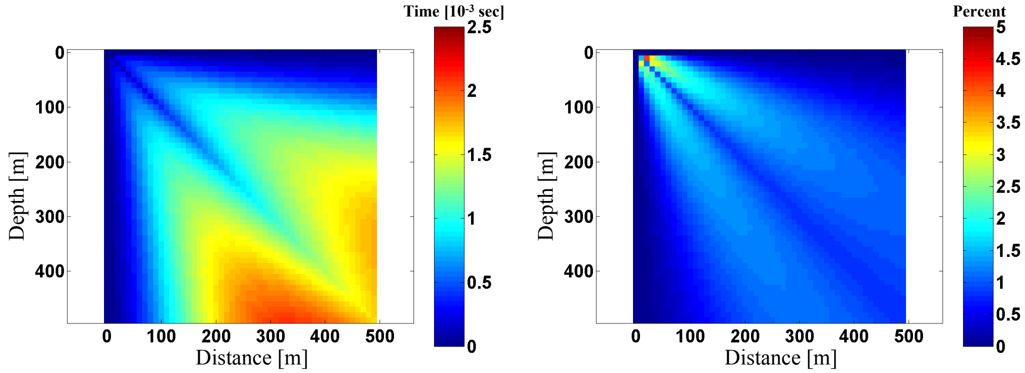

a) b)

Figure 2.24. Transverse isotropy traveltime error between estimated and analytically computed traveltimes for a homogeneous anisotropic medium: a) traveltime error and b) percent error.

The asymmetric nature of the absolute error plot reflects the asymmetric nature of the anisotropic wavefront. The largest amount of curvature is clearly indicated in red at a depth of 450 meters and a lateral distance of 300 meters in Figure 2.24a. The error increase is attributed to the increase in curvature between nodes and the inability of a planewave to accurately approximate it. Note again that the percent error decreases as the distance from the source increases.

Figure 2.25 below, shows the comparison between the estimated raypaths and the theoretically correct raypaths in a transversely isotropic media. Note that the receiver positions are the same used in the isotropic case.

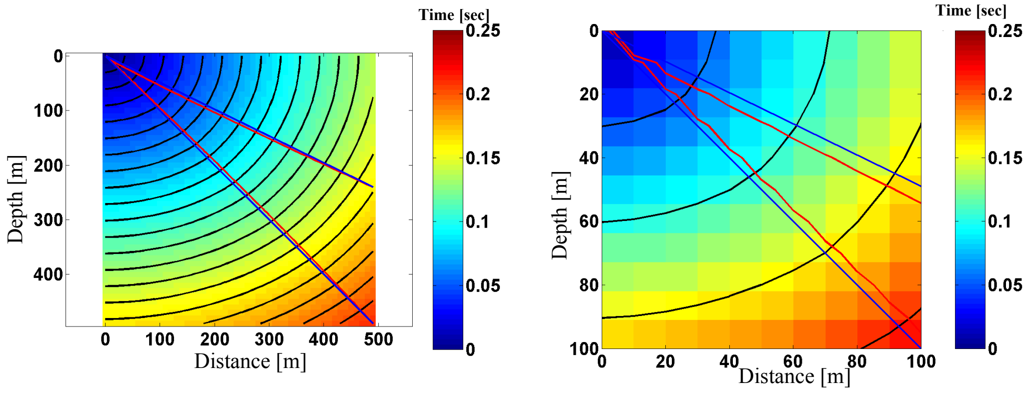

a) b)

Figure 2.25. Transverse isotropy raypath plots showing raypath error for a homogeneous anisotropic medium: a) receiver at 490 and 240 meters depth and b) close up view of raypath error near the source.

This simple test shows the error increase in raypath estimation for transversely isotropic media. These figures also show the direct correlation between the traveltime accuracy and raypath accuracy. The increase in error from the isotropic model to the transversely isotropic model is attributed to the incompatibility between the wavefront and cell geometry. The optimal geometry would increase the concentration of cell nodes in areas of greatest wavefront curvature. This would depend on the anisotropic parameters of ε and δ, making optimal traveltime and raypath estimation model dependent. In general however, given that the distance between source and receiver is sufficiently far (at least 10 cells), the accuracy is sufficient to produce accurate tomograms. This is especially true when the accuracy of picking traveltimes from data becomes an issue.

2.9 Summary

This chapter discussed the theoretical foundations of the modelling algorithm to be used in tomography. After deriving the eikonal equation for a general inhomogeneous anisotropic media, a finite-difference solution is proposed based on work by Vidale (1988), Thomsen (1986) and Qin et al (1992) for isotropic and transversely isotropic media. This solution attempts to honour expanding wavefronts, computing them in a causal fashion. Once traveltimes have been computed, raypaths are then determined based on the principle of reciprocity and Fermat's principle of least time. These tools now serve as the foundation for traveltime inversion.

CHAPTER 3: TOMOGRAPHIC VELOCITY ANALYSIS

Interpreting seismic data in complex structures requires accurate subsurface images that may be obtained through prestack depth migration. Prestack depth migration inherently requires an accurate velocity model that can be determined via tomography. These tomographic methods use recorded traveltimes and modelled traveltimes through an initial velocity estimate to estimate a new velocity model. Velocity models are updated such that the error between the modelled and observed traveltimes is minimized. It is assumed that the velocity model yielding the minimum residual traveltimes provides the best representation of subsurface velocities.

Unfortunately the set of equations relating observed values to estimated velocities are ill-posed. Most ill-posed tomographic problems are mixed-determined: a combination of overdetermined and underdetermined problems. This is a result of acquisition geometry in combination with subsurface velocity structures. The solutions to mixed-determined problems are often nonunique and consequently require additional information. Using a priori information can reduce the solution space and identify a unique solution.

This chapter develops the theory for isotropic and transversely isotropic traveltime tomography for transmitted and reflected waves. Linear equations are presented for each waveform representing the physical mechanism of the responses recorded. Finally the inherent nonuniqueness and possible constraint options for traveltime tomography are discussed.

3.1 Tomography

In a typical seismic survey, a wavefield is propagated into the earth and reflected back to surface where amplitudes and traveltimes are recorded by receivers. The geophones record a number of coherent signals including transmitted and reflected energy. Based on the acquisition geometry, different tomographic data are used that best represents the mechanics of the seismic experiment.

There are two basic types of tomography used in this thesis, crosswell and surface tomography, each referring to the acquisition geometry commonly associated with the signal used for inversion: transmission and reflection respectively. Crosswell or transmission tomography deals with a signal that has not undergone any reflection. In croswell tomography the signals of interest do not arise from reflection due to changes in seismological impedance. The recorded amplitudes correspond to signal following the path of least time from source to receiver, in this thesis modelled as transmitted waves. Cross borehole acquisition geometries highlight such signals. The direct source to receiver traveltime reveals information of the unknown parameters to be determined: the subsurface velocities of the survey area.

Surface tomography attempts to determine subsurface velocities using a signal that has undergone reflection at seismologic impedance contrast along its travel path. A seismic reflection survey with both sources and receivers located at the surface is the typical geometry involved in surface tomography. Sources create the initial signal that propagates into the earth, is reflected and later measured by receivers located at the surface. Surface tomography can estimate the velocities of the medium as well as reflector position.

Choosing the traveltimes used for tomography, representing either transmitted or reflected energy, must be accomplished carefully to assure inversion quality. For the transmission case, one seismic event is chosen for each shot gather that best exemplifies the purely transmitted wavefront. In the reflection case, the number of seismic events chosen depends on the number of reflectors. For one shot gather that contains four reflectors, there will be four coherent signals that best represents the wavefront traveltime function.

Traveltime picking will not be discussed further in this work, though the quality of the picks directly affects quality of the inversion solution.

3.1.1 Formulation of the problem: isotropic tomography

The inversion problem will be formulated by adopting a notation that is similar to that of Bishop et al (1985). Let x denote the horizontal distance along the earth's surface and let z represent depth. The two-dimensional area of interest is divided into nx by nz square cells each with a slowness denoted by $s(j)$ numbered from left to right and top to bottom. There are n reflectors in the model with depths denoted as $z_n(x)$. The column vector $\boldsymbol{m}$ is constructed containing all of the parameters that describe the model. In crosswell tomography, the parameters consist of $(nx \cdot nz)$ velocities, $s(1)$ to $s(nx \cdot nz)$. Surface tomography requires the number of parameters in $\boldsymbol{m}$ to be $(nx \cdot nz + n \cdot nx)$. This includes the number of slowness cells added to the product of the number of reflectors and the number of points needed to describe a reflector. Figure 3.1 illustrates the model variables.

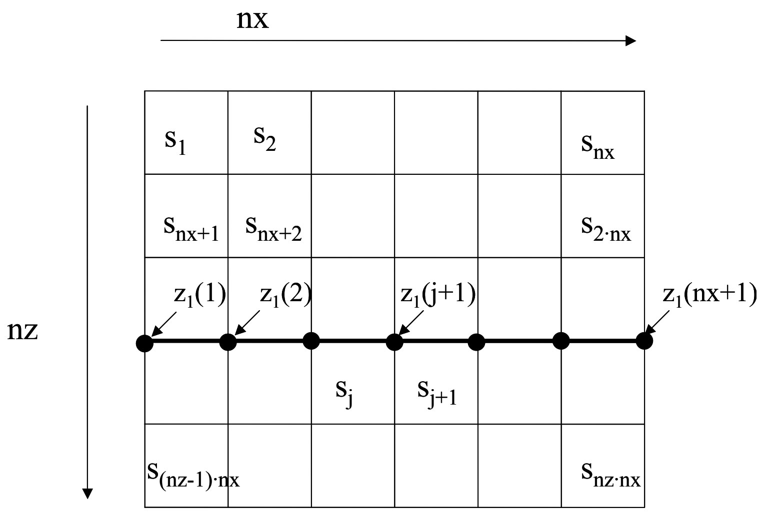

Figure 3.1 Diagram illustrates an nx by nz model with one reflector defined by nx+1 points.

A column vector $\boldsymbol{t}$ is defined to represent the recorded data of the survey. The number of entries in $\boldsymbol{t}$ is a function of the number of sources (ns), receivers (nr) and reflectors (n) in the model. This is equivalent to the number of rays (N) that have been recorded. In crosswell tomography there are $n_r \cdot n_s$ rays while in surface tomography, the number of reflectors adds an additional factor of *n* leading to $n \cdot n_r \cdot n_s$ rays. The sources and receivers are numbered so that the first entry in the ***t*** vector corresponds to the traveltime between the first source and the first receiver. The traveltime between the next *nr* receivers and that first source comprise of the next *nr*-1 entries. The pattern is followed for all remaining sources. Thus, in surface tomography, each source-receiver pair will contain *n* times more entries than crosswell tomography. Figure 3.2 illustrates a simple experiment of one source, three receivers and 2 reflectors resulting in six recorded rays.

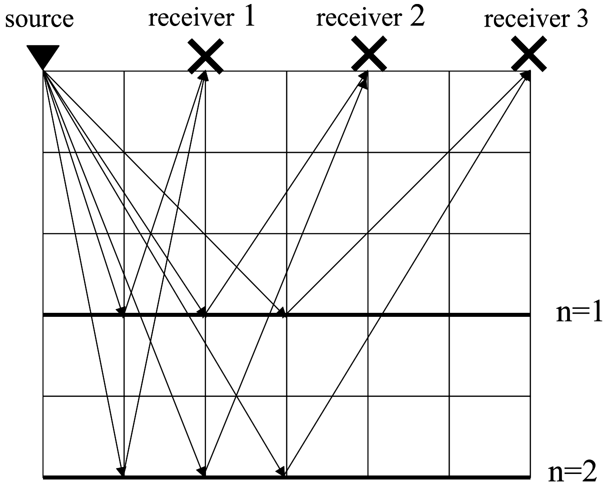

Figure 3.2 Diagram illustrating the number of rays as a function of the number of sources, receivers and reflectors. The corresponding vector ***t*** will contain entries of $[t_{111},t_{121},t_{131},t_{112},t_{122},t_{132}]^T$ where t_{ijk} correspond to the *i*th source, *j*th receiver and *k*th reflector.

The method proposed to determine subsurface velocities consists in offering an initial model through which traveltimes are simulated and compared to the recorded data. The problem consists of minimizing the error between the modelled traveltimes and the recorded traveltimes. By minimizing the error, the vector ***m*** ascertained correctly defines the subsurface properties. When the traveltime error is zero, it is assumed that the resulting velocity model and reflector depth locations are exactly those that are found in the subsurface. However, the fitting of data traveltimes with model response is a necessary but not sufficient criterion for finding the correct solution to the traveltime inversion problem. There are many possible solutions since in practice most tomographic problems are never uniquely determined.

The mathematical formulation is neatly presented in Lines and LaFehr (1989), and is summarized below. The traveltime for the *i*th ray, t_i, is the sum of the product between the slowness and the distance travelled through each cells. i.e.,

$$t_i = \sum_j d_{ij} m_j \tag{3.1}$$

where d_{ij} is the distance of the *i*th ray in the *j*th cell and m_j is the slowness of the *j*th cell. An illustration shown in Figure 3.3 demonstrates a ray whose traveltime is t_1.

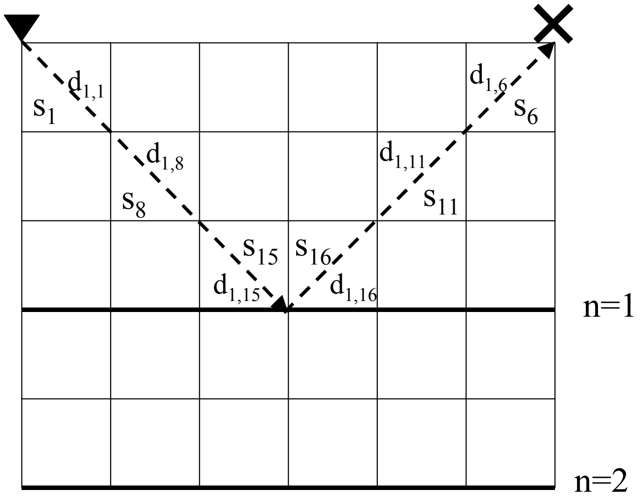

$$d_{1,1} \cdot s_1 + d_{1,8} \cdot s_8 + d_{1,15} \cdot s_{15} + d_{1,16} \cdot s_{16} + d_{1,11} \cdot s_{11} + d_{1,6} + s_6 = t_1$$

Figure 3.3 Traveltime corresponds to the sum of the product of distances travelled and slowness within each cell for a ray that traverses from source (triangle) to receiver (x).

In matrix notation the traveltime equations can be written succinctly as

$$\mathbf{Dm} = \mathbf{t} \tag{3.2}$$

where the matrix ***D*** has elements d_{ij} which are the partial derivatives of time with respect to slowness $\left(\frac{\partial t}{\partial s}\right)$, ***m*** is the slowness vector and ***t*** is the traveltime vector. The matrix ***D*** is a

Jacobian matrix as it maps model parameters ***m*** into data parameters ***p*** (Marsden and Tromba, 1996). The elements of ***D*** correspond to the distances travelled by the rays within a cell. In heterogeneous media equation 3.2 becomes nonlinear in slowness due to Snell's law. However, model parameters are computed iteratively by solving linearized equations from some starting model. In full matrix form this is expressed as

$$\begin{bmatrix} d_1^1 & \cdot & d_{nx\cdot nz}^1 \\ \cdot & \cdot & \cdot \\ d_1^N & \cdot & d_{nx\cdot nz}^N \end{bmatrix} \begin{bmatrix} s_1 \\ \cdot \\ s_{nx\cdot nz} \end{bmatrix} = \begin{bmatrix} t^1 \\ \cdot \\ t^N \end{bmatrix} \tag{3.3}$$

where D_j^i refers to the *i*th ray and the *j*th cell. Since the initial model is usually incorrect it is useful to rewrite equation 3.3 as

$$\mathbf{D\Delta m} = \mathbf{\Delta t} \tag{3.4}$$

where ***Δt*** is the residual traveltime, whose components correspond to the difference between the modelled and recorded traveltimes, and ***Δm*** the parameter update vector. The updated slowness solution is given by adding ***Δm*** to the original vector ***m***. Note that it is assumed that between equations 3.2 and 3.4, **D** does not change.

For surface tomography some information of the reflecting interface is required. The reflecting interface can be represented as unknowns in the tomographic formulation, interpreted after each iteration or assumed to be known throughout the entire process. In this thesis the reflector depth will be assumed to be known leaving equation 3.3 to represent both crosswell and surface tomography. Once the values of ***D*** are computed, model update parameters are computed by construction of a pseudo-inverse discussed in the subsequent chapter.

3.1.2 Formulation of the problem: anisotropic tomography

A greater number of unknowns are parameterized within the Jacobian matrix to include anisotropy in the tomographic inversion. Since slowness becomes a function of four Thomsen parameters α_0, β_0, δ and ε the model vector ***m*** now increases in length to $4 \cdot nx \cdot nz$ elements for crosswell and surface tomography.

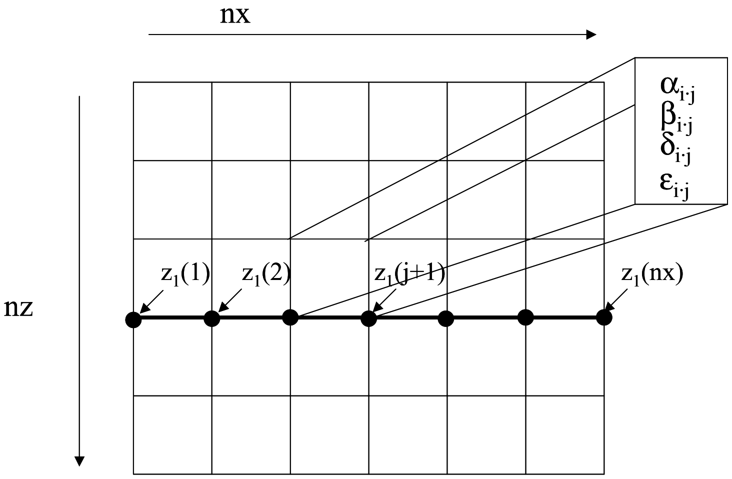

Figure 3.4 Figure illustrates the number of parameters required to model transversely isotropic media.

Similarly, for the matrix ***D***, the number of columns increases to equal the number of rows of the column vector ***m***. However the number of rows in ***D*** remains the same as it was in the isotropic case, representing the number of rays.

The matrix ***D*** is constructed from the partial derivatives of time with respect to α_0, β_0, δ and ε are computed using the following analytical expression. With the traveltime defined as

$$t = \alpha_0^{-1}\left(1 + \varepsilon \sin^2 \theta + D^*(\theta)\right)^{-1/2} d \tag{3.5}$$

where *d* is the distance travelled by the ray in the cell multiplied by cell slowness determined by the anisotropic parameters and the propagation angle θ. These partial derivatives show to first order how each parameter affects traveltime. Each of these variables can now be perturbed to minimize traveltime error.

However, there are complications in attempting to minimize such a complex system of equations. Two main complications that arise are the large number of unknowns as well as the inherent nonlinearity in the problem. Using a weak anisotropic assumption Thomsen linearized the problem and decreased the number of unknowns. The inversion solution will tend to converge by expressing the problem in a linear form and by decreasing the number of unknowns. Using Thomsen's linear expression change the traveltime function to

$$t = \alpha_0^{-1}\left(1 + \delta \sin^2\theta \cos^2\theta + \varepsilon \sin^4\theta\right)^{-1} d \quad . \tag{3.6}$$

Note that there is no longer a linear dependence on β_0. This equation can be further simplified if $\delta \sin^2\theta \cos^2\theta + \varepsilon \sin^4\theta$ is << 1 which is most often the case. Taking the binomial series expansion further approximates expression 3.6 to

$$t \approx p_0\left(1 - \delta \sin^2\theta \cos^2\theta - \varepsilon \sin^4\theta\right) d \tag{3.7}$$

where p_0 is the inverse of α_0. The traveltime expression is reduced to three unknowns: p_0, δ and ε. It is chosen to solve for three parameters in two steps: the first solves for p_0, while the second solves for ε and δ. To solve for p_0, the derivative of equation 3.7 with respect to p_0 is given by

$$\left(\frac{\partial t}{\partial p_0}\right) = \left(1 - \delta \sin^2\theta \cos^2\theta - \varepsilon \sin^4\theta\right) d \quad . \tag{3.8}$$

This equation shows how p_0 affects traveltime and how the Jacobian matrix is determined for the only dependent variable on time. Updates to p_0 follow by solving

$$\begin{bmatrix} a_1^1 & \cdot & a_{nz\cdot nx}^1 \\ \cdot & \cdot & \cdot \\ a_1^N & \cdot & a_{nz\cdot nx}^N \end{bmatrix} [\Delta p] = \begin{bmatrix} \Delta t^1 \\ \cdot \\ \cdot \\ \cdot \\ \Delta t^N \end{bmatrix} \tag{3.9}$$

where a represents $\left(\frac{\partial t}{\partial p_0}\right)$. Updating values for second and third parameters uses the derivative of time with respect to ε and δ defined as

$$\left(\frac{\partial t}{\partial \varepsilon}\right) = -d\left(\sin^4 \theta\right) p_0 \tag{3.10}$$

and

$$\left(\frac{\partial t}{\partial \delta}\right) = -d\left(\sin^2 \theta \cos^2 \theta\right) p_0 \, . \tag{3.11}$$

These parameters are updated by solving

$$\begin{bmatrix} e_1^1 & \cdot & e_{nz\cdot nx}^1 & d_1^1 & \cdot & d_{nz\cdot nx}^1 \\ \cdot & \cdot & \cdot & \cdot & \cdot & \cdot \\ e_1^N & \cdot & e_{nz\cdot nx}^N & d_1^N & \cdot & d_{nz\cdot nx}^N \end{bmatrix} \begin{bmatrix} \Delta\varepsilon_{\cdot} \\ \cdot \\ \Delta\varepsilon_{nx\cdot nz} \\ \Delta\delta_1 \\ \cdot \\ \Delta\delta_{nx\cdot nz} \end{bmatrix} = \begin{bmatrix} \Delta t^1 \\ \cdot \\ \cdot \\ \cdot \\ \Delta t^N \end{bmatrix} \tag{3.12}$$

where e and d denote the derivatives of $\left(\frac{\partial t}{\partial \varepsilon}\right)$ and $\left(\frac{\partial t}{\partial \delta}\right)$ respectively. Inverting ***D*** solves for the model update parameters.

3.2 Uniqueness of Solution

Most geophysical problems are overdetermined, underdetermined or mixed-determined. As a result, even with noise free observations, perfect modelling, and minimization of the sum of the squares of the errors, the solution computed is still nonunique. Nevertheless, using geologic knowledge of the area as constraints an acceptable solution can be found.

Mixed-determined problems occur when a combination of underdetermined and overdetermined model parameters exist. The overdetermined parts of the problem correspond to parts of the model with a high number of raypaths while the underdetermined parts of the model have no or very low number of raypaths. Mixed-determined problems are best defined when compared to even-determined problems. In the even-determined case, there exists exactly enough information to determine model parameters uniquely. This corresponds to the matrix ***D*** containing an equal number of linearly independent ray equations as there are model parameters. Overdetermined parameters are those in which there are more equations than model parameters in the system of equations. Underdetermined problems consist of model parameters with an insufficient number of equations required to solve the system of equations. In both the overdetermined, underdetermined and thus mixed-determined cases, more than one possible solution exists. In practice, tomographic problems are neither overdetermined nor underdetermined but a combination of both making it more difficult to solve the inversion problem uniquely.

3.2.1 Overdetermined problems

The nonuniqueness associated with overdetermined problems consists of the number of equations constraining the model parameter values. Given modelling or traveltime picking errors, each equation results in a different solution for a given model parameter. With an inconsistency in parameter solution, any number of estimates can yield equally adequate inversion results.

3.2.2 Underdetermined problems

The nonuniqueness inherently present in an underdetermined problem is a function of the number of combinations in which the parameters can be modified to achieve the recorded response. A typical example is found in isotropic surface tomography. Given a survey area containing one reflecting interface, inherent ambiguity exists in determining reflector depth and the velocity of the medium. Increasing the velocity of the medium and increasing the depth of the interface will yield the same traveltimes as decreasing the velocity and decreasing the depth of the interface. This ambiguity is demonstrated in Figure 3.5.

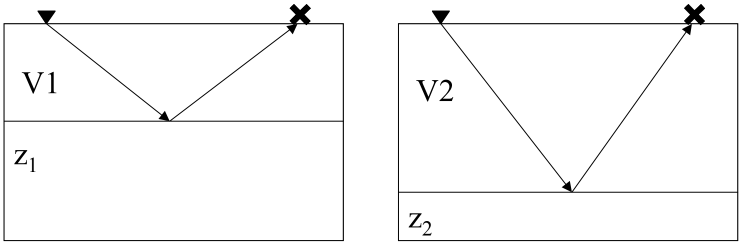

Figure 3.5 Illustration of the inherent ambiguity in surface tomography. Both models yield the same traveltime response since V1 > V2 and $z_2 > z_1$.

It follows that with an increase in the number parameters that define the recorded response, translates into a greater number of combinations that can recreate the recorded response. With an increase in the number of unknowns, as in anisotropic surface tomography, there will be an increase in solution ambiguity. In practice, underdetermined values consist of model cells with little or no ray coverage. These areas within survey area are called shadow zones and are illustrated in Figure 3.6.

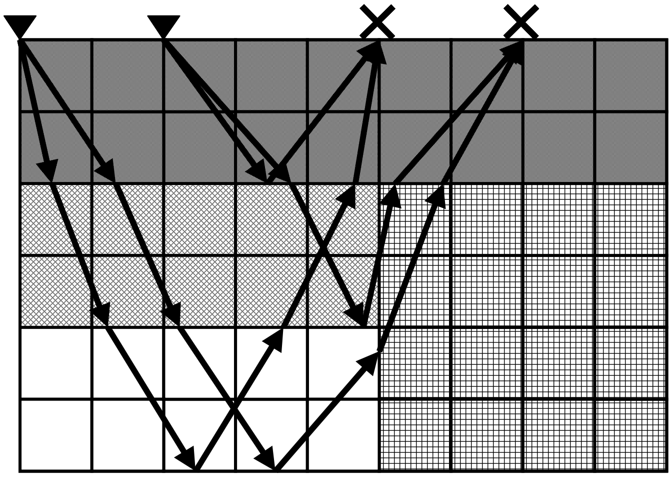

Figure 3.6 Reflection experiment demonstrating cells with no ray coverage. Each different cell pattern denotes different velocities

Cells within the shadow zone do not contribute to the solution and can adopt any parameter value without affecting the inversion result. These cells lead to the possibility of an infinite number of solutions. These types of situations are referred to as ill-posed problems.

3.2.3 Physical causes of nonuniqueness

Most tomographic problems are ill-posed and mixed-determined. This is a function of the acquisition geometry and the subsurface physical properties. The inability to construct an experiment which leads to an even-determined problem is an intrinsic trait of traveltime tomography.

A necessary condition for achieving an even-determined problem and thus a unique solution is the equal number of linearly independent equations and unknowns. The number of observations is easily controlled by the number of sources and receivers in the experiment. To ensure that the number of observations is equal to the number of unknowns, the cell size can be modified as well as the number of parameters used to describe the physical properties of a cell.

However, it is not sufficient that the number of observations equal the unknown parameters because the observations must comprise of a uniform ray distribution. A uniform ray distribution is defined as an equal number of linearly independent rays traversing through each cell. A set of linearly independent rays are those with different raypath distances and angles through cells. The raypaths are a function of the velocity model and the acquisition geometry. Slow velocity zones will repel rays acting as underdetermined parameters while high velocity zones will attract rays and act as overdetermined parameters. In most heterogeneous models an appropriate acquisition geometry must be used which will correctly distribute rays equally amongst all cells while accounting for ray bending due to velocity contrasts. In practice this is impossible. Supplying the appropriate acquisition geometry is not always feasible since it can only be determined once the nature of the subsurface structure is known. Thus given that no tomographic problem will be uniquely solved, adding constraints to the problem becomes important in inverting for physical parameters.

3.3 Constraints

Along with processes of modelling and solving a set of linear equations, constraining the inversion problem is one of the most important component of tomography. Constraints are required for determining accurate and unique solutions. The constrained values include any of the unknown variables to be determined. This can range from velocity in transmission tomography to the anisotropic parameters of α, δ, ε and reflector depth in anisotropic reflection tomography. The constraints consist of fixing cell values, limiting the range of cell values and even filtering the result. The constrained values are determined using basic knowledge of the surrounding geology or any well log information in the area. In general, inversion constraints lead to a solution that is more accurate and reliable.

3.3.1 High-frequency constraint

The simplest inversion constraint to apply is a high-cut filter to the output tomogram. The resulting tomogram is filtered to eliminate inaccuracies that arise from data errors after inversion. These errors arise from either having noisy data or inaccurate modelling. The noisy data points correspond to small singular values which are amplified after inversion. Filtering removes unrealistic discontinuous anomalies in tomograms. Common filters applied are simple two-dimensional smoothers that take the average value of the surrounding cells. Other smoothing methods have been used such as the α-trim means (Scales and Gersztenkorn, 1988) in an attempt to increase tomogram fidelity. This filter works within a range of the mean and median of the data. The range is tailored to smooth the tomogram without destroying sharp geologic features. Spatial coherency filters are also used and are devised to smooth out high frequency noise while leaving coherent tomogram values unchanged (Zhou, 1993). Unfortunately, the majority of the available methods are unable to determine the quality of the inversion solution and blindly filter the tomogram to remove any high frequency components. An optimal tomogram resolves the high frequency velocity anomalies for depth imaging.

3.3.2 A priori information

Another method in obtaining a unique result is to constrain the inversion solution by adding additional information. For overdetermined problems two different types of constraints can be used to stabilize the solution. The first type of additional information constrains the solution to be situated as close to the original model estimate as possible while minimizing the residual traveltimes. The second is to weight certain data points more than others thereby minimizing any solution ambiguity from two different observations. Using these two methods, additional criteria are added to discriminate between possible solutions.

To circumvent the nonuniqueness of an underdetermined problem, a number of different techniques can be used. One technique is to reacquire a larger number of observations leading to a greater number of equations and as a result better ray coverage through each cell. Another method to overcome underdetermined problems is to constrain the solution to a range of parameter values. By limiting the possible model parameter values the solution subspace is decreased thereby eliminating a number of the possible solutions dominated by shadow zones. It is apparent that by constraining the range of allowable model parameter values both underdetermined and overdetermined problems can solved uniquely. Thus by imposing such a constraint, mixed-determined problems can also be solved.

3.4 Summary

Tomography is a statistical technique that, when applied to geophysics, determines geologic parameters from recorded observations. Assuming an initial model, traveltimes are simulated and compared to the recorded traveltimes. This technique allows determination of an accurate velocity profile suitable for prestack depth migration.

The tomographic techniques presented allow for determination of isotropic and transversely isotropic properties. The greatest problem for the method presented is the nonuniqueness of the solution, a function of acquisition geometry and the subsurface properties. Most tomographic problems are mixed-determined thereby containing parameters which are underdetermined and others which are overdetermined. The natural physical system makes it almost impossible to obtain an even-determined problem thus leading to the use of constraints within the solution process. Constraints are required to discern between the unreasonable and reasonable solutions. The constraint techniques proposed are developed in the following chapter.

CHAPTER 4: CONSTRAINED INVERSION

A common problem in seismic tomography is the lack of adequate data required for accurate traveltime inversion. The inherent nature in which data are acquired and the subsurface velocities of the survey area results in a nonuniform distribution of raypaths. In such instances the statistical nature of tomographic inversion biases the solution to reflect acquisition parameters instead of geologic properties.

Ill-posed inversion problems fall within three different classes: underdetermined, overdetermined and mixed-determined problems. Underdetermined problems are those in which there are more unknowns than observations while overdetermined problems have more observations than unknowns. Mixed-determined problems are a combination of underdetermined and overdetermined problems with both overdetermined and underdetermined unknowns. In each of these cases inversion constraints are necessary for determining a unique solution.

This chapter outlines the method used for solving the traveltime tomography problem, discusses the theory of inversion and presents the two distinct techniques in stabilizing the inversion process. The methods presented solve the problem by constructing a pseudo-inverse and introducing a stabilization technique based on the quasi-null space. Two different stabilizing methods are presented each using the quasi-null space to assess solution reliability. The first stabilization method is a dynamic smoother that filters unreliable solutions. The second stabilization method integrates two velocity tomograms, each computed from different seismic experiments over the same geologic region. Testing demonstrates that using the quasi-null space as the foundation for inversion reliability yields superior tomograms. Before introducing the two new techniques, concepts eigenvalues, eigenvectors, null spaces and the theory of Singular Value Decomposition are developed following the work done by Scales et al. (2001).

4.1 Some Linear Algebra

The linear geophysical inverse problem is characterized by the following equation

$$\mathbf{Dm} = \mathbf{t} \tag{4.1}$$

where ***D*** is a $n\times m$ matrix in a linear vector space defined by $R^{n\times m}$ with n rows (data) and m columns (model parameters). The vector ***m*** is an m-component model vector and ***t*** is the n-component data vector. The notation used in this thesis is as follows: in equations, uppercase letters will denote matrices and lowercase letters denote vectors. In addition they appear in bold in the text while scalar values are in italics and are not bold. The matrix ***D*** in equation 4.1 maps the model vector ***m*** into a data vector ***t***. In traveltime tomography the model parameters ***m*** are unknown, ***t*** represents the acquired data in the form of traveltimes and ***D*** is the Jacobian matrix which contains the physics governing the relationship between model parameters and traveltimes. In general we would like to find the inverse to ***D*** to determine the model parameters ***m***,

$$\mathbf{m} = \mathbf{D}^{-1}\mathbf{t} \; . \tag{4.2}$$

The matrix ***D*** is often rectangular and has no inverse. Therefore a method of determining a generalized inverse of ***D*** must be devised. To do so the properties of an $n\times m$ matrix of interest in inversion theory are first discussed based on the work by Scales et al (2001).

4.1.1 Subspaces

A subspace is defined as a nonempty subset of a vector set that satisfies the following conditions: 1) the sum of any two elements in ***D*** is an element in ***D*** and 2) the scalar multiple of any element from ***D*** is an element in ***D***. In general, an $n\times m$ matrix ***D*** can be divided into four subspaces. In a matrix ***D*** in $R^{n \times m}$, the span of columns must be a subspace of R^n and is called the column space. Similarly the span of rows is a subset of R^m and is called the row space. Another important subspace of ***D*** is one that satisfies the homogeneous equation

$$\mathbf{Dx} = \mathbf{0} \tag{4.3}$$

This subspace of ***D*** is called the null space. Just as there is a null space for the columns of ***D*** there is also a null space for the rows of ***D***. The row null space, known as the left null space is defined by

$$\mathbf{D^T x} = \mathbf{0}\,. \tag{4.4}$$

The null space and the row space are subspaces of R^m while the left null space and the column space are subspaces of R^n.

To determine the size, or dimension, of the null spaces the number of linearly independent columns and rows must be known. In fact, the number of linearly independent columns is equal to the number of linearly independent rows for any matrix ***D*** in $R^{n \times m}$. This number *r*, is known as the rank of the matrix and is the dimension of the column space. The dimension of the null space is then *m-r*. The dimension of the row space also equals *r* and the dimension of the left null space is *n-r*.

4.1.2 Eigenvalues and eigenvectors

There are special vectors, ***x***, that when operated on by a matrix, ***D***, only scales the vector by λ,

$$\mathbf{Dx} = \lambda\mathbf{x} \quad . \tag{4.5}$$

If equation 4.5 is satisfied then $\boldsymbol{x}$ is an eigenvector of the square matrix $\boldsymbol{D}$ associated with the eigenvalue λ. In order that $\boldsymbol{x}$ be an eigenvector, λ must chosen so that ($\boldsymbol{D}$-$\lambda\boldsymbol{I}$) has a null space and $\boldsymbol{x}$ lies in that null space. This means that

$$Det(\mathbf{D} - \lambda\mathbf{I}) = 0 \quad . \tag{4.6}$$

Let $\boldsymbol{D}$ be an $n\times n$ matrix with n linearly independent eigenvectors. $\boldsymbol{D}$ can at most have n linearly independent eigenvectors although not all square matrices posses' n linearly independent eigenvectors.

Let $\boldsymbol{S}$ be a matrix whose columns are these eigenvectors. The matrix $\boldsymbol{S}$ has the property that it diagonalizes $\boldsymbol{D}$ via

$$\mathbf{\Lambda} = \mathbf{S}^{-1}\mathbf{DS} \tag{4.7}$$

where the elements of the diagonal matrix $\boldsymbol{\Lambda}$ are the eigenvalues of $\boldsymbol{D}$. In general, any matrix in $R^{n\times n}$ with n distinct eigenvalues can be diagonalized. Note that a matrix can be invertible without being diagonalizable.

Determining if the eigenvectors are linearly independent consists of eigenvector/eigenvalue decomposition. If n eigenvectors of an $n\times n$ matrix correspond to n different eigenvalues, then the eigenvectors are linearly independent.

4.1.3 Orthogonal, projection and symmetric matrices

Important classes of matrices are orthogonal matrices. Such a matrix $\boldsymbol{D}$ satisfies the equation of the form

$$\mathbf{D}^{\mathbf{T}}\mathbf{D} = \mathbf{I} \tag{4.8}$$

Such matrices map a vector into another vector of the same length. Let d_i denote the *i*th column of the matrix ***D***. The outer product of $d_i d_i^T$ is an $m \times m$ matrix. The action of this matrix is to project a vector on the one-dimensional subspace spanned by d_i. Consider the sum of two projection operators $v_i v_i^T$ and $v_j v_j^T$,

$$v_i v_i^T + v_j v_j^T \, . \tag{4.9}$$

This will project any vector in R^m onto the plane spanned by v_i and v_j. In general this property is written as

$$\sum_{i=1}^{p} v_i v_i^T \, . \tag{4.10}$$

If the only terms included in the sum are associated with the r nonzero eigenvalues then the projection operator on the non-null space

$$\sum_{i=1}^{r} v_i v_i^T \equiv \mathbf{V_r V_r^T} \tag{4.11}$$

is a projection on the row space. By the same reasoning

$$\sum_{i=r+1}^{m} v_i v_i^T \equiv \mathbf{V_0 V_0^T} \tag{4.12}$$

is a projection onto the null space. This says that any vector in R^m can be written in terms of its components in the null space and its components in the row space,

$$\mathbf{x} = \mathbf{Ix} = \left(\mathbf{V_r V_r^T} + \mathbf{V_0 V_0^T}\right)\mathbf{x} = \mathbf{x_{row}} + \mathbf{x_{null}} \, . \tag{4.13}$$

Another important class of matrices for inverse theory is the class of real symmetric matrices for which ***D***=***D***^{T}. In the geophysical inverse problem, the matrix ***D*** is often rectangular. The inversion problem is easier to deal with using the square matrices of $\boldsymbol{D^T D}$

and $\boldsymbol{DD^T}$ instead of $\boldsymbol{D}$. These matrices are always symmetric and as such their eigenvector decomposition is trivial since the diagonalizing matrix can be chosen to be an orthogonal matrix.

4.2 Matrix Inverses and Singular Value Decomposition

In general the geophysical inverse problem is ill-posed. There are cases when there are many more model parameters m than data n or vice versa. In such circumstances it is important to know if a solution does exist and if it does, is it unique. To this end, left and right inverses are defined which depend on the relative number of model parameters to data. The left inverse $\boldsymbol{B}$ of a matrix $\boldsymbol{D}$ is defined as

$$\mathbf{BD} = \mathbf{I} \tag{4.14}$$

where the right inverse $\boldsymbol{C}$ of $\boldsymbol{D}$ is defined as

$$\mathbf{DC} = \mathbf{I}\,. \tag{4.15}$$

If both left and right inverses exist they must be equal. The existence of solutions to equation 4.1 is related to the concept of left and right inverses. The system $\boldsymbol{Dm}=\boldsymbol{t}$ has at least one solution $\boldsymbol{m}$ for every $\boldsymbol{t}$ if and only if the columns span R^n (r=n) in which case there exists an $m\times n$ right inverse $\boldsymbol{C}$ such that $\boldsymbol{DC}=\boldsymbol{I}$. This is only possible if there are more or equal number of model parameters than data, $n \le m$. For this same system there will be a unique solution to equation 4.1 if and only if the columns of $\boldsymbol{D}$ are linearly independent (r=m) in which case there exists an $m\times n$ left inverse $\boldsymbol{B}$ such that $\boldsymbol{BD}=\boldsymbol{I}$. This is only possible if there is more or equal number of data than model parameters, $n \ge m$. It follows that to have the existence of a unique solution then r=m=n. Equation 4.1 can therefore be regarded in two ways: is there a vector $\boldsymbol{m}$ that satisfies the equation, or equally, is $\boldsymbol{t}$ compatible with the columns (model parameters) of $\boldsymbol{D}$?

As shown through equation 4.6, a square matrix can be decomposed into its eigenvectors quite simply. Given that the matrix ***D*** is rectangular some other method is required. There is a powerful generalization for any matrix ***D*** in $R^{n\times m}$ that says it can be factored as

$$\mathbf{D=U\Lambda V^T} \tag{4.16}$$

where the square orthonormal matrix ***U*** has columns in $R^{n\times n}$ and eigenvectors of DD^T, and the square orthonormal matrix ***V*** has columns of in $R^{m\times m}$ are the eigenvectors of D^TD. The matrix ***Λ*** is a rectangular $n\times m$ matrix with singular values on its main diagonal and zero elsewhere. The *r* singular values (where *r* is the rank) are the square roots of the eigenvalues of D^TD which are the same as the nonzero eigenvalues of DD^T. Additionally, the first *r* columns of ***U*** span the column space of ***D*** and the first *r* columns of ***V*** span the row space. The left null space of ***D*** is spanned by the last *n-r* columns of ***U*** and the null space of ***D*** is spanned by the last *m-r* columns of ***V***.

To create the ***U*** and ***V*** matrices involves creating a symmetric matrix ***S***.

$$\mathbf{S} = \begin{bmatrix} \mathbf{0} & \mathbf{D} \\ \mathbf{D^T} & \mathbf{0} \end{bmatrix}. \tag{4.17}$$

S is symmetric and it has orthogonal eigenvectors w_i with real eigenvalues λ_i

$$\mathbf{Sw_i} = \lambda_i \mathbf{w_i}. \tag{4.18}$$

Splitting the eigenvector $\boldsymbol{w_i}$ into the *n*-dimensional data and *m*-dimensional model parts

$$\mathbf{w}_i = \begin{bmatrix} \mathbf{u}_i \\ \mathbf{v}_i \end{bmatrix}, \tag{4.19}$$

the eigenvalue problem for ***S*** is reduced to coupled eigenvalue problems

$$\mathbf{D}^{\mathbf{T}}\mathbf{u}_i = \lambda_i \mathbf{v}_i \tag{4.20}$$

and

$$\mathbf{D}\mathbf{v}_i = \lambda_i \mathbf{u}_i . \tag{4.21}$$

Multiplying both sides of equation 4.20 by $\boldsymbol{D}$ and equation 4.21 by $\boldsymbol{D}^{\boldsymbol{T}}$ results in

$$\mathbf{D}\mathbf{D}^{\mathbf{T}}\mathbf{u}_i = \lambda_i^2 \mathbf{u}_i \tag{4.22}$$

$$\mathbf{D}^{\mathbf{T}}\mathbf{D}\mathbf{v}_i = \lambda_i^2 \mathbf{v}_i . \tag{4.23}$$

This shows that the model eigenvectors are $\boldsymbol{u}_i$ which are eigenvectors of $\mathbf{D}\mathbf{D}^{\mathbf{T}}$ and the data eigenvectors are $\boldsymbol{v}_i$ and are eigenvectors of $\mathbf{D}^{\mathbf{T}}\mathbf{D}$.

It is important to distinguish between the eigenvectors associated with zero and nonzero eigenvalues. Let $\boldsymbol{U_r}$ and $\boldsymbol{V_r}$ be the matrices whose columns are the *r* model and data eigenvectors associated with the *r* nonzero eigenvalues and $\boldsymbol{U_o}$ and $\boldsymbol{V_0}$ be the matrices whose columns are associated with the zero eigenvalues. Also let $\boldsymbol{\Lambda_r}$ be the *r*×*r* square diagonal matrix containing the *r* nonzero eigenvalues. Then from equations 4.20 and 4.21

$$\mathbf{D}^{\mathbf{T}}\mathbf{U}_r = \mathbf{V}_r \boldsymbol{\Lambda}_r \tag{4.24}$$

$$\mathbf{D}\mathbf{V}_r = \mathbf{U}_r \boldsymbol{\Lambda}_r \tag{4.25}$$

for the *r* non zero singular values and

$$\mathbf{D}^{\mathbf{T}}\mathbf{U}_0 = 0 \tag{4.26}$$

$$\mathbf{D}\mathbf{V}_0 = 0 \tag{4.27}$$

for the *n-r* and *m-r* singular values respectively. Since the full matrices $\boldsymbol{U}$ and $\boldsymbol{V}$ are orthonormal it can be readily seen that $\mathbf{DV}=\mathbf{U\Lambda}$ implies $\mathbf{D}=\mathbf{U\Lambda V}^{\mathbf{T}}$ and therefore

$$\mathbf{D} = [\mathbf{U}_r, \mathbf{U}_0]\begin{bmatrix} \mathbf{\Lambda}_r & 0 \\ 0 & 0 \end{bmatrix}\begin{bmatrix} \mathbf{V}_r^T \\ \mathbf{V}_0^T \end{bmatrix} = \mathbf{U}_r \mathbf{\Lambda}_r \mathbf{V}_r^T \,. \tag{4.28}$$

Notice that since $\boldsymbol{\Lambda}_r$ is $r \times r$ and $\boldsymbol{\Lambda}$ $n \times m$ then the lower left block of zeros must be n- $r \times r$, the upper right must be $r \times m$-r and the lower right must be n-$r \times m$-r. These zero singular values represent the null space. It is important to keep track of the subscript r in that $\boldsymbol{D}$ can be reconstructed by the nonzero eigenvalues. This means that the experiment is unable to see the contribution due to the eigenvectors associated with the zero eigenvalues.

SVD can be used to define the generalized inverse of $\boldsymbol{D}$. Given that $\boldsymbol{U}$ is $n \times n$, $\boldsymbol{V}$ is $m \times m$ and $\boldsymbol{\Lambda}$ is $n \times m$, if there are no singular values the following matrix provides a one sided inverse of $\boldsymbol{D}$

$$\mathbf{D}^* = \mathbf{V}\mathbf{\Lambda}^{-1}\mathbf{U}^{\mathbf{T}} \tag{4.29}$$

where $\boldsymbol{\Lambda}^{-1}$ refers to the $m \times n$ with $1/\lambda_i$ on its main diagonal. The matrix $\boldsymbol{D}^*$ is called the generalized inverse of $\boldsymbol{D}$ or the pseudo inverse. Whether $\boldsymbol{D}^*$ will be a left inverse or a right inverse depends on whether there are more equations than unknowns or vice versa. If there are zero singular values computing the inverse is calculated using only the nonzero singular values. The SVD then becomes

$$\mathbf{D} = \mathbf{U_r}\mathbf{\Lambda_r}\mathbf{V_r^T} \tag{4.30}$$

and the generalized inverse is then defined to be

$$\mathbf{D}^* \equiv \mathbf{V_r}\mathbf{\Lambda_r^{-1}}\mathbf{U_r^T} \,. \tag{4.31}$$

The generalized solution to equation 4.1 is then

$$\mathbf{m} = \mathbf{V_r}\mathbf{\Lambda_r^{-1}}\mathbf{U_r^T}\mathbf{t}\ . \tag{4.32}$$

Taking a closer look at the solution written in its expanded form yields a weighted vector product sum

$$\mathbf{m} = \frac{1}{\lambda_1}\mathbf{v_1}\mathbf{u_1^T}\mathbf{t} + \frac{1}{\lambda_2}\mathbf{v_2}\mathbf{u_2^T}\mathbf{t} + \cdots + \frac{1}{\lambda_r}\mathbf{v_r}\mathbf{u_r^T}\mathbf{t}\ . \tag{4.33}$$

The solution vector is the weighted sum of the *m* parameter eigenvectors v_i with weights of $\frac{\mathbf{u_i^T}\Delta\mathbf{t}}{\lambda_i}$. Equivalently, expression 4.33 shows that each data eigenvector is projected onto the model eigenvector space and scaled by the inverse of the singular value. The generalized inverse projects the data onto the column space of ***D***. Thus if this weight is small then v_i has little influence on the solution. Also if λ_i is small then the term $\frac{\mathbf{u_i^T}\Delta\mathbf{t}}{\lambda_i}$ will have a large influence on the solution. It follows that the small singular values $\lambda_{i,}$ are most problematic in inversion problems

4.3 Model and Data Null Spaces

As mentioned previously, it is important to determine the effects of data and model null spaces in the inversion process. In an ideal case there would be no data or model null space. This can only happen when r=m=n in which case one can determine a unique ordinary inverse. There are three other options considered: 1) a data null space, 2) a model null space and 3) both data and model null spaces.

4.3.1 Data null space

First consider the case where there is a data null space but no model null space. This case can only occur when there are more data than model parameters (n>m). In this case the forward operator ***D*** will map model parameters into vectors that have no component in ***U***, whose columns space the data space. This means that if there is a data null space and if the data have a component in this null space it will be impossible to fit it exactly. This being the case it seems reasonable to minimize the misfit between the observed and predicted data

$$\min\|\mathbf{Dm}-\mathbf{t}\|^2 . \qquad (4.34)$$

This is the least-squares minimization model and it is found by differentiating equation 4.34 with respect to ***m*** and setting the result equal to zero. This yields the normal equations

$$\mathbf{D^T Dm} = \mathbf{D^T t} . \qquad (4.35)$$

From a different perspective, it is known that if ***t*** were in the column space of ***D*** then there would exist a vector ***m*** such that ***Dm***=***t***. However if ***t*** were not in the column space of ***D*** then a reasonable strategy would be to find an approximate solution from the column space: find a linear combination of the columns in ***D*** that is as close as possible in a least-squares sense to the data. This solution is the least squares solution denoted by $\boldsymbol{m}_{LS}$. Since $\boldsymbol{Dm}_{LS}$ is confined to the column space of ***D*** then $\boldsymbol{Dm}_{LS}$-***t*** must be in the *orthogonal compliment* of the column space. The orthogonal compliment of the column space is the left null space so $\boldsymbol{Dm}_{LS}$-***t*** must get mapped into zero by $\boldsymbol{D}^T$

$$\mathbf{D^T}\left(\mathbf{Dm_{LS}}-\mathbf{t}\right)=0 \qquad (4.36)$$

or

$$\mathbf{D^T Dm_{LS}} = \mathbf{D^T t} \qquad (4.37)$$

which is just the normal equation again.

From SVD theory, when there is no model null space $\mathbf{D^T D}$ can be written as

$$\mathbf{D^T D} = \left(\mathbf{U_r \Lambda_r V_r^T}\right)^{\mathbf{T}} \mathbf{U_r \Lambda_r V_r^T} = \mathbf{V_r \Lambda_r^T U_r^T U_r \Lambda_r V_r^T} = \mathbf{V_r \Lambda_r^2 V_r^T} . \qquad (4.38)$$

Equation 4.36 can then be solved by

$$\mathbf{m}_{\mathbf{LS}} = \left(\mathbf{V}_{\mathbf{r}}\mathbf{\Lambda}_{\mathbf{r}}^{2}\mathbf{V}_{\mathbf{r}}^{\mathbf{T}}\right)^{-1}\left(\mathbf{U}_{\mathbf{r}}\mathbf{\Lambda}_{\mathbf{r}}\mathbf{V}_{\mathbf{r}}^{\mathbf{T}}\right)^{\mathbf{T}}\mathbf{t} = \mathbf{V}_{\mathbf{r}}\mathbf{\Lambda}_{\mathbf{r}}^{-1}\mathbf{U}_{\mathbf{r}}^{\mathbf{T}}\mathbf{t}, \qquad (4.39)$$

which is precisely the definition of the generalized inverse of equation 4.32.

4.3.2 Model null space

Consider the existence of a model null space $\boldsymbol{V_0}$ but no data null space $\boldsymbol{U_0}$, so $m>n>r$. SVD shows that

$$\mathbf{Dm}^{*} = \mathbf{DD}^{*}\mathbf{t} = \mathbf{U}_{\mathbf{r}}\mathbf{\Lambda}_{\mathbf{r}}\mathbf{V}_{\mathbf{r}}^{\mathbf{T}}\mathbf{V}_{\mathbf{r}}\mathbf{\Lambda}_{\mathbf{r}}^{-1}\mathbf{U}_{\mathbf{r}}^{\mathbf{T}}\mathbf{t} = \mathbf{t}, \qquad (4.40)$$

since $\mathbf{V}_{\mathbf{r}}^{\mathbf{T}}\mathbf{V}_{\mathbf{r}} = \mathbf{I}_{\mathbf{r}}$ and $\mathbf{U}_{\mathbf{r}}\mathbf{U}_{\mathbf{r}}^{\mathbf{T}} = \mathbf{I}_{\mathbf{r}}$. But since $\boldsymbol{m}^{*}$ is expressible in terms of $\boldsymbol{V_r}$ it is clear that the generalized inverse solution is a model that is entirely confined by $\boldsymbol{V_r}$. The least squares solution (any solution to the normal equations) can be represented as the sum of the generalized solution with some component in the model null space:

$$\mathbf{m}_{\mathbf{LS}} = \mathbf{m}^{*} + \sum_{i=r+1}^{M}\alpha_i v_i \qquad (4.41)$$

where $\sum_{i=r+1}^{M}\alpha_i v_i$, represents the component in the model null space. The immediate consequence of equation 4.41 is that the length, $\sqrt{\mathbf{m}_{\mathbf{LS}} \cdot \mathbf{m}_{\mathbf{LS}}}$, of the least squares solution must at least be as great as the generalized inverse solution, $\boldsymbol{m}^{*}$. This shows the minimum length property of the generalized inverse. Of all the infinite solutions available, through the addition of components in the model null space, the generalized inverse finds the one of minimum length. Physically, a model nulls pace can be thought of cells within the model which have not been illuminate by raypaths. In this case, these cells could adopt any velocity and not change the solution.

4.3.3 Model and data null space

The previous two subsections have shown the solutions for case with a data null space and the case with a model null space. In the case of data null space the generalized inverse finds the inverse solution that minimizes the least squares misfit of data and model response. In the case of a model null space the generalized inverse solution minimized the length of the solution itself. If there are both data and model null spaces then the generalized inverse simultaneously optimizes these goals. In other words when there exists a model and data null space the generalized solution $\boldsymbol{m}^*$ is the least squares solution of minimum norm.

4.4 Resolution

Resolution is defined as how precisely one can infer model parameters from data. The issue is complicated by all the uncertainties in the inverse problem: uncertainties in the forward modelling, the discretization of the model itself, noise of the data, and in the a priori information. Assuming however that the errors are zero, the basic expression consists of

$$\mathbf{t} = \mathbf{Dm} \; , \tag{4.42}$$

with a pseudo-inverse solution of

$$\mathbf{m}^* = \mathbf{D}^*\mathbf{Dm} \; . \tag{4.43}$$

Equation 4.43 has $\mathbf{D}^*\mathbf{D}$ acting as a filter relating the true earth model to the computed earth model. When $\mathbf{D}^*\mathbf{D}$ equals the identity matrix implies perfect resolution. From SVD equation 4.43 can be expressed as

$$\mathbf{m}^* = \mathbf{V_r \Lambda_r^{-1} U_r^T U_r \Lambda_r V_r^T m} = \mathbf{V_r V_r^T m} \; . \tag{4.44}$$

From this expression it follows that $\mathbf{V_r V_r^T}$ is the filter relating the computed earth parameters to the true ones. This quantity is known as the resolution matrix where values of unity mean that the parameter is perfectly resolved and zero meaning they will never be resolved.

Data resolution is connected to the fact that the observed data may be different than the data predicted by the generalized inverse. The latter is just $\boldsymbol{Dm}^*$ which equals what we now define as $\boldsymbol{t}^*$. This results in an expression similar to that of the resolution matrix

$$\mathbf{t}^* = \mathbf{DD}^*\mathbf{t} = \mathbf{U_r \Lambda_r V_r^T V_r \Lambda_r^{-1} U_r^T t} = \mathbf{U_r U_r^T t} \tag{4.45}$$

The matrix $\mathbf{U_r U_r^T}$ says how well the data is predicted by the computed model. When there is no data null space the data is predicted perfectly.

4.5 Quasi-Null Space

As a method to alleviate the problem of nonuniqueness by applying constraints, the quasi-null space, a measure of reliability to the inversion solution, is presented. The null space is defined for matrices that are rank deficient. For such matrices, $\boldsymbol{D}$, there exists a nontrivial vector $\boldsymbol{u_0}$ such that

$$\mathbf{Du_0} = \mathbf{0} \; . \tag{4.46}$$

With such a matrix $\boldsymbol{D}$ and the vector $\boldsymbol{u_0}$ an infinite number of solutions to equation (4.9) exist since

$$\mathbf{\Delta t} = \mathbf{D}(\mathbf{\Delta s} + \boldsymbol{\alpha}\mathbf{u_0}) = \mathbf{D\Delta}s + \boldsymbol{\alpha}\mathbf{Du_0} = \mathbf{D\Delta}s \tag{4.47}$$

where α is any real number. Vesnaver (1994) defines the quasi-null singular values as those singular values below a given threshold. A property of singular value decomposition is that the corresponding columns of the matrix ***V*** to the zero singular values constitute an orthonormal basis of the null space. The quasi-null space is the sum of squares of the entries in the columns of ***V*** whose corresponding singular values are above a predefined threshold. This is expressed mathematically as

$$m_i = \sum V_{ij}^2 \tag{4.48}$$

where only the values above the prescribed threshold are included within the summation. A map of this quasi-null space highlights the cells that are most reliable for traveltime inversion.

The quasi-null space was first applied by Bohm and Vesnaver (1999) using it to determine an appropriate cell size, which would limit the effects of poor ray distribution. This equates into an increase in cell size in areas of poor ray coverage yet also reducing resolution. The stabilization methods proposed in this work consist of dynamic smoothing and dual inversion integration all based on the quasi-null space. Determining the quasi-null space, more stable inversion cells are chosen increasing the reliability of the inversion without reducing resolution.

To demonstrate the different applications of the quasi-null space implemented to constrain the inversion solution, Figure 4.1 shows a simplistic four-layer model.

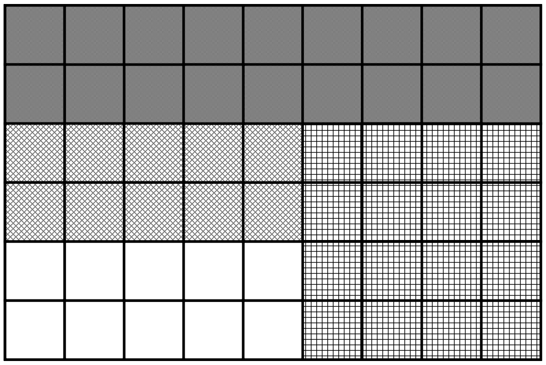

Figure 4.1 Four-layer model.

Two seismic experiments each consisting of two sources and two receivers are performed: a transmission and a reflection experiment displayed in Figure 4.2.

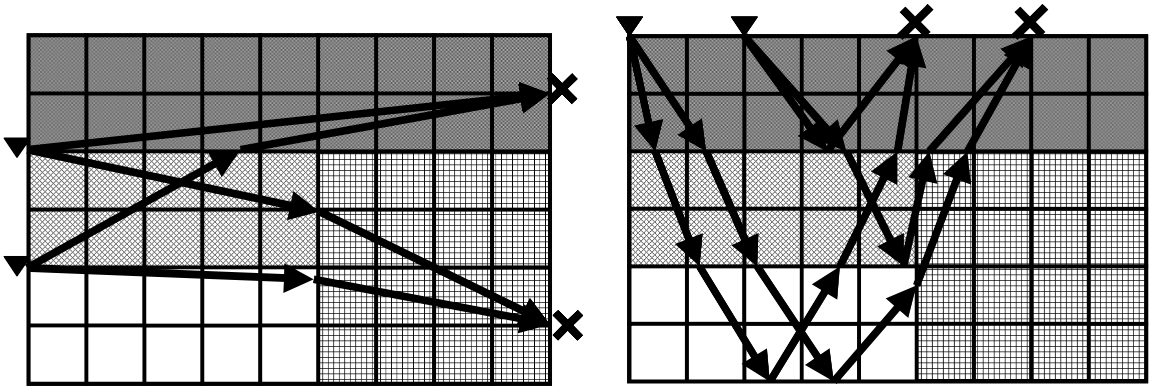

Figure 4.2 Transmission (left) and reflection (right) experiment over four-layer model.

Figure 4.2 illustrates how each experiment has a different ray distribution illuminating different areas of the model. As shown in Figure 4.3, some cells do not contain any rays.

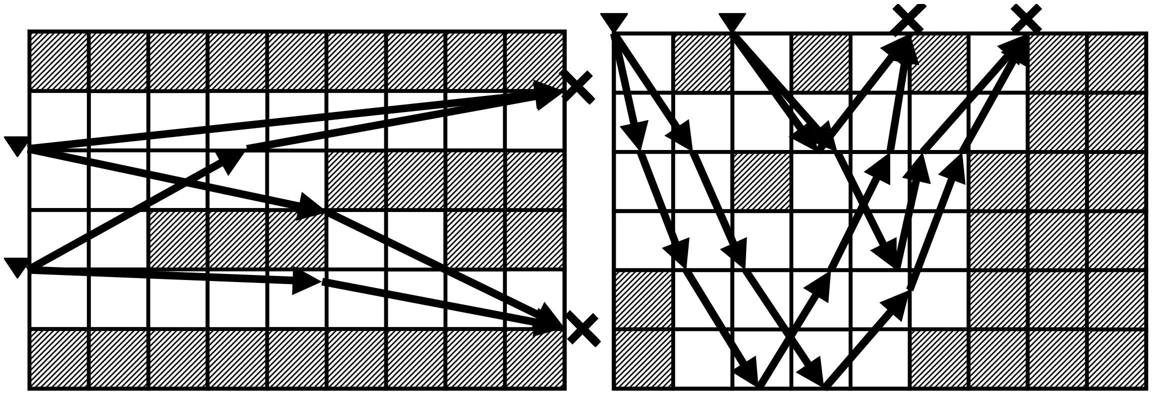

Figure 4.3 Transmission (left) and reflection (right) experiment showing striped cells with no raypaths.

The striped cells are the source of unstable inversion. Using the quasi-null space, the solution is constrained yielding a more reliable tomogram.

4.5.1 Quasi-null space dynamic smoothing

A reliable tomogram can be constructed given a seismic experiment and performing traveltime inversion. Using the quasi-null space as a measure of reliability, unreliable cells are smoothed so as to lessen their effects. Predefining a tolerance level and denoting any values below it as unreliable the reliability tomogram is determined seen Figure 4.4.

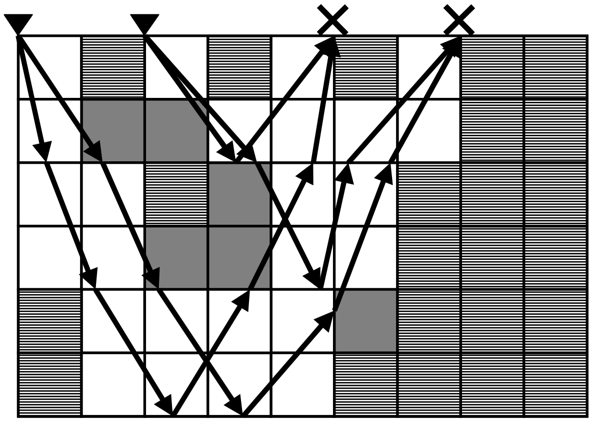

Figure 4.4 Quasi-null space tomogram of the reflection experiment. White cells denote reliable cells, grey cells denote moderately reliable cells and striped cells denote unreliable cells.

Smoothing the unreliable cells lessens their impact on the solution. In Figure 4.4 a reliable cell is shown as those with a significant amount of raypath. If the unreliable cells were not modified the acquisition geometry would bias the solution. Figure 4.5 shows a 3×3 smoother operator on an unreliable cell.

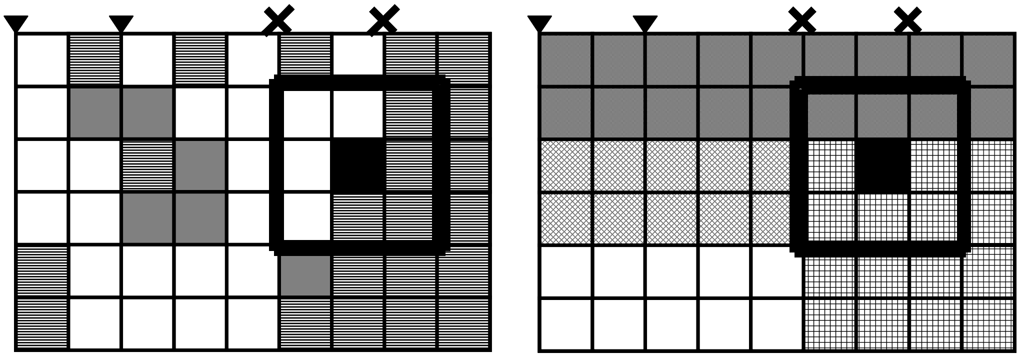

a) b)

Figure 4.5 Quasi-null space (a) has white cell denoting reliable cells, grey cells denoting moderately reliable cells and striped cells denoting unreliable cells as well as showing the size of the 3 by 3 smoothing operator on an unreliable cell. Resulting velocity tomogram (b) consists of smoothing over an area as defined by the same smoothing operator.

Smoothing the unreliable cells keeps the same resolution of the original experiment while still constraining the solution. Reliable cells remain unchanged and are used to stabilize the final tomogram. This technique uses the surrounding data to determine the value of the cell honouring regional trends. After each iteration, unreliable cell values are determined by surrounding cells eliminating inversions artefacts that may otherwise be introduced.

4.5.2 Quasi-null space integration

The second quasi-null space stabilization technique integrates two different experiments over the same model using the quasi-null space to isolate reliable cells. Each inversion solution has the quasi-null space computed. A final tomogram is constructed integrating the most reliable cells of each quasi-null space. Figure 4.6 shows the quasi-null space for the reflection and transmission experiment.

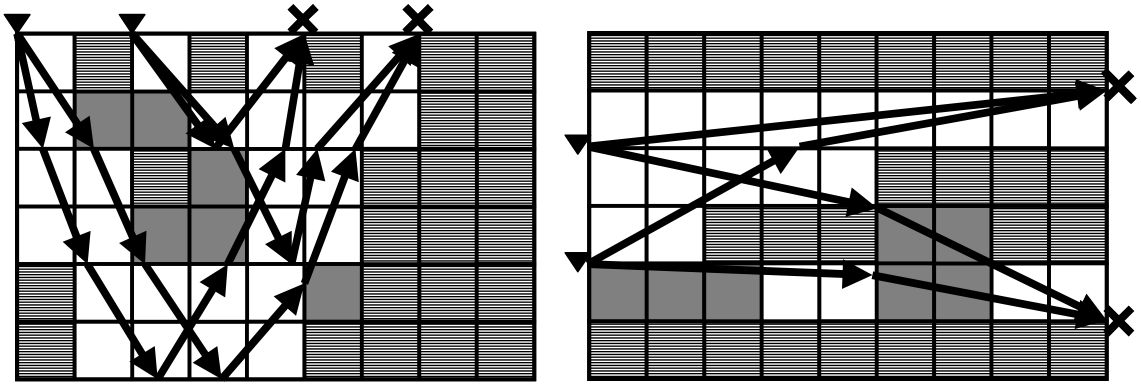

Figure 4.6 Quasi-null spaces for the reflection (left) and transmission experiment (right). White cells denote reliable cells, grey cells denote moderately reliable cells and striped cells denote unreliable cells.

After integration the final tomogram is a combination of the reliable cells in the experiment. This is shown in Figure 4.7

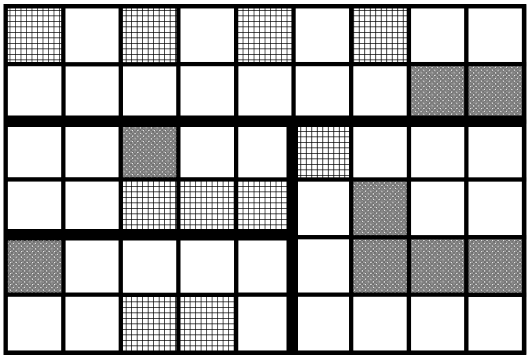

Figure 4.7 Final tomogram after quasi-null space integration. Striped cells denote a reflection experiment value while grey cells denote a transmission experiment value. White cells are those that could be either a reflection or transmission value.

This final tomogram contains a minimal amount of unreliable cells while maintaining the original resolution. No low or high frequency approximations are made in favour of an optimal integration of two distinct experiments. This solution most accurately represents the model properties.

4.6 Summary

Tomography is a statistical technique that determines geologic parameters from recorded observations. Assuming an initial model, traveltimes are simulated and compared to the recorded traveltimes. Singular Value Decomposition ascertains the model that minimizes the difference between the modelled and recorded traveltimes. This is done for mixed determined problems by choosing the solution of minimum length and finding the best fit to the data from the model space eigenvectors. Due to the inherent nature of seismic tomography the solution is never uniquely determined. Solution stability is a function of raypath distribution that is controlled by the acquisition geometry used and the underlying velocity model. The quasi-null space is used as a tool in constraining the inversion to converge to a stable solution. The two quasi-nulls space constraining methods aimed to maintain tomogram resolution while increasing inversion stability. Dynamic smoothing follows a low-frequency trend using surrounding inversion values to constrain solution. The quasi-null space integration technique uses two experiments to minimize the amount of unreliable cells leading to a stable inversion result. Using either of these techniques allows for an accurate tomogram to be used for prestack depth migration.

CHAPTER 5: APPLICATIONS AND RESULTS

The velocities and Thomsen parameters will be estimated from models using the methods developed in the previous chapters. The methods outlined in previous chapters are tested and analyzed in this section. Two sets of models were chosen to test the algorithm. The first set consists of simple velocity models, one containing a horizontal high-velocity layer while the second has a centered high-velocity square. These models were specifically designed to determine the biases of the acquisition geometry on the solution as well as establish a tomographic impulse response that can be used to interpret velocity and/or anisotropic artefacts in more complex velocity models. The second set of velocity models are more complex, representing the structural settings often encountered in more difficult imaging environments. The final tomograms from these models demonstrate the capabilities of the inversion process.

The surface seismic for the simple set of models will only use one reflector at the bottom of the model to estimate the velocities. It should be noted that a much more accurate velocity model could be obtained by identifying and evaluating each reflecting surface (in a downward sequence), but that is not the intent of this chapter. The intent is to evaluate the tomographic inversion process, independent of the model building process. Consequently, some estimated models that may appear inferior at an initial glance, may actually contain significant results.

The testing will be evaluated on two quantities: the capability to resolve velocity anomalies accurately and the stability of the inversion process. Ultimately the resolution of the process will be a function of the acquisition geometry and the underlying velocity structure. How well the inversion process handles the inherent biases is a measure of success.

The large size of the chapter is indicative of the complex nature of the inversion process and contains many figures that progress from simple to complex models. They have all been included as each provides a unique description of steps leading to practical tomographic solutions.

5.1 Isotropic Tomography

5.1.1 Simple isotropic velocity models

Two simple models are introduced that are aimed to determine the effects of acquisition geometry on tomography. The models consist of 30 by 40 square cell grids, 20 by 20 meters in dimension with a background velocity of 3000 m/s. In the first model, a 3300 m/s horizontal layer is present while the second model has a high-velocity anomaly centered in the middle of the model. These high-velocity anomalies are the targets that tomography would like to detect. These models are seen in Figure 5.1 below.

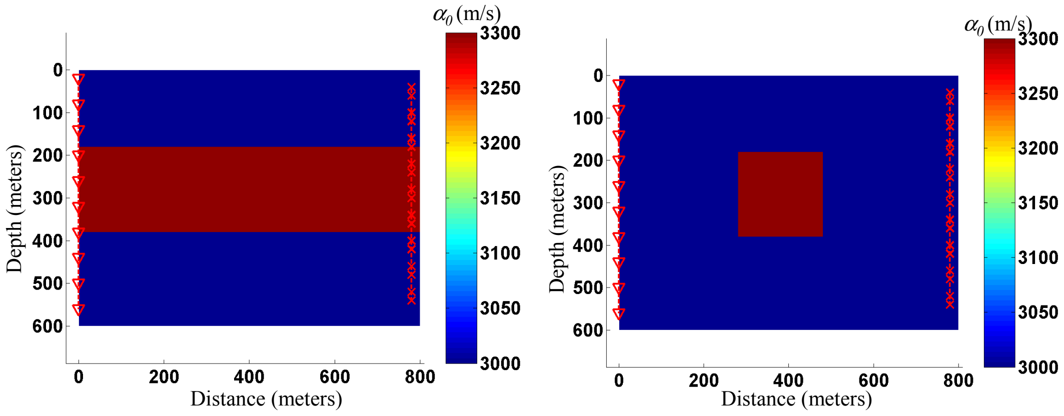

a) b)

Figure 5.1 Velocity models containing horizontal (a) and centered high-velocity anomaly (b).

Since all the velocity fields are smoothed prior the calculation of traveltimes, it follows that the best velocity profile that one could achieve is the smoothed version of the velocity models defined. These are shown in Figure 5.2 below.

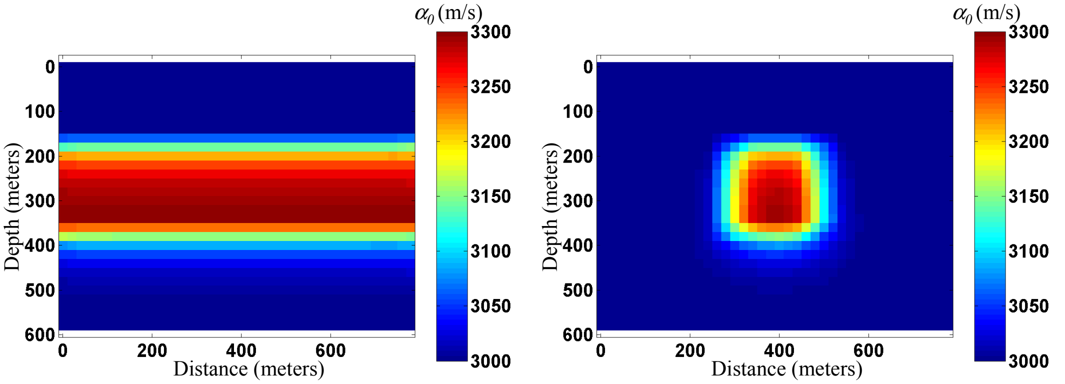

a) b)

Figure 5.2 Smoothed velocity models (5 by 5 cell operator) containing a horizontal (a) and centered (b) high-velocity anomaly.

These two velocity models will be detected using two distinct acquisition geometries. The first simulates a seismic crosswell experiment with receivers in one well and sources in the other. The second is a surface experiment where both sources and receivers are located at the surface of the earth. The crosswell experiment, for the purposes of all subsequent testing, will have 10 sources located on the left side of the model and 18 receivers on the right side of the model. Similarly, for all subsequent tests, the surface experiments will contain 8 sources and 14 receivers all evenly distributed at the surface. Figure 5.3 illustrates the two distinct acquisition geometries used.

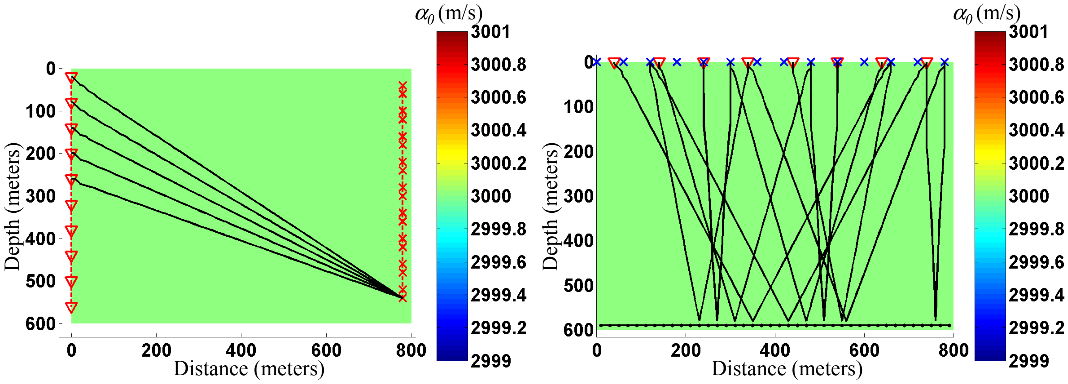

a) b)

Figure 5.3 Display of two acquisition geometries used: crosswell (a) and surface (b). (Note that the surface model only contains one reflecting layer.)

The sections that follow test the different acquisition geometries (crosswell or surface) as well as identify the initial starting models used in the tomographic process. Testing will consist of three iterations as the differences between the third and fourth iteration solutions are minimal and the solution has converged.

The isotropic tomographic workflow consists of the following steps:

1. The initial model estimate is the first guess of what the underlying velocity structure is. The estimate can come from well control or stacking velocities or both. In this thesis the initial model estimate will vary so as to determine the tomographic methods ability to converge to the correct solution and to test inversion stability.
2. The velocity model is smoothed and traveltimes and raypaths are computed using the methods presented in Chapter 2.
3. The raypaths are used to construct a matrix which maps model parameters to traveltimes. This matrix is inverted to solve for model parameters from traveltimes.
4. The output velocity model is smoothed with a 5 by 5 cell operator.
5. Output model from step 4 is used as input for step 2. Steps 2 and 5 are repeated until three iterations are complete. The final model after three iterations is the final output tomogram. Only three iterations are used as after three iterations, testing has shown that the solution converges to a final solution which further iterations do not improve upon, or the solution diverges and becomes unstable.

5.1.1.1 Horizontal anomaly model

Testing begins with the horizontal anomaly model of Figure 5.2a. Both crosswell and surface tomography methods are tested.

5.1.1.1.1 Crosswell tomography

The initial velocity estimate used in this crosswell tomography experiment is a constant velocity of 3000 m/s. The resulting tomogram gives a clear indication that the anomaly is detectable. Consider the results for each iteration of crosswell tomography in Figure 5.4.

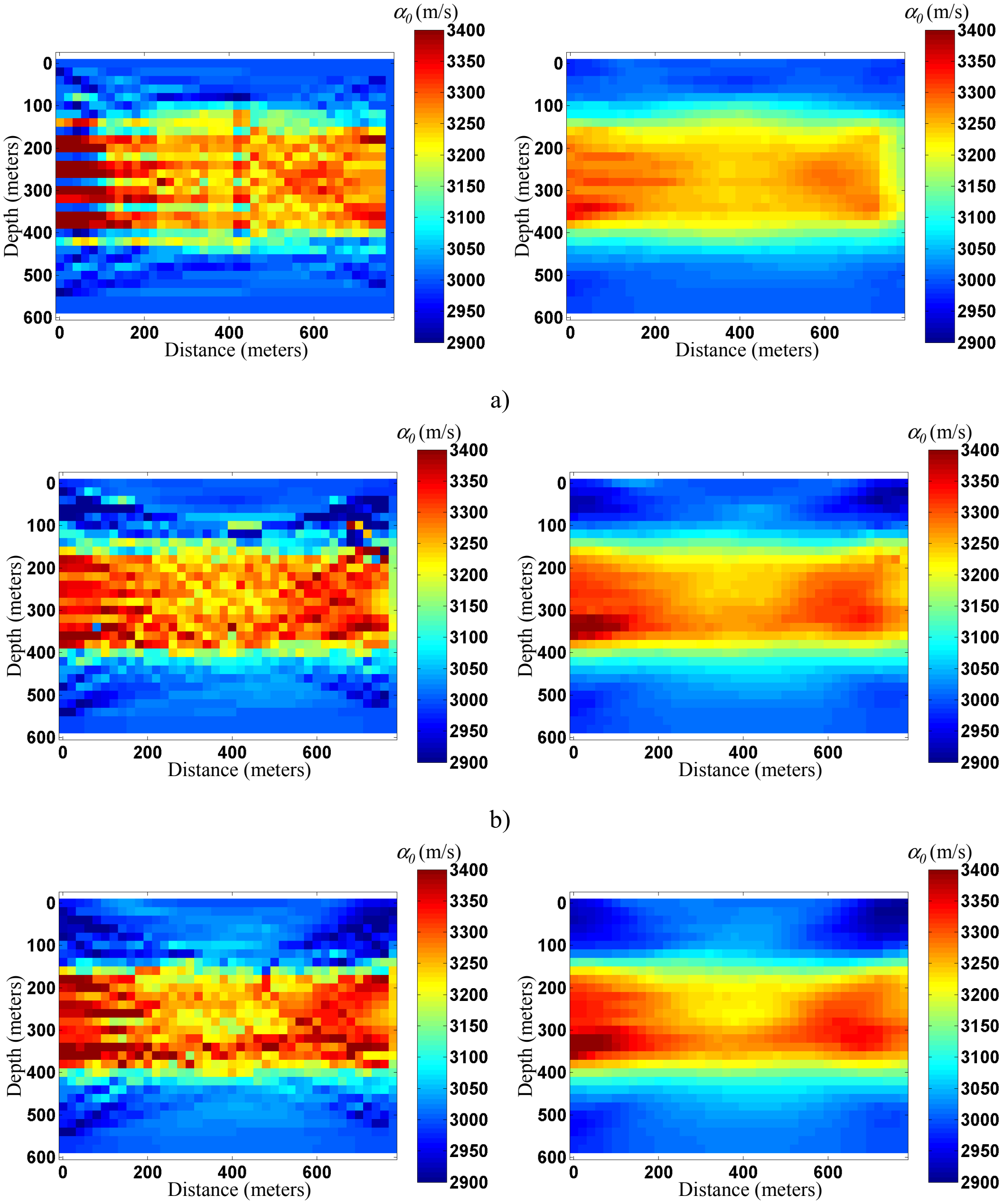

a)

b)

c)

Figure 5.4 Crosswell tomography results on the horizontal velocity model: (left) no post processing, (right) 5 by 5 cell smoother applied; (a) first iteration (b) second iteration (c) third iteration.

The resulting tomogram shows that the horizontal velocity anomaly is clearly detectable and the result is quite good considering that the initial model estimate had no such layer. The average value of the high-velocity layer in the third iteration tomogram (Figure 5.4c) is approximately 3300 m/s and the surrounding low-velocity zone also shows a quite accurate value of 3000 m/s. This result is quite encouraging and shows the merits using tomography in building velocity models.

5.1.1.1.2 Surface tomography

Surface tomography, which has surface sources and detectors, yields the following tomograms after each of the first 3 iterations. Again, the initial velocity estimate is a constant velocity of 3000 m/s.

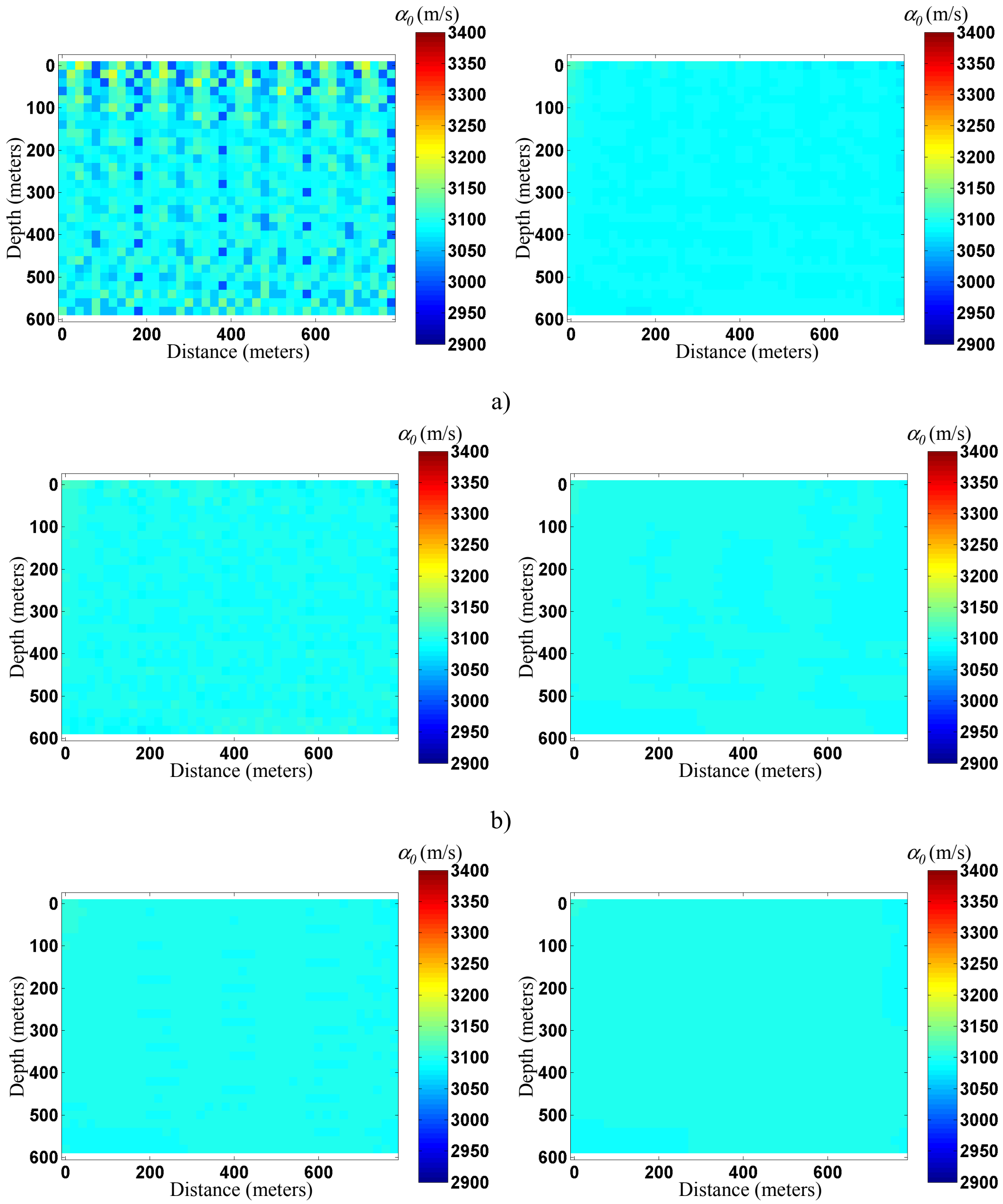

a)

b)

c)

Figure 5.5 Surface tomography results of horizontal high-velocity layer model: (left) no post processing, (right) 5 by 5 cell smoother applied; (a) first iteration (b) second iteration (c) third iteration.

This result is not a good one, yielding a solution that does not accurately represent the true velocity profile. In fact, it represents the weighted average velocity of the background and the high-velocity layer. This averaging is a consequence of the acquisition geometry. Such geometry requires additional information. Without any further information it cannot detect vertical velocity variations. In this case the information required consists of reflecting interface specifying the location of the velocity contrast. It is interesting to note that the results of this horizontally layered model supports the assumption in that offset traveltimes can be defined by hyperbolic moveout that uses an RMS (or stacking) velocity. This RMS assumption implies that no structural information above the reflector is required for estimating the traveltimes. Consequently, inverting for the structure above the reflector (from this reflector alone) would be virtually impossible. Using all three reflecting surfaces would produce a superior result.

5.1.1.2 Center anomaly model

Testing continues with the center anomaly model of Figure 5.2b. Both crosswell and surface tomography methods are tested.

5.1.1.2.1 Crosswell tomography

Consider the centered velocity anomaly model for the crosswell experiment. The crosswell tomography results are seen in Figure 5.6 below.

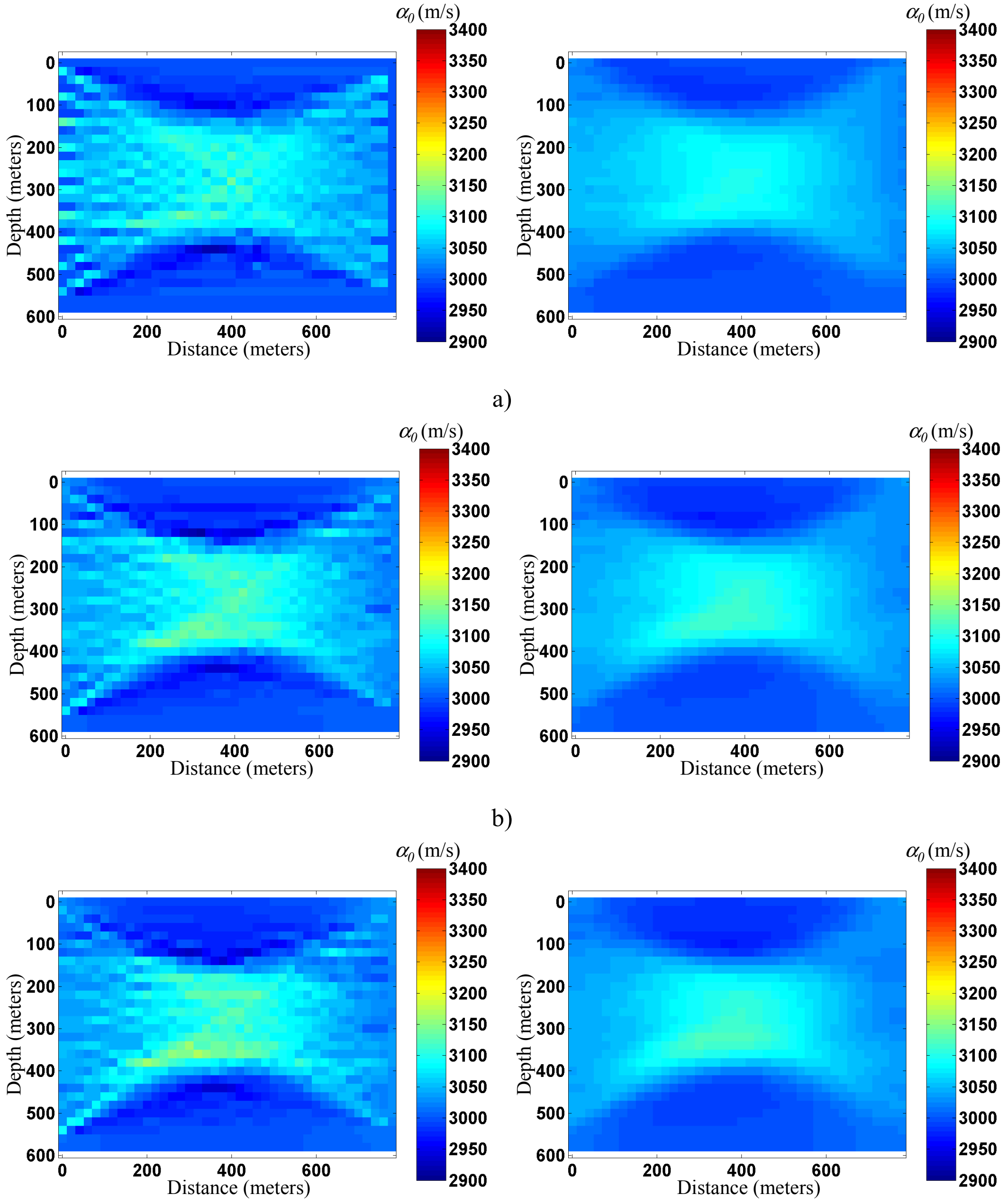

a)

b)

c)

Figure 5.6 Crosswell tomography for centered anomaly model: (left) no post processing, (right) 5 by 5 cell smoother applied; (a) first iteration (b) second iteration (c) third iteration.

In this case, the acquisition geometry has smeared the result along the directions of the predominant raypath. The resultant velocity of the centered anomaly is less than the model because of the smearing. The increase in size of the anomaly distributes the velocity along the direction of the predominant raypath. The result is not as poor as the horizontal high-velocity layer with surface tomography as there are some rays that do not traverse the anomaly at all. These rays show that there is a vertical extent to the anomaly. The rays that traverse the model from shallow sources to deep receivers and vice versa attempt to outline the lateral extent of the anomaly but do so only mildly. This is because the numbers of rays traversing the anomaly outnumber the delineation rays and thus bias the solution. This lack of delineation rays is further decreased with each iteration as the general outline of the high-velocity anomaly is detected. Each subsequent iteration after the first will have a larger number of rays become "attracted" to the high velocity anomaly thus further limiting the number of delineation rays. This is an example of the acquisition geometry and the underlying velocity structure biasing the final tomogram solution.

5.1.1.2.2 Surface tomography

The results of surface tomography for the centered high-velocity anomaly are seen in Figure 5.7.

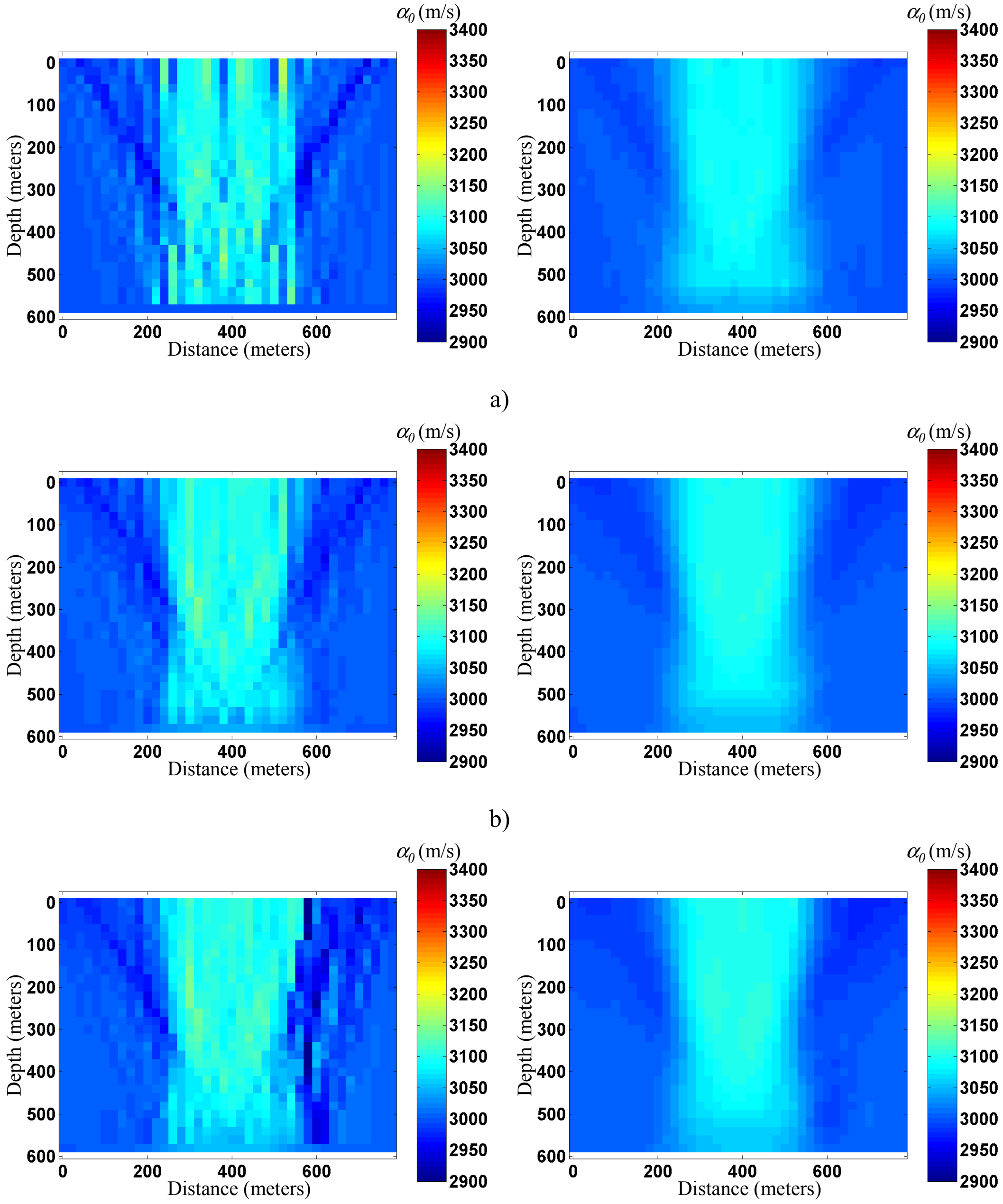

a)

b)

c)

Figure 5.7 Surface tomography results for centered anomaly: (left) no post processing, (right) 5 by 5 cell smoother applied; (a) first iteration (b) second iteration (c) third iteration.

Notice that the results again are biased by the acquisition geometry. In this case the main raypath direction is in the z-direction smearing the centered anomaly in that direction. The lateral extent of the anomaly is well defined; more so than the vertical extent of the anomaly in crosswell result. This is also a function of the acquisition geometry. The surface acquisition geometry will have twice as many delineation rays due to the reflecting interface. As a result, surface tomography is able to resolve the lateral extents of the anomaly.

The results of crosswell and surface tomography show two main results: acquisition geometry biases the solution and crosswell and surface experiments complement each other. Crosswell and reflection tomography complement each other in that the crosswell experiment delineates the vertical extent while the surface experiment outlines the lateral extent.

5.1.2 Quasi-null space analysis: simple isotropic models

The next set of tests will consider the quasi-null space for each of the previous experiments. The quasi-null space workflow is similar to the initial isotropic workflow described. The difference is that between steps 3 and 4, the quasi-null space stabilization technique is applied. The quasi-null space will be directly related to the acquisition geometry used as the raypaths determine which of the cells within the model will contribute to the output tomogram solution. An illumination plot, which shows the total ray distance traversing through a given cell, can at times be useful but it fails in distinguishing between linearly independent rays, i.e. non-parallel rays. The crosswell tomography quasi-null space for the horizontal velocity model and the illumination plot for the first iteration is shown Figure 5.8

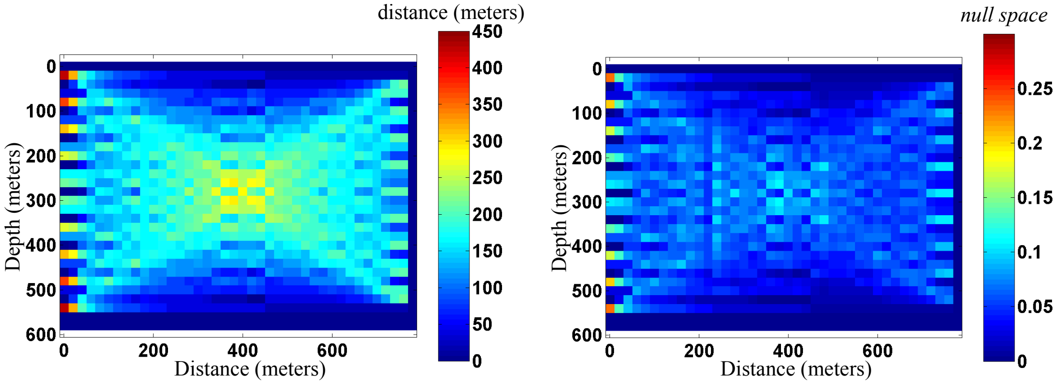

a) b)

Figure 5.8. Crosswell illumination plot (a) and quasi-null space (b) of the first iteration.

There are differences between the illumination plot and the quasi-null space. If both these plots were to designate a degree of reliability in determining the cell's inversion solution the illumination plot would have a larger reliability radius around the center of the model than would the quasi-null space plot. This relates to the notion of linearly independent rays. The larger reliability radius of the illumination plot comes from the amount of similar raypaths taken from source to receiver, a function of the acquisition geometry. The quasi-null space can differentiate between linearly dependent and independent rays thus placing more emphasis on rays that have taken different paths. It follows then that the areas most distant from sources and receivers in the model could have the largest number of independent raypaths. It is important to note that the source and receiver locations are designated as reliable on both plots as they have a large number of rays.

5.1.2.1 Dynamic filtering: horizontal anomaly model

The quasi-null space is now used to apply a dynamic filtering process. The process designed such that all cell values that are 35% or less of the maximum cell reliability will be treated as unreliable and as such will be lowpass filtered. Figure 5.9 shows the three iterations of using the quasi-null space to dynamically filter the tomogram.

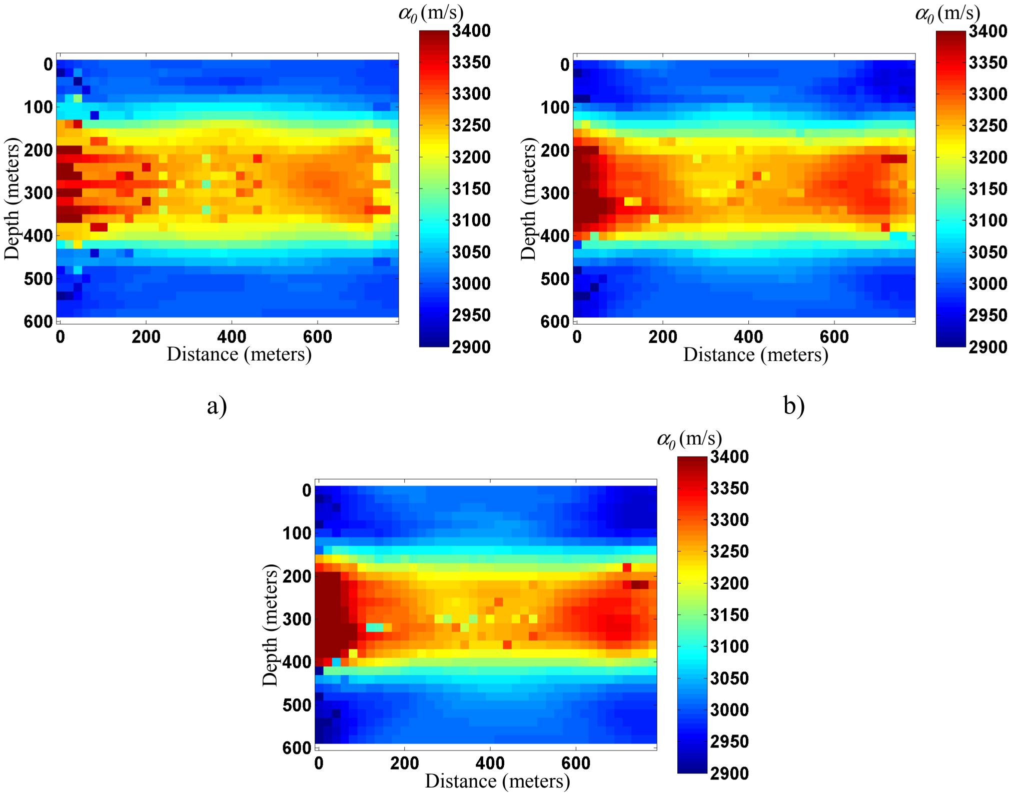

a) b)

c)

Figure 5.9 Quasi-null space dynamic smoothing for crosswell tomography on the horizontal velocity model: (a) first iteration (b) second iteration (c) third iteration.

A relatively stable solution is achieved, not much different from the conventional crosswell tomography result. The differences exist in the resolution aspects of the tomogram. The edges of the high-velocity anomaly are sharper and the horizontal layer is more continuous from a velocity perspective. The surface tomography experiment is not considered for dynamic smoothing as everything is equally unreliable.

5.1.2.2 Integration: horizontal anomaly model

Integrating both experiments show the relative reliability between the crosswell and surface experiments. Figure 5.10 shows the quasi-null space for the crosswell and surface tomography respectively.

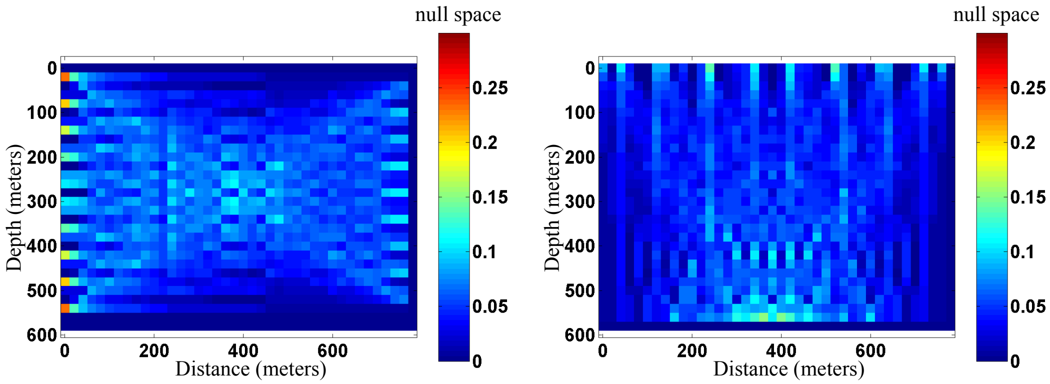

a) b)

Figure 5.10 Quasi-null space for crosswell (a) and surface tomography (b).

Comparing these two spaces it easily determined that in general, the crosswell experiment is more reliable in the center of the model space. Note that there are also areas of relatively high reliability near the sources and receivers for each experiment. Additionally, surface tomography has high reliability zones at the reflection points.

An integrated tomogram is constructed, by selecting the more reliable inversion solution between the crosswell and surface experiment based on quasi-null space, on a cell by cell basis. The results of the integration for 3 iterations are seen in Figure 5.11.

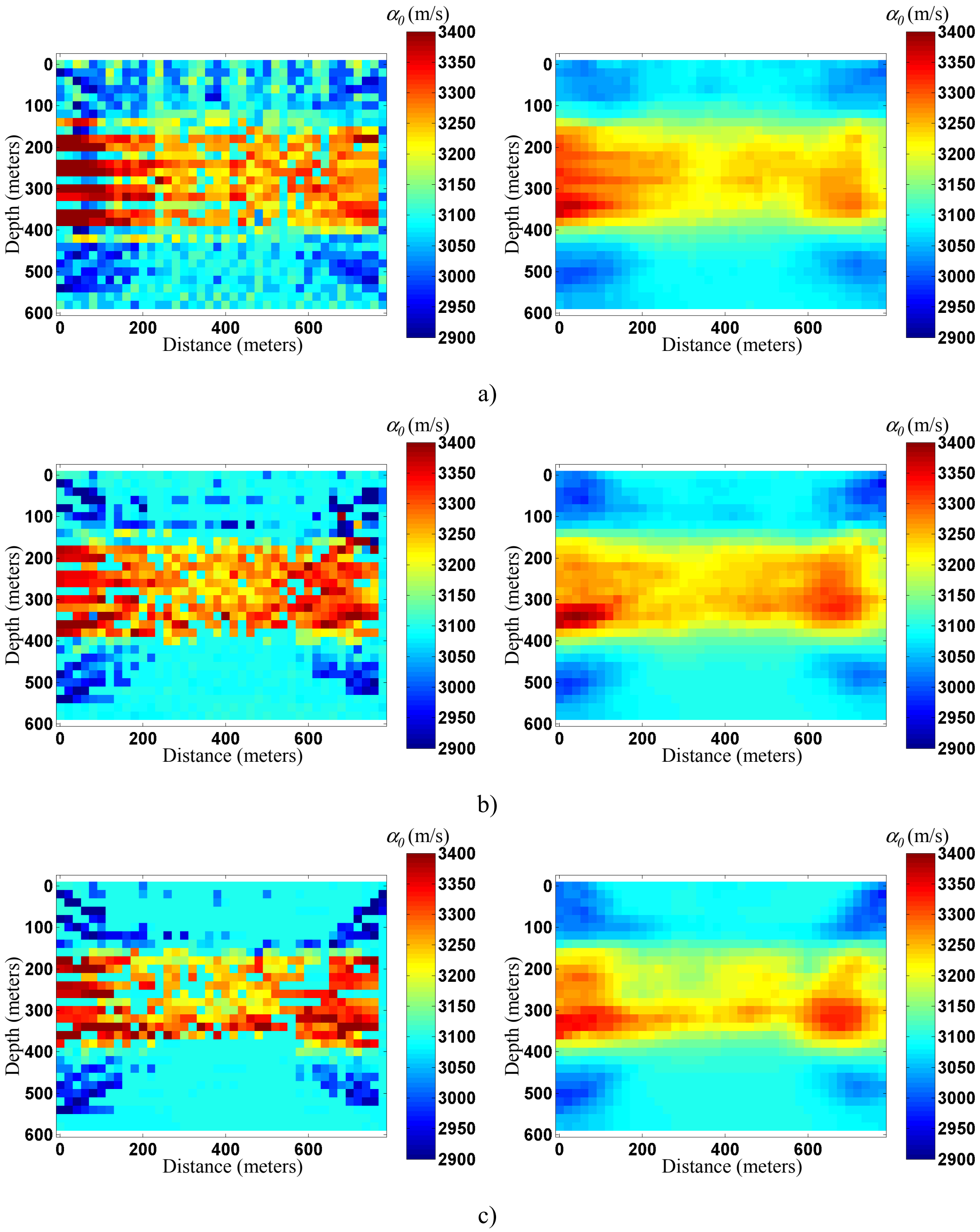

a)

b)

c)

Figure 5.11 Quasi-null space integrated tomograms: (left) no post processing, (right) 5 by 5 cell smoother applied; (a) first iteration (b) second iteration (c) third iteration.

As evidenced in the above figures the quasi-null space integration scheme correctly chose the more reliable solution in general. The unsmoothed integrated tomograms show a definite trend in the data clearly separating the high-velocity zones from the surrounding lower-velocity background.

5.1.2.3 Dynamic filtering: center anomaly model

Applying the same techniques to the centered high-velocity anomaly will determine whether the quasi-null space can be used to harness the complimentary nature of crosswell and surface tomography. Figure 5.12 shows the first iteration quasi-null space for the crosswell and surface tomography experiments.

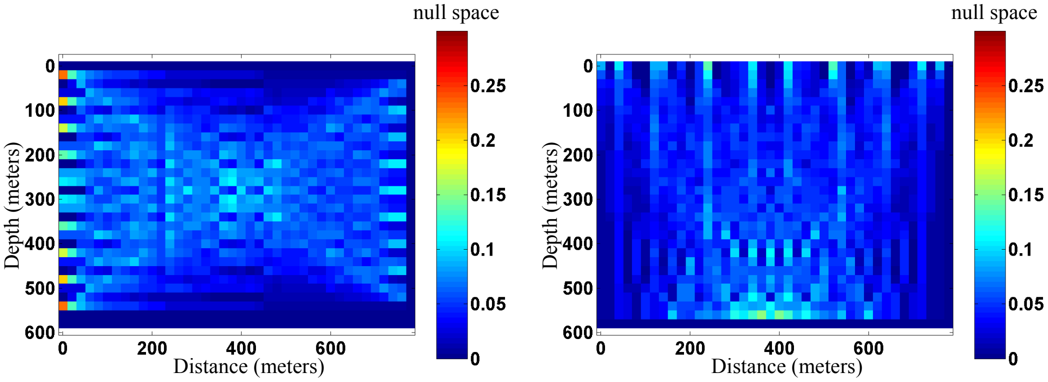

a) b)

Figure 5.12 Quasi-null space for crosswell (a) and surface (b) tomography

The following figures show the results of the dynamic smoothing process applied to the centered high-velocity anomaly.

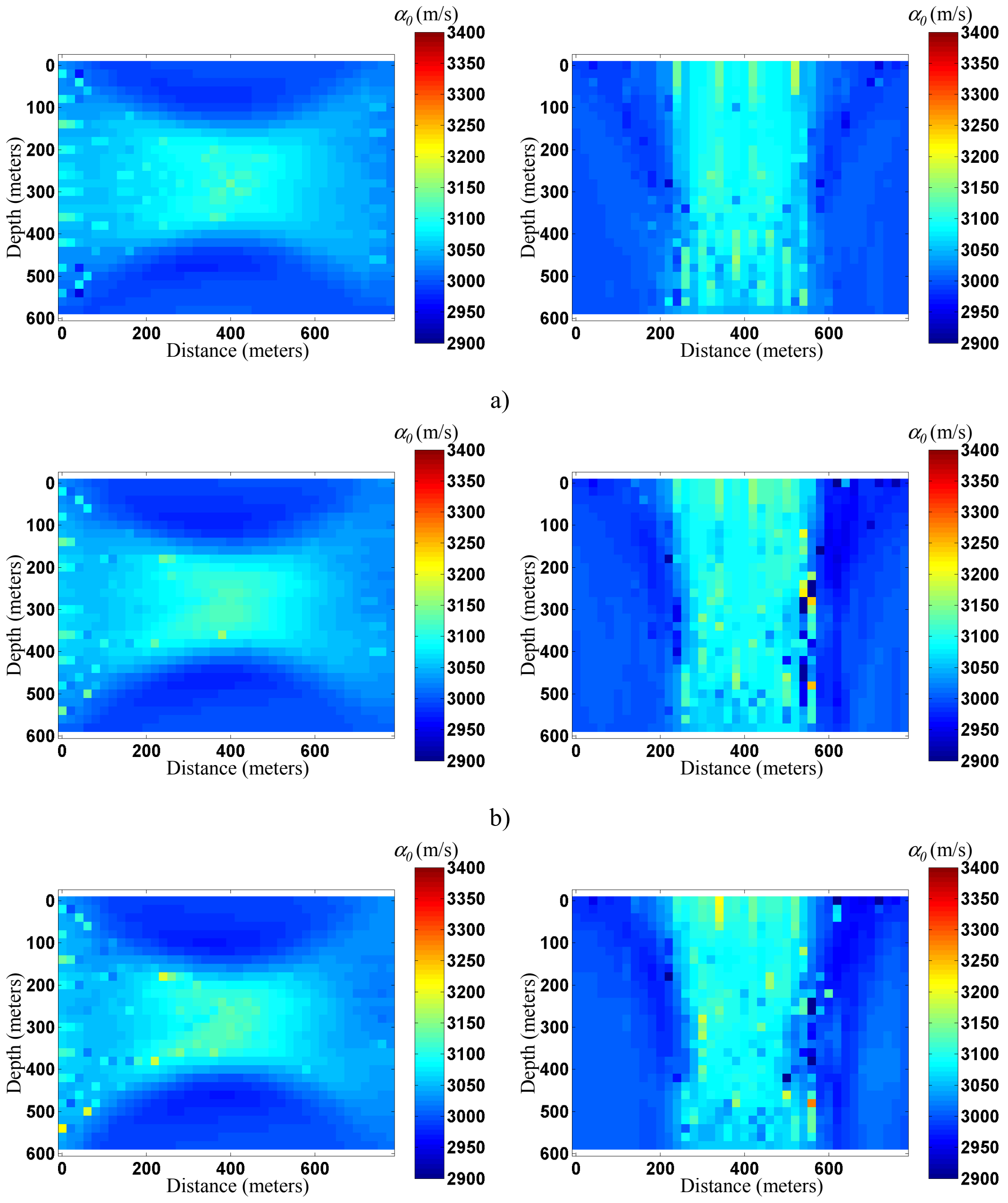

a)

b)

c)

Figure 5.13 Quasi-null space dynamic smoothing tomograms: (left) crosswell, (right) surface; (a) first iteration (b) second iteration (c) third iteration.

Again the results are similar to that of the previous model's dynamic smoothing. Resolution is increased by only filtering the unreliable inversion cells resulting in sharper edges. These edges are perpendicular to the dominant raypath direction for each experiment respectively. Also, it appears as though there has been an increase in lateral resolution in the crosswell experiment, even though dynamic smoothing has been applied. In particular, Figure 5.13c shows sharper hints of what could be interpreted as lateral extents to the high velocity anomaly, suggesting that it is confined to the centre of the model. This is explained as a function of the quasi-null space in Figure 5.12. The center of the model is shown to be the most reliable and is not smoothed. The cells at the edges of the model are also considered reliable due to their high ray density and are also not smoothed. There is a space, however, between the high reliability zones that are less reliable and these are the values that are smoothed. The smoothing filters the values that are less reliable and lessens their impact on the solution creating a sense that there is a lateral extent to the anomaly.

5.1.2.4 Integration: center anomaly model

Figure 5.14 shows the results of integrating the crosswell and surface surveys for the centre high-velocity model anomaly based on the quasi-null spaces seen in Figure 5.12.

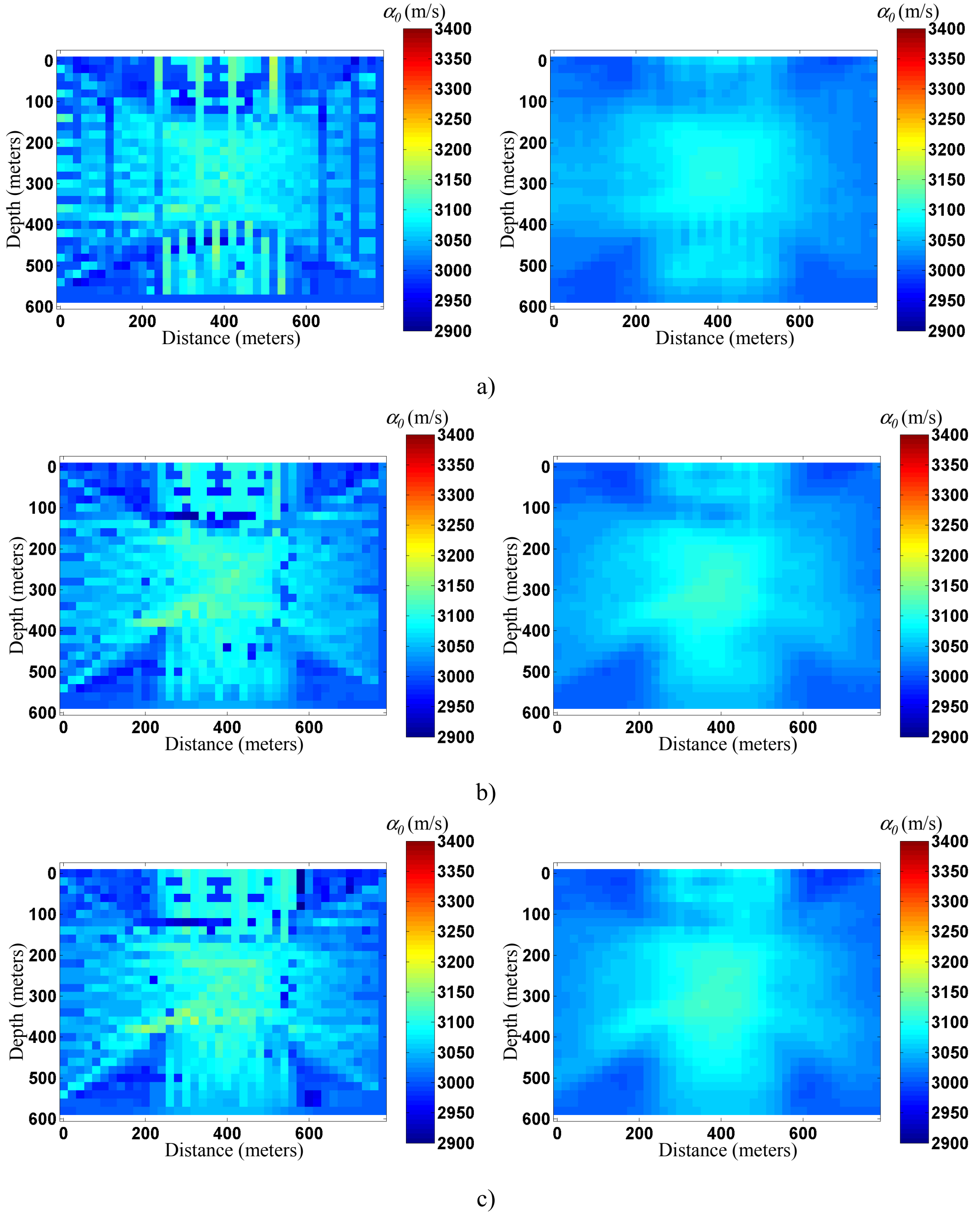

Figure 5.14 Quasi-null space integrated tomograms for centered velocity anomaly: (left) no post processing, (right) 5 by 5 cell smoother applied; (a) first iteration (b) second iteration (c) third iteration.

Notice that the complementary nature of crosswell and reflection experiments is exploited by the quasi-null space in integrating the tomograms. Also note that there are still acquisition footprints in the resulting tomograms. This footprint suggests that though integration using the quasi-null space is possible, it cannot overcome the inherent limitations of the acquisition geometry and the underlying velocity structure.

The results of the two simple velocity models reveal the limitations and capabilities of isotropic crosswell and surface tomography. The conventional tomographic process of applying a high-cut filter to the tomogram produces reasonable results although it is not data dependent and degrades tomogram resolution. As tomography is a nonlinear process due to raybending, it would make sense to use a data dependent stabilization technique. The quasi-null space is such a data dependent tool. The quasi-null space changes after each iteration adopting itself to the acquisition geometry and velocity structure. By knowing which cells contribute to the solution and their relative reliability, appropriate filtering can be applied. This is superior to filtering all cells. It is an interpretive process however, as tomography knows nothing of realistic geologic structures.

5.1.3 Complex isotropic velocity models

Consider now two complex velocity models shown in Figure 5.15.

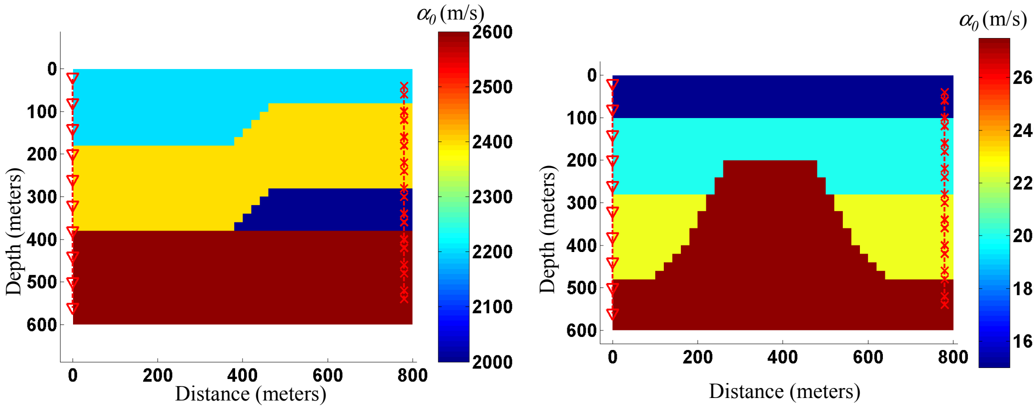

a) b)

Figure 5.15 Complex velocity models shown: model 1 (a) and model 2 (b).

Again, two acquisition geometries will be considered: crosswell and surface surveys. In model 1 (left), the target of interest is the low velocity layer of 2000 m/s while in model 2 the zone of interest is the layer of 2250 m/s which pinches against the flank of the dome-like structure.

5.1.3.1 Complex model 1

5.1.3.1.1 Crosswell tomography

Testing begins by using a constant initial velocity model of 2500 m/s. The crosswell tomographic results are shown in Figure 5.16

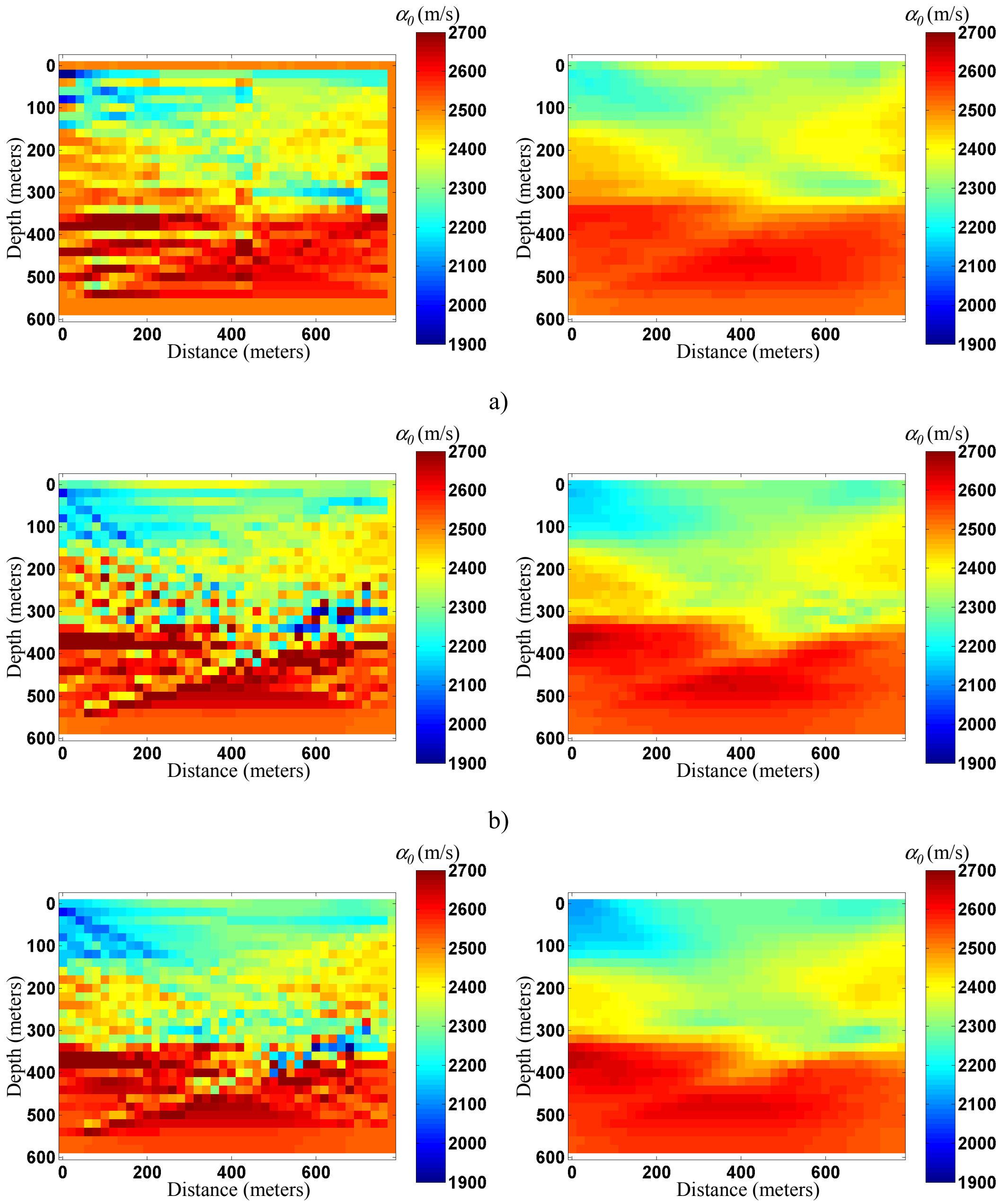

a)

b)

c)

Figure 5.16 Crosswell tomography results: (left) no post processing, (right) 5 by 5 cell smoother applied; (a) first iteration (b) second iteration (c) third iteration.

As shown in the simple velocity model results, the crosswell experiment is able to detect the vertical velocity variations quite well. In this case it also seems to detect the low-velocity zone of interest. The velocity values and outline of the zone of interest are skewed yet there are indications of a velocity anomaly in the general area specifically in Figure 5.16c.

5.1.3.1.2 Surface tomography

The surface tomography results are shown in Figure 5.17. Note that three reflecting interfaces have been included in the model. The one missing interface is that between the 2400 m/s layer and 2000 m/s zone of interest. This is done so as to determine the velocity anomaly detection capabilities of surface tomography.

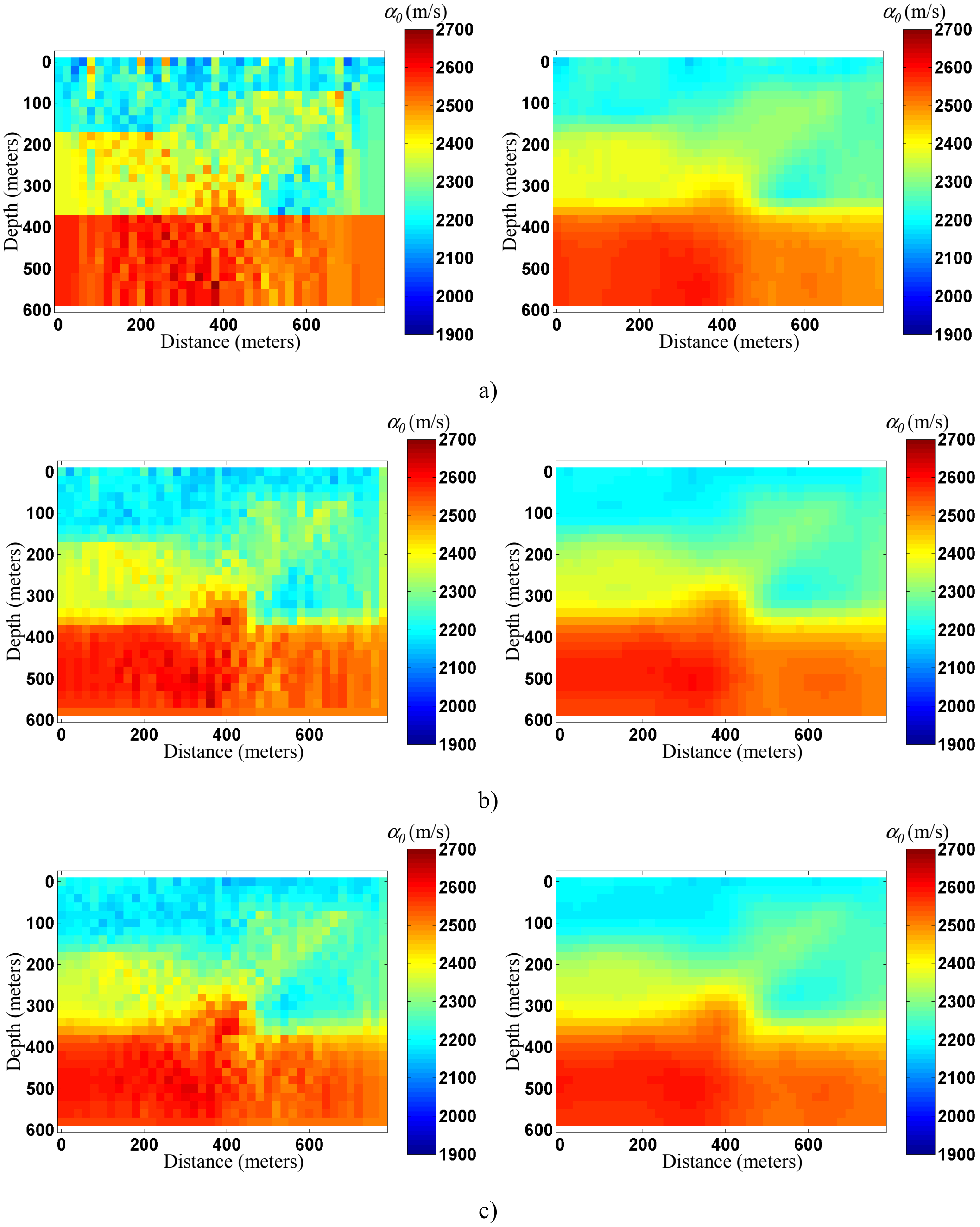

Figure 5.17 Surface tomography results: (left) no post processing, (right) 5 by 5 cell smoother applied; (a) first iteration (b) second iteration (c) third iteration.

The resulting tomograms from the surface experiment detect the low velocity anomaly though its magnitude and shape are not as accurate and sharp as one would like. Upon interpretation of the first output tomogram, it is not too far-fetched to include an extra reflecting interface once the slow-velocity anomaly has been detected. As shown in the simple velocity models, and as shown here, surface tomography resolves lateral velocity variations quite well. In fact, with the additional information provided to the model, in the form of reflecting interfaces, surface tomography is able to resolve vertical variations in velocity as well. For this model, the surface survey produces a better tomogram than that of the crosswell survey. The reason for this is that the reflection survey has the advantage of increasing the ray coverage each time an additional reflector is added to the model. Unfortunately, crosswell tomography does not have this advantage and will always fall short in this respect.

5.1.3.2 Complex model 2

Next consider crosswell tomography for the second complex velocity model. In this model the targets of interest are the 2250 m/s structures that pinch against the high-velocity dome-like structure. With all the lateral velocity variations present in this model, the best result is expected to be from surface tomography. In this case the surface tomography experiment will consist of 3 reflectors. The reflector defining the interface outlining the top of the layer of interest is missing, intending to show the detection capabilities of surface tomography.

5.1.3.2.1 Crosswell tomography

Figure 5.18 shows the results for each of the three iterations of crosswell tomography.

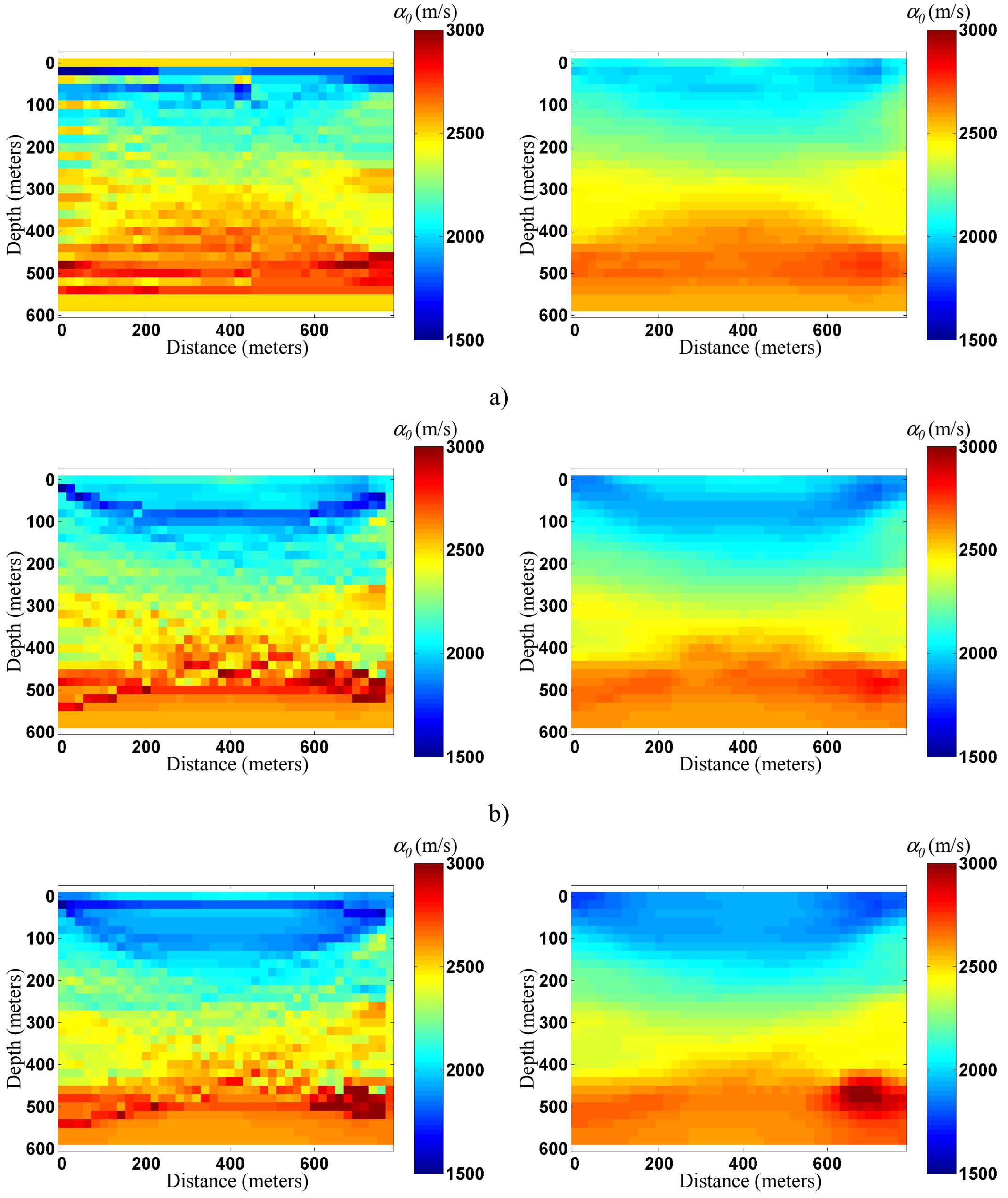

a)

b)

c)

Figure 5.18 Crosswell tomography results for second complex velocity model assuming an initial constant velocity model: (left) no post processing, (right) 5 by 5 cell smoother applied; (a) first iteration (b) second iteration (c) third iteration.

The results show a lack of lateral velocity resolution and good detection of vertical velocity variations as expected. The dome-like structure begins to disappear with each iteration as crosswell tomography biases the solution laterally, the direction of its dominant raypath. The slow-velocity anomaly has been obscured by the high-velocity dome. The average velocity however is such that the residual traveltime errors are minimized. Note that the resulting tomogram is asymmetric. This is a result of the asymmetry in the model used as well as the modelling algorithm used. As stated previously, due to the planewave approximation made in calculating traveltimes, raypaths closer to the source increase in error while raypaths closer to the receivers are sufficiently far away from the source that the planewave approximation is valid.

5.1.3.2.2 Surface tomography

The surface tomography results are seen in Figure 5.19

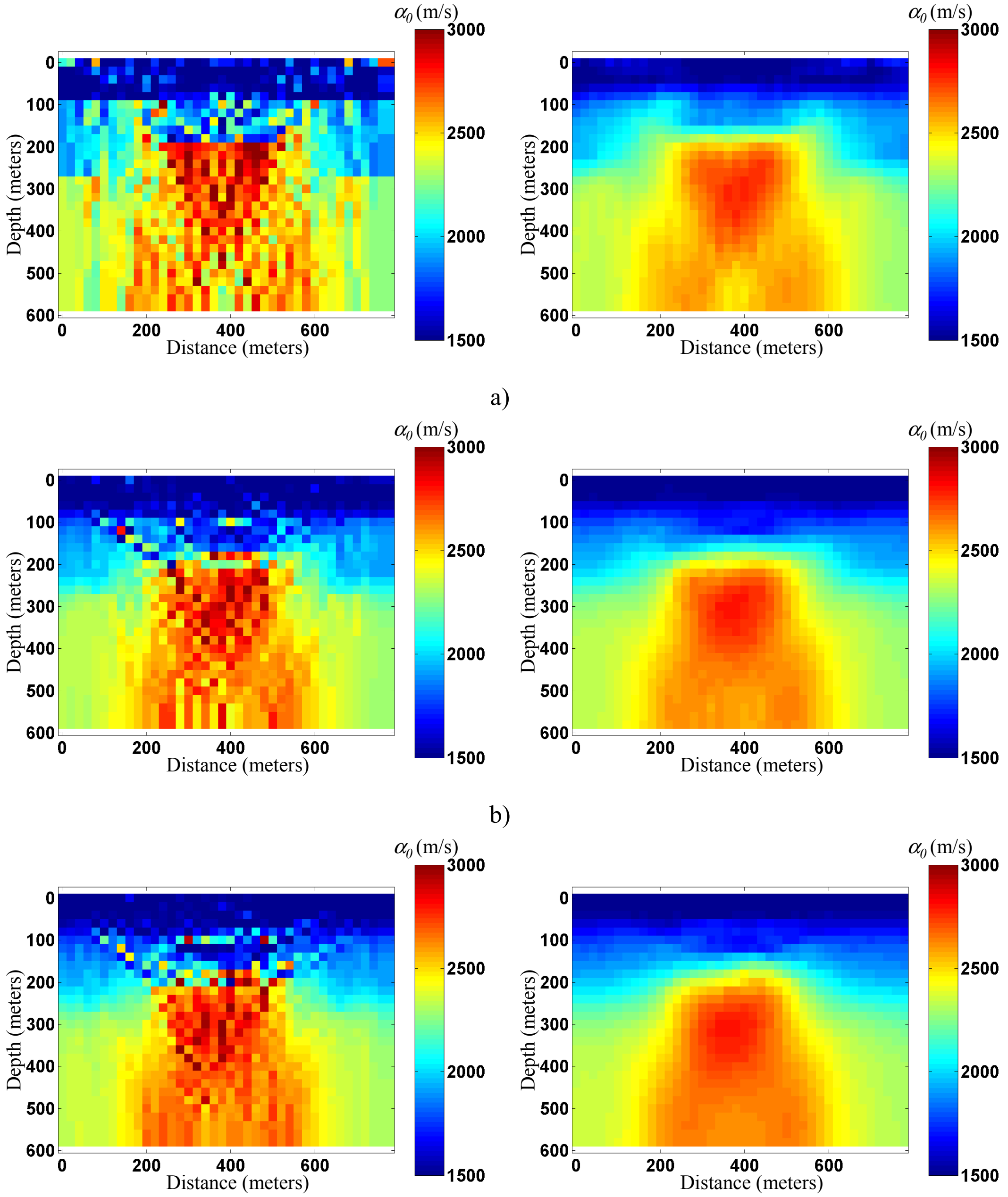

a)

b)

c)

Figure 5.19 Surface tomography results for second complex velocity models: (left) no post processing, (right) 5 by 5 cell smoother applied; (a) first iteration (b) second iteration (c) third iteration.

Surface tomography does not detect the vertical velocity variation without the specification of a reflector and uses a velocity that is an average of the interval above and the interval of interest. However the lateral definition of the dome-like structure is far superior to that of crosswell tomography.

5.1.4 Quasi-null space analysis – complex isotropic models

5.1.4.1 Dynamic smoothing: complex model 1

Implementing the dynamic smoothing technique built upon the quasi-null space the results are expected to be of sharper edges and smoothing over of the less reliable results. A quick look at quasi-null space shows the general solution reliability for model 1.

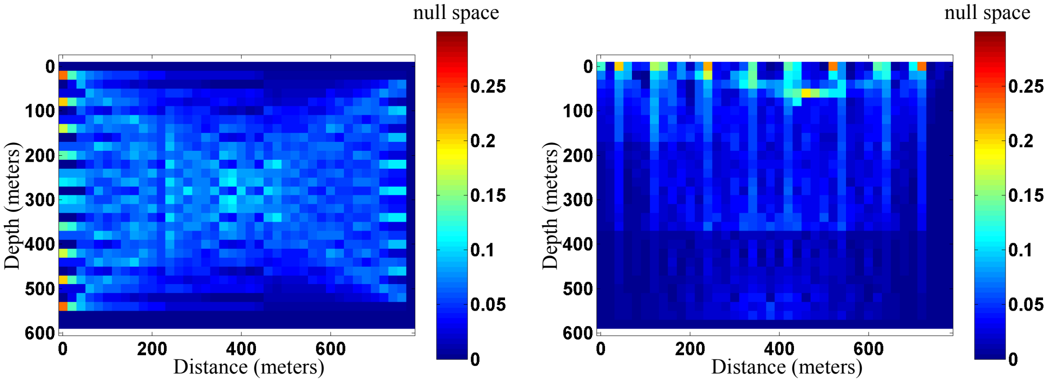

a) b)

Figure 5.20 Quasi-null space for crosswell (a) and surface (b) tomography.

In these two distinct experiments a general comment can be made which impacts the tomographic solution and the applicability of the dynamic smoothing technique. The quasi-null space on the left (crosswell) has better ray distribution in that the reliability space is spread out over a larger extent of the model in comparison. This will adversely affect the dynamic smoothing capabilities for the surface experiment (quasi-null space on the right) as the reliability values will be measured against the high values close to the surface. In this case, the increase in the number of modelled rays hinders the experiment as it biases the measure of reliability. This is another example of how acquisition geometry and the underlying velocity structure work against the ability to find an accurate solution.

Consider the results of the dynamic smoothing technique on the crosswell and surface experiments seen in Figure 5.21.

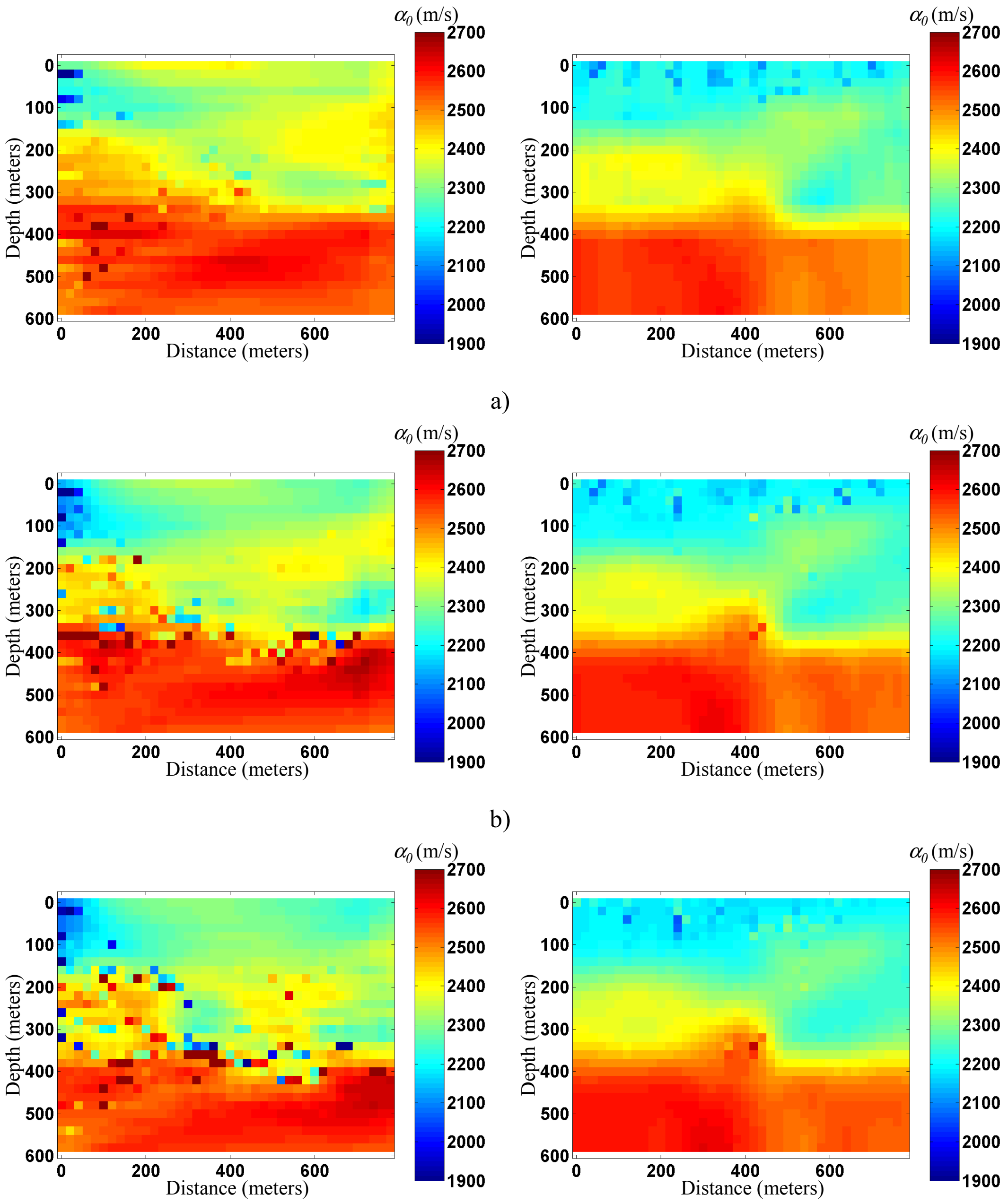

a)

b)

c)

Figure 5.21 Quasi-null space dynamic smoothing for crosswell (left) and surface (right) tomography: (a) first iteration (b) second iteration (c) third iteration.

As expected, most of the deeper cells of the surface experiment are considered unreliable and thus smoothed due to a relative lack of rays. The crosswell experiment attempts to maintain resolution integrity however it is unable to do so accurately in areas of lateral velocity variations. To understand this fully it is worthwhile view the third iteration quasi-null space for both experiments.

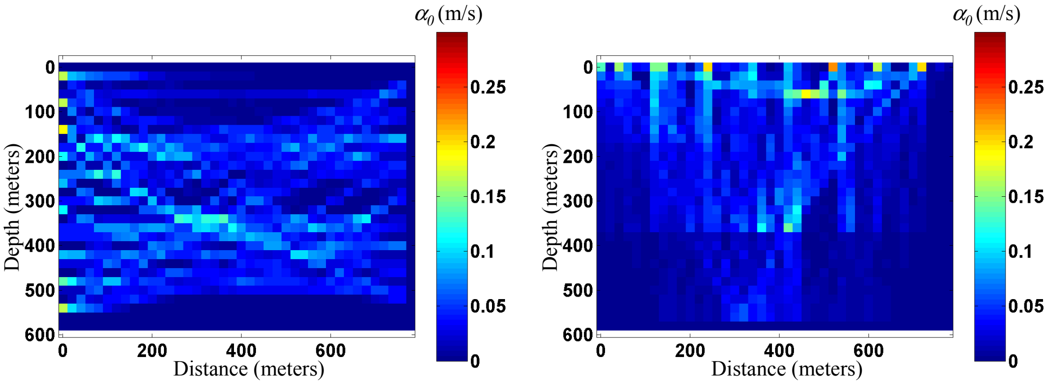

a) b)

Figure 5.22 Third iteration quasi-null space: crosswell (a) and surface (b) geometry

The crosswell quasi-null space reveals how the low-velocity zone is ray deficient (at a location approximately centered at a depth of 300 m and a distance of 600 m) and thus has unreliable solution results. Similarly, the surface quasi-null space response shows that rays tend to avoid the low-velocity zone although the acquisition geometry prevents this from happening in the extent seen in the crosswell case. The question still remains as to why quasi-null space dynamic smoothing does not produce results as comparable to those of the simple velocity model.

Consider first the crosswell experiment. In this case the reliability space represents the acquisition geometry. On average the reliability is spread out laterally although there are localized areas in the middle of the survey of relatively high reliability where the rays are refracted. Since the reliability is spread out laterally, dynamic smoothing parameters can be chosen to either smooth so that the entire tomogram is considered unreliable and thus all the cells are smoothed or to identify cells where this are no raypaths (specifically top and bottom of model) as unreliable. In this case, the tomograms were deemed for the most part reliable and only the top and bottom was smoothed. As a consequence, there exists some sharp velocity boundaries but at the expense of the appearance of anomalous cell velocities. For the surface experiment the reliability space is dominated by the near surface thus making the deeper section appear less reliable and thus more smoothed. The quasi-null space can be used to interpret relative reliability in a vertical sense in crosswell tomography and laterally in surface tomography.

5.1.4.2 Integration: complex model 1

The following figures show the results of integrating the crosswell and surface based upon the quasi-null space.

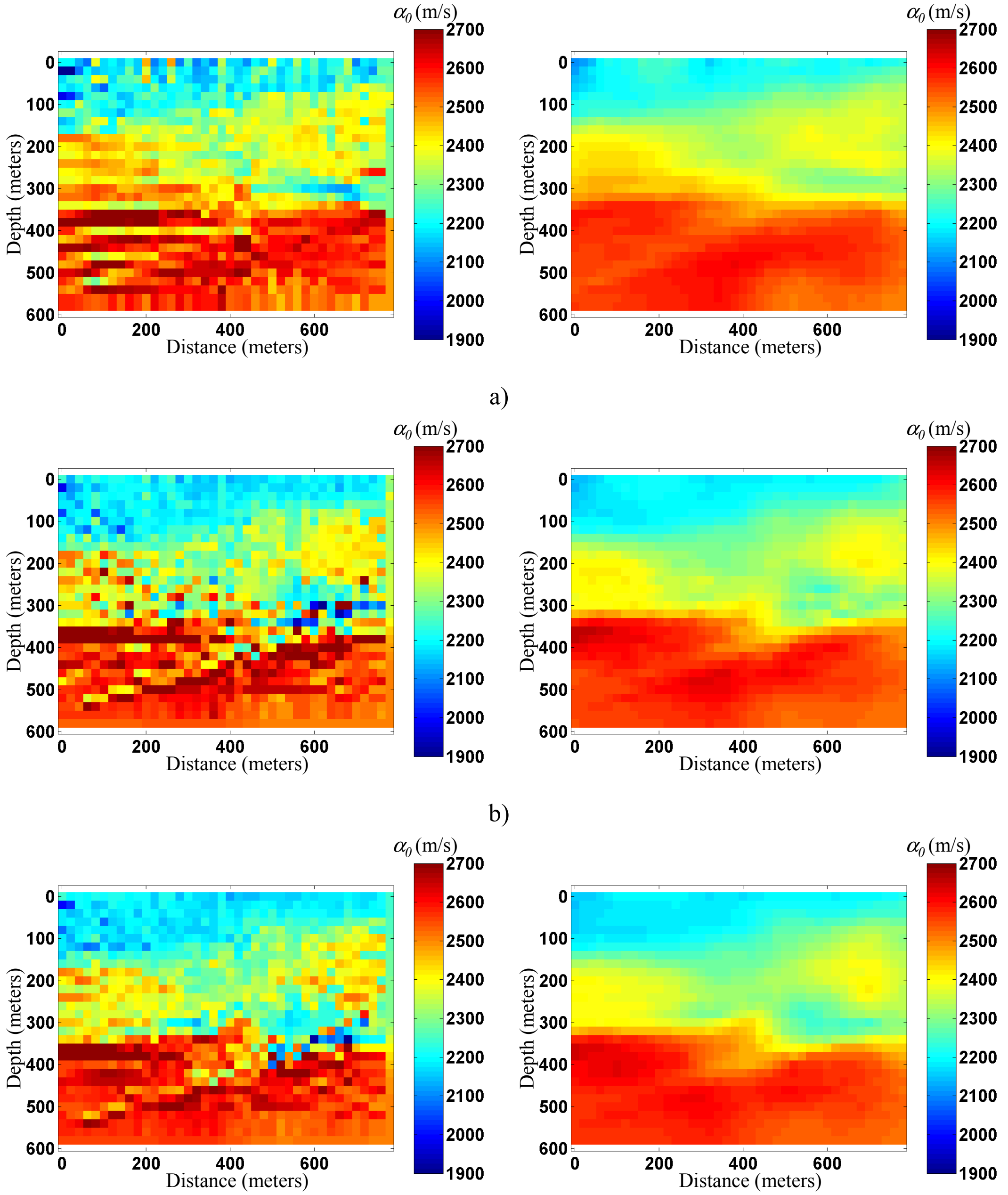

a)

b)

c)

Figure 5.23 Quasi-null space crosswell and surface integration: crosswell (left) and surface (right) geometry; (a) first iteration (b) second iteration (c) third iteration.

The quasi-null space integration technique does not fail in this case. In this case there the more reliable solution of each experiment is chosen and takes the best part of each to construct a stable tomogram. The complex nature of the velocity model aids in clearly identifying the strengths and weakness of each tomographic solution. The smoothed third iteration result shows the best identification of the slow-velocity anomaly while maintaining the highest amount of accuracy in shape and magnitude of the surroundings.

5.1.4.3 Dynamic smoothing: complex model 2

Figure 5.24 shows the results of dynamic smoothing applied to crosswell and surface tomography.

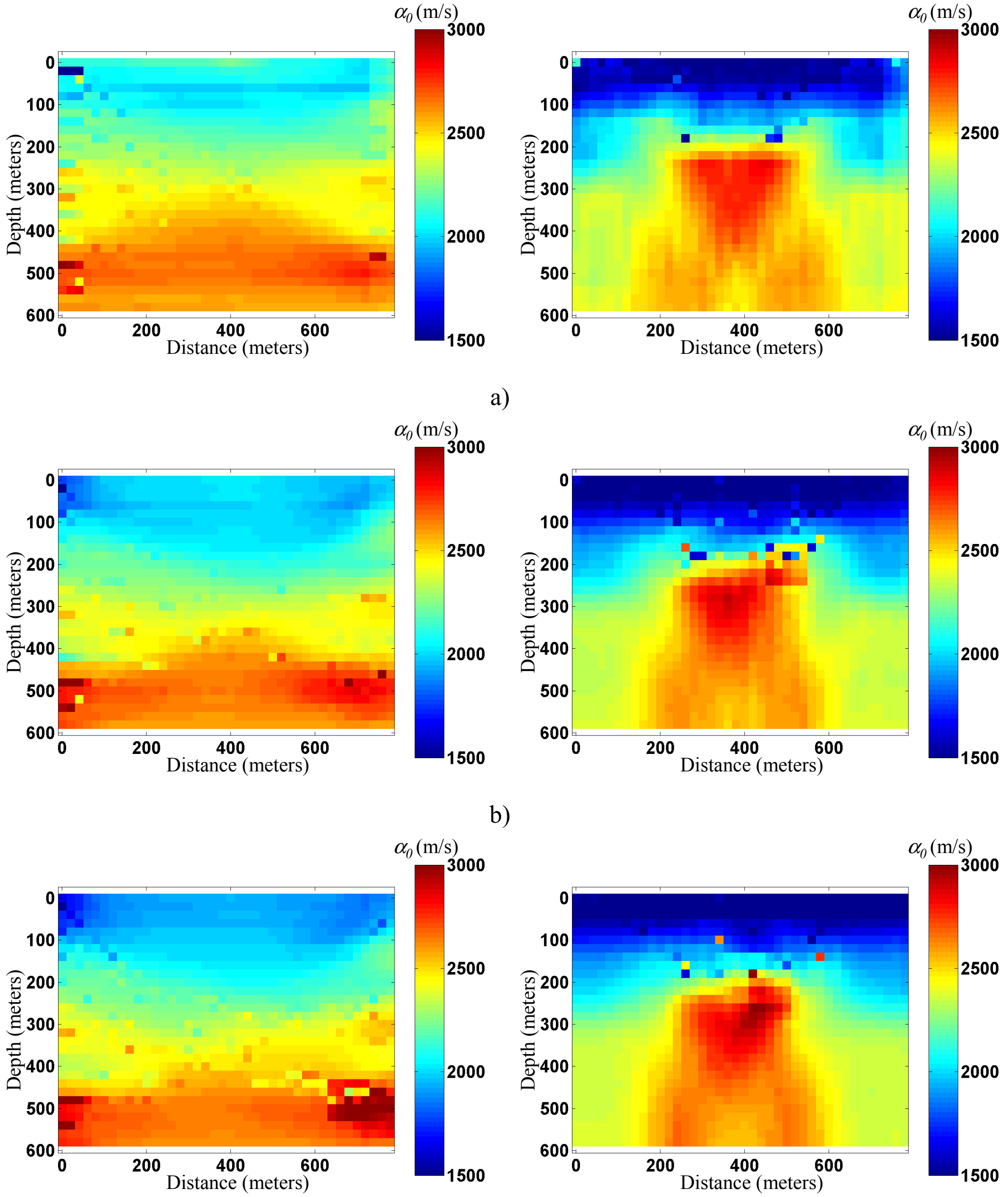

a)

b)

c)

Figure 5.24 Quasi-null space dynamic smoothing on the second complex velocity model: crosswell (left) and surface (right) (a) first iteration (b) second iteration (c) third iteration.

These results are similar in nature to those of the first complex velocity model. Figure 5.24c shows concisely the different capabilities of each acquisition technique and the most reliable zones of each. Crosswell tomography correctly identifies 4 intervals of interest while surface tomography delineates the lateral extent of the dome-like structure. Crosswell tomography has the most reliable zones spread out laterally in the middle of model while surface tomography is more reliable closer to the surface. It is appropriate that the deeper cells are less reliable than those closer to the surface as the deeper values are dependent upon the velocity values above. In a sense the deeper cells values measure of reliability reflects the fact that it is conditional on the level of correctness of the values in the shallow section.

<u>*5.1.4.4 Integration: complex model 2*</u>

Integrating both crosswell and surface results hope to yield a superior tomogram. For the integration technique, since there is a discrepancy in the quasi-null space, it is worthwhile to use different threshold levels in each reliability space determination. The purpose of this is to obtain similar reliability values such that the reliability in the centre of the model is comparable. The quasi-null spaces for each are in Figure 5.25.

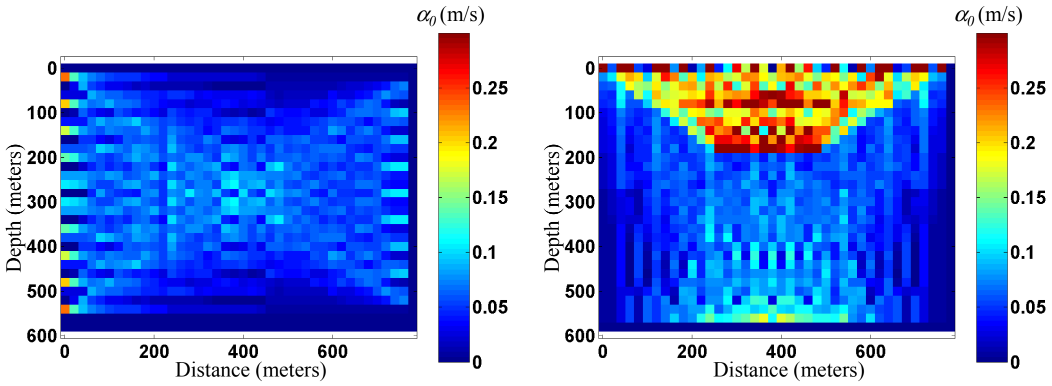

a) b)

Figure 5.25 Quasi-null space for crosswell (a) and surface (b) geometries.

Visually inspecting the quasi-null reliability spaces it becomes evident that the reliability in the crosswell experiment is greater laterally and for the surface experiment the reliability is greater vertically. Also note that the quasi-null spaces chosen to guide integration have been scaled so that the centers of the models have similar reliability values. Integrating the experiments it is hoped that the output tomogram will provide the best resolution from both experiments. The results are seen in Figure 5.26.

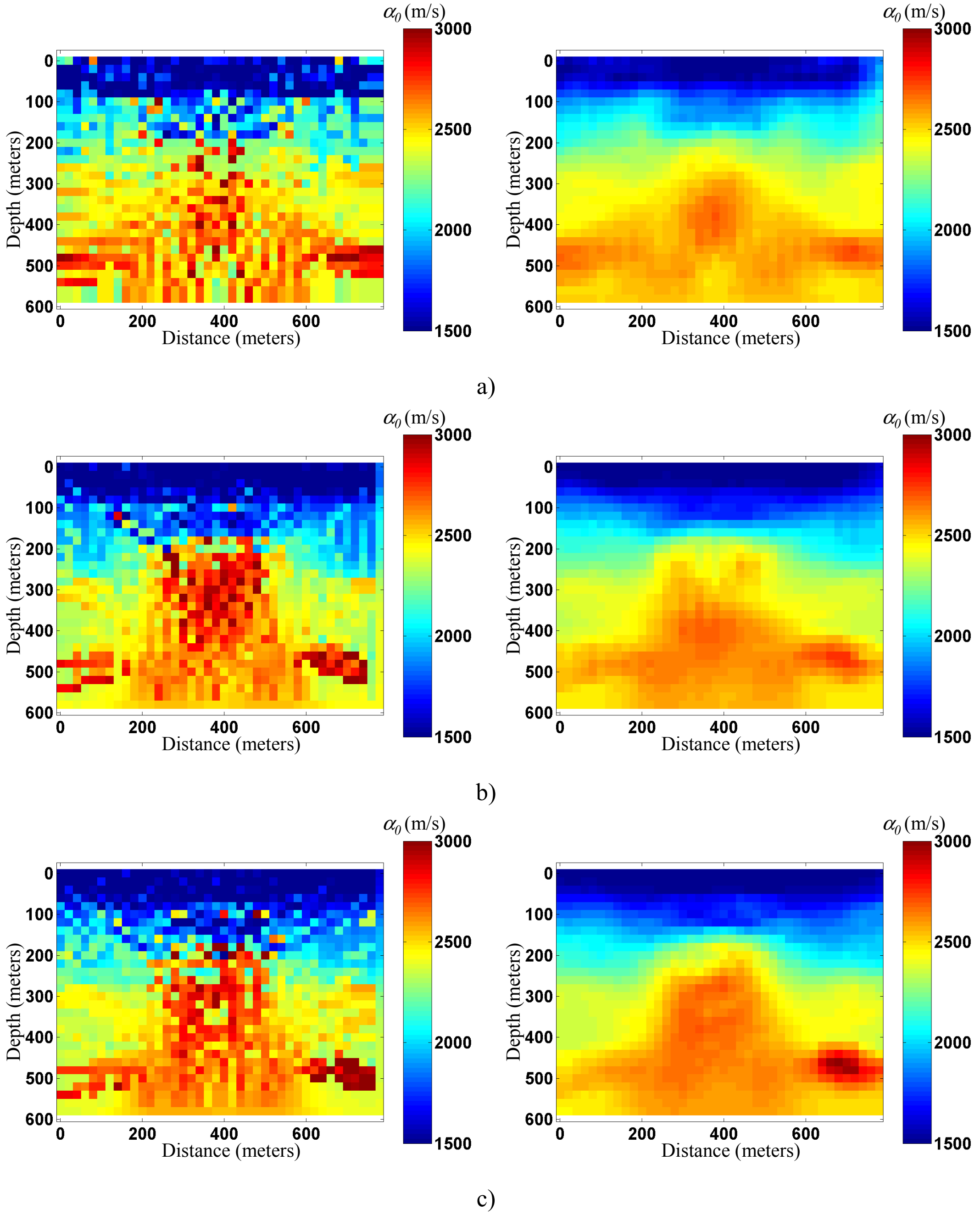

Figure 5.26 Quasi-null space crosswell and surface tomography integration tomograms: (left) no post processing, (right) 5 by 5 cell smoother applied; (a) first iteration (b) second iteration (c) third iteration.

Note that the results in general have the basic shapes that are similar to the original velocity model. In the third iteration of integration, there is good evidence of 4 distinct velocity layers as well as good lateral resolution of the dome like structure. Comparing the original results of crosswell and surface tomography to the final iteration of the combined tomogram clearly shows that the quasi-null space integration method is a good tool in providing more accurate velocity profiles.

5.2 Anisotropic Tomography

Anisotropic tomography attempts to determine Thomsen's parameters of ε and δ. These parameters are perturbations to the isotropic velocity, α_0. The ability to distinguish between α_0, the vertical P-wave velocity, and the Thomsen parameters is of great importance as there are multiple solutions that can replicate the observed traveltimes. The method tested here inverts for the parameters of ε and δ independently of α_0 by using a two-step process. The anisotropic tomography workflow follows the same template of the isotropic workflow. The differences are highlighted in the description that follows:

1. The initial model estimate consists of estimates for α_0, ε and δ. The estimate for these parameters can be based on well information.
2. Anisotropic traveltimes and raypaths are computed through a smoothed model estimate through methods presented in Chapter 2.
3. Two distinct matrices are constructed. One that relates the effect of the parameter α_0 on traveltimes and the other relating ε and δ to traveltimes.
4. Parameter updates are computed first for α_0 and then separately for ε and δ.
5. The α_0, ε and δ tomograms are smoothed with a 5 by 5 cell operator.

6. Steps 2 through 5 are for two more iterations. The last set of tomograms after the final iteration is the final solution.

Testing begins with the two simple velocity models shown in the isotropic case, the horizontal high-velocity anomaly and the centered high-velocity anomaly. Thomsen's parameters are added to the model, shown in Figure 5.27

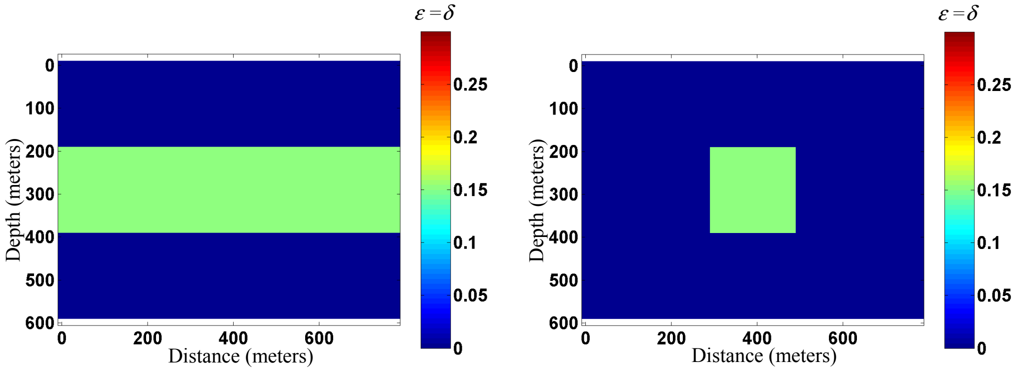

a) b)

Figure 5.27 Two simple anisotropic models, a) anisotropic horizontal layer and b) center anisotropic anomaly: $\varepsilon=\delta=0.15$ for both.

Both ε and δ are equal to 0.15 in both models. This specific case of transverse isotropy is called elliptical anisotropy. Elliptical anisotropy, like isotropy, has hyperbolic moveout and therefore anisotropic layers cannot be distinguished from isotropic ones through the time based process of applying normal moveout correction (Alkhalifah and Tsvankin, 1995). In time processing, only vertical velocity variations, v(z), can be accounted for. Tomography is a depth process and allows for the compensation of non-hyperbolic moveout. Non-hyperbolic moveout can arise from two different methods. Far offset data gives rise to non-hyperbolic moveout in isotropic media as a function of lateral velocity variations. Non-hyperbolic moveout can also be accounted for by the presence anisotropy. Thus ambiguity exists for both the hyperbolic and the non-hyperbolic moveout relation. The anisotropic workflow presented attempts to alleviate both hyperbolic and non-hyperbolic ambiguity by solving for the isotropic velocity component, α_0, and the anisotropic components ε and δ independently. As will be shown, the best case scenario for inverting for ε and δ, is when α_0 is known so that any residual traveltime errors can be compensated for by adding anisotropy.

The acquisition geometry for both crosswell and surface experiments is identical to those seen in the isotropic case. Six different initial model estimate scenarios are considered. The first consists of flooding the model with a constant velocity of 3000 m/s and assuming isotropy. The second will assume that the vertical P-wave velocity is known completely and the goal is to estimate the anisotropic parameters. The third will assume that the anisotropic parameters are known completely and the goal is to estimate α_0. The last three scenarios will have 10, 20 and 50 percent random error added to the correct models of α_0, ε, and δ.

5.2.1 Simple anisotropic velocity models

5.2.1.1 Horizontal anomaly model: initial model estimate α_0=3000 m/s, ε=δ=0

5.2.1.1.1 Crosswell tomography

Consider the third iteration results of crosswell tomography in Figures 5.28 using as an initial model a constant velocity background of 3000 m/s and a constant anisotropic parameters $\varepsilon = \delta = 0$.

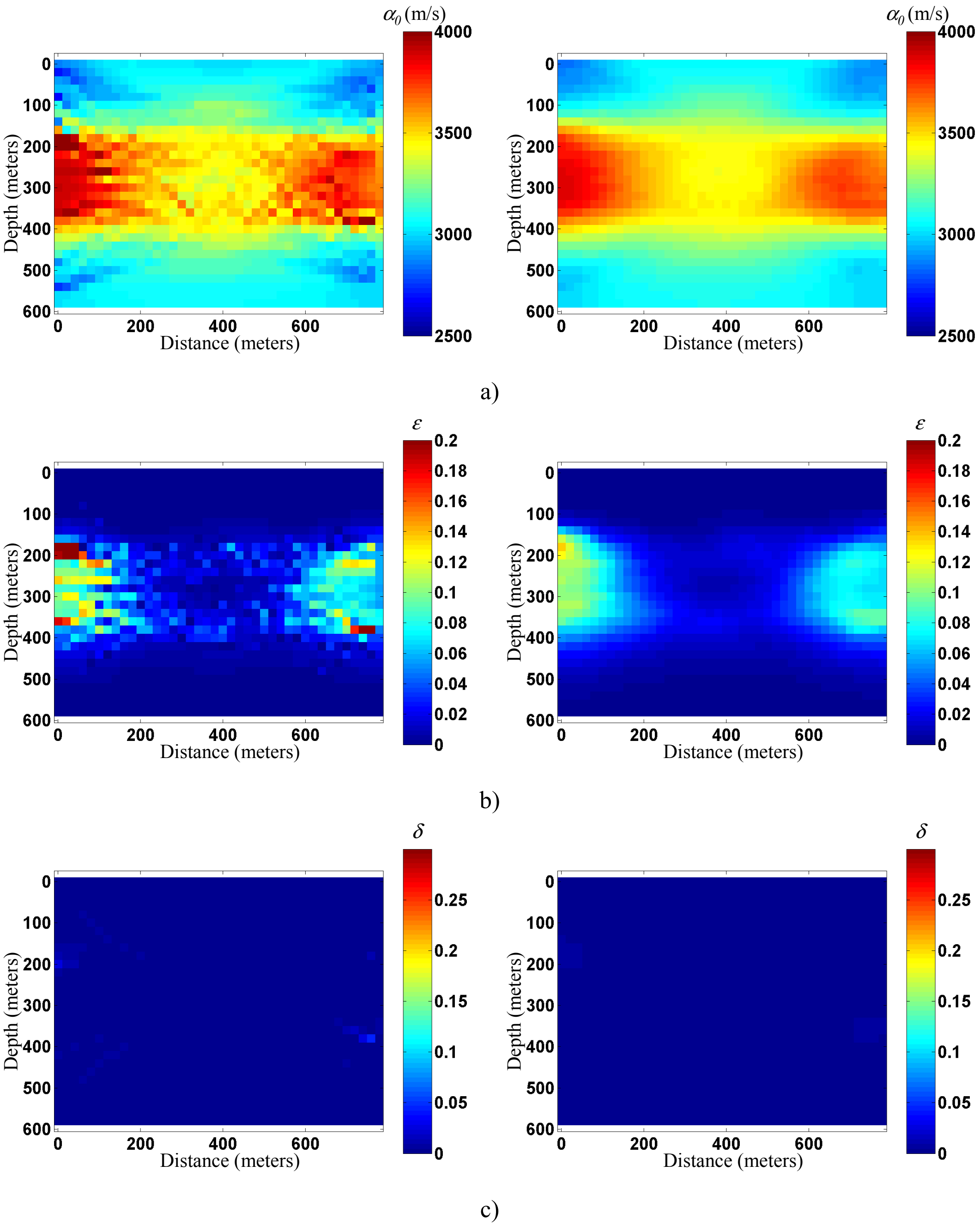

a)

b)

c)

Figure 5.28 Third iteration crosswell tomography results: (left) no post processing, (right) 5 by 5 cell smoother applied; (a) α_0 (b) ε (c) δ. Colorbars represent values of $\alpha_{0,}$ ε and δ.

Notice that result for the vertical P-wave velocity is higher than the actual, approaching velocities of up to 3800 m/s. This is a consequence of the anisotropy providing smaller measured traveltimes than the isotropic case. This translates into an apparently faster velocity in the anomaly. The results for ε are encouraging as the correct shape of the anomaly has been detected even in the magnitude and continuity of the anomaly is lacking in accuracy. The results for the parameter δ are discouraging as all the traveltimes residuals have been accounted for either by increasing the vertical P-wave velocity or ε. Given the predominant raypath direction it should not be unexpected that ε carry the majority of the load in adjusting for traveltime residuals. Recall that ε relates the vertical P-wave velocity to the horizontal P wave velocity.

5.2.1.1.2 Surface tomography

The third iteration results of surface tomography are seen in Figure 5.29.

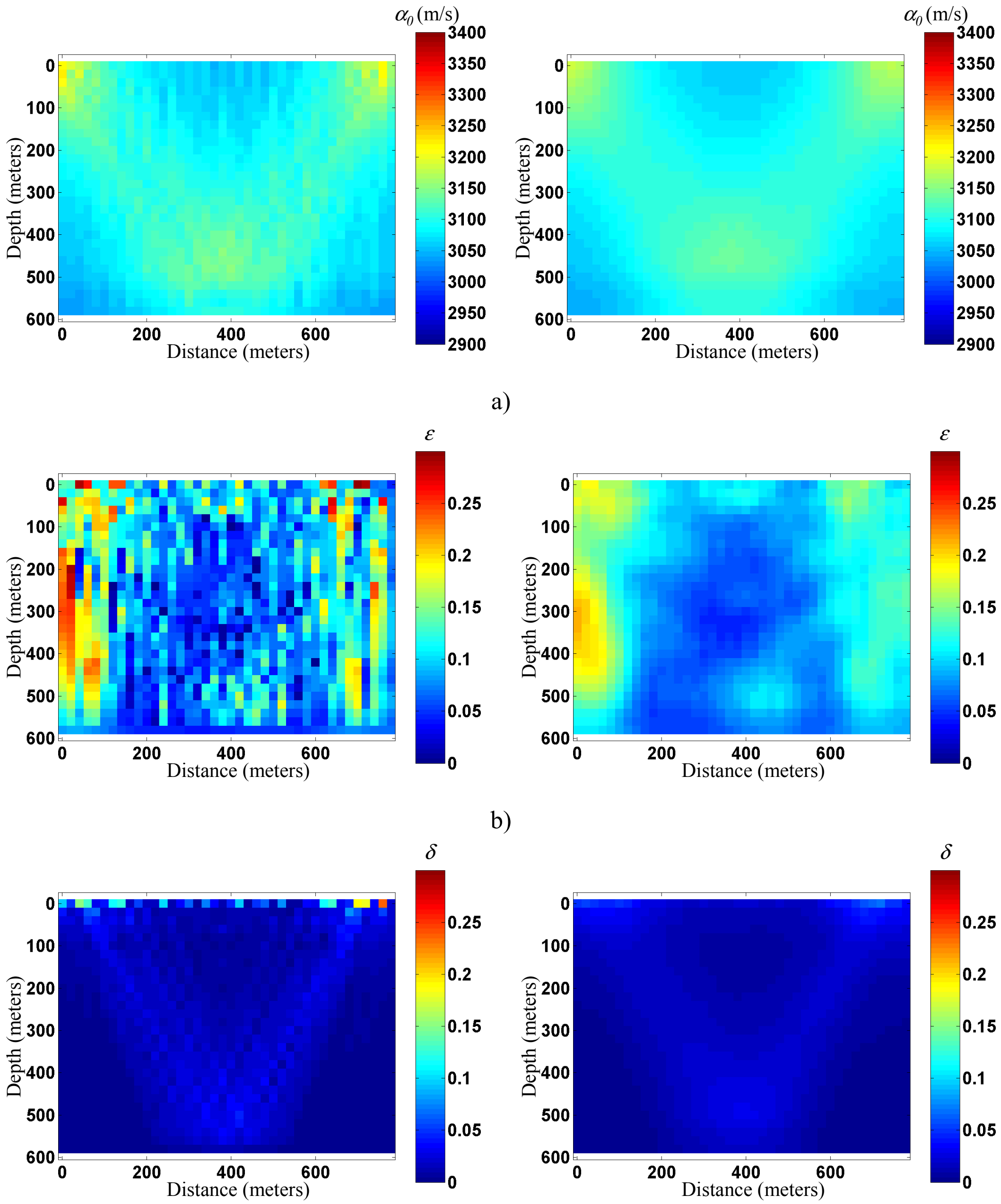

a)

b)

c)

Figure 5.29 Third iteration surface tomography results for the horizontal high-velocity anisotropic layer: unsmoothed result (left) and smoothed, 5 by 5 cell filter (right) for α_0 (a), ε (b), and δ (c).

Note that these results are similar to those seen in isotropic surface tomography. There is a distinct difference however that may lead to some insight in distinguishing between a completely isotropic model and an anisotropic one. In the results shown in Figure 5.29 there is a high-velocity "V" shape in the resulting profiles. This is a consequence of the increase in velocity with angle of transversely isotropic media. This “V” shape is not evident in the isotropic case since there is no angle dependency. This difference can be used as a template to help interpret an isotropic velocity response versus an anisotropic response. The surface tomography experiment will no longer be pursued for the horizontal model as further iterations or quasi-null space analysis can provide no more detail as was the case in the isotropic model.

5.2.1.2 Horizontal anomaly model: initial model estimate α_0=3000 m/s, ε=δ=known

5.2.1.2.1 Crosswell tomography

Next consider the vertical P-wave results using an initial background model where ε and δ are known completely and an initial estimate for α_0 of 3000 m/s is used. The third iteration crosswell results are seen in Figure 5.30.

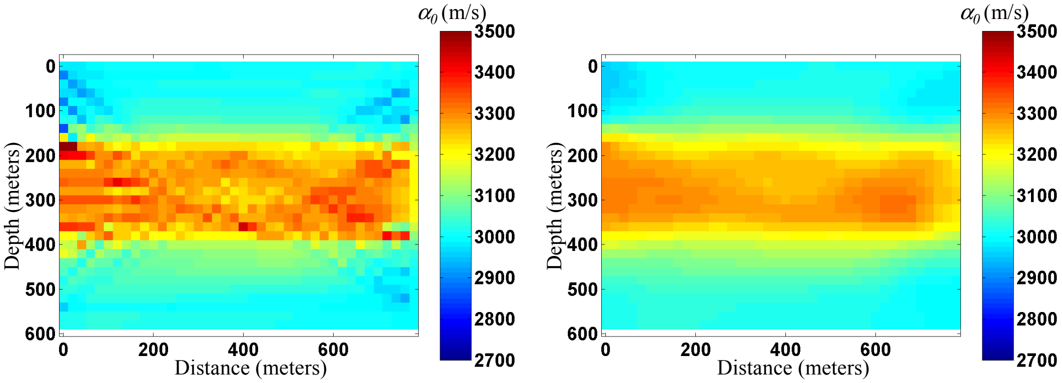

a) b)

Figure 5.30 Vertical P-wave velocity tomograms after third iteration; ε and δ known.

This result is comparable to that of the isotropic crosswell result. The high-velocity anomaly is clearly distinguishable and the magnitude of the layer and it surroundings are quite accurate. This result indicates that if the correct initial model for ε and δ are used, it is possible to converge to the correct solution for α_0. Interpreting the results becomes of vital importance as the correct geologic-like velocity model is more likely to produce the smallest residual traveltimes.

5.2.1.3 Horizontal anomaly model: initial model estimate α_0=known, ε=δ=0

5.2.1.3.1 Crosswell tomography

Next consider the solutions to ε and δ assuming an initial model in which the vertical P-wave velocity is known completely while ε and δ are assumed to be zero. The results after a third iteration are shown in Figure 5.31.

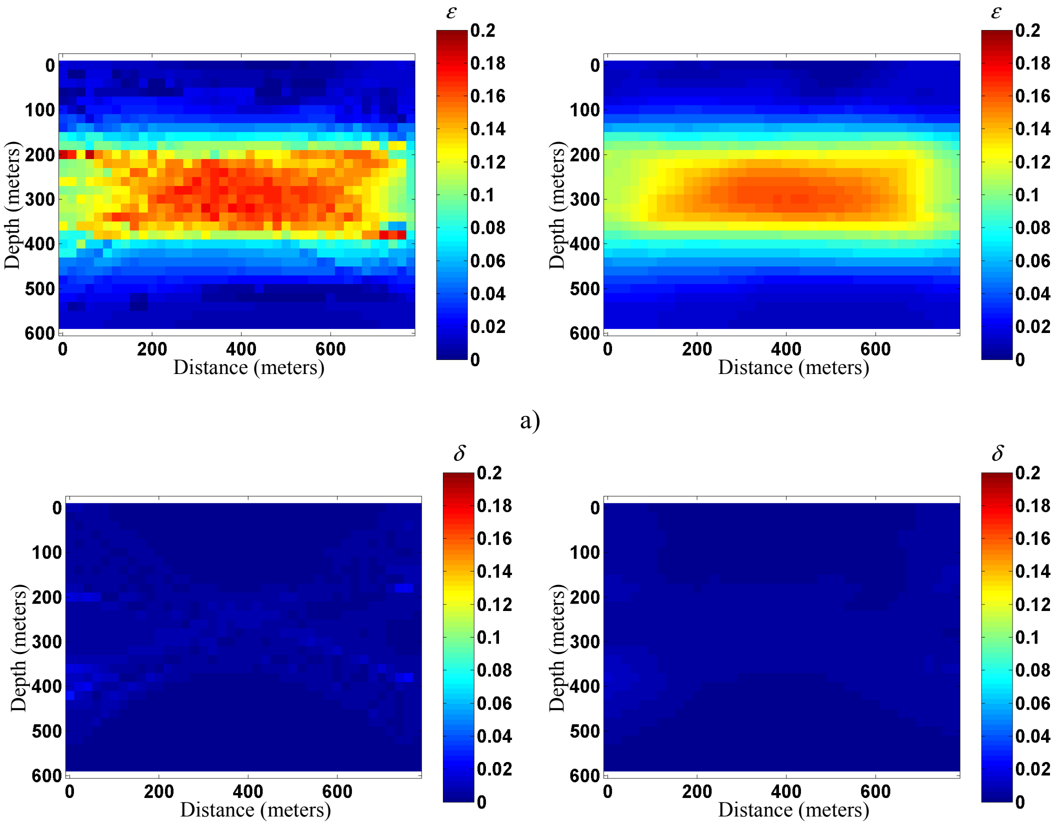

a)

b)

Figure 5.31 Final tomogram for Thomsen parameter ε (a) and δ (b) after third iteration: unsmoothed (left) and smoothed (right).

These results are both encouraging and discouraging. For ε the results are quite promising as it shows that once the correct vertical P-wave velocity is known, it is possible to establish a reasonable estimate for ε, although it has been overestimated. The final tomogram for δ is not as accurate in magnitude as one would like although upon close inspection the general outline of the horizontal layer is discernable. This result is expected however since there are only a minimal amount of vertical rays that are required to determine δ.

5.2.1.4 Horizontal anomaly model: initial model estimate α_0, ε, δ with random error

The next set of tests begin with initial model estimates where 10, 25 and 50 percent of random error is added into actual velocity, ε and δ. These initial models are seen in Figures 5.32 through 5.34. For visual purposes, figures for ε and δ are shown as the amount of error added to the actual model.

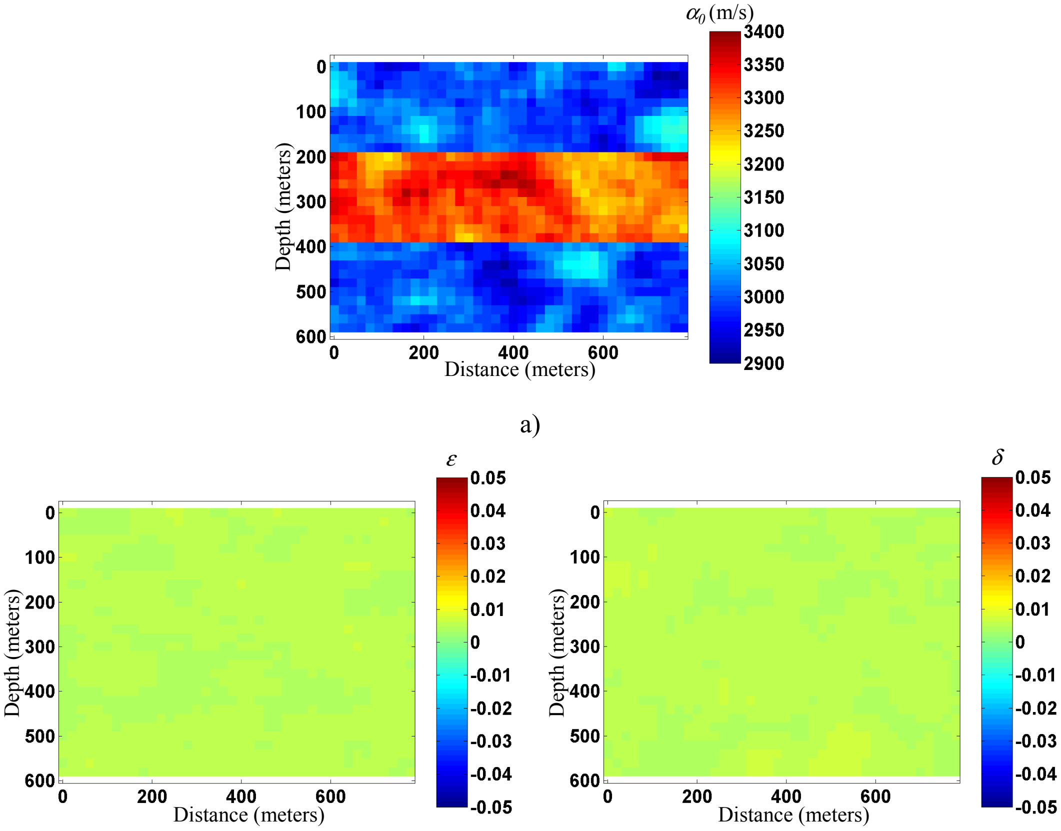

a)

b)

c)

Figure 5.32 Ten percent error added to initial model (a) α_0, (b) ε and (c) δ.

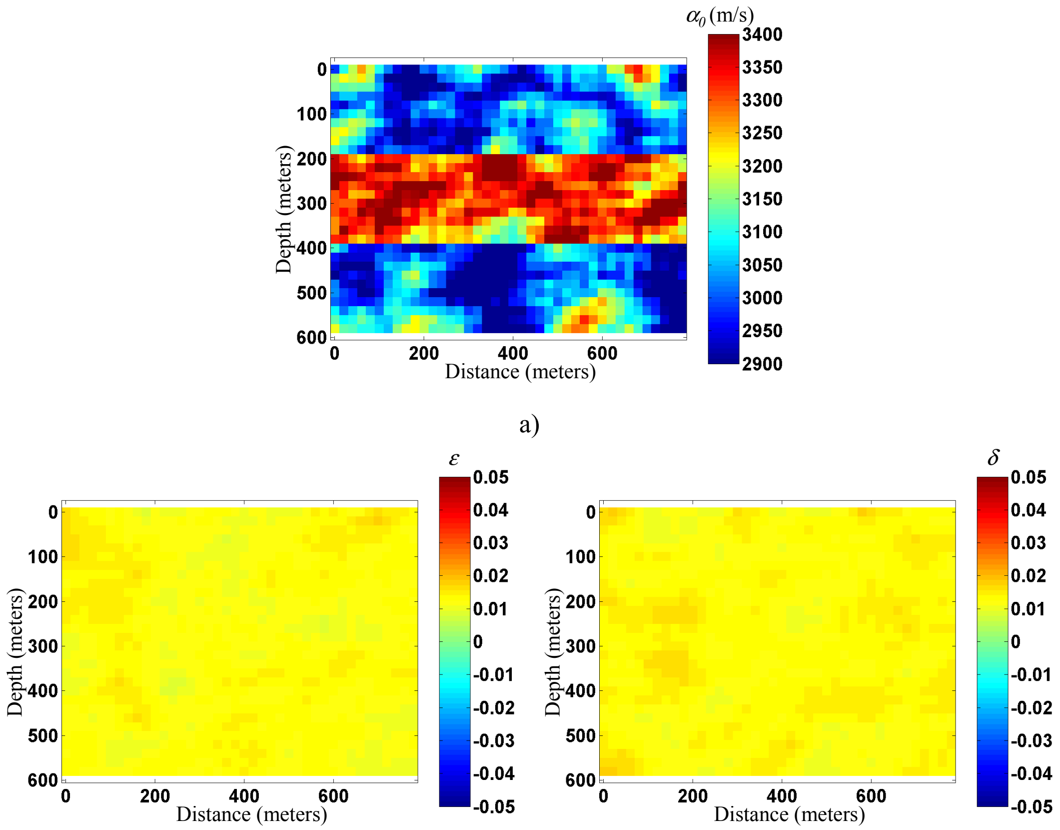

a)

b)

c)

Figure 5.33 Twenty-five percent error added to initial model (a) α_0, (b) ε and (c) δ.

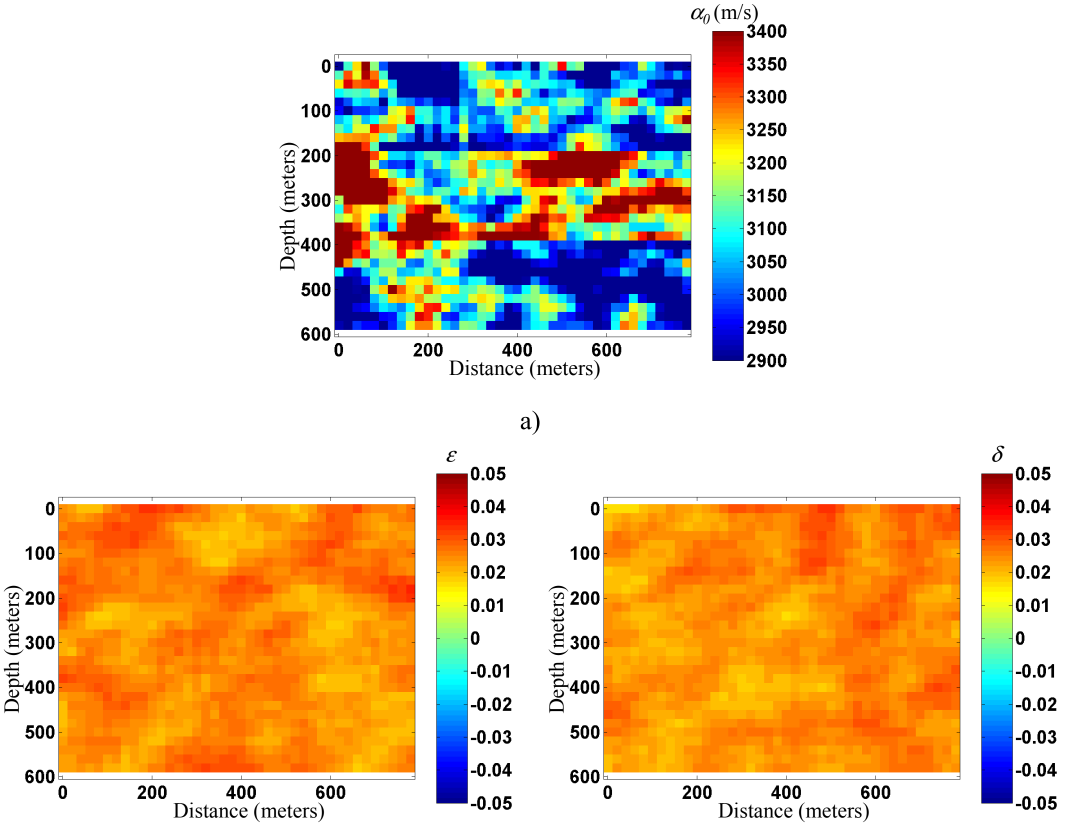

a)

b) c)

Figure 5.34 Fifty percent error added to initial model (a) α_0, (b) ε and (c) δ.

With the increase of random error, the true model becomes obscured and allows for testing of the algorithms convergence and stability capabilities.

5.2.1.4.1 Crosswell tomography

The resulting crosswell tomograms for the 10 percent error initial model (Figure 5.32) are seen in Figure 5.35.

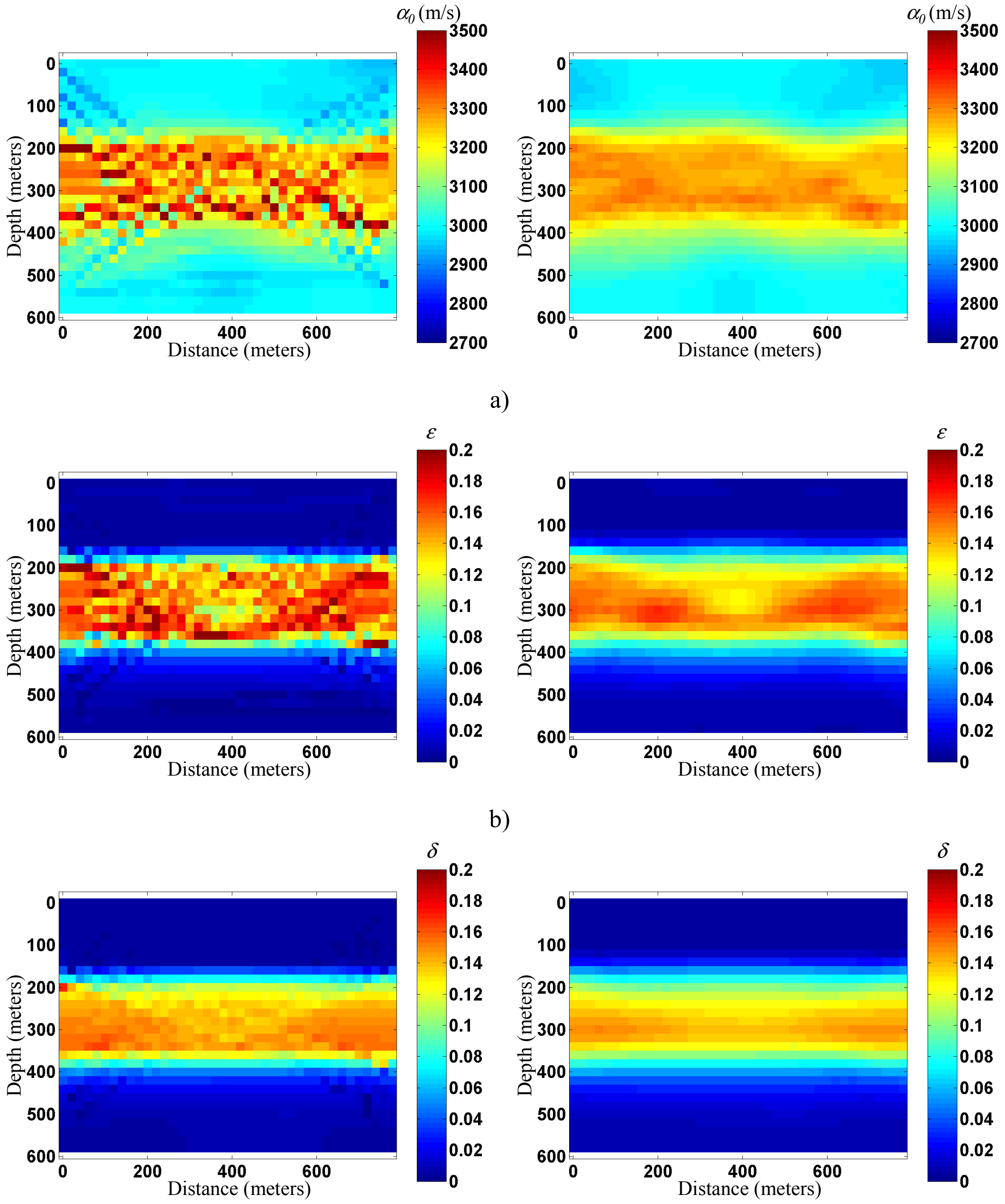

a)

b)

c)

Figure 5.35 Third iteration crosswell tomography results using initial model with 10 percent random error added: (left) no post processing, (right) 5 by 5 cell smoother applied; (a) α_0 (b) ε (c) δ.

These results are encouraging from the point of view that convergence is possible for anisotropic crosswell tomography. This indicates that the solution is stable and not too sensitive to error either in the data or from modelling.

Figure 5.36 shows the third iteration crosswell tomogram results when using an initial model with 25 percent random error added (Figure 5.33).

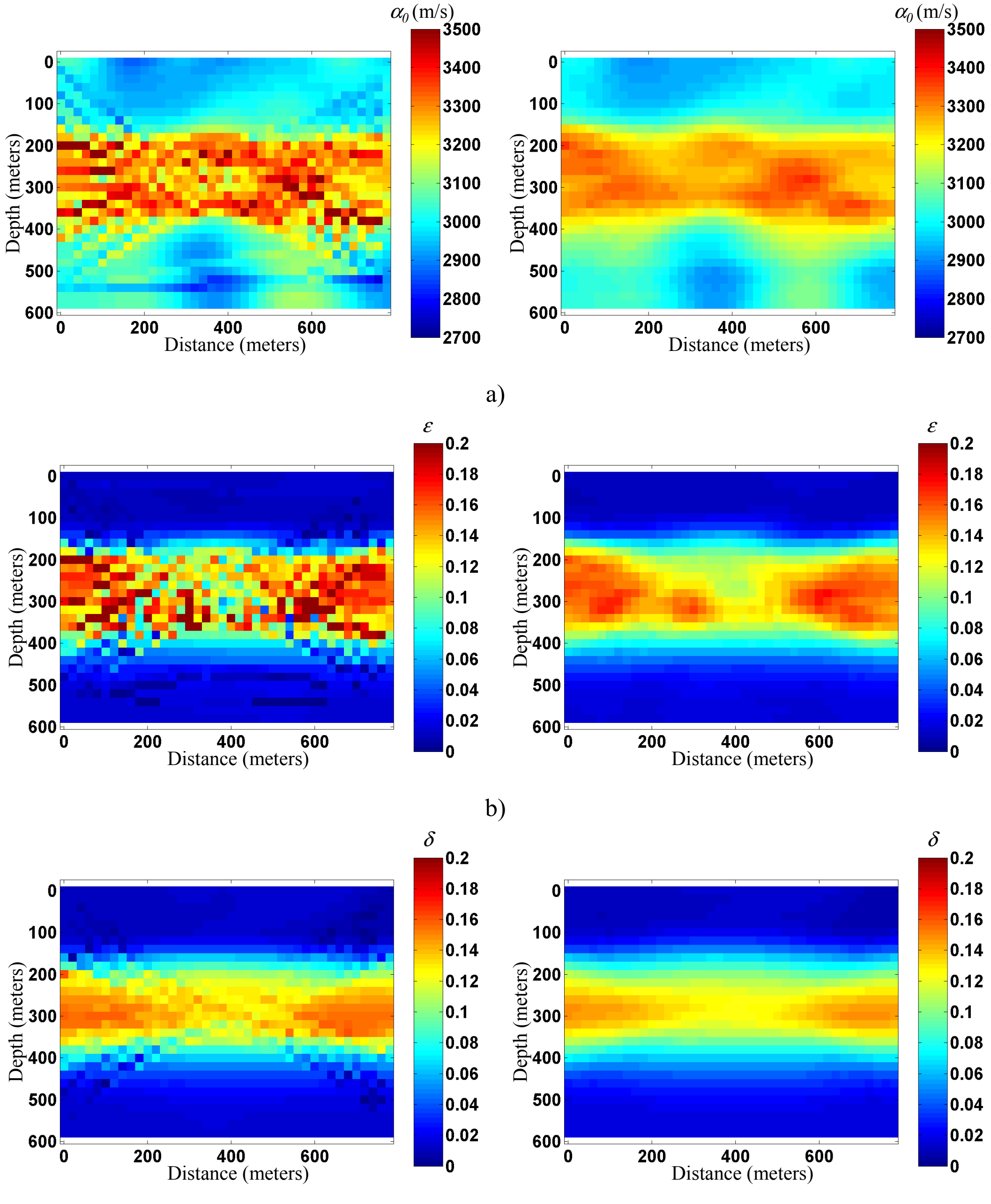

a)

b)

c)

Figure 5.36 Third iteration crosswell tomography results using initial model with 25 percent random error added: (left) no post processing, (right) 5 by 5 cell smoother applied; (a) α_0 (b) ε (c) δ.

These results are also quite good. In general, the tomograms converge to the correct result. The result however it is not as accurate as the results when using 10 percent error in the initial model.

Crosswell results from using a 50 percent random error in the model (Figure 5.34) are in Figure 5.37.

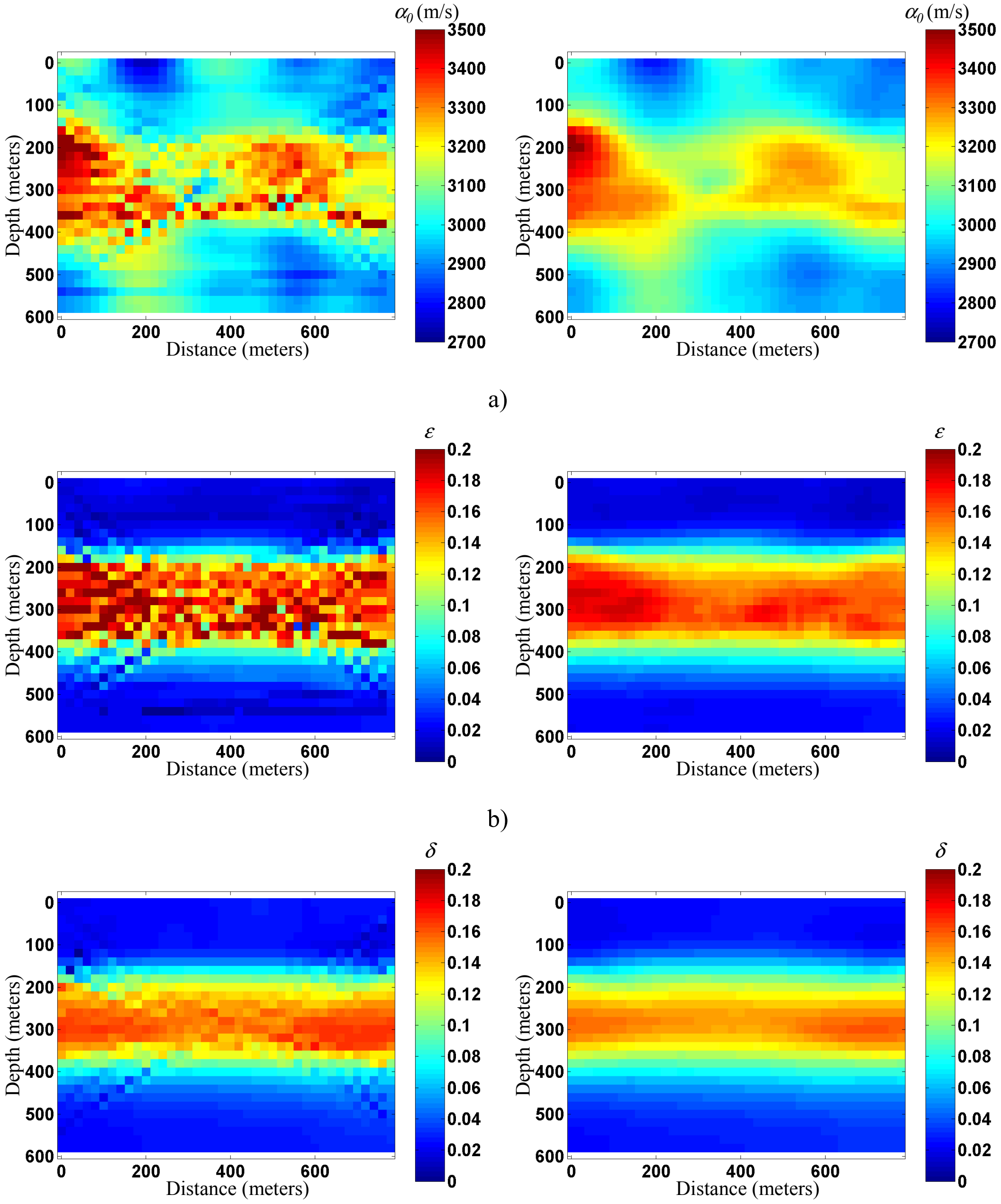

a)

b)

c)

Figure 5.37 Third iteration crosswell tomography results using initial model with 50 percent random error added: (left) no post processing, (right) 5 by 5 cell smoother applied; (a) α_0 (b) ε (c) δ.

These results are also encouraging. For α_0, ε and δ tomograms some general comments can be made. For the α_0 tomograms it becomes immediately obvious that it dominates the residual traveltime response compared to that of ε and δ. This is the reason that the variables were separated during tomography. Separation allows for the residual traveltime error to be compensated by the velocity perturbation parameters of ε and δ. For the ε tomogram the results are optimized as the acquisition geometry used is ideal for obtaining an estimate for ε. Comparing the ε and δ tomograms show that ε is allowed to vary more than δ. That being said, the resulting δ tomograms are quite impressive considering that the dominant raypath direction is not conducive for δ inversion. This is a function of the smoothing operator applied to all tomograms. The conventional smoother deals with random noise very well. Summing up these results, all of the isotropic traits are applicable to the anisotropic case for all three parameters. Additionally, ε affects traveltime residuals much more than δ and given the appropriate amount of information accurate tomograms for each of the parameters can be obtained. Perhaps most importantly, Figure 5.29 shows the angle dependent response of the presence of anisotropy which potentially can be used to interpret velocity artifacts.

5.2.1.5 Center anomaly model: initial model estimate α_0=3000 m/s, ε=δ=0

The next sets of results are for the second simple velocity model. This anomaly contained horizontal and vertical extents and as such can use both crosswell and surface tomography to construct a final velocity model. The purpose of the following tests is to determine the effects of crosswell tomography in estimating ε and δ and how they compare with the surface results.

5.2.1.5.1 Crosswell tomography

The resulting third iteration tomograms using an initial model using a vertical P-wave velocity of 3000 m/s and no ε and δ information are displayed in Figure 5.38.

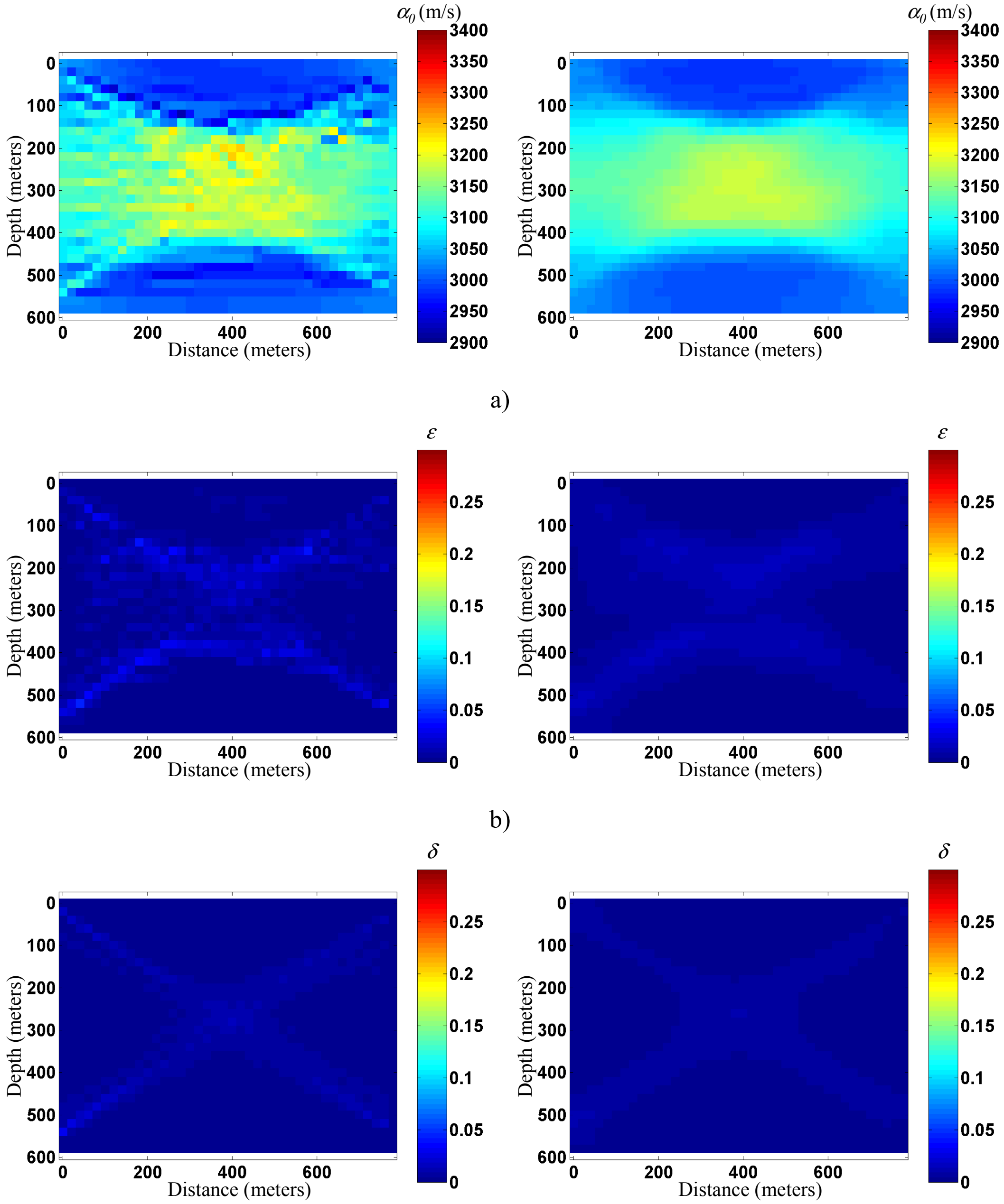

a)

b)

c)

Figure 5.38 Third iteration crosswell tomography results using initial constant velocity model with and no anisotropy: (left) no post processing, (right) 5 by 5 cell smoother applied; (a) α_0 (b) ε (c) δ.

These crosswell tomography results are encouraging considering the minimal amount of information given. The vertical P-wave velocity tomogram, Figure 5.38a, is similar to the result in the isotropic case although the magnitude anomaly is not as accurate. This is a consequence of two factors: the acquisition geometry and the non-uniqueness in anisotropic inversion. The crosswell geometry spreads out the high velocity layer laterally amongst neighbouring cells, resulting in an average ε and δ values for these cells. The non-uniqueness of the inversion process has biased the solution to increase the vertical P-wave velocity more than is necessary resulting in underestimating both ε and δ. The ε and δ tomograms detect the center anomaly although both fail in determining the magnitude of the parameters. The δ tomogram appears to represent the acquisition geometry more than detecting the center anomaly.

5.2.1.5.2 Surface tomography

The next set of tests uses surface tomography on the centered high-velocity anomaly. The results of using constant velocity of 3000 m/s and assuming isotropy (ε=δ=0) can be viewed in Figure 5.39.

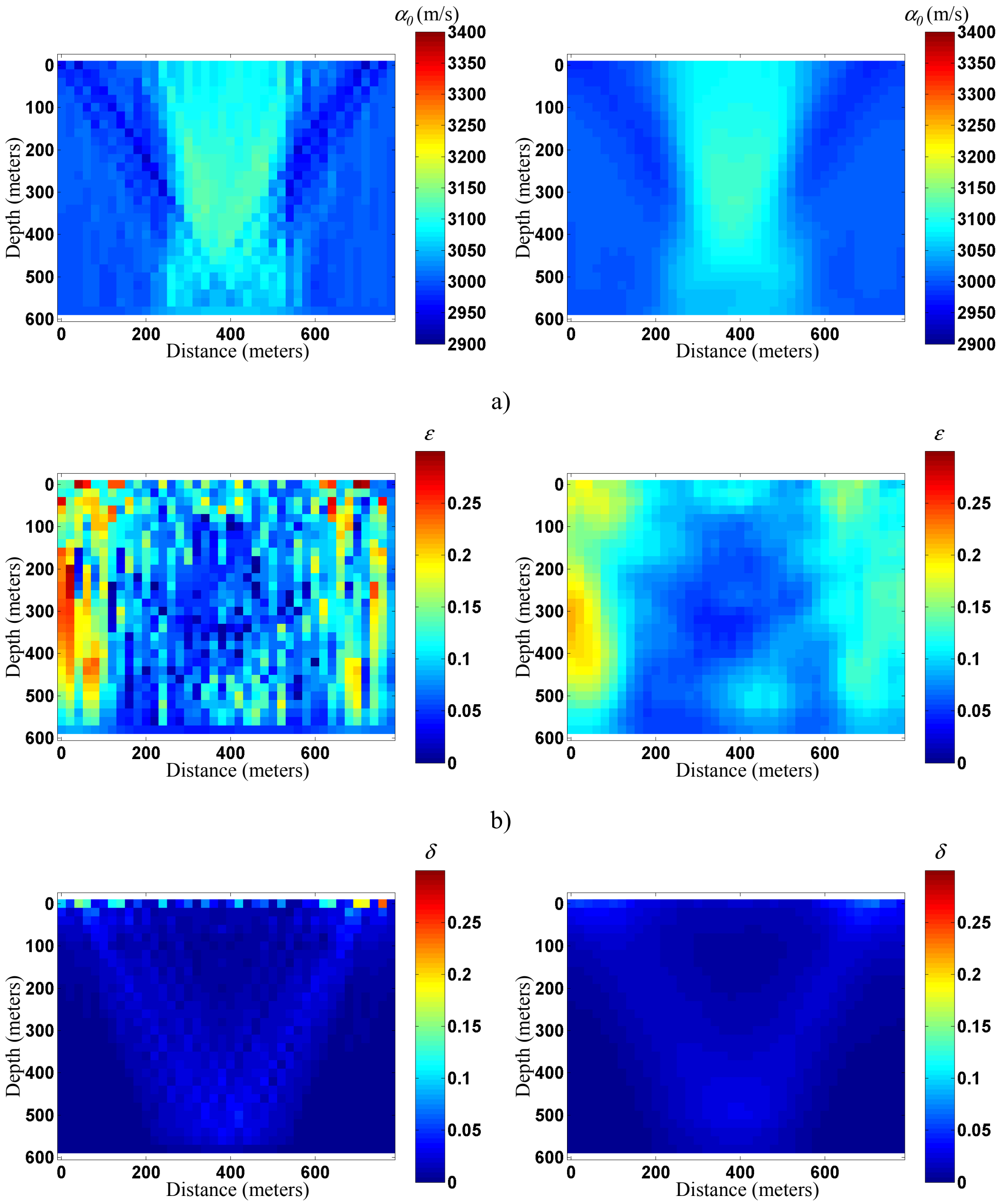

a)

b)

c)

Figure 5.39 Third iteration surface tomography results using initial model with constant vertical P-wave velocity of 3000 m/s: (left) no post processing, (right) 5 by 5 cell smoother applied; (a) α_0 (b) ε and (c) δ.

The results of surface tomography for the center anomaly velocity model are mixed. In determining the vertical P-wave velocity the results are adequate given the limitations inherent in the acquisition geometry in conjunction with the size and shape of the anomaly. The anomaly is smeared vertically, a characteristic of surface tomography, biasing the solution to accommodate the predominant vertical raypath. The tomogram for ε is far from perfect. The lack of horizontal raypaths in the center of the model makes it difficult to get an accurate estimate for ε. In fact, in areas where there is a lack of raypaths necessary to determine the appropriate vertical P-wave velocity (near the edges of the model), the residual traveltimes are compensated for by ε. The third iteration tomogram for δ is also quite discouraging as it is biased by the predominant raypath governing the experiment. The physics of anisotropic propagation limit the contributions of δ to the traveltime residual. Only in areas of high reliability, where the singular values are relatively high, will δ get a chance to contribute to the solution. The high singular values will be dominated by the raypaths resulting in a δ tomogram that depicts the predominant raypath of the acquisition geometry rather than the true model structure. Due to the nature of the expression for δ within the Jacobian matrix, it will be very difficult to determine an accurate estimate for δ.

5.2.1.6 Center anomaly model: initial model estimate α_0=3000 m/s, ε=δ=known

5.2.1.6.1 Crosswell tomography

Figure 5.40 shows the crosswell results for α_0 assuming that ε and δ are known completely.

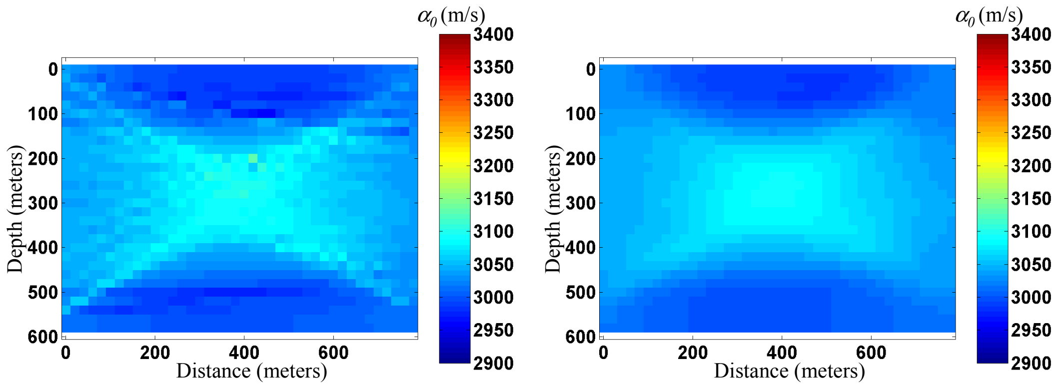

a) b)

Figure 5.40 Third iteration α_0 tomogram where ε and δ are known completely; a) unsmoothed b) smoothed

These results are compatible with those of the isotropic tomography. This indicates that when the correct ε and δ are chosen for the initial estimate, the anisotropic problem reduces to that of an isotropic one.

5.2.1.6.2 Surface tomography

Figure 5.41 shows the surface tomography results for vertical P-wave velocity assuming that anisotropic model is known completely.

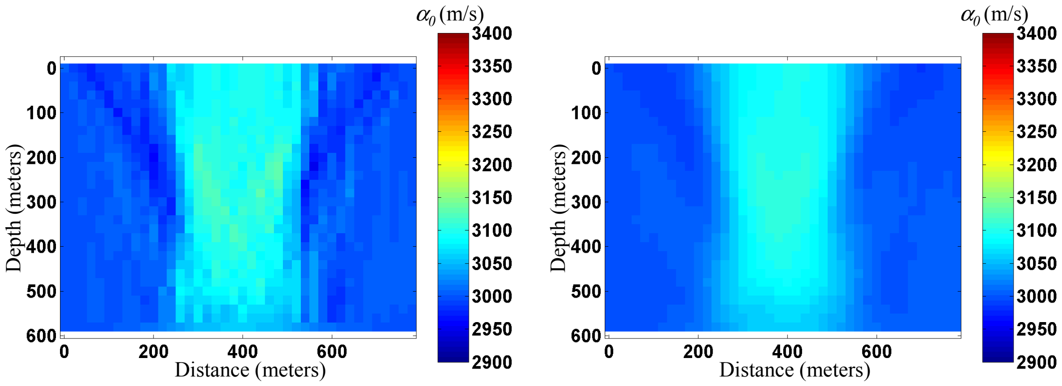

a) b)

Figure 5.41 Third iteration tomogram of α_0 assuming ε and δ are known; a) unsmoothed b) smoothed.

This result is similar to that of the isotropic tomography result. Given correct anisotropic information, inversion must still cope with the acquisition geometry and the velocity structure. It also shows that if the anisotropy of the model is modelled correctly, the diagnostic "V" is missing from the tomograms.

5.2.1.7 Center anomaly model: initial model estimate α_0=known, $\varepsilon=\delta=0$

This next set of test assumes that the vertical P-wave velocity has been determined correctly and the parameters yet to be determined are Thomsen’s anisotropic parameters of ε and δ.

5.2.1.7.1 Crosswell tomography

Figure 5.42 shows the resulting crosswell tomgrams for ε and δ using an initial model where the vertical P-wave velocity is known completely and isotropy is assumed.

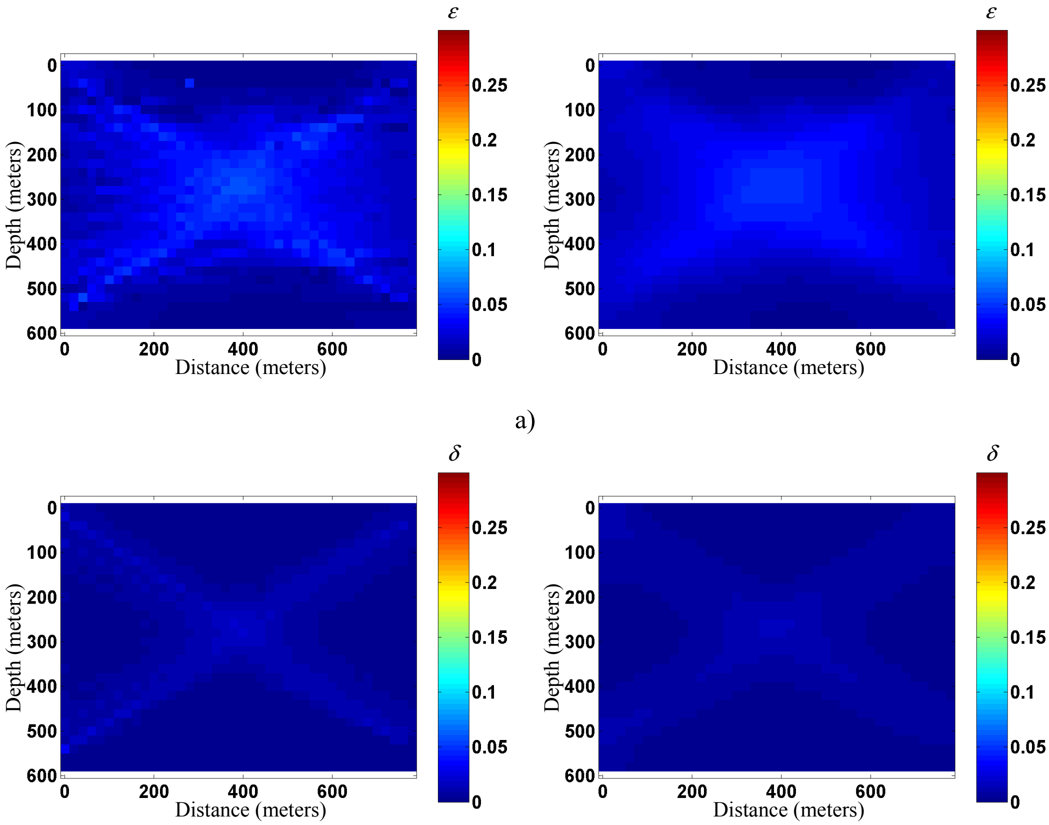

a)

b)

Figure 5.42 Third iteration crosswell tomography results using initial model where α_0 is known completely: (left) no post processing, (right) 5 by 5 cell smoother applied; (a) ε (b) δ.

The resulting tomogram for ε is superior to that of δ, a consequence of the abundance of horizontal raypaths. The basic shape for the anomaly is detected for both parameters and the ε tomogram approaches a more accurate solution to ε from a magnitude perspective. Both parameters show a lateral smear, a characteristic of crosswell tomography.

5.2.1.7.2 Surface tomography

Figure 5.43 shows the crosswell results for ε and δ assuming an initial model estimate in which the vertical P-wave velocity is known completely and isotropy is assumed.

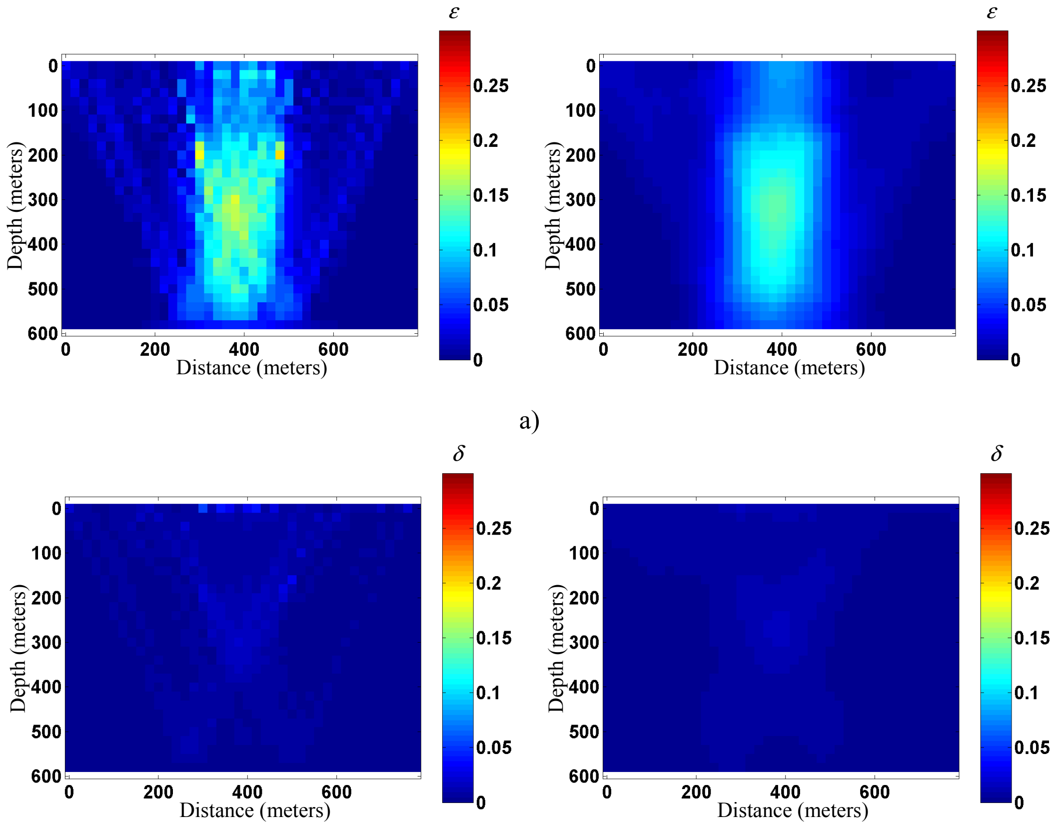

a)

b)

Figure 5.43 Third iteration tomogram unsmoothed (left) and smoothed (right) for ε (a) and δ (b).

These results show a relatively good inversion result for ε and a poor one for δ. This example allows for further investigation of why there is a repeatedly more accurate determination of ε in comparison to δ. Recall the derivative of time with respect to ε. This derivate is nonlinear with respect to θ, the phase angle. More importantly the function does not have any local maxima or minima and increases monotonically in magnitude with an increase in θ. In this example, due to high-velocity anomaly present, there is sufficient ray-bending allowing for determination of the parameter ε. The parameter δ is also nonlinear in θ, but it contains a local maximum. The maximum occurs at the propagation angle of 45 degrees dictating whether the wavefront is convex or concave at that point. This derivative is very unstable and on average contributes less to the traveltime perturbations than does ε. As a result the anisotropic parameter that will be estimated with any degree of accuracy will be ε.

5.2.1.8 Center anomaly model: initial model estimate α_0, ε, and δ with random error

5.2.1.8.1 Crosswell tomography

Figures 5.44 through 5.46 show the crosswell results of α_0, ε and δ tomograms for 10, 25 and 50 percent random error respectively.

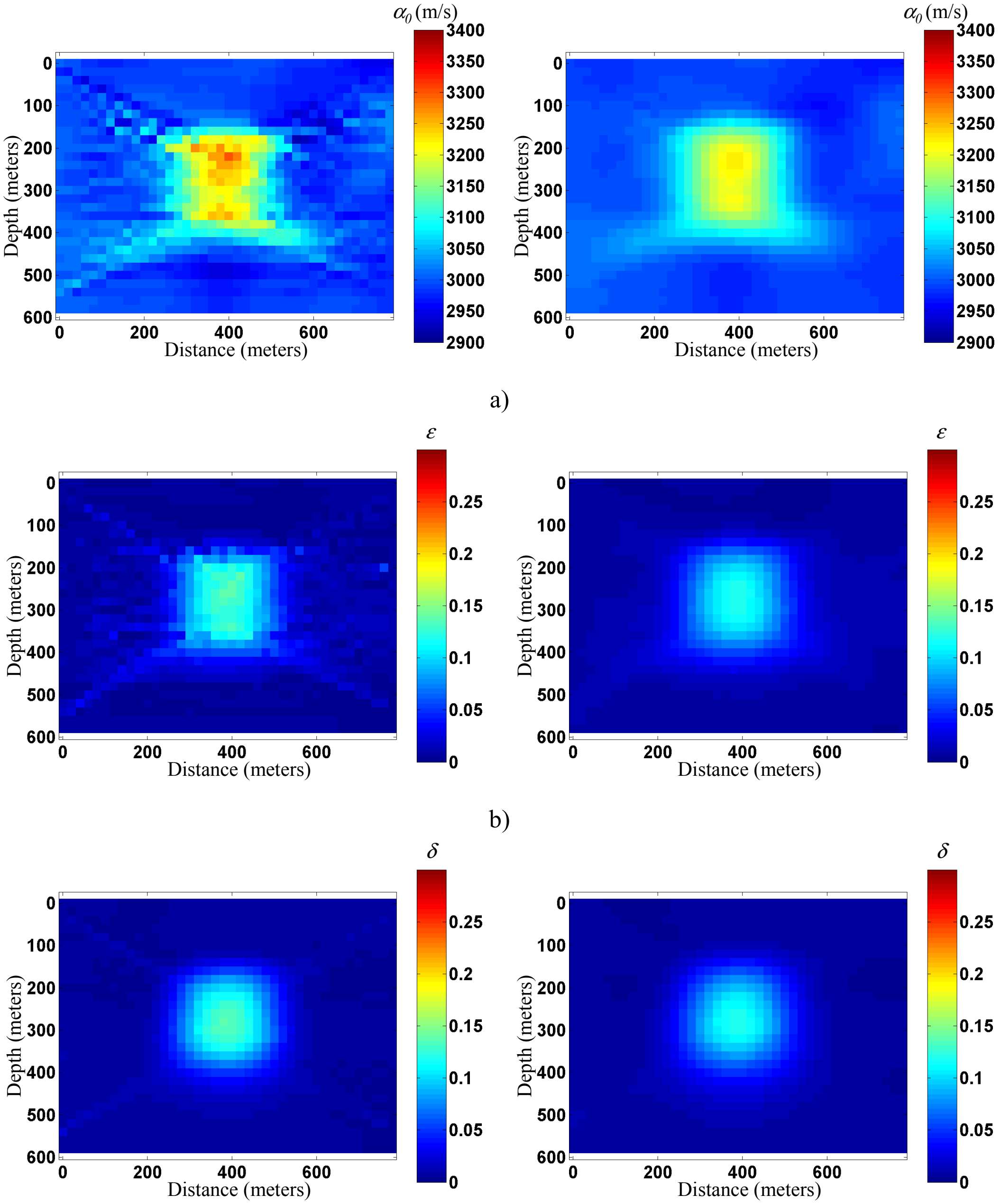

a)

b)

c)

Figure 5.44 Third iteration crosswell tomography results using initial model with 10 percent random error added: (left) no post processing, (right) 5 by 5 cell smoother applied; (a) α_0 (b) ε and (c) δ.

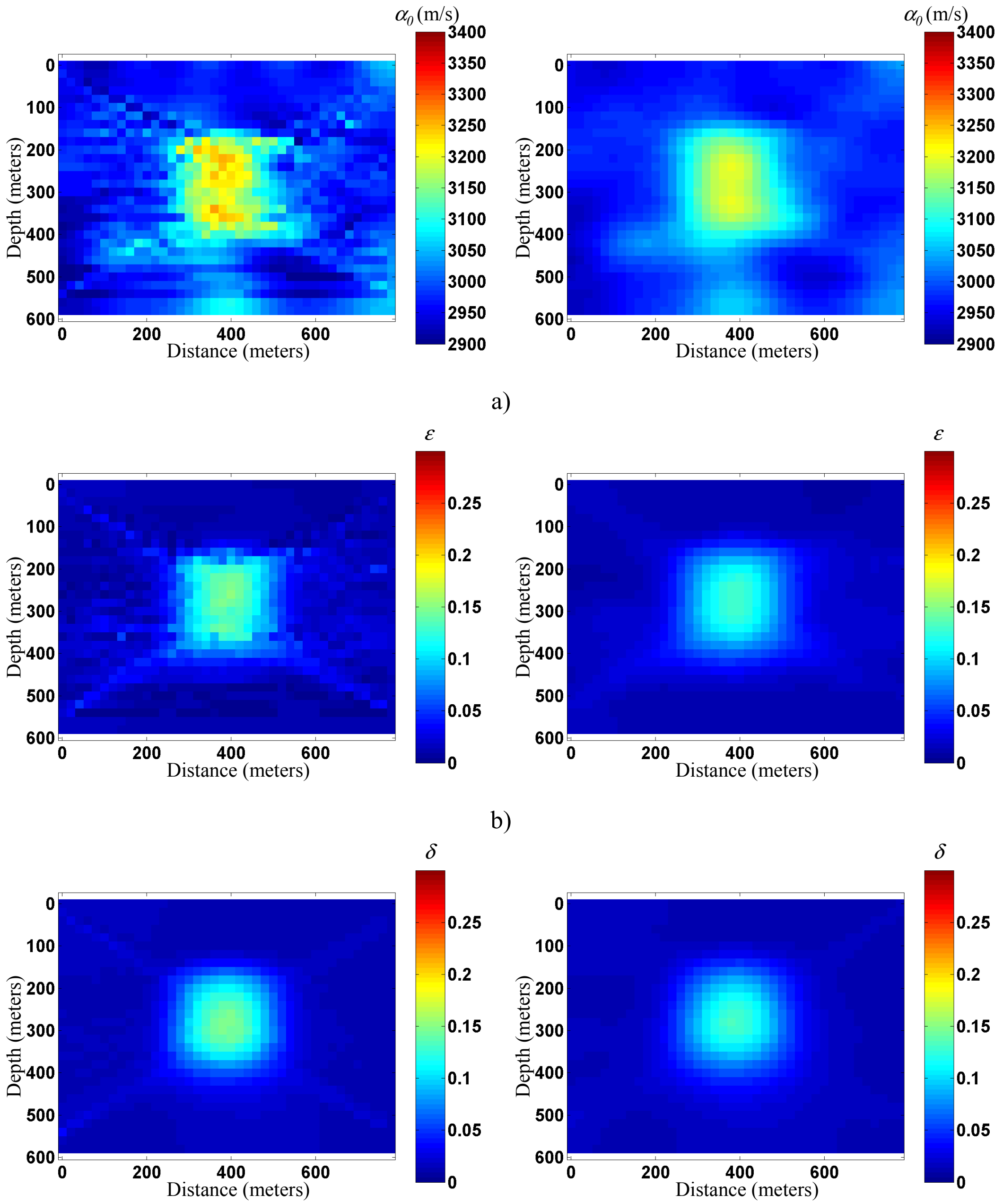

a)

b)

c)

Figure 5.45 Third iteration crosswell tomography results using initial model with 25 percent random error added: (left) no post processing, (right) 5 by 5 cell smoother applied; (a) α_0 (b) ε and (c) δ.

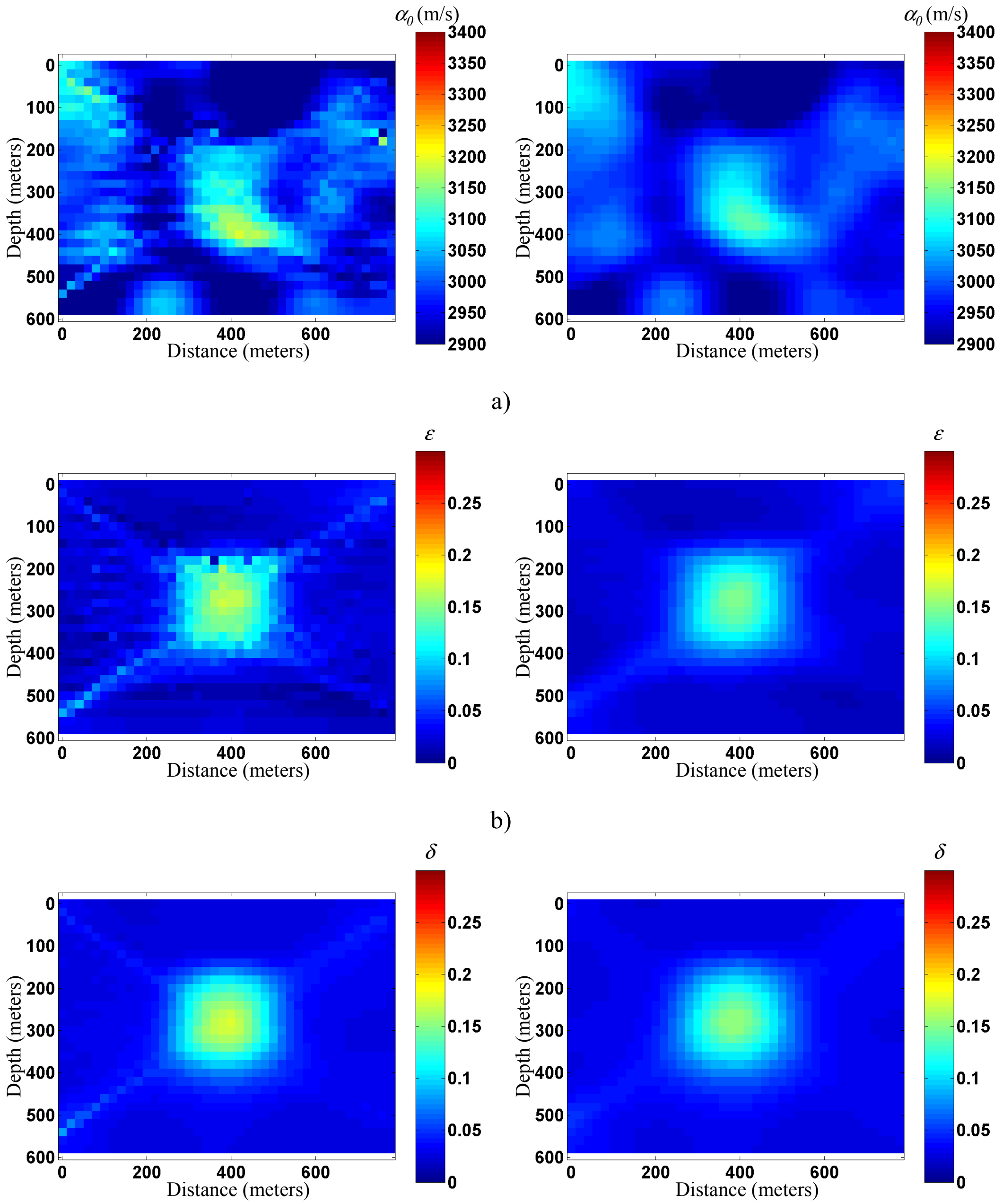

a)

b)

c)

Figure 5.46 Third iteration crosswell tomography results using initial model with 50 percent random error added: (left) no post processing, (right) 5 by 5 cell smoother applied; (a) α_0 (b) ε and (c) δ.

These results reiterate that dividing the inversion process into two parts, one for α_0 and another for ε and δ, and computing the generalized inverse solution for each is a stable process. Specifically:

- Inversion results when using a model with 10 percent random error shows that when the initial model is relatively close to the correct model, the acquisition geometry can only affect the resulting tomogram if residual traveltime errors exist. The initial model estimate is quite good and as such the inversion process does not allow the acquisition geometry to impose its lateral smearing bias on the solution. This is an important result in that though the crosswell acquisition geometry will tend to produce a laterally smeared solution, it will not adversely affect correct solutions that have laterally extensive velocity anomalies.
- Inversion results when using a model with 25 percent random error shows that as the residual traveltime errors increase, the acquisition geometry is able to bias the solution by laterally smearing the result for α_0. It also shows that when the residual traveltime errors are small enough, they can be compensated fully by the α_0 tomogram. The ε and δ tomograms have been only minimally modified and is mostly a result of the smoothing applied. The random error added is handled quite adequately by the smoother.
- Inversion results when using a model with 50 percent random error shows that if the residual traveltime are large enough, the resulting tomogram will compare very poorly to the correct velocity model. With the large enough traveltime residuals, the ε tomogram will also begin to adopt the acquisition geometry bias. The δ will not become biased as the appropriate angles required for δ parameter updates (45 degrees) are not accentuated in crosswell tomography.

5.2.1.8.2 Surface tomography

The next series of Figures (5.47 through 5.49) show surface inversion results using an initial model estimate with 10, 25 and 50 percent random error added to the correct model.

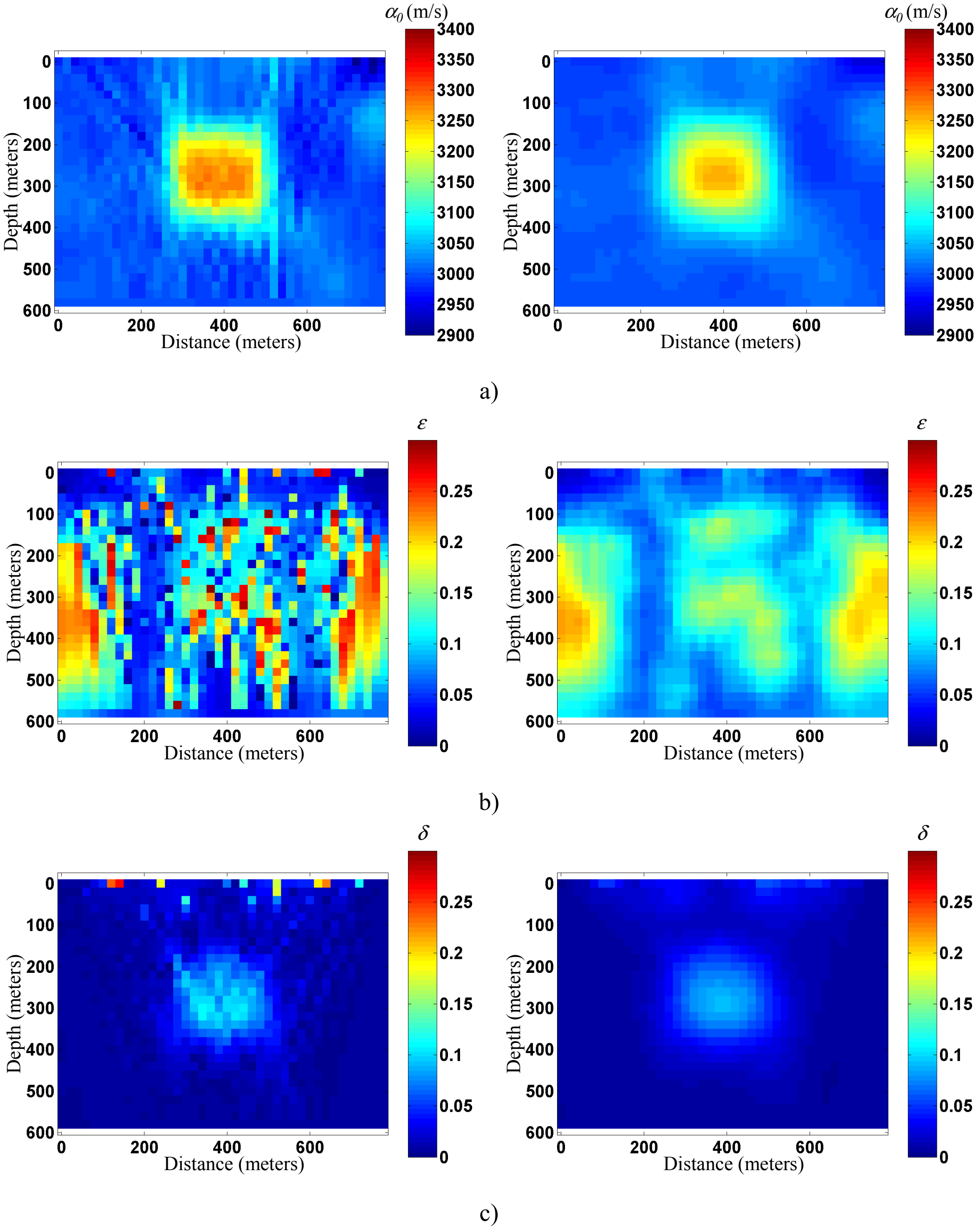

Figure 5.47 Third iteration surface tomography results using initial model with 10 percent random error added: (left) no post processing, (right) 5 by 5 cell smoother applied; (a) α_0 (b) ε (c) δ.

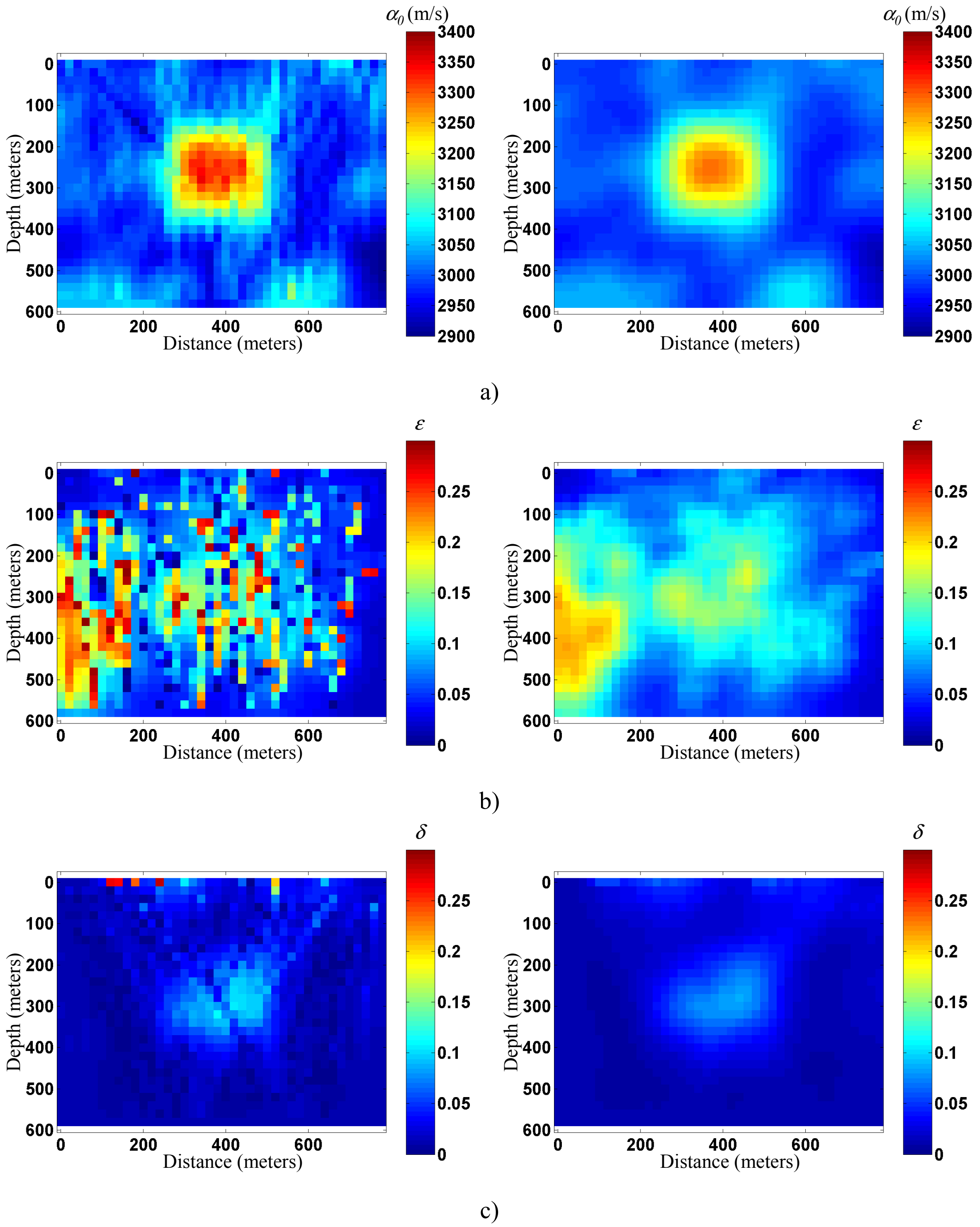

Figure 5.48 Third iteration surface tomography results using initial model with 25 percent random error added: (left) no post processing, (right) 5 by 5 cell smoother applied; (a) α_0 (b) ε (c) δ.

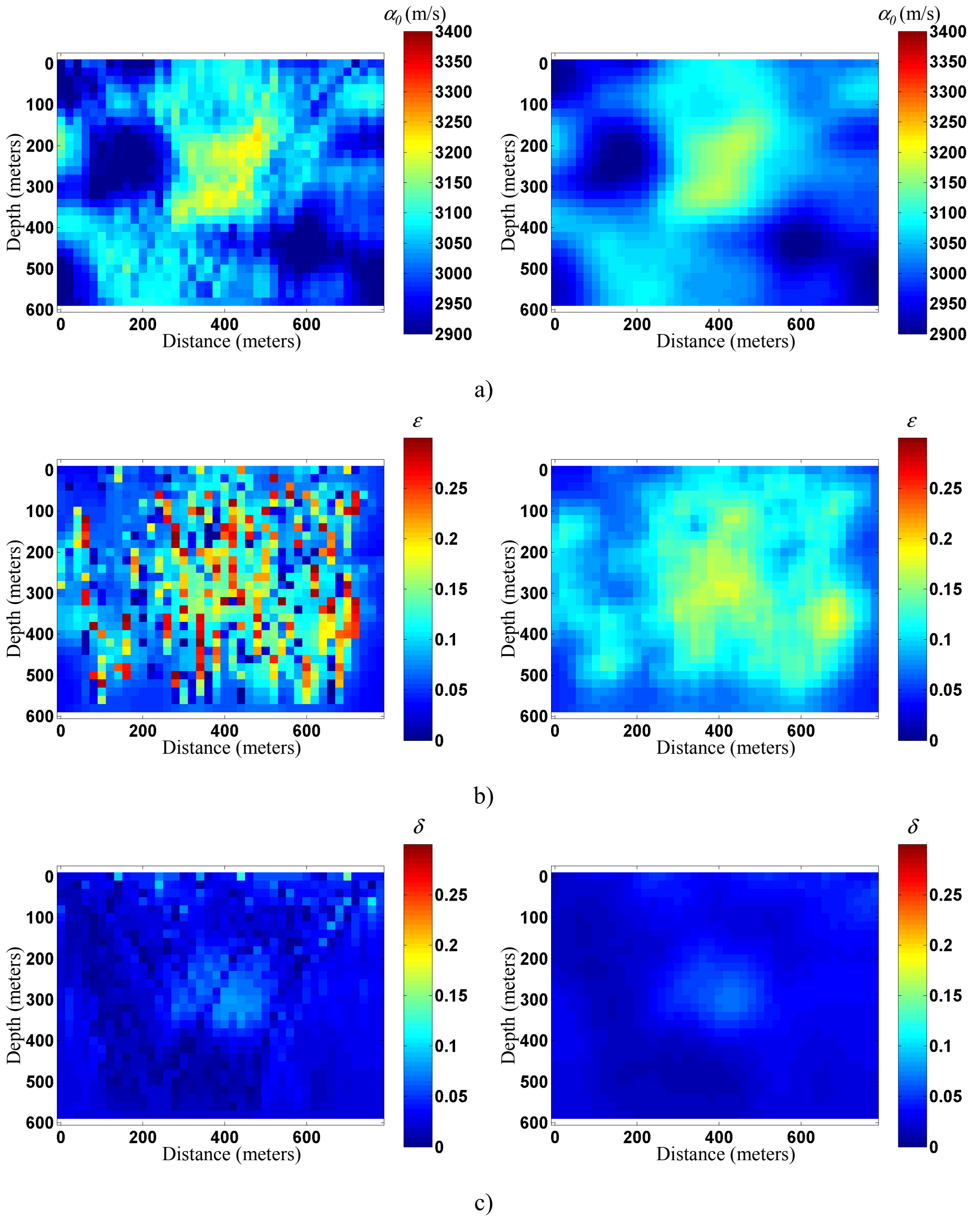

Figure 5.49 Third iteration surface tomography results using initial model with 50 percent random error added: (left) no post processing, (right) 5 by 5 cell smoother applied; (a) α_0 (b) ε (c) δ.

These results reveal the nature of anisotropic inversion by demonstrating the differences in parameter sensitivity. The vertical P-wave parameter α_0 is the parameter most affecting the velocity of the medium and thus has the greatest impact on residual traveltime minimization. As a result it is a well constrained parameter converging to an adequate solution in terms of shape and magnitude. The Thomsen parameters of ε and δ are dependent on the vertical P-wave velocity and in general the inversion solution is nonunique with respect to these parameters. The parameter ε is unstable and does not converge without accurate knowledge of the vertical P-wave velocity. Comparing crosswell and surface tomography it is clear that crosswell tomography is better suited and provides a more stable estimates of ε. The parameter δ varies little and in general deviates very little from the initial model estimate. The resulting δ tomogram is more a reflection of the smoothing applied. Specifically, the following can be said of each inversion test:

- The surface inversion result when using an initial model estimate with 10 percent random error added shows the stability of the α_0 and δ tomograms and instability of the ε tomogram. This is clearly a function of the acquisition geometry as the crosswell inversion results did not show the ε instability. As seen in the simple anisotropic models, the ε tomogram is unstable near the edges of the survey. This is a consequence of the lack of rays required to accurately constrain the inversion.
- The surface inversion result when using an initial model estimate with 25 percent random error added again shows the ε instability. It also shows results similar to that of Figure 5.45 in that as the residual traveltime errors increase, the α_0 and δ tomograms are updated to accommodate the traveltime discrepancies. A major difference between the crosswell and surface results however is that in the crosswell result, the inversion for ε was a stable one. With the instability in ε inversion, the errors compensated for by the α_0 tomogram and to a lesser extent by the δ tomogram, are from both the traveltime residuals and the errors created by ε tomogram. The dependence of each parameter on each other means that if one

parameter inversion becomes unstable, the whole process becomes unstable. This instability is clearly seen when comparing crosswell and surface α_0 tomograms of Figure 5.45a and 5.48a respectively.

- The surface inversion result when using an initial model estimate with 50 percent random error added again shows the ε instability. The results of Figure 5.49 are similar to those seen in the 25 percent random error model seen in Figure 5.48. The main difference is that the residual traveltime errors and the instability of the ε inversion have skewed the tomogram for α_0 to a greater extent and have even started to adversely affect the δ tomogram.

5.2.2 Quasi-null space analysis – simple anisotropic models

The section will apply the quasi-null space techniques of dynamic smoothing and integration that worked successfully in an isotropic environment to the anisotropic cases. The quasi-null space analysis workflow adds to the initial anisotropic tomographic workflow by adding the quasi-null space stabilization technique. The stabilization techniques is added between steps 4 and 5 after parameter updates for α_0, ε and δ, and before the 5 by 5 smoother is applied. All resulting tomograms from the six initial model estimates will have the quasi-null space applied demonstrating the wide range of applicability. As in the isotropic case, quasi-null space analysis will not be performed on the reflection tomography results of the horizontal anomaly as the formulation of the problem (acquisition geometry and velocity structure) makes it impossible to determine the α_0, ε and δ.

5.2.2.1 Dynamic filtering: horizontal anomaly models

5.2.2.1.1 Initial model estimate α_0=3000m/s, $\varepsilon=\delta=0$

Figure 5.50 shows the quasi-null space dynamic filtering results of crosswell tomography on the horizontal anomaly model as well as the corresponding quasi-null space.

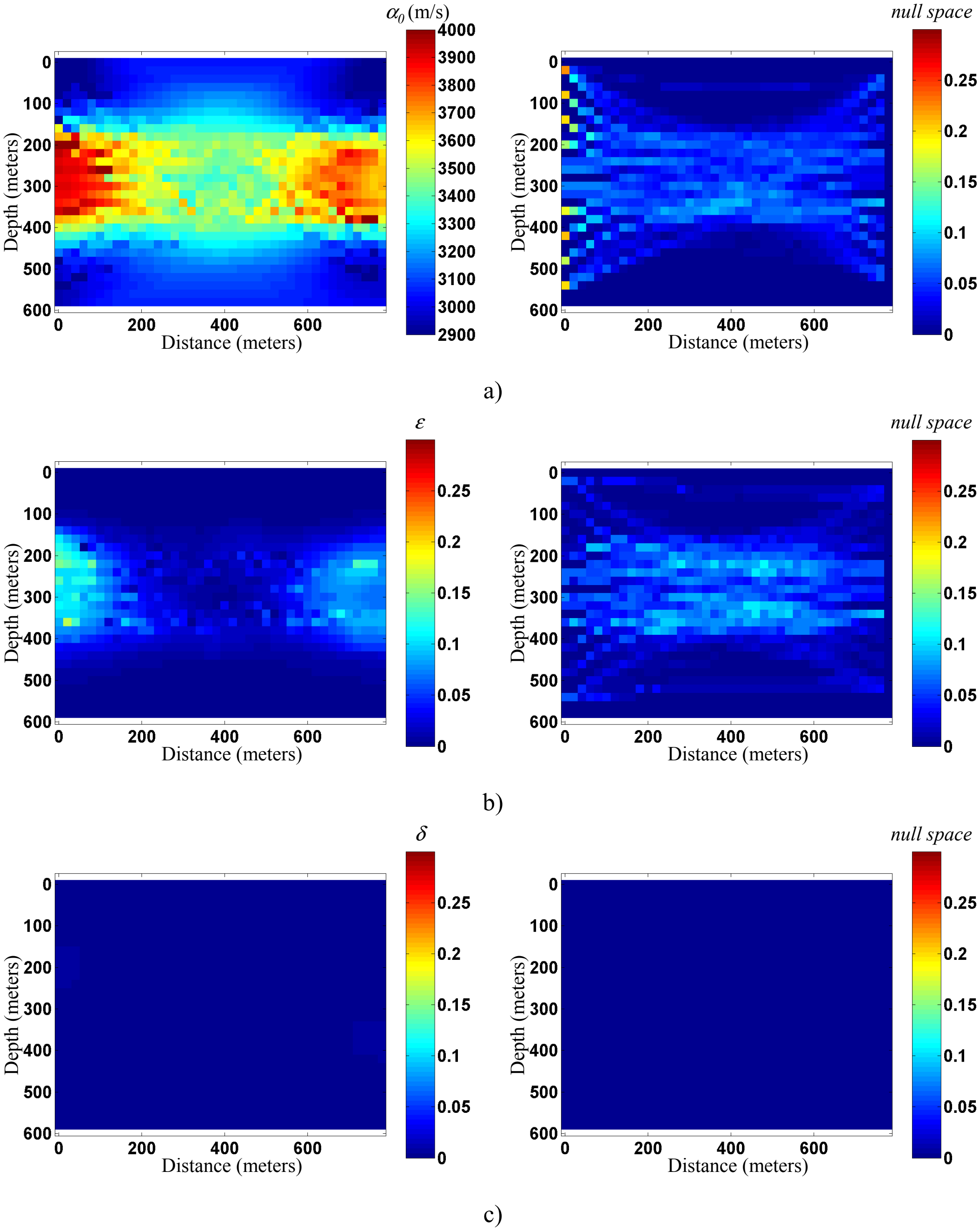

Figure 5.50 Quasi-null space dynamic smoothing results using an initial model estimate which has a constant vertical P-wave velocity and assuming isotropy; tomogram (left) and quasi-null space (right): α_0 (a) ε (b) and δ (c).

Note that the quasi-null space for δ shows the unreliable nature of inversion. The result is a tomogram that is filtered blindly. The quasi-null space shows what was most clearly seen in Figure 5.46. The first parameter that is updated to minimize residual traveltime errors in crosswell tomography is α_0. The second is ε followed by δ. This is reflected in the quasi-nulls spaces. The quasi-null space for α_0 and ε are clearly more reliable than of δ and as such will be modified first in an attempt to minimize the errors.

5.2.2.1.2 Initial model estimate α_0=3000 m/s, ε=δ=known

Figure 5.51 shows the third iteration dynamic smoothing tomogram and quasi-null space from using an initial model where the anisotropy is known completely.

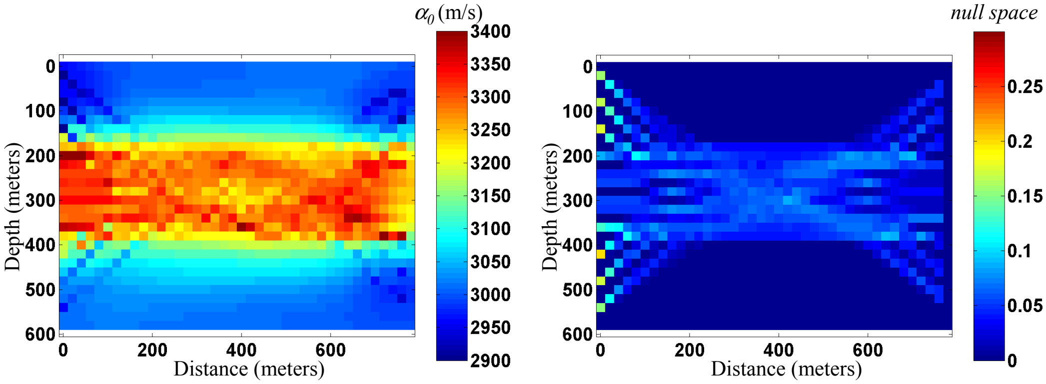

a) b)

Figure 5.51 Third iteration quasi-null space dynamic smoothing results using an initial model estimate which has a constant vertical P-wave velocity and anisotropy is known exactly; tomogram (a) and quasi-null space (b).

The result is quite good and the quasi-null space clearly shows how high-velocity zones act as ray attractors. This quasi-null space clearly sets up a filtering process where the resolution of the high-velocity layer can be maintained.

5.2.2.1.3 Initial model estimate α_0=known, ε=δ=0

Figure 5.52 shows the dynamic filtering process and quasi-null space applied to tomograms which had as an initial model estimates the exact background P-wave velocity.

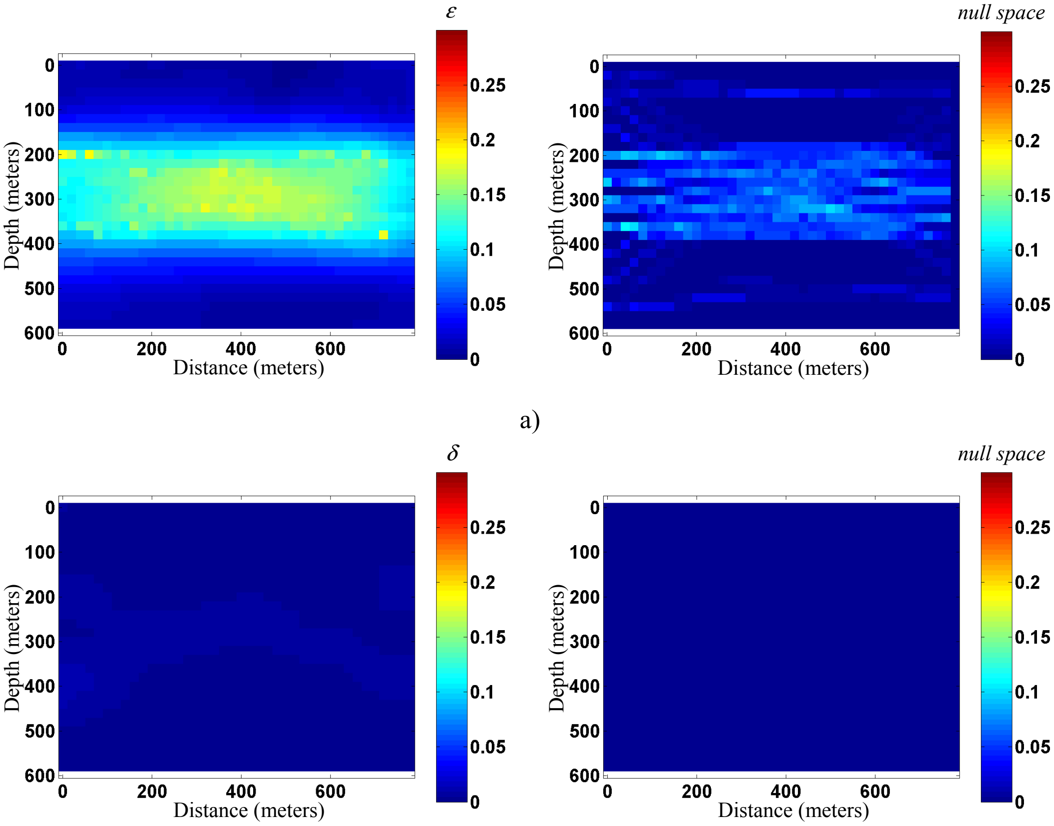

a)

b)

Figure 5.52 Quasi-null space dynamic smoothing results using an initial model estimate in which vertical P-wave velocity is known exactly and with no anisotropy; tomogram (left) and quasi-null space (right): ε (a) and δ (b).

This result again shows the crosswell tomography bias towards ε. The result for δ shows hints of the horizontal layer at the appropriate depth (Figure 5.52b), but after smoothing the layer is undetectable.

5.2.2.1.4 Initial model estimate α_0, ε, and δ with random error

Figures 5.53 through 5.55 show the crosswell dynamic filtering results and the respective quasi-null spaces for the initial model estimates with 10, 25 and 50 percent random error added.

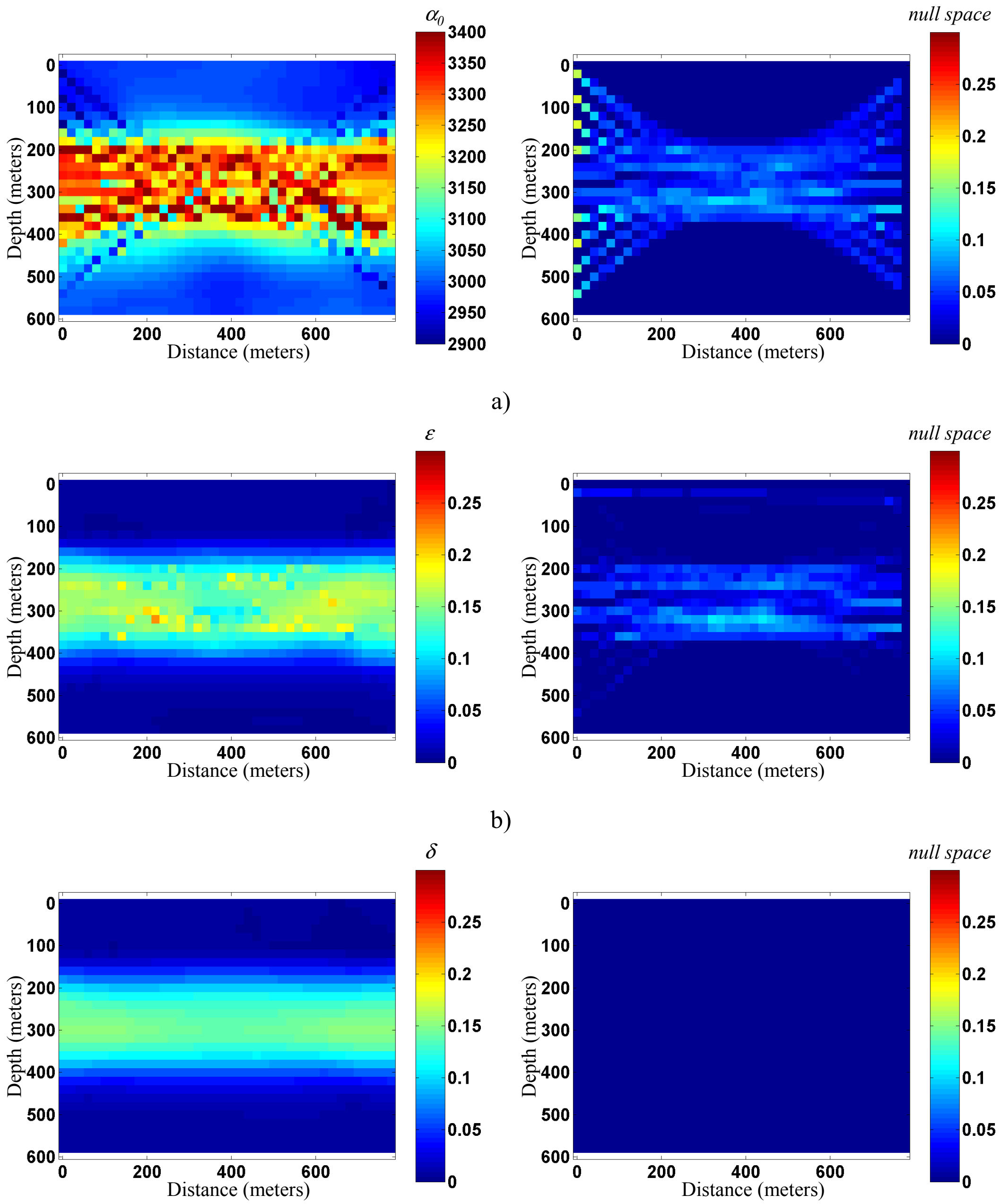

a)

b)

c)

Figure 5.53 Third iteration quasi-null space dynamic smoothing results using an initial model estimate which has 10 percent random error: tomogram(left) and quasi-null space (right): α_0 (a) ε (b) and δ (c).

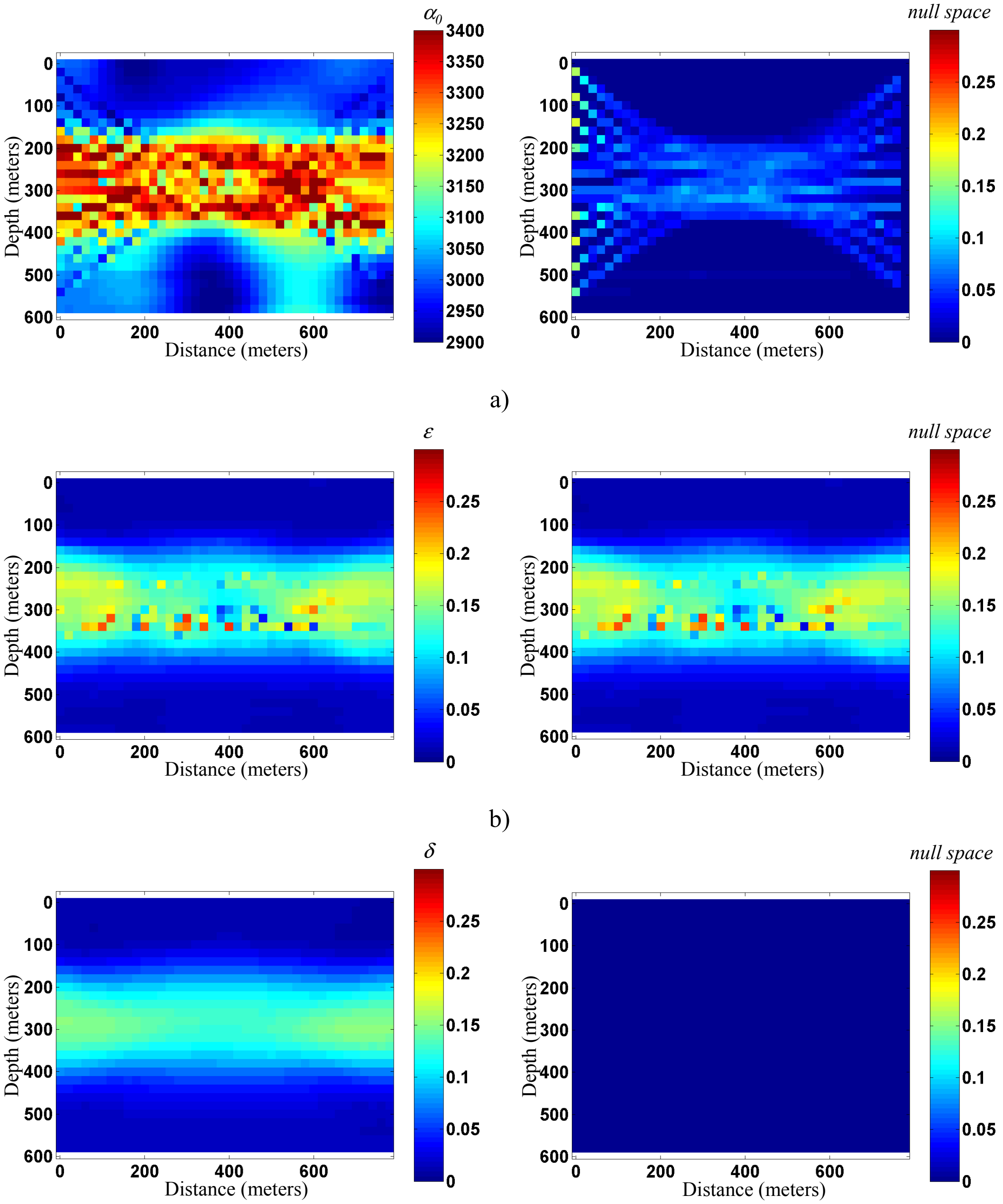

a)

b)

c)

Figure 5.54 Third iteration quasi-null space dynamic smoothing results using an initial model estimate which has 25 percent random error: tomogram (left) and quasi-null space (right): α_0 (a) ε (b) and δ (c).

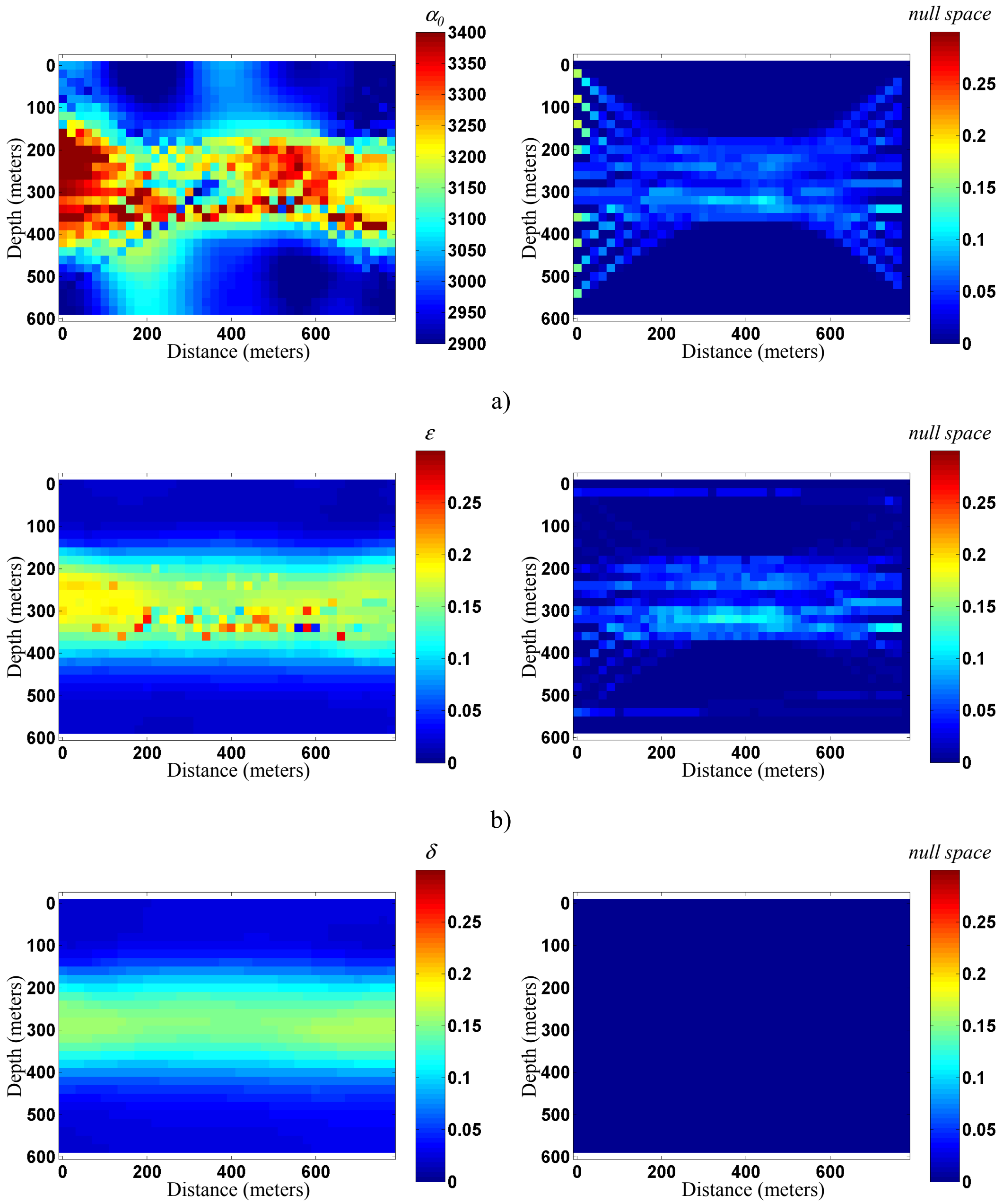

a)

b)

c)

Figure 5.55 Third iteration quasi-null space dynamic smoothing results using an initial model estimate which has 50 percent random error; tomogram (left) and quasi-null space (right): α_0 (a) ε (b) and δ (c).

The addition of random error is lessened when applying the dynamic filtering process. This is predominantly seen in Figure 5.53 with the α_0 and ε tomograms compared to Figure 5.37. Figure 5.53 in particular, gives more of an indication that the correct velocity mode is in fact one with a high-velocity layer.

5.2.2.2 Dynamic filtering: center anomaly

5.2.2.2.1 Initial model estimate: α_0=3000 m/s, ε=δ=0

Figure 5.56 shows the dynamic smoothing results applied to the third iteration results of crosswell and surface tomography for the centered model.

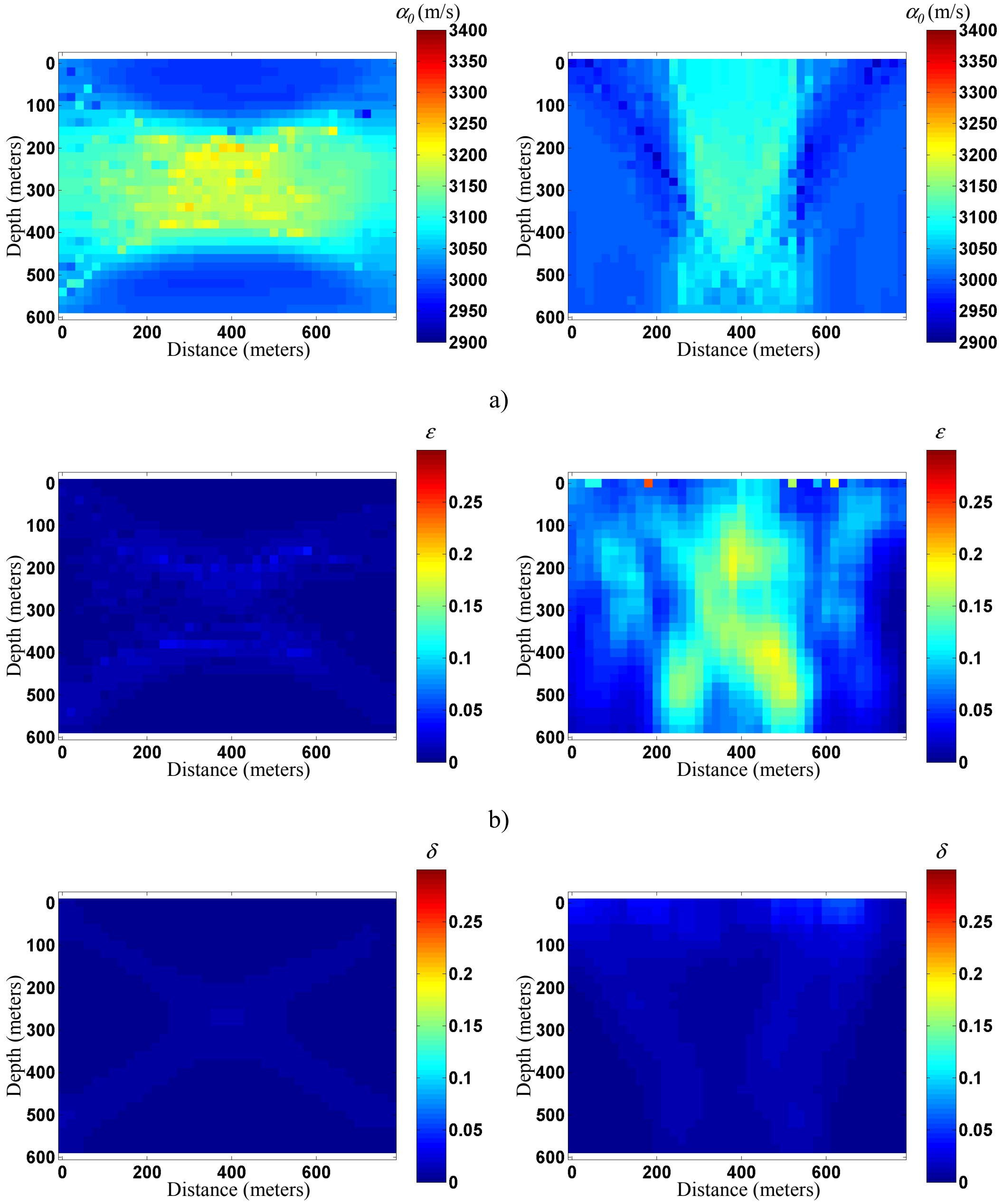

a)

b)

c)

Figure 5.56 Quasi-null space dynamic smoothing results using an initial model estimate which has a constant vertical P-wave velocity and no anisotropy for crosswell (left) and surface (right) tomography: α_0 (a) ε (b) and δ (c).

These results show very little improvement over the original tomogram results. However they do show a general reliability profile. There is less dynamic smoothing applied on the crosswell experiment than for the surface experiment. This is most clearly seen in Figure 5.56b. The differences in the crosswell and surface tomography solutions are also quite diagnostic. If the correct solution was found, they would converge to the same model. Instead, each solution is biased by the acquisition geometry. The α_0 tomogram shows this by the preferential smearing direction. The ε tomogram shows this as a contrast in inversion stability and the δ tomogram expresses this as a clear angle dependency on the solution. Taking these results into consideration, the user would restart the tomographic process and attempt to construct a model that would allow convergence to a single tomographic solution.

5.2.2.2.2 Initial model estimate α_0=3000 m/s, ε=δ=known

Figure 5.57 shows the dynamic smoothing results when using an initial model where the anisotropy is known.

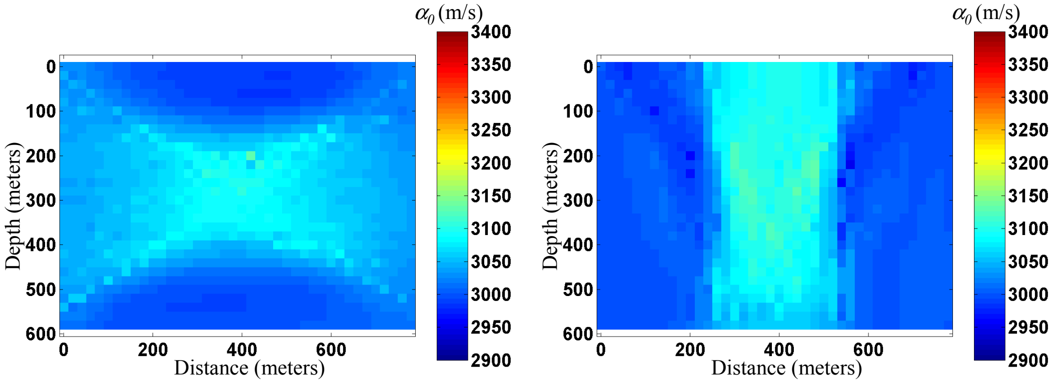

a) b)

Figure 5.57 Third iteration quasi-null space dynamic smoothing results using an initial model estimate which has a constant vertical P-wave velocity and anisotropy is known exactly for crosswell (a) and surface (b) tomography.

This result is similar to that of the isotropic case showing that the anisotropic inversion problem reduces to that of an isotropic problem is the anisotropy is known.

5.2.2.2.3 Initial model estimate α_0*=known,* $\varepsilon=\delta=0$

Figure 5.58 shows the third iteration results of dynamic smoothing for ε and δ using an initial model where the vertical P-wave velocity is known completely and isotropy is assumed.

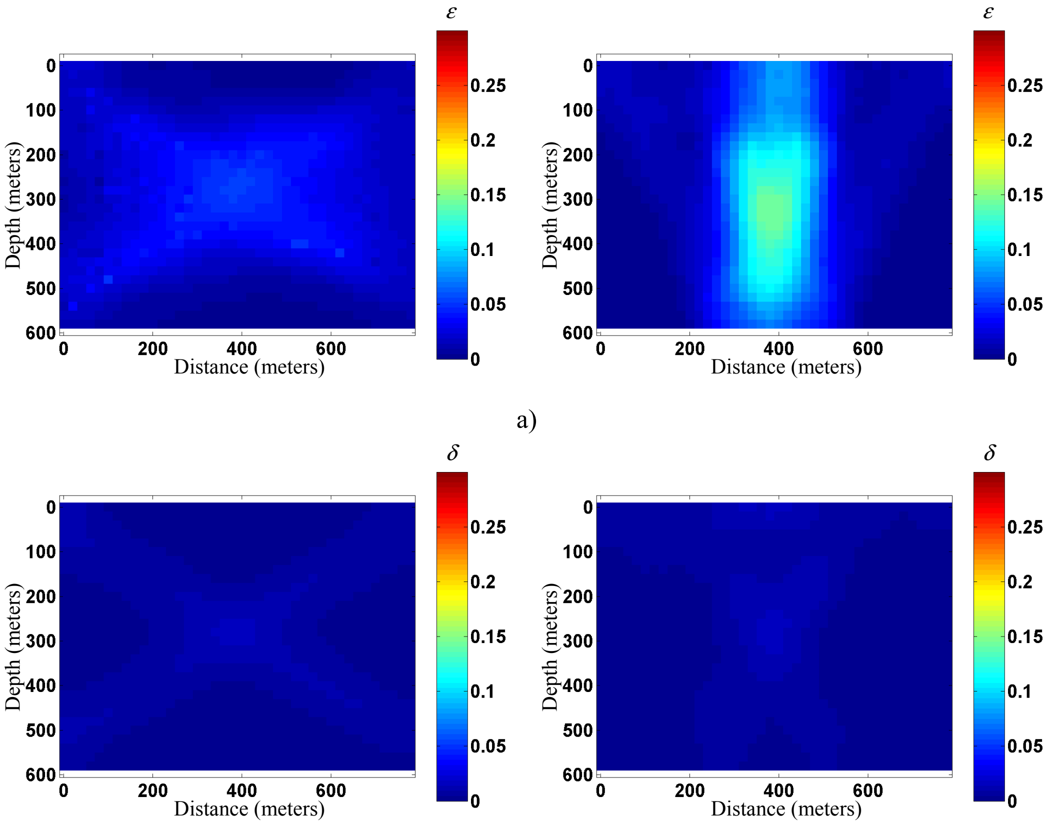

a)

b)

Figure 5.58 Quasi-null space dynamic smoothing results using an initial model estimate in which vertical P-wave velocity is known exactly and with no anisotropy for crosswell (left) and surface (right) tomography: ε (a) and δ (b).

In general the reliability of the tomograms is minimal and as such a majority of the cells are smoothed. In fact the most reliable cells are those in which there is no anisotropy present. The results do however indicate the presence of centered anisotropic anomaly even though there are remnants of crosswell and surface inversion present in the results.

5.2.2.2.4 Initial model estimate α_0, ε, and δ with random error

Figure 5.59 through 5.61 show the dynamic smoothing results for crosswell and surface tomography for the initial model estimates where 10, 25 and 50 percent random error is added.

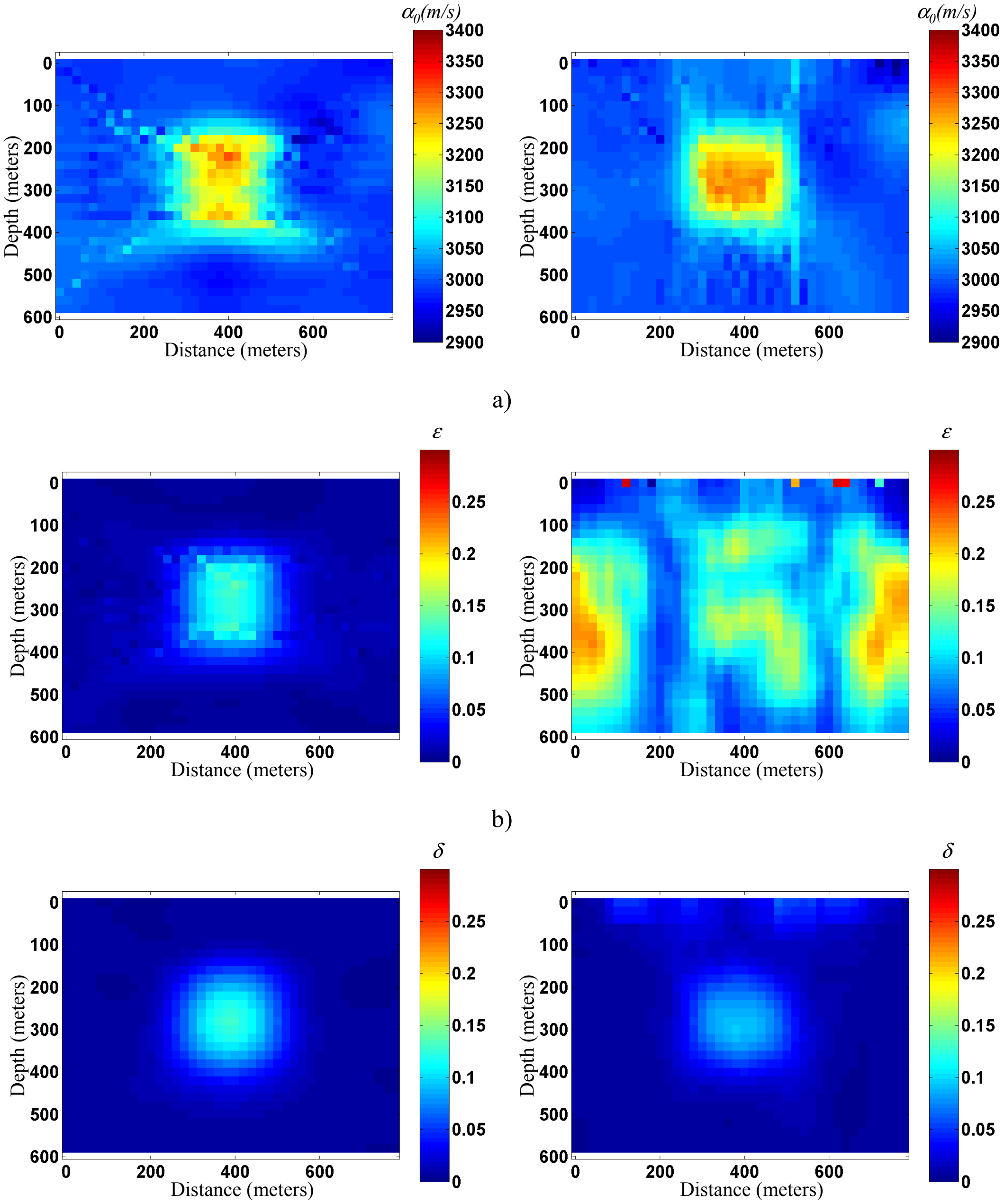

a)

b)

c)

Figure 5.59 Third iteration quasi-null space dynamic smoothing results using an initial model estimate which has 10 percent random error for crosswell (left) and surface (right) tomography: α_0 (a) ε (b) and δ (c).

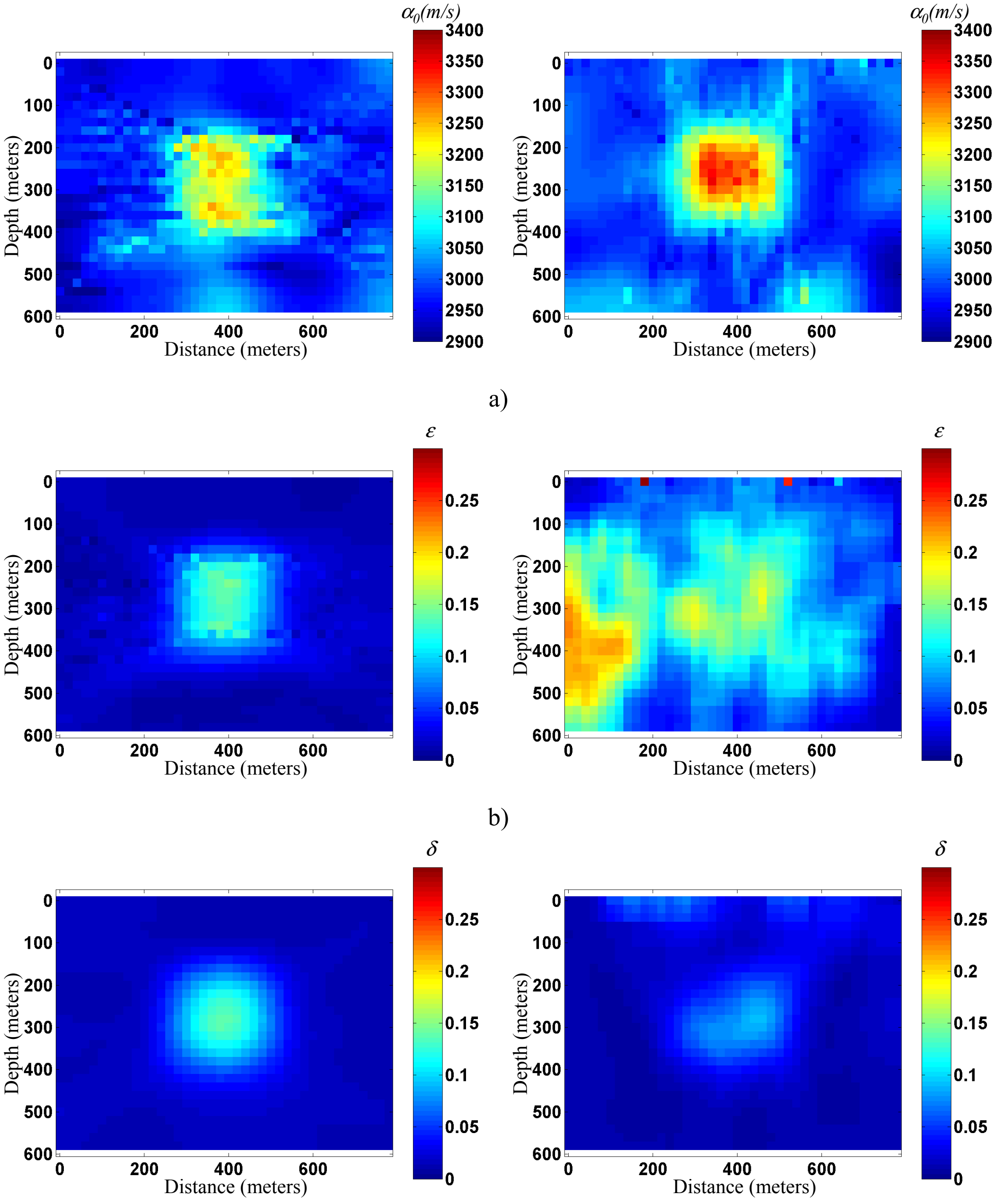

Figure 5.60 Third iteration quasi-null space dynamic smoothing results using an initial model estimate which has 25 percent random error added for crosswell (left) and surface (right) tomography: α_0 (a) ε (b) and δ (c).

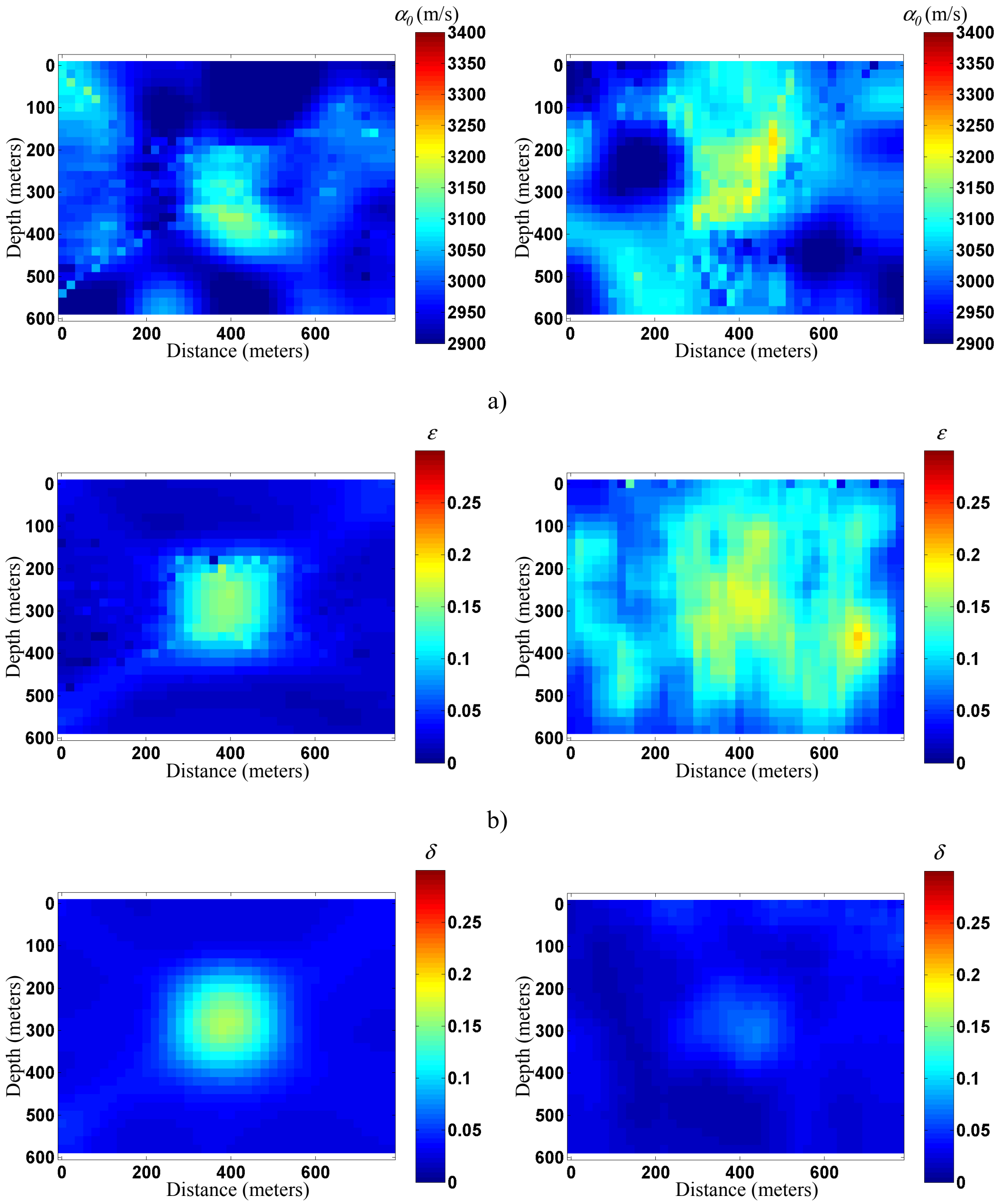

a)

b)

c)

Figure 5.61 Third iteration quasi-null space dynamic smoothing results using an initial model estimate which has a 50 percent random error added for crosswell (left) and surface (right) tomography: α_0 (a) ε (b) and δ (c).

These results show general solution stability for crosswell tomography in the presence of random noise and solution instability for surface tomography in the presence of random noise. It also shows the limitations of this quasi-null space stabilization technique. Because the dynamic smoothing is a post inversion process that it is based entirely on the initial inversion result and the quasi-null space to assess solution reliability, if the entire solution is deemed unreliable, as it is for the surface tomography results, the entire tomogram is smoothed. The dynamic smoothing can only do so much to stabilize inversion results. The important thing to recognize are the unstable or unrealistic tomogram results such as the surface tomography results in Figures 5.59 through 5.61. It would not be unreasonable to interpret the result to indicate that the model that has not been accounted for properly in ε and δ and as such a different starting model should be used.

5.2.2.3 Integration: center anomaly model

5.2.2.3.1 Initial model estimate α_0*=3000 m/s,* $\varepsilon=\delta=0$

Figure 5.62 shows the integration results using as an initial model estimate of a constant P-wave velocity, 3000 m/s and assuming isotropy.

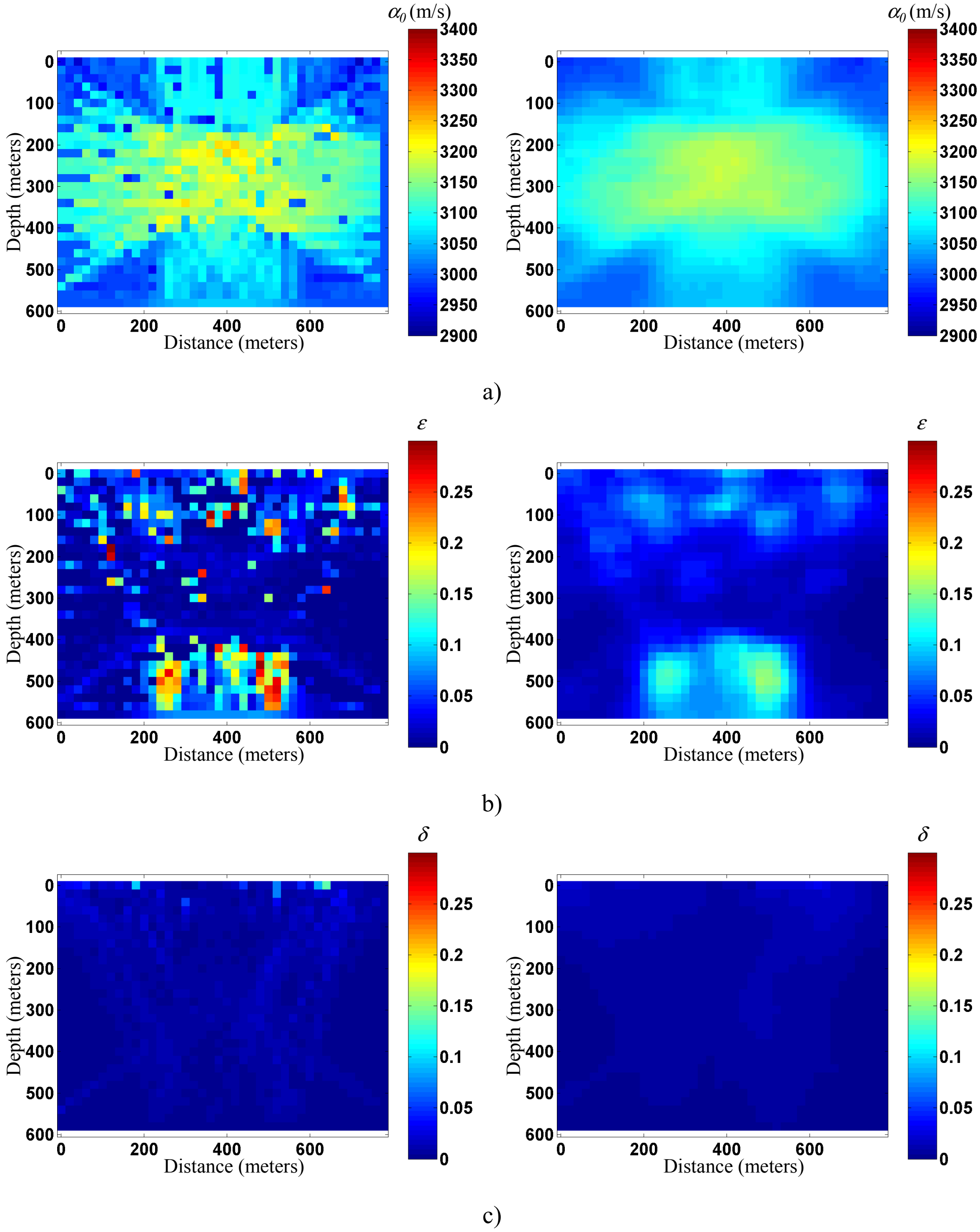

Figure 5.62 Quasi-null space integration results using an initial model estimate which has a constant vertical P-wave velocity and no anisotropy unsmoothed (left) and smoothed (right): α_0 (a) ε (b) and δ (c).

The quasi-null space integration results are relatively good for the vertical P-wave velocity and quite poor for the Thomsen parameters. The integration technique uses the original crosswell and reflection tomograms and if they do not have good results, combining them will not produce better results.

5.2.2.3.2 Initial model estimate α_0=3000 m/s, ε=δ=known

Figure 5.63 shows the integration results when using an initial model estimate where the anisotropy of the model is known completely and an initial P-wave estimate of 3000 m/s is used.

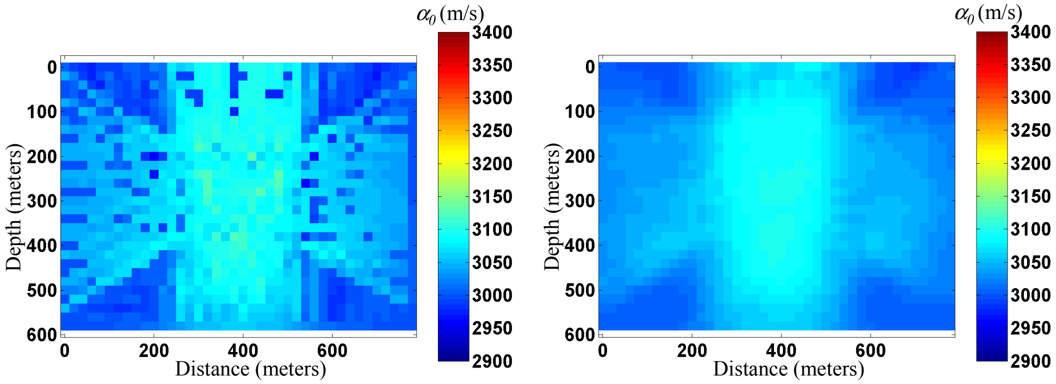

a) b)

Figure 5.63 Quasi-null space integration results of α_0 using an initial model estimate where anisotropy is known completely; unsmoothed (a) and smoothed (b)

These results are similar to those of the isotropic integration. There is evidence of the vertical and lateral limits of the anomaly. Given the acquisition geometry limitations and the underlying velocity structure this is the best of a result that one can hope for given no additional information.

5.2.2.3.3 Initial model estimate α_0=known, ε=δ=0

Figure 5.64 shows the integrated tomography results where the initial model estimate of vertical P-wave velocity is known completely and isotropy is assumed.

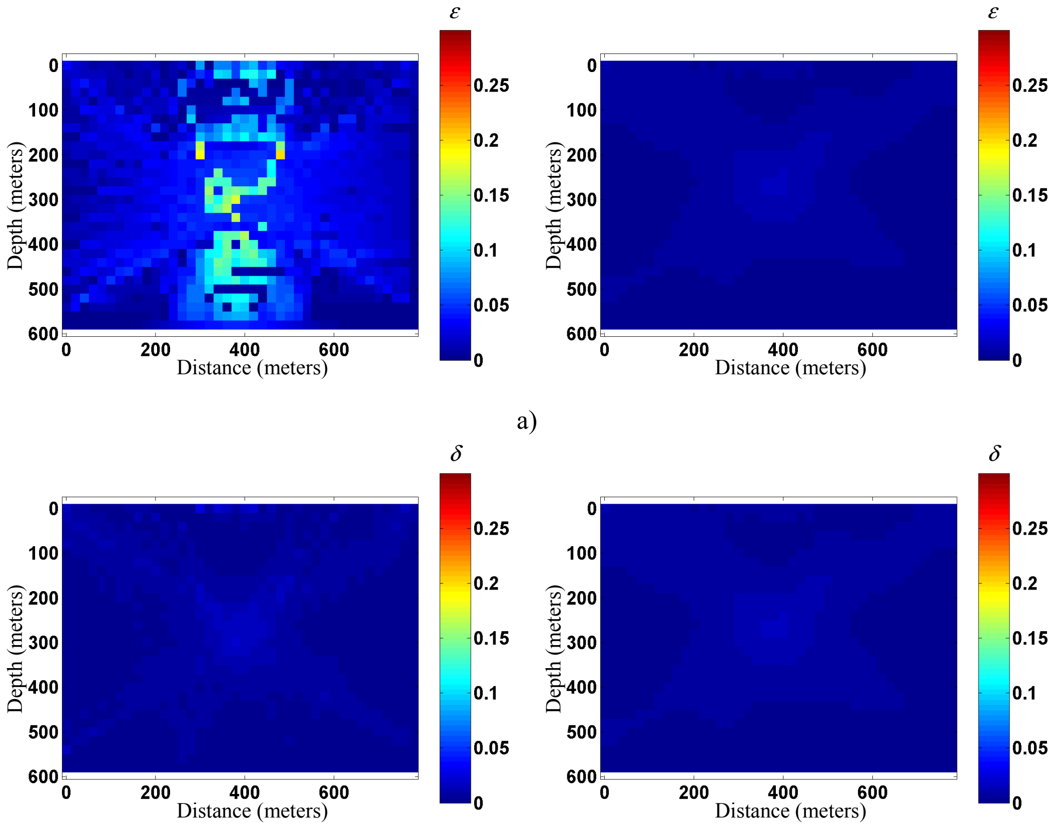

a)

b)

Figure 5.64 Quasi-null space integration results using an initial model estimate which vertical P-wave velocity is known completely; unsmoothed (left) and smoothed (right): ε (a) and δ (b).

The result for ε is adequate. The unsmoothed tomogram shows the consensus of the two experiments in determining that there is a centralized anisotropic anomaly. The δ tomograms does seem to indicate the general shape of the anisotropic anomaly, however it is a consequence of the area where the raypaths of both experiments overlap the most.

5.2.2.3.4 Initial model estimate α_0, ε, δ, with random error

Figures 5.65 through 5.67 show the integration results using an initial model that has had 10, 25 and 50 percent random error added respectively.

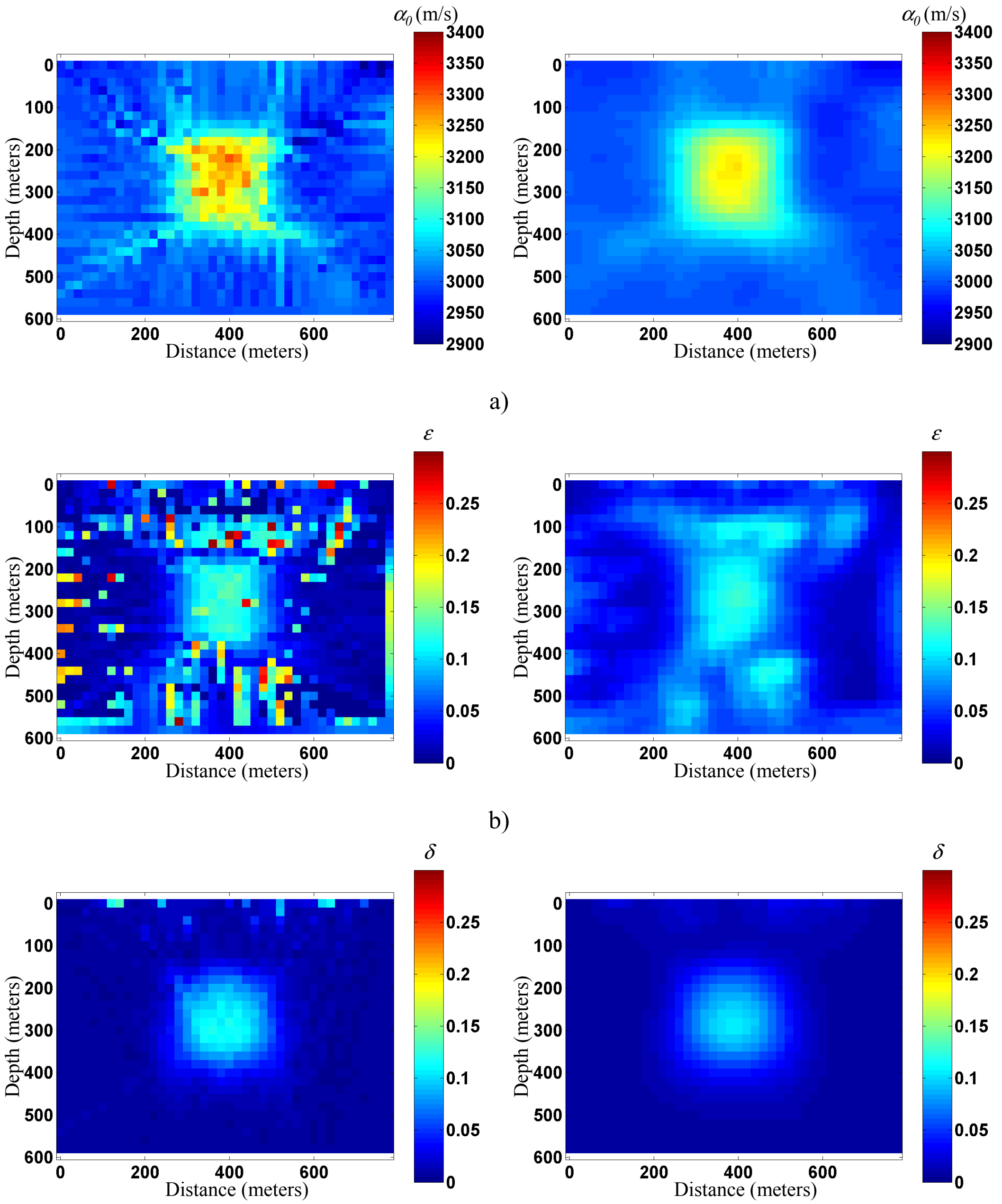

a)

b)

c)

Figure 5.65 Third iteration quasi-null space integration results using an initial model estimate which has random 10 percent model error; unsmoothed (left) and smoothed (right): α_0 (a) ε (b) and δ (c).

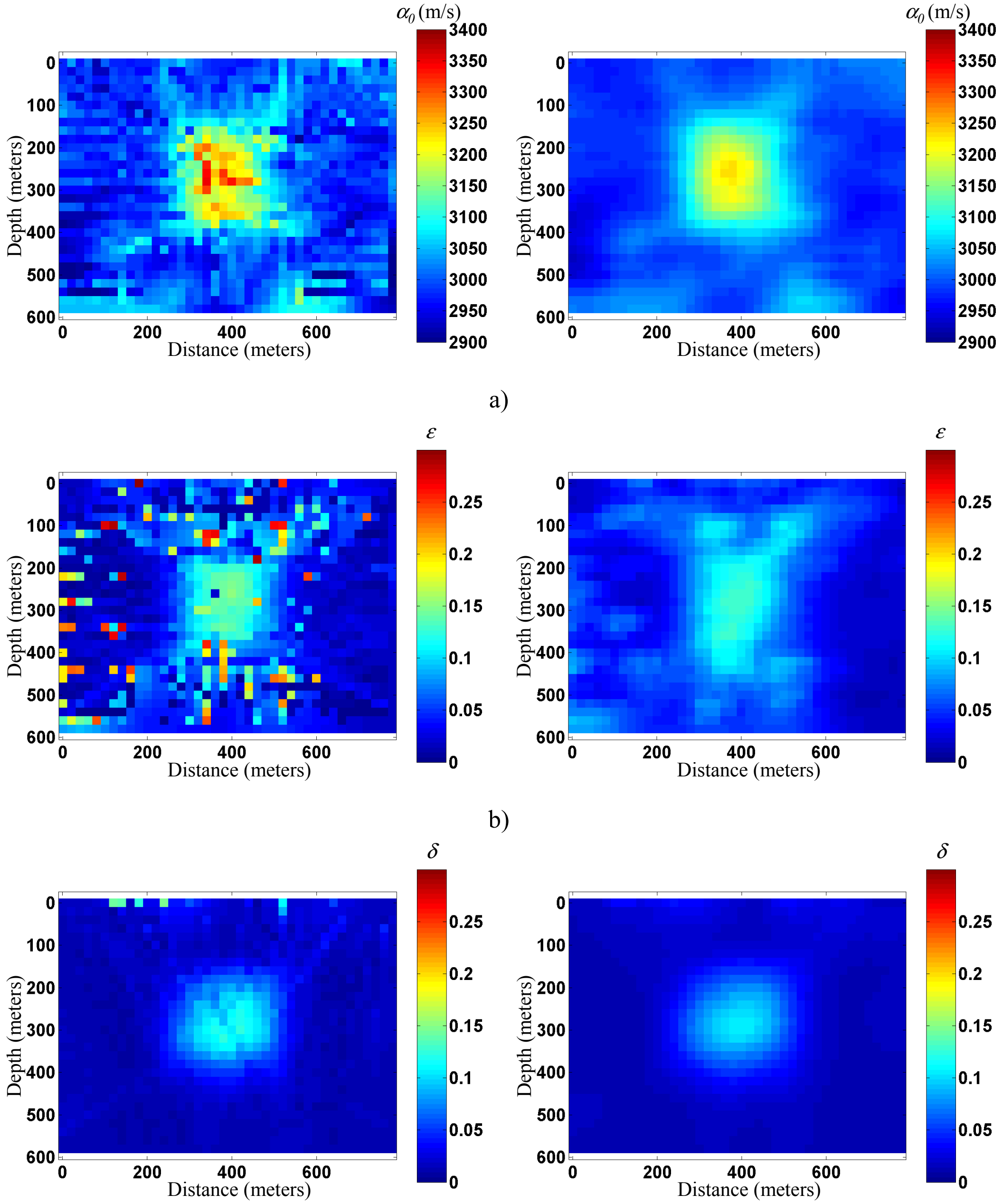

a)

b)

c)

Figure 5.66 Third iteration quasi-null space integration results using an initial model estimate which has random 25 percent model error; unsmoothed (left) and smoothed (right): α_0 (a) ε (b) and δ (c).

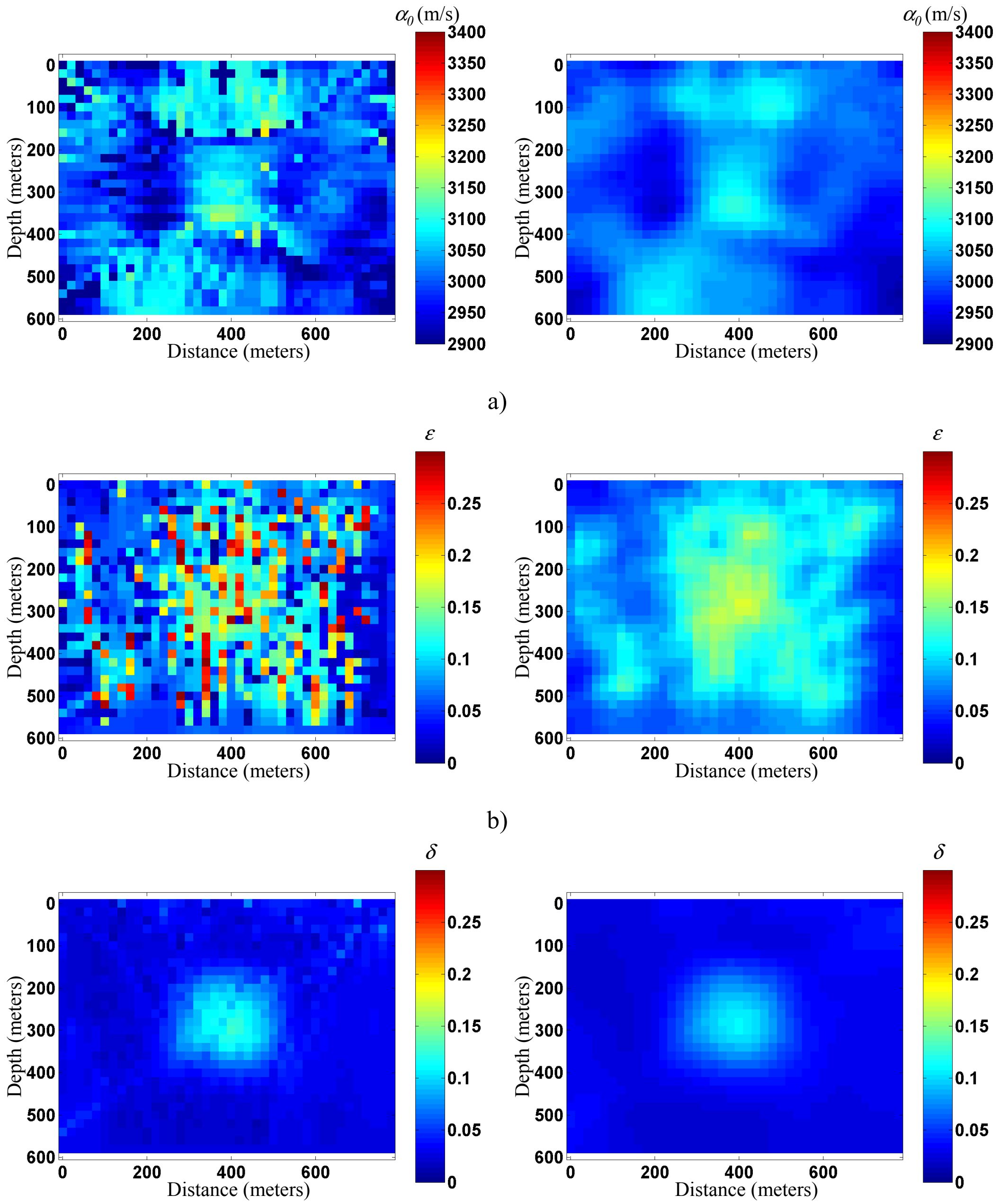

a)

b)

c)

Figure 5.67 Quasi-null space integration results using an initial model estimate which has 50 percent random model error; unsmoothed (left) and smoothed (right): α_0 (a) ε (b) and δ (c).

This suite of results shows a few general trends. In general, vertical P-wave velocity inversion is well constrained, inversion for ε is unstable and δ inversion is minimal outputting a smoothed version of the initial model estimate. It is noted that if the estimate of the vertical P-wave velocity is incorrect, the estimate for ε will attempt to compensate for residual traveltime errors. It follows then, that the inclusion of noise will adversely affect ε inversion. Given that the inversion for ε is governed by the residual traveltime errors remaining after α_0 inversion, velocity noise that is not minimized by α_0 inversion, translates into small residual traveltimes errors that are compensated by ε. As a result ε is very sensitive to noise. Specifically, the following comments are for the inversion results of Figures 5.65 through 5.67:

- The quasi-null space integration stabilization result for the initial model estimate with 10 percent error added is quite good for α_0, ε and δ. The technique correctly identified the more reliable solution and produces a tomogram that is superior to either the crosswell or surface tomogram alone.
- The quasi-null space integration stabilization result for the initial model estimate with 25 percent error is quite impressive given that the original surface tomography results are quite poor. The integrated tomograms are dominated by the crosswell experiment. This was quite evident in the dynamic smoothing results as the surface results had most of the cells deemed as unreliable and thus the mostly smoothed tomograms.
- The quasi-null space integration stabilization result for the initial model estimate with 50 percent error isn't quite as good as the two previous results. This is because the amount of noise added to the initial models is large enough that the resulting crosswell and surface tomograms become equally reliable. The integration result shows that the α_0 and ε inversion become quite unreliable while δ inversion, due to its lack of impact on the traveltime residuals is dominated by the smoothing filter applied after each tomographic iteration.

5.2.3 Complex anisotropic velocity models

Two new models are introduced similar to the complex velocity model introduced in the isotropic testing stage. The difference is in the addition of anisotropy in interval of interest. The first model will have an anisotropic layer above the low-velocity target and the second model will have anisotropy as part of the target unit, testing the ability of the anisotropic inversion algorithm to solve for α_0, ε and δ. The two models are displayed in Figure 5.68.

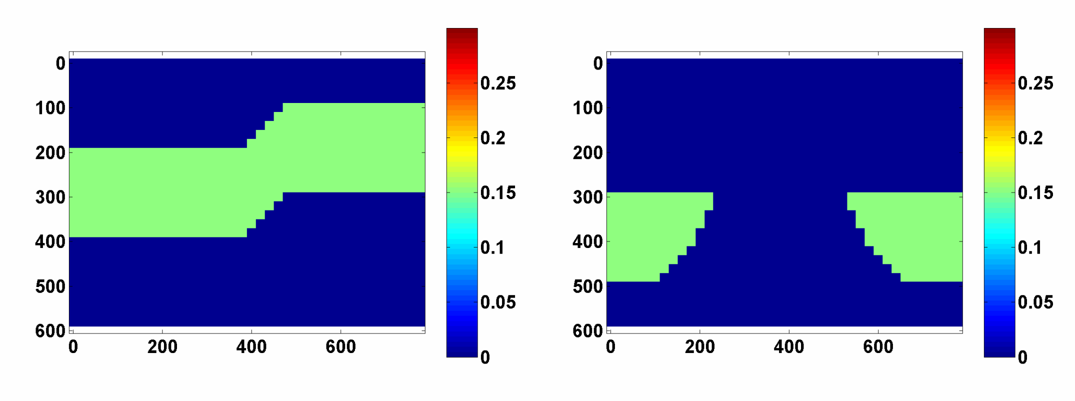

a) b)

Figure 5.68 Anisotropic layers representing values for both ε and δ of 0.15. First complex model (left), second complex model (right).

5.2.3.1 Complex model 1: initial model estimate α_0=2500 m/s, $\varepsilon=\delta=0$

5.2.3.1.1 Crosswell tomography

Testing begins by performing crosswell tomography on the first complex velocity model. Assuming a constant initial background velocity model of 2500 m/s and assuming that the velocity model is isotropic, the results are quite impressive. Figure 5.69 shows the crosswell tomographic results after the third iteration.

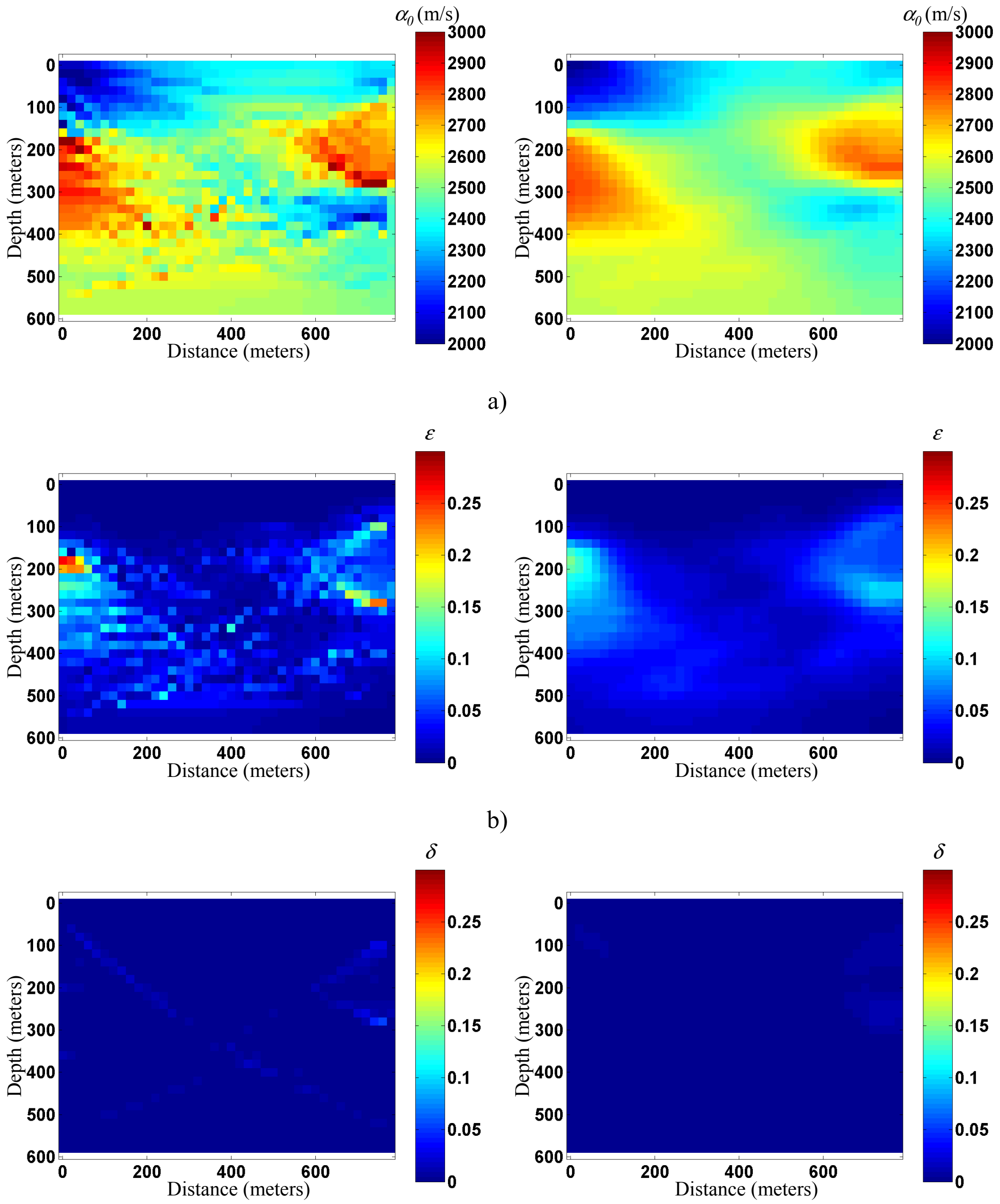

c)

Figure 5.69 Third iteration crosswell tomography results using initial model with a constant vertical P-wave velocity of 2500 m/s and no anisotropy: (left) no post processing, (right) 5 by 5 cell smoother applied; (a) α_0 (b) ε (c) δ.

The results are adequate for α_0 and ε tomogram and quite inadequate for the δ tomogram. The results seen are expected upon analysing the results of the simple models. Crosswell tomography detects the vertical velocity variations and seems to provide insight into the possibility of an anisotropic layer with the inversion of the parameter ε. The inversion for

α_0 shows a lateral discontinuity that can be ascribed to the anisotropy present. The simple model results have shown that there is an angle dependency signature that can be detected when using the incorrect model, in all three tomogram results of α_0, ε and δ. This is the case in the results of Figure 5.69. Also, as noted earlier, inversion for the parameter δ reveals little information primarily a function of the acquisition geometry.

5.2.3.1.2 Surface tomography

The next set of tests determines the capabilities of anisotropic surface tomography in a complex regime. As in the isotropic case, the reflector between the target zone of interest and the overlying velocity is not placed in the model. Figure 5.70 shows the results using an initial constant velocity of 2500 m/s and assuming isotropy.

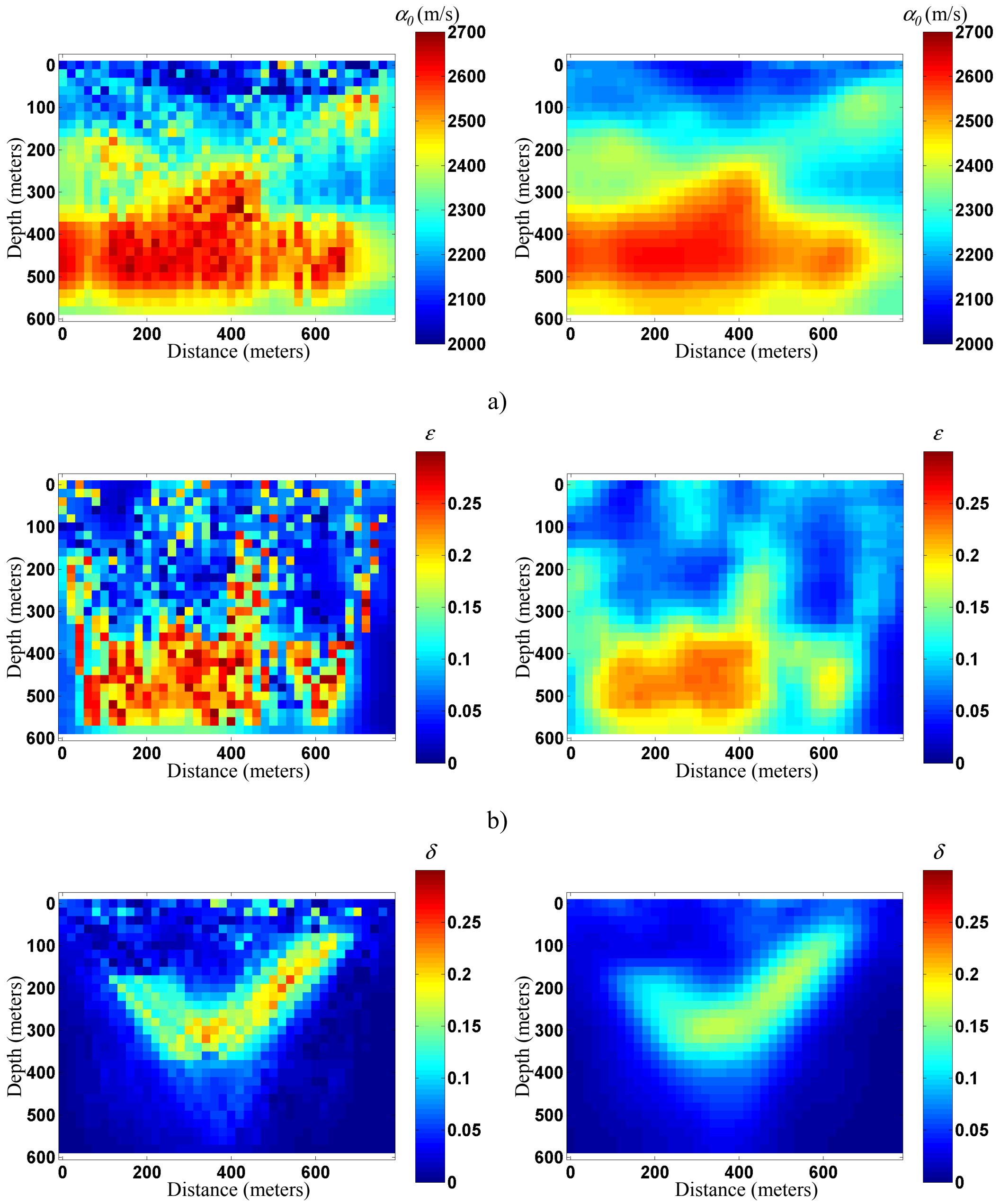

a)

b)

c)

Figure 5.70 Third iteration surface tomography results using initial model with a constant vertical P-wave velocity of 2500 m/s: (left) no post processing, (right) 5 by 5 cell smoother applied; (a) α_0 (b) ε (c) δ.

The results of Figure 5.70 reveals information about surface tomography not previously seen when using the simple model. The α_0 tomogram results are quite good and detect the low-velocity layer of interest as well as the other layers present. The tomograms of greater interest in this set of figures are those of ε and δ. The ε tomogram solution is quite unstable and erroneous. The major difference between these results and results of the simple models is that the error in ε increases with an increase in depth. The reason for this is that most of the layers have been identified by reflectors and it has allowed for isolation of the anisotropic layer leading to a more stable ε solution. As shown in Figure 5.70b, most of the ε instability occurs below the anisotropic layer. This is partly to do with the initial model estimate. The initial model estimate is a velocity that is too slow for the recorded traveltimes. This is where the discrepancy between the initial model and correct model is the largest and as such will have the largest residual traveltimes. After the first iteration of α_0, the remaining residual error is accounted for by ε. Solution error for ε also increases with depth as function of the increase in solution ambiguity with depth. As discussed previously for surface tomography, and seen in Figure 5.22b, the solution reliability for deeper cells decreases since it is a function of the cells overlying it.

The result that is most surprising is that of the δ tomogram. Visual inspection of the tomogram reveals that δ is highest at values where the predominant raypath is at 45 degrees, the maximum value of the time derivative with respect to δ, ($-d\sin^2\theta\cos^2\theta$). This in conjunction with the increase of ray density produces the best estimate of δ yet. In areas where the appropriate angles are not present, the residual traveltimes are compensated for by ε.

5.2.3.2 Complex model 1: initial model estimate α_0=2500 m/s, ε=δ=known

5.2.3.2.1 Crosswell tomography

Figure 5.71 show the results of crosswell α_0 inversion given that the anisotropic parameters are known completely.

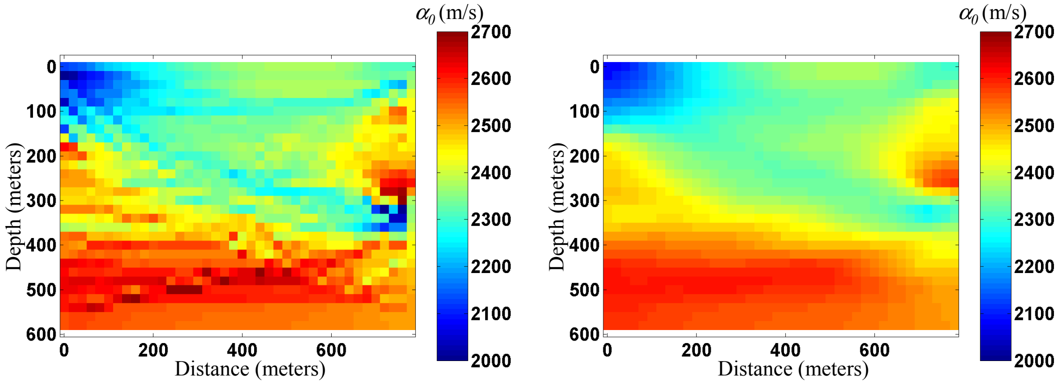

a) b)

Figure 5.71 Third iteration crosswell tomogram estimate for α_0 using model in which the anisotropy is known completely: (a) no post processing, (b) 5 by 5 cell smoother applied.

This result is similar to that of the isotropic case. Notice the lateral discontinuity of the result. This is a function of the refracted ray that travels between the velocity layers. The low-velocity layer is detected but it has been smeared drastically. This basic crosswell characteristic of lateral velocity smearing was seen in the simplest as models. Recognizing it as an inversion artifact will help in determining that new initial model estimate is required.

5.2.3.2.2 Surface tomography

Figure 5.72 shows the third iteration result of reflection tomography using an initial model estimate where the amount of anisotropy is known.

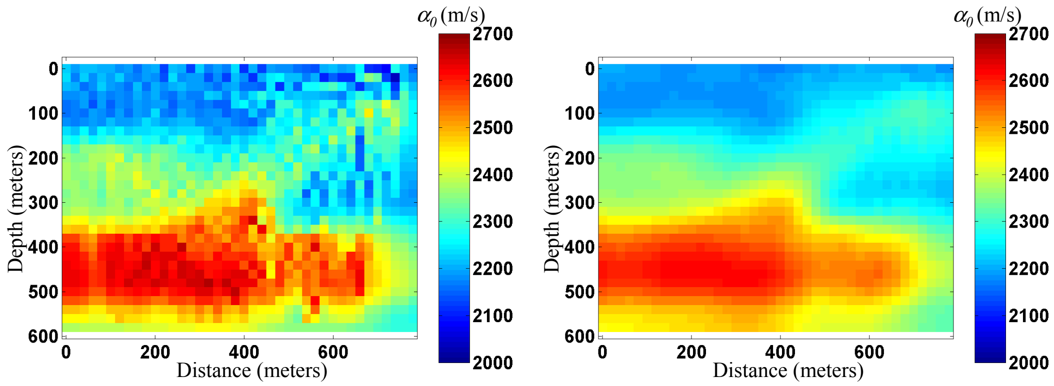

a) b)

Figure 5.72 Third iteration surface tomography results using initial model where the anisotropy is known completely: (a) no post processing, (b) 5 by 5 cell smoother applied.

The resulting tomograms detect the slow velocity layer as there are enough reflectors to determine vertical changes in velocity and since reflection tomography is best suited to detect lateral variations the lateral extent of the anomaly is well resolved. This result is similar to those seen in the isotropic case. This shows that if the anisotropy is known completely the problem is reduced to an isotropic problem.

5.2.3.3 Complex model 1: α_0=known; $\varepsilon=\delta=0$

5.2.3.3.1 Crosswell tomography

The crosswell traveltime inversion results using an initial model in which the vertical P-wave velocity is known exactly yields ε and δ estimates shown in Figure 5.73.

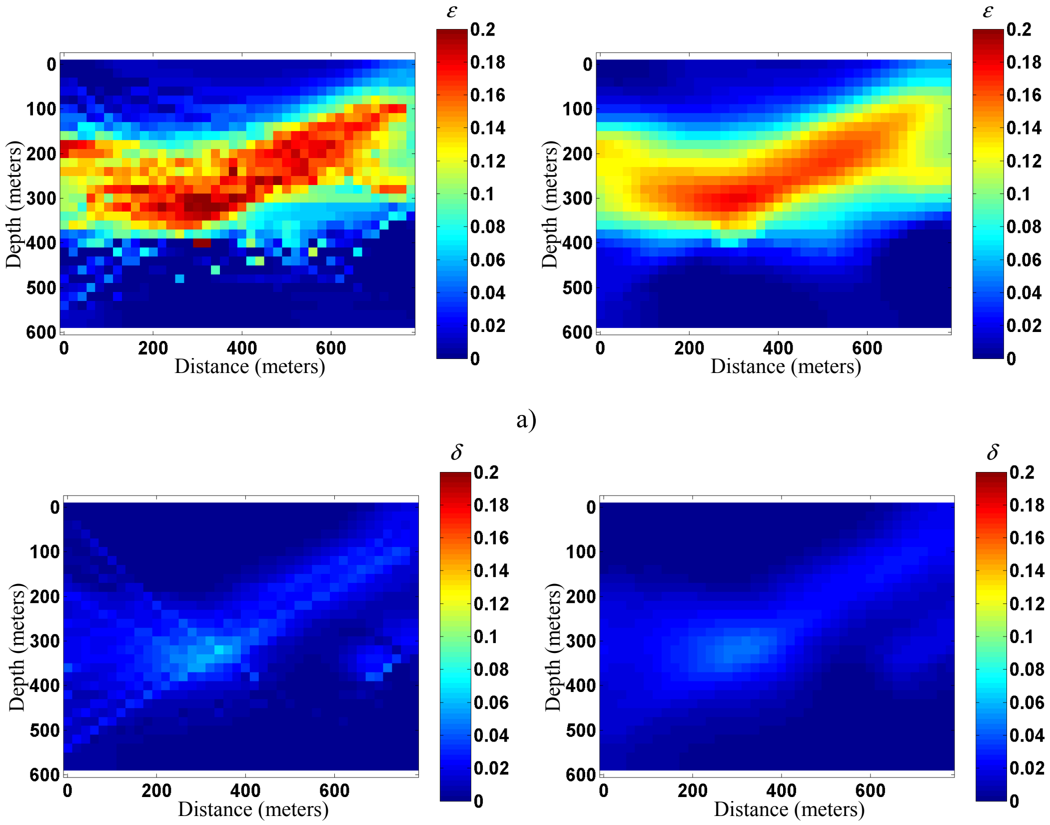

a)

b)

Figure 5.73 Third iteration crosswell tomography results using initial model where vertical P-wave velocity is known completely: (left) no post processing, (right) 5 by 5 cell smoother applied; (a) ε (c) δ.

Here the estimate for ε is quite accurate while the estimate for δ is inadequate given the amount of information provided. Note that the values for ε are larger than they should be compensating for the lower δ values. As shown in the simple models, this is a function of the crosswell acquisition geometry preferentially updating ε due to its predominant raypath direction.

5.2.3.3.2 Surface tomography

Figure 5.74 shows the results of surface tomography using an initial model estimate where the vertical P-wave velocity is known completely.

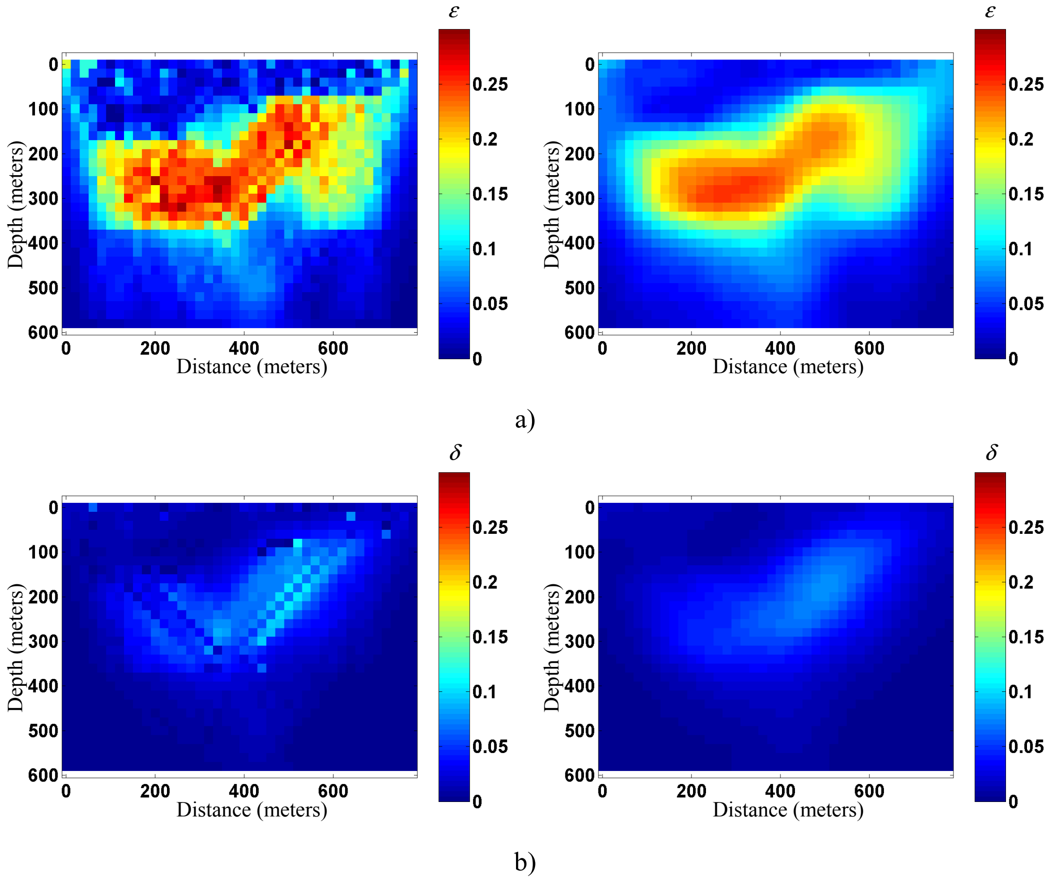

Figure 5.74 Third iteration surface tomography results using initial model where α_0 is known completely: (left) no post processing, (right) 5 by 5 cell smoother applied; (a) ε (b) δ.

These results seem to contradict the statements of the previous test results: that crosswell tomography will best invert for ε and surface tomography will invert best for δ. However, given the initial P-wave velocity model is correct there would be a lot more ray bending at the first interface leading to rays with more of a horizontal component. As a result the solution is biased to reflect ε. There still is an increase in raypath over the interval and some rays approaching 45 degrees leading the inversion solution to δ seen in Figure 5.74b.

5.2.3.4 Complex model 1: initial model estimate, α_0, ε and δ with random error

5.2.3.4.1 Crosswell tomography

The following sets of Figures (5.75 through 5.77) show the crosswell results when using an initial model containing 10, 25 and 50 percent random errors.

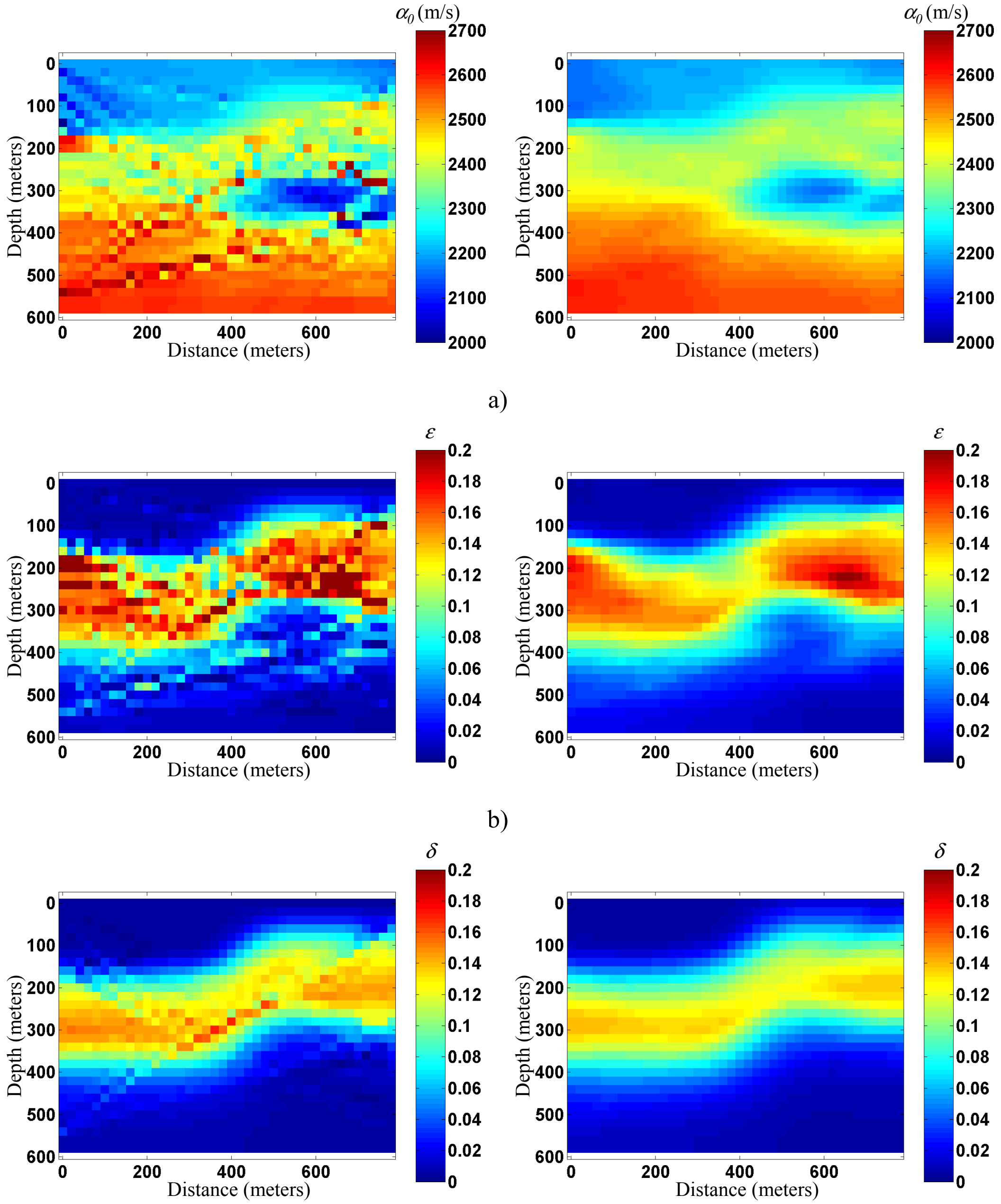

a)

b)

c)

Figure 5.75 Third iteration crosswell tomography results using initial model with 10 percent random error added: (left) no post processing, (right) 5 by 5 cell smoother applied; (a) α_0 (b) ε (c) δ.

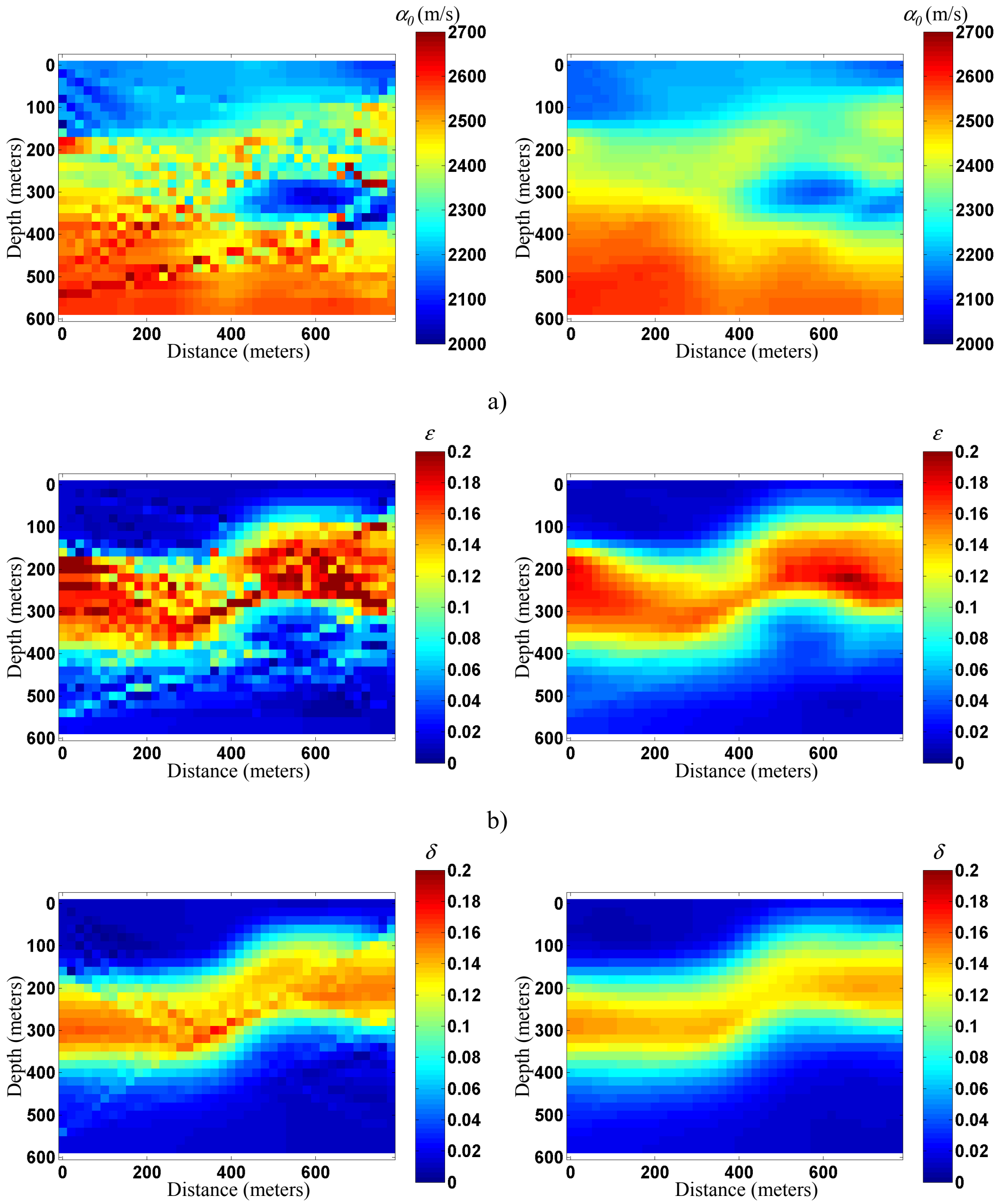

a)

b)

c)

Figure 5.76 Third iteration crosswell tomography results using initial model with 25 percent random error added: (left) no post processing, (right) 5 by 5 cell smoother applied; (a) α_0 (b) ε (c) δ.

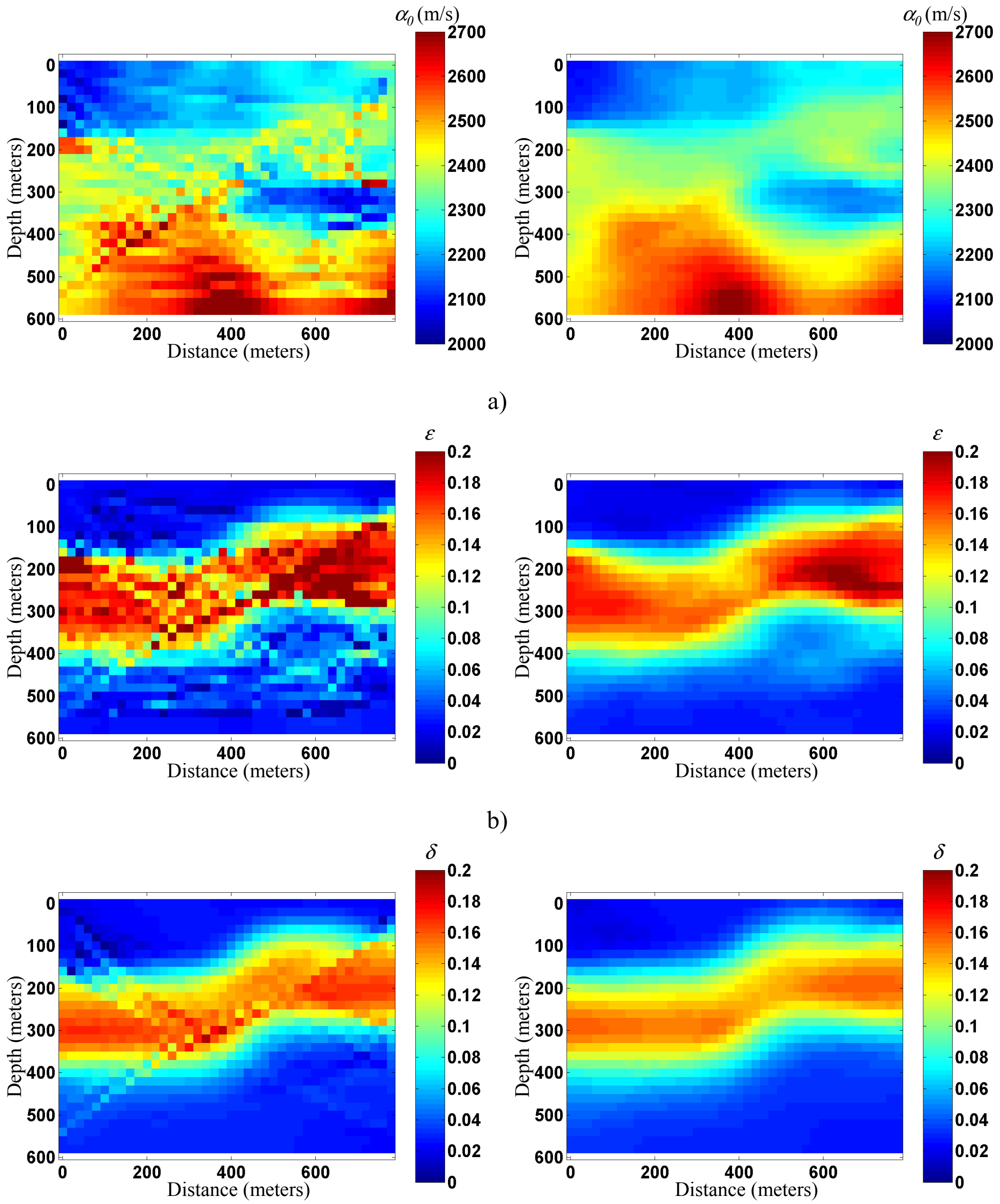

a)

b)

c)

Figure 5.77 Third iteration crosswell tomography results using initial model with 50 percent random error added: (left) no post processing, (right) 5 by 5 cell smoother applied; (a) α_0 (b) ε (c) δ.

The inversion results shown in the previous three sets of figures are quite good. The random noise is suppressed by the tomographic process. Crosswell tomography is conducive to stable inversion processes. The inversion results using an initial model estimate with 10, 25 and 50 percent error are solutions that are a result of the smoothing applied and the constrained model parameter updates. These results show that crosswell tomography is stable enough a process to handle a random model error.

5.2.3.4.2 Surface tomography

Figures 5.78 through 5.80 show the results of surface tomography using an initial model estimate with 10, 25 and 50 percent random error.

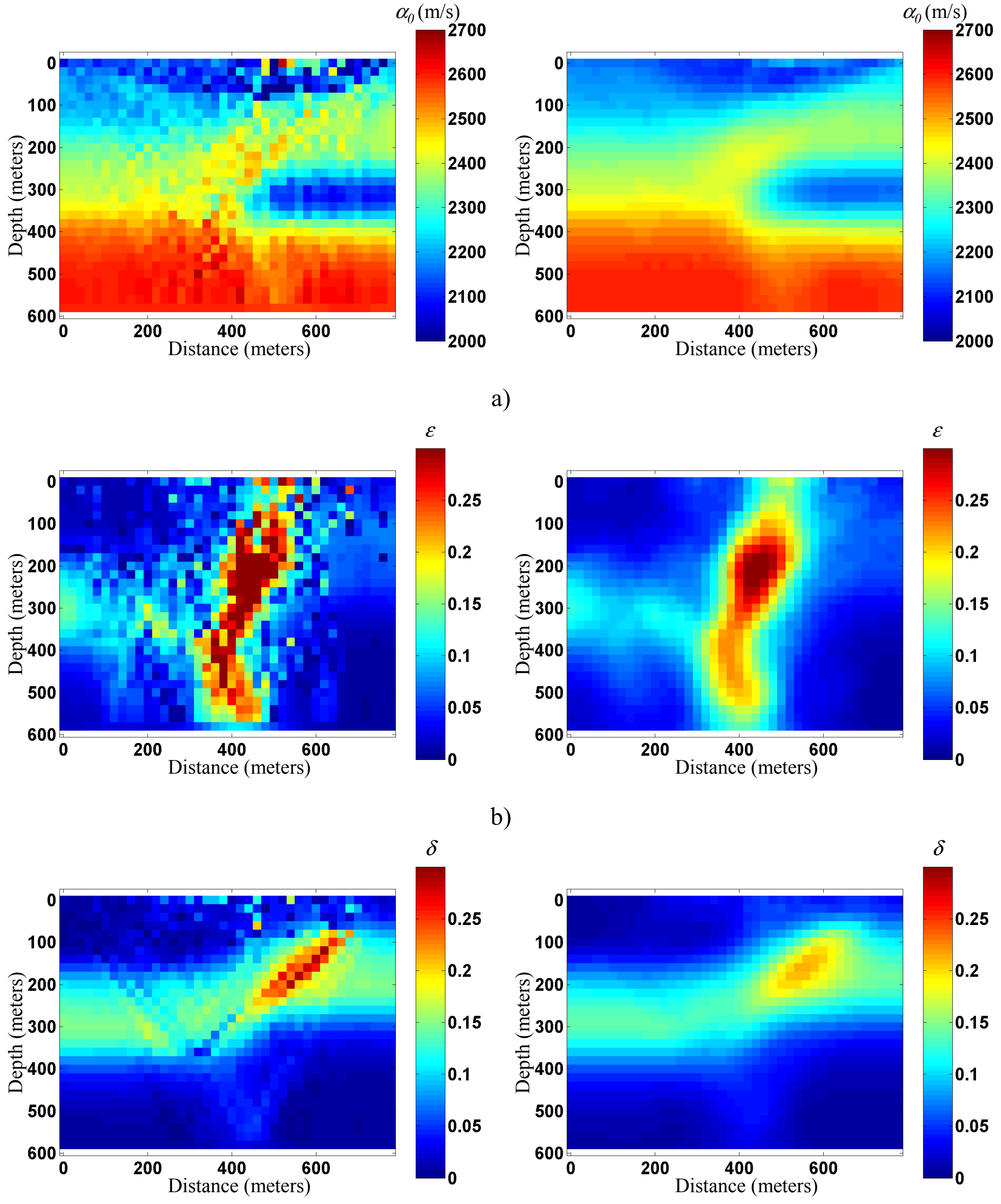

a)

b)

c)

Figure 5.78 Third iteration surface tomography results using initial model estimate with 10 percent random error added: (left) no post processing, (right) 5 by 5 cell smoother applied; (a) α_0 (b) ε (c) δ.

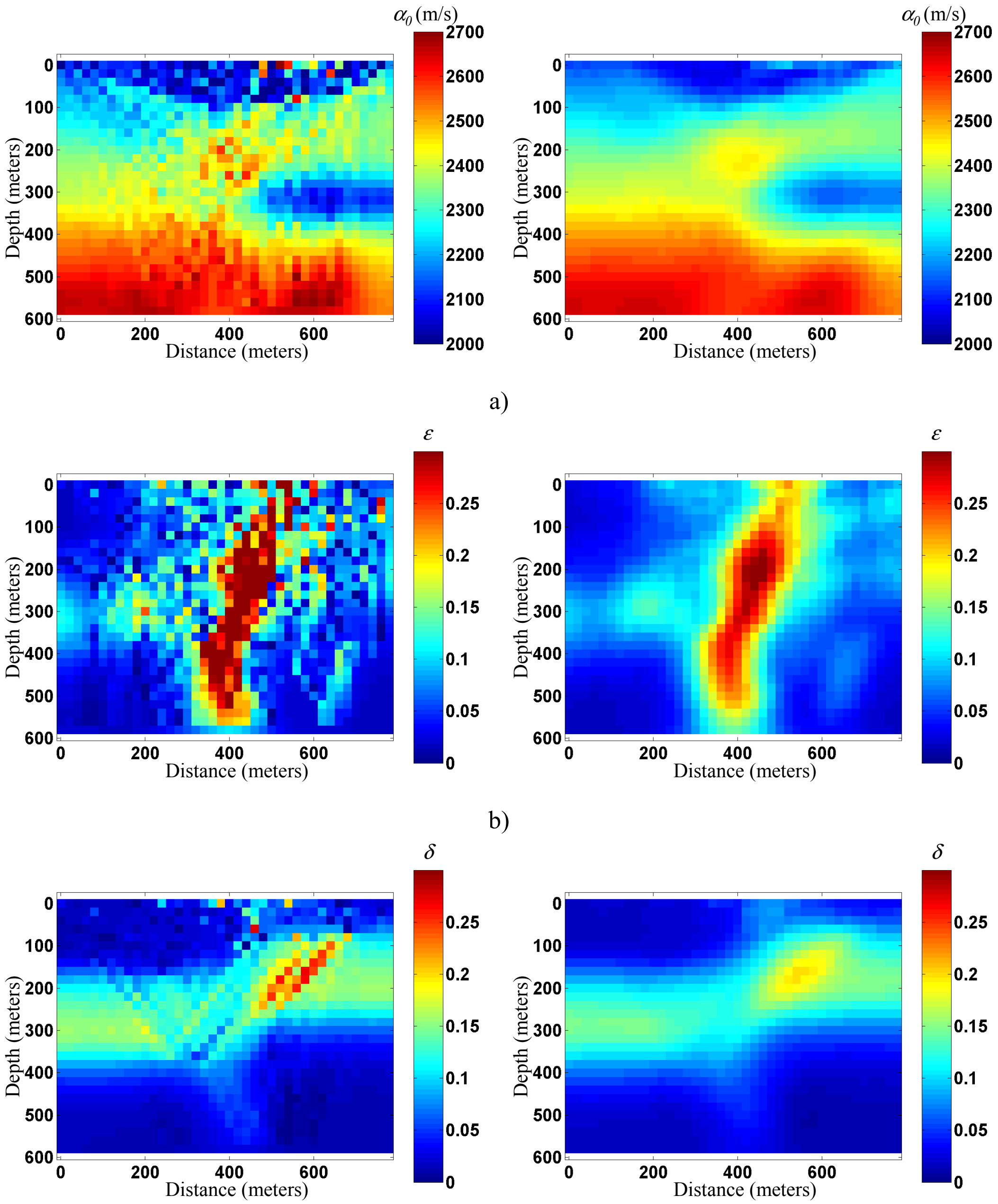

a)

b)

c)

Figure 5.79 Third iteration surface tomography results using initial model estimate with 25 percent random error added: (left) no post processing, (right) 5 by 5 cell smoother applied; (a) α_0 (b) ε (c) δ.

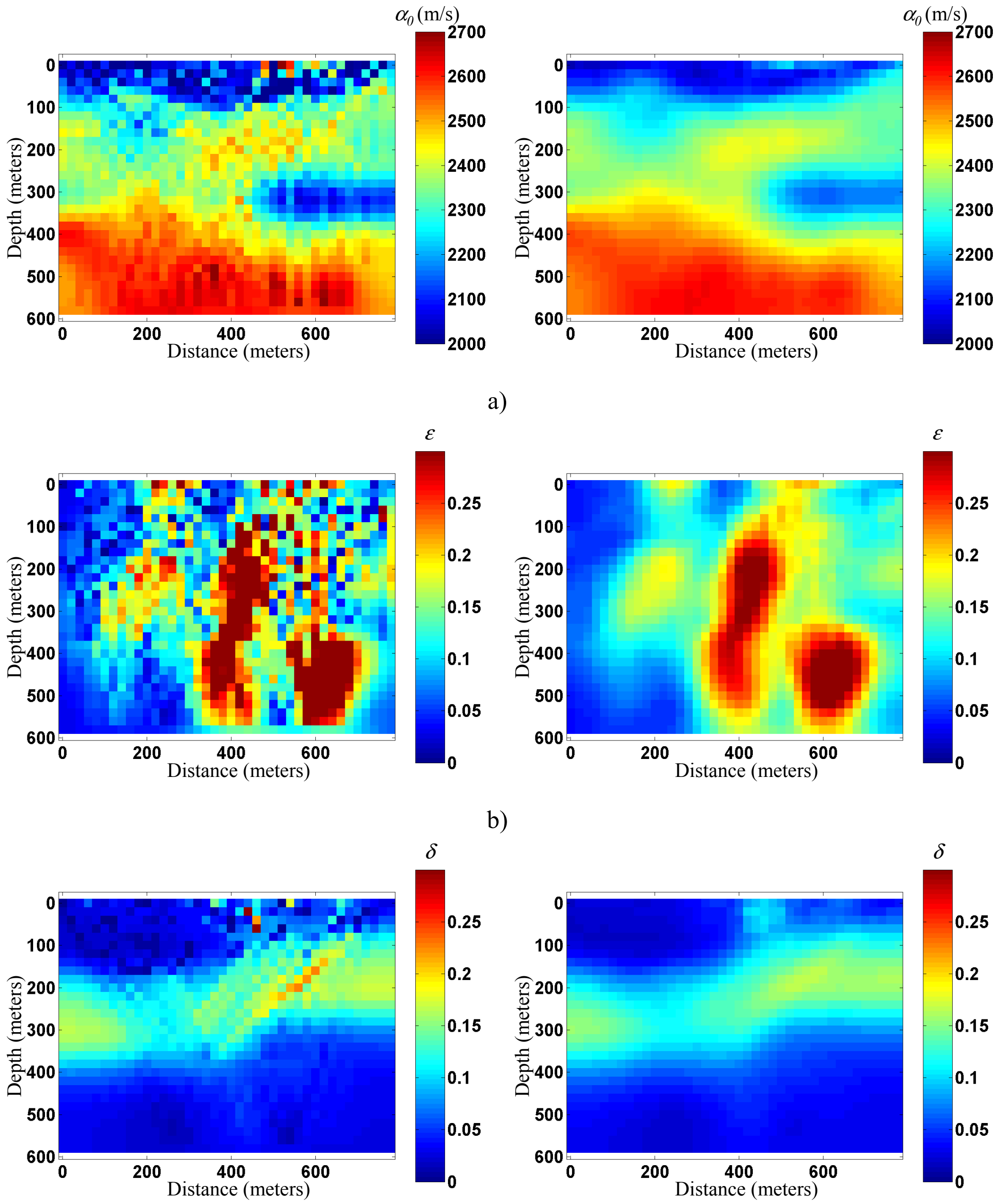

a)

b)

c)

Figure 5.80 Third iteration surface tomography results using initial model estimate with 50 percent random error added: (left) no post processing, (right) 5 by 5 cell smoother applied; (a) α_0 (b) ε (c) δ.

These results show the amount of inversion stability with the presence of noise in the initial model estimate. The vertical P-wave velocity results within the bounds outlined by the complex isotropic results and the anisotropic tomography results from the simple models. The ε and δ and tomograms however show solution quality and stability that are quite different. The δ tomogram response is quite different from the simple model results as a result of the increase in ray density in the zone of interest as well as the near 45 degree raypaths. Recall that 45 degree raypaths are required for optimal δ inversion. The δ tomogram shows the correct anisotropic layer and a reasonable estimate of the amount of anisotropy. The tomogram for ε, however shows quite unstable results. In concordance with the characteristic of reflection tomography the anomaly is spread vertically along the predominant raypath. As determined in the simple models, as well as being unstable, the solution does not converge to the correct value or shape even when only 10 percent error added. The main difference in results between the simple models and the complex models is that the tomogram for α_0 is stable and quite accurate. This is a function of the interfaces added to the model which outline the isotropic layers surrounding the anisotropic one. The added layers allow for a "layer by layer" inversion which makes the tomographic much more stable. In general these results, in conjunction with the crosswell results shows the superiority of crosswell tomography for determining ε and the increased capability of surface tomography to estimate δ.

5.2.3.5 Complex model 2: initial model estimate α_0=2500 m/s, ε=δ=0

5.2.3.5.1 Crosswell tomography

The next sets of tests are on complex model 2. Figure 5.81 shows the results of crosswell tomography using an initial model estimate where α_0=2500 m/s and isotropy is assumed.

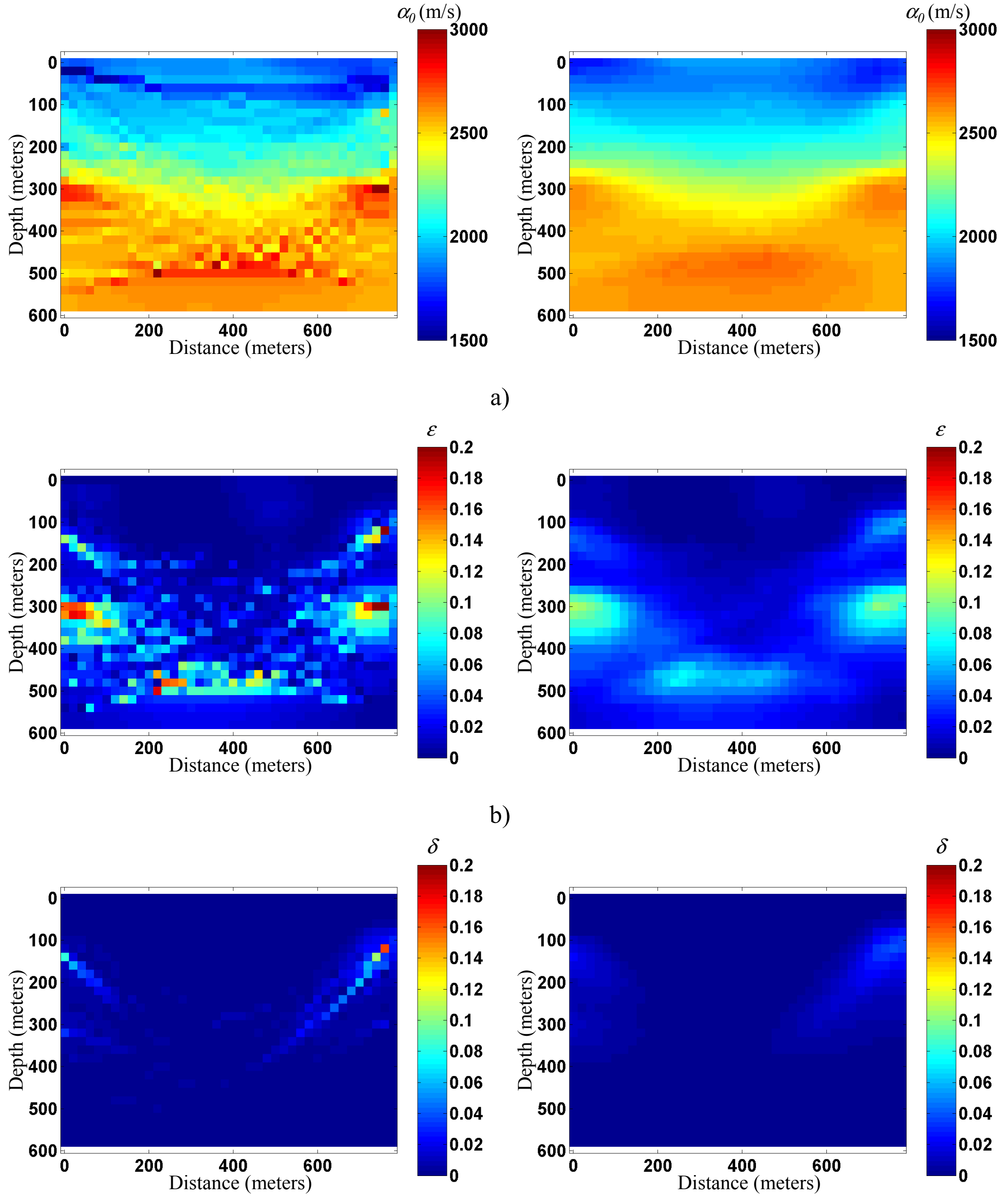

a)

b)

c)

Figure 5.81 Third iteration crosswell tomography results using initial model estimate of 2500 m/s vertical P-wave velocity and no anisotropy (left) no post processing, (right) 5 by 5 cell smoother applied; (a) α_0 (b) ε (c) δ.

These results are very encouraging given the lack of detail in the initial model used. The vertical P-wave velocity response is as good as can be expected as lateral velocity variations cannot be detected. The estimate for δ is quite good when compared to previous estimates of δ for the different models used. The anisotropic layers are smeared vertically, as expected, however due to the high velocity layer present it allows for the presence of the required 45 degree raypath allowing for a better estimate of δ. This is the best result for δ yet from crosswell tomography. The initial estimate for ε is relatively accurate in both shape and magnitude. The greatest error comes at the lower edge of the survey vertically a function of the acquisition geometry.

5.2.3.5.1 Surface tomography

The following tests show the results of anisotropic surface tomography on the second complex velocity model. Figure 5.82 shows the third iteration results using an initial model estimate of 2500 m/s and assuming isotropy.

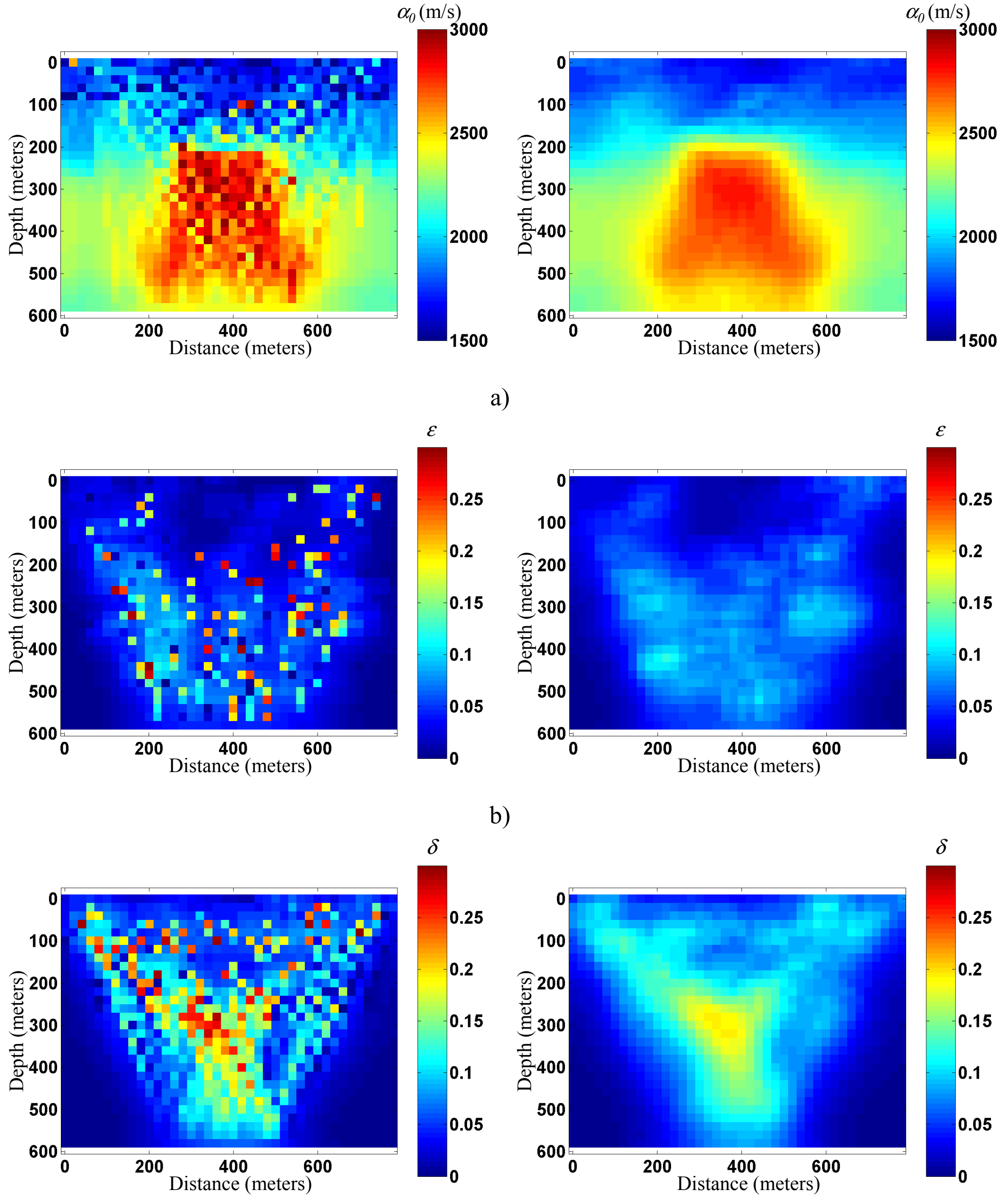

a)

b)

c)

Figure 5.82 Third iteration surface tomography results using initial model estimate with constant vertical P-wave velocity of 2500 m/s and no anisotropy (left) no post processing, (right) 5 by 5 cell smoother applied; (a) α_0 (b) ε (c) δ.

Results are similar to those of complex model 1. The vertical P-wave velocity estimate is good, though it does not detect the vertical velocity change without the additional information the missing reflector would provide. The results are disappointing as the ε and

δ tomograms are not accurate representations of the correct model. The ε tomogram is not expected to perform well but the δ tomogram result is discouraging. This result can be explained by noting that the δ tomogram highlights the raypaths with 45 degree angle. This is the angle dependency that had been seen in the simple models as a "V". This shape leads to correct assumption that there is an angle dependency to the model that can be accounted for by the correct anisotropic model.

5.2.3.6 Complex model 2: initial model estimate α_0=2500 m/s, ε=δ=known

5.2.3.6.1 Crosswell tomography

Figure 5.83 shows the results of crosswell tomography using an initial model estimate where the amount of anisotropy is known completely.

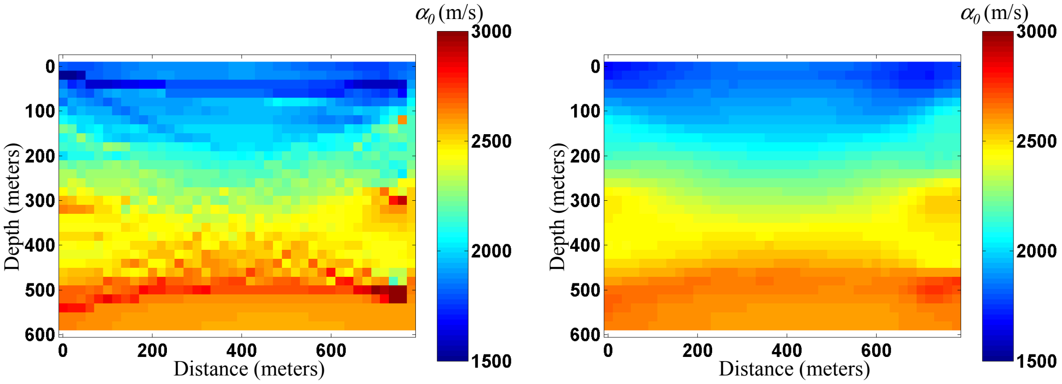

a) b)

Figure 5.83 Third iteration crosswell tomography results using initial model estimate where anisotropy is known completely (a) no post processing, (b) 5 by 5 cell smoother applied.

These results are similar to those seen in the isotropic crosswell tomography for the second complex model: good vertical velocity detection and poor lateral resolution.

5.2.3.6.2 Surface tomography

Figure 5.84 shows the results of surface tomography using an initial model estimate where the amount of anisotropy is known exactly.

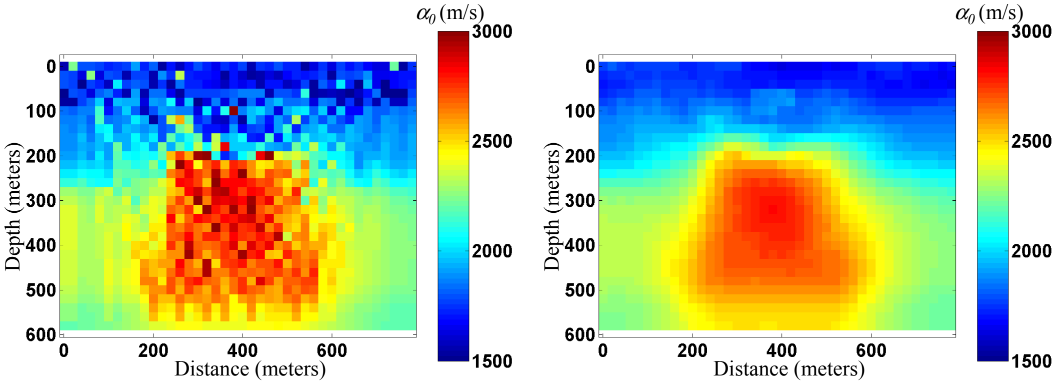

a) b)

Figure 5.84 Third iteration surface tomography results using initial model estimate where the amount of anisotropy is known completely (a) no post processing, (b) 5 by 5 cell smoother applied.

Surface tomography accurately demonstrates the lateral extent of the velocity structure yet fails to outline the velocity layer on interest. This result is as expected. As with the isotropic results, the fact that there is a lack of vertical resolution in the layer of interest is a function of the acquisition geometry and the missing reflecting interface in the model.

5.2.3.7 Complex model 2: initial model estimate α_0=known, $\varepsilon=\delta=0$

5.2.3.7.1 Crosswell tomography

Figure 5.85 shows the crosswell results using an initial model estimate where the vertical P-wave velocity is known exactly.

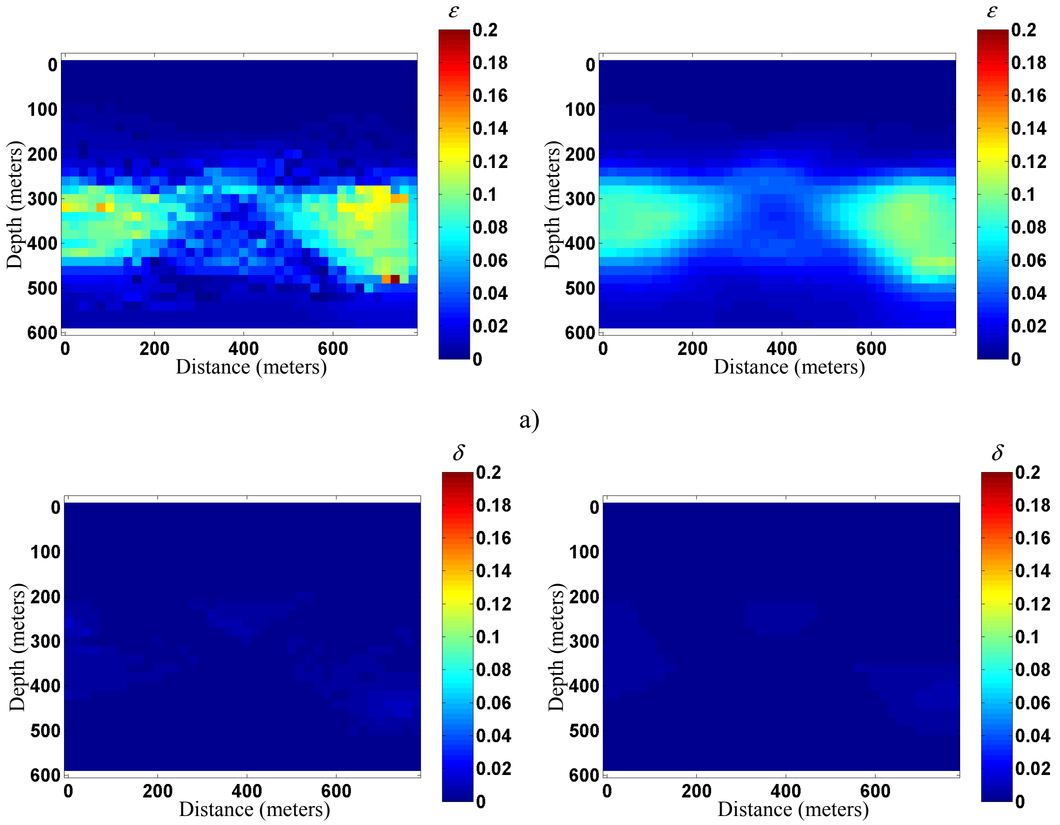

a)

b)

Figure 5.85 Third iteration crosswell tomography results using initial model estimate where vertical P-wave velocity is known completely: (left) no post processing, (right) 5 by 5 cell smoother applied; (a) ε (b) δ.

As now expected from crosswell tomography, the estimates for ε are excellent while the estimate for δ leaves much to be desired. That being said, taking into consideration that the acquisition geometry is not optimal for δ inversion there are hints of a δ layer in the correct position. This result is the best that can be realistically achieved; the isotropic component is known completely allowing for a stable inversion for the two remaining anisotropic parameters.

5.2.3.7.2 Surface tomography

Figure 5.86 shows the result of surface tomography using an initial model estimate where the anisotropy is known completely.

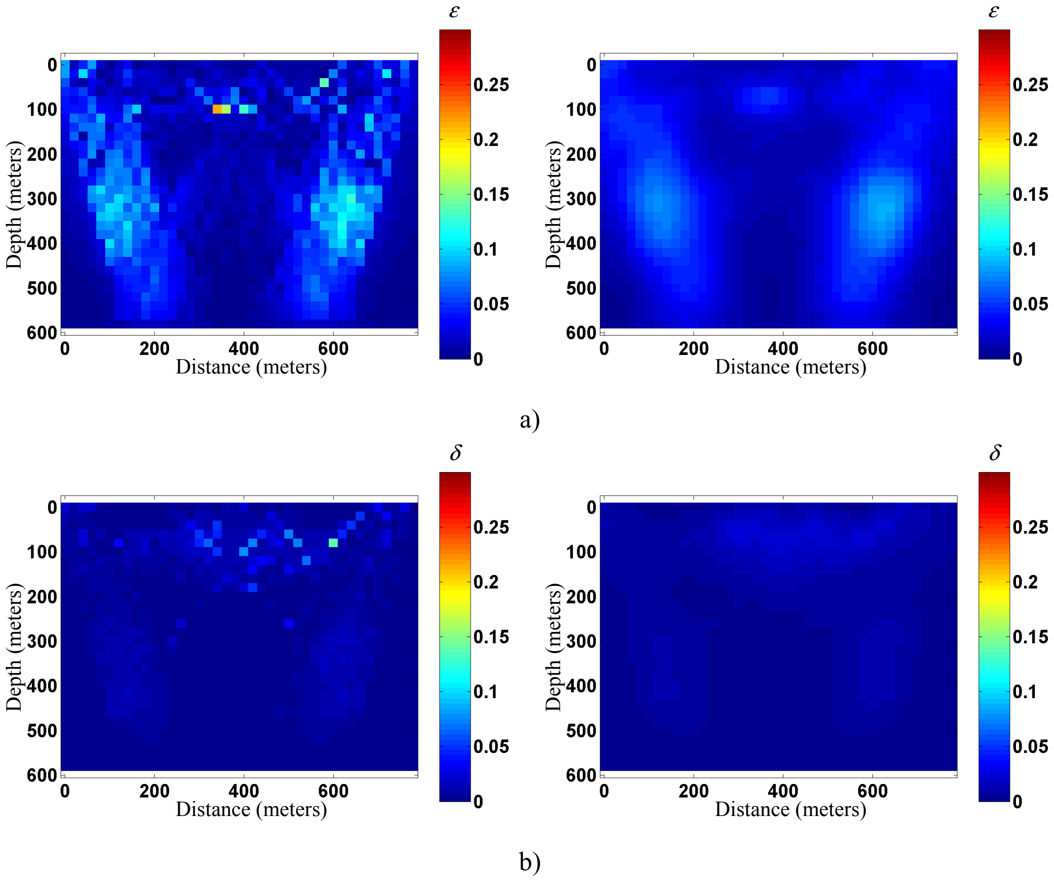

Figure 5.86 Third iteration surfacetomography results using initial model estimate where anisotropy is known completely (left) no post processing, (right) 5 by 5 cell smoother applied.

These results confirm the isotropic results for surface tomography. The estimates for ε and δ are somewhat accurate in shape, correctly locating the main anisotropic zones of interest. However the magnitude of anisotropy present is underestimated. The estimate of ε is inaccurate because of the lack of near horizontal rays and the inaccurate estimate of δ due to the lack of rays near 45 degrees due the depth of anisotropic anomaly. Notice that this result, as opposed to those seen in Figure 5.82, is a stable result, where the presence of anisotropic anomalies is confirmed by both ε and δ. With unstable solutions are identified, the first step in producing better results is choosing a new initial model estimate.

5.2.3.8 Complex model 2: initial model estimate of α_0, ε and δ with random error

5.2.3.8.1 Crosswell tomography

Figures 5.87 through 5.89 show the crosswell tomography results using an initial model estimate which has 10, 25 and 50 percent random error added to the exact model.

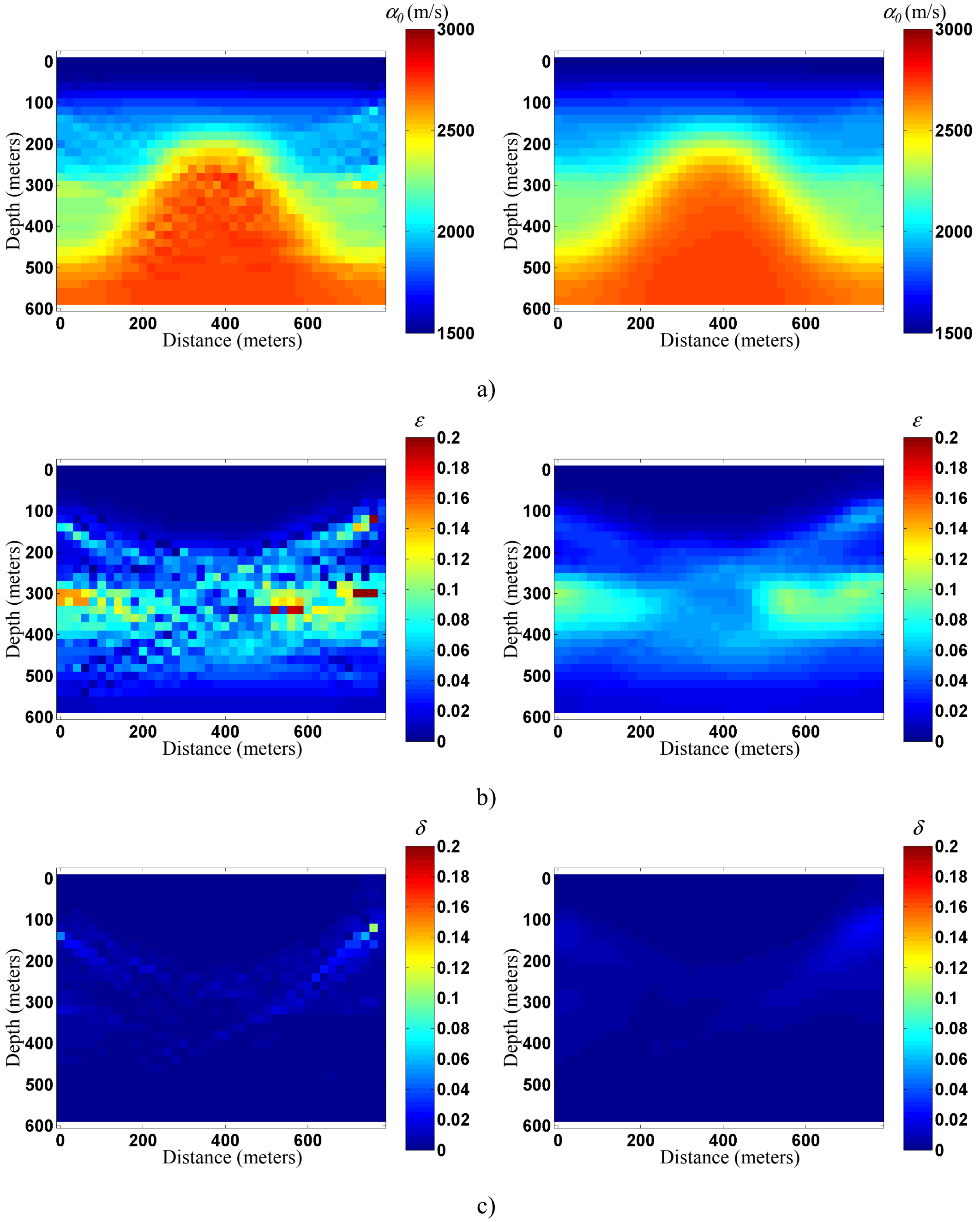

Figure 5.87 Third iteration crosswell tomography results using initial model estimate with 10 percent random error added (left) no post processing, (right) 5 by 5 cell smoother applied; (a) α_0 (b) ε (c) δ.

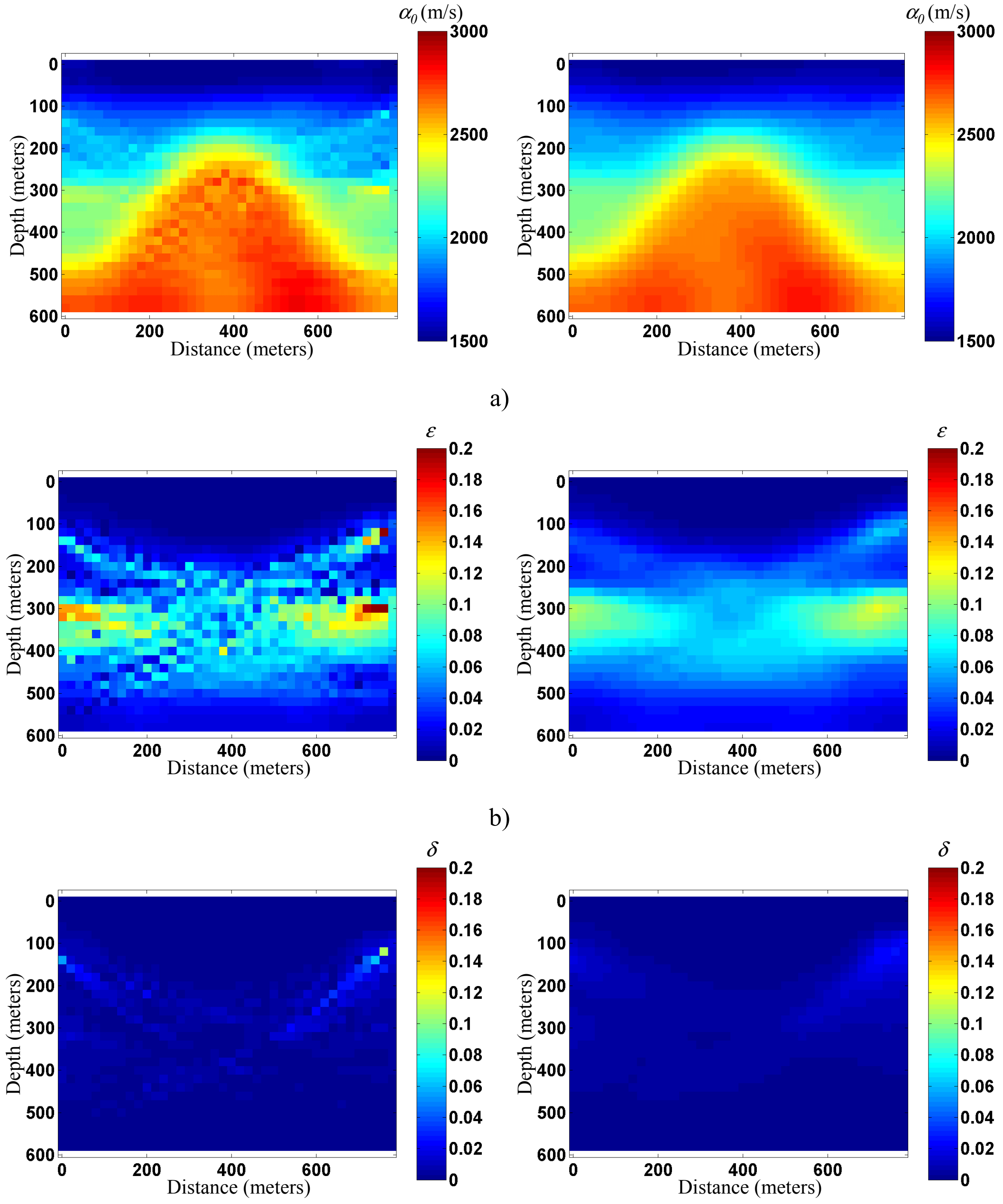

a)

b)

c)

Figure 5.88 Third iteration crosswell tomography results using initial model estimate with 25 percent random error added (left) no post processing, (right) 5 by 5 cell smoother applied; (a) α_0 (b) ε (c) δ.

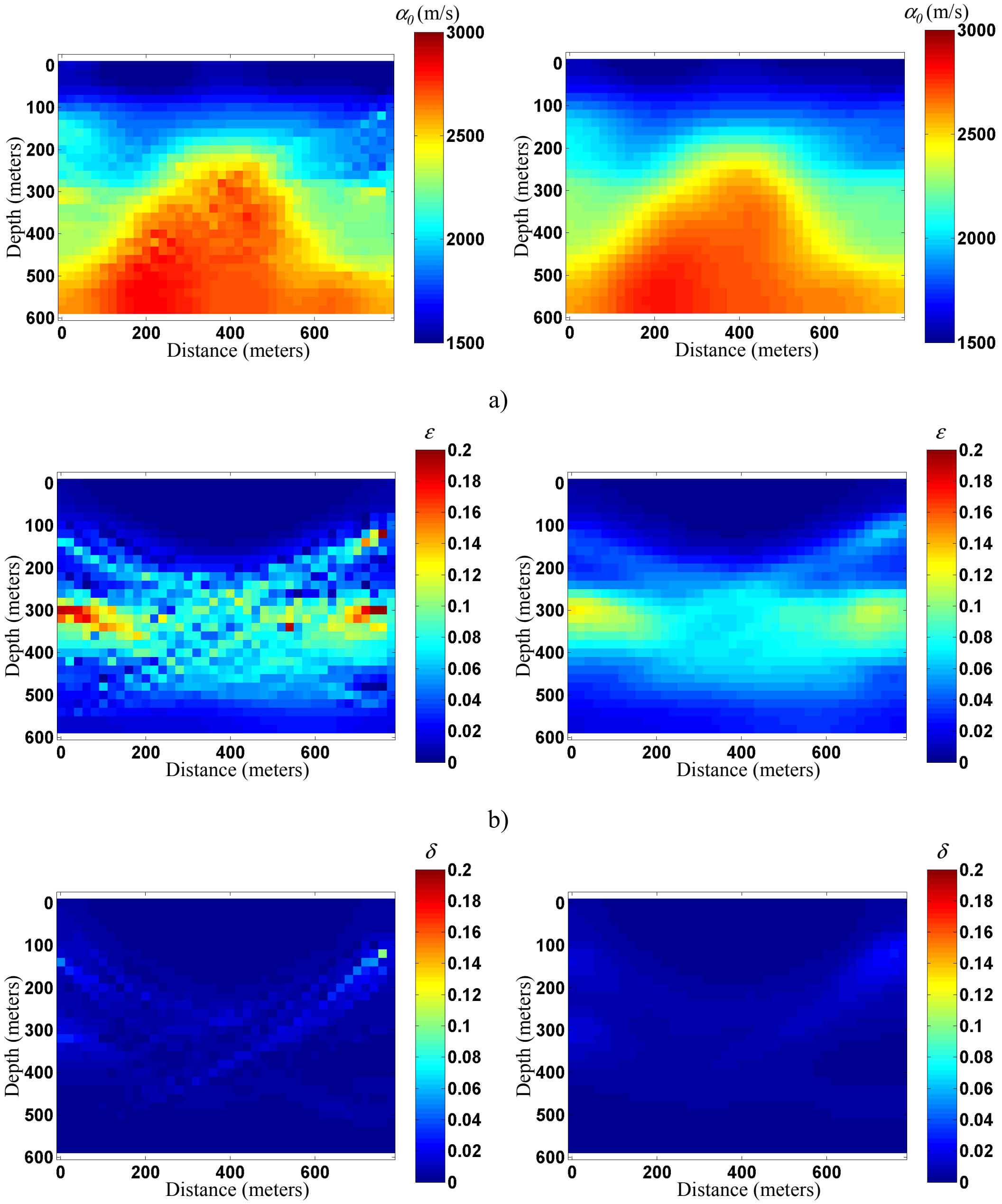

a)

b)

c)

Figure 5.89 Third iteration crosswell tomography results using initial model estimate with 50 percent random error added (left) no post processing, (right) 5 by 5 cell smoother applied; (a) α_0 (b) ε (c) δ.

As shown in the first complex velocity model, the results for α_0 and ε are quite stable. The tomogram for δ is a consequence of the crosswell geometry: horizontal rays are not conducive to inverting for δ. Figure 5.89 shows asymmetry in the model. The asymmetry is a function of the planewave assumption of the raytracing algorithm used.

5.2.3.8.2 Surface tomography

Figures 5.90 through 5.92 show the anisotropic surface tomography results using initial model estimates with 10, 25 and 50 percent random error added to the correct model.

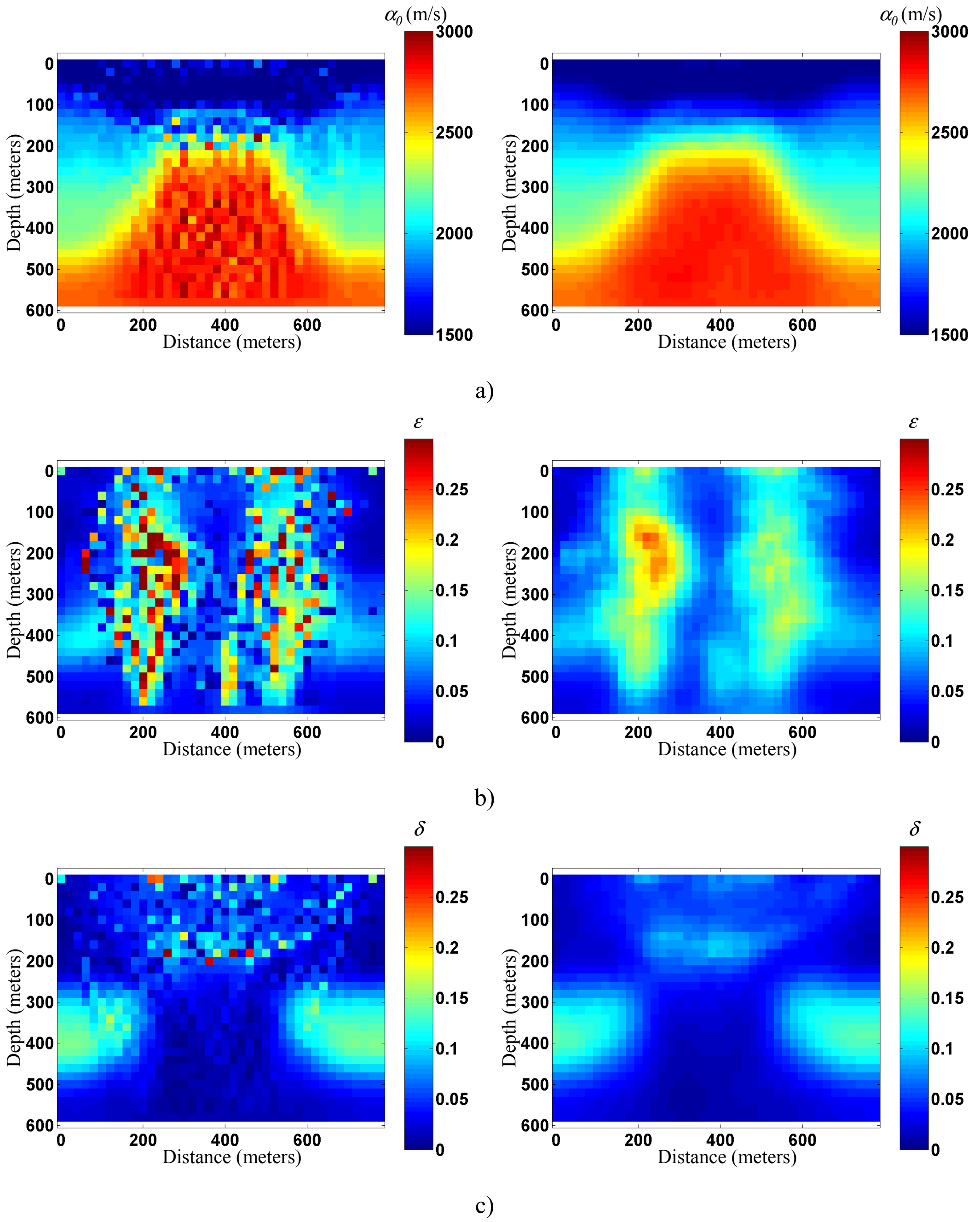

a)

b)

c)

Figure 5.90 Third iteration surface tomography results using initial model estimate with 10 percent random error added (left) no post processing, (right) 5 by 5 cell smoother applied; (a) α_0 (b) ε (c) δ.

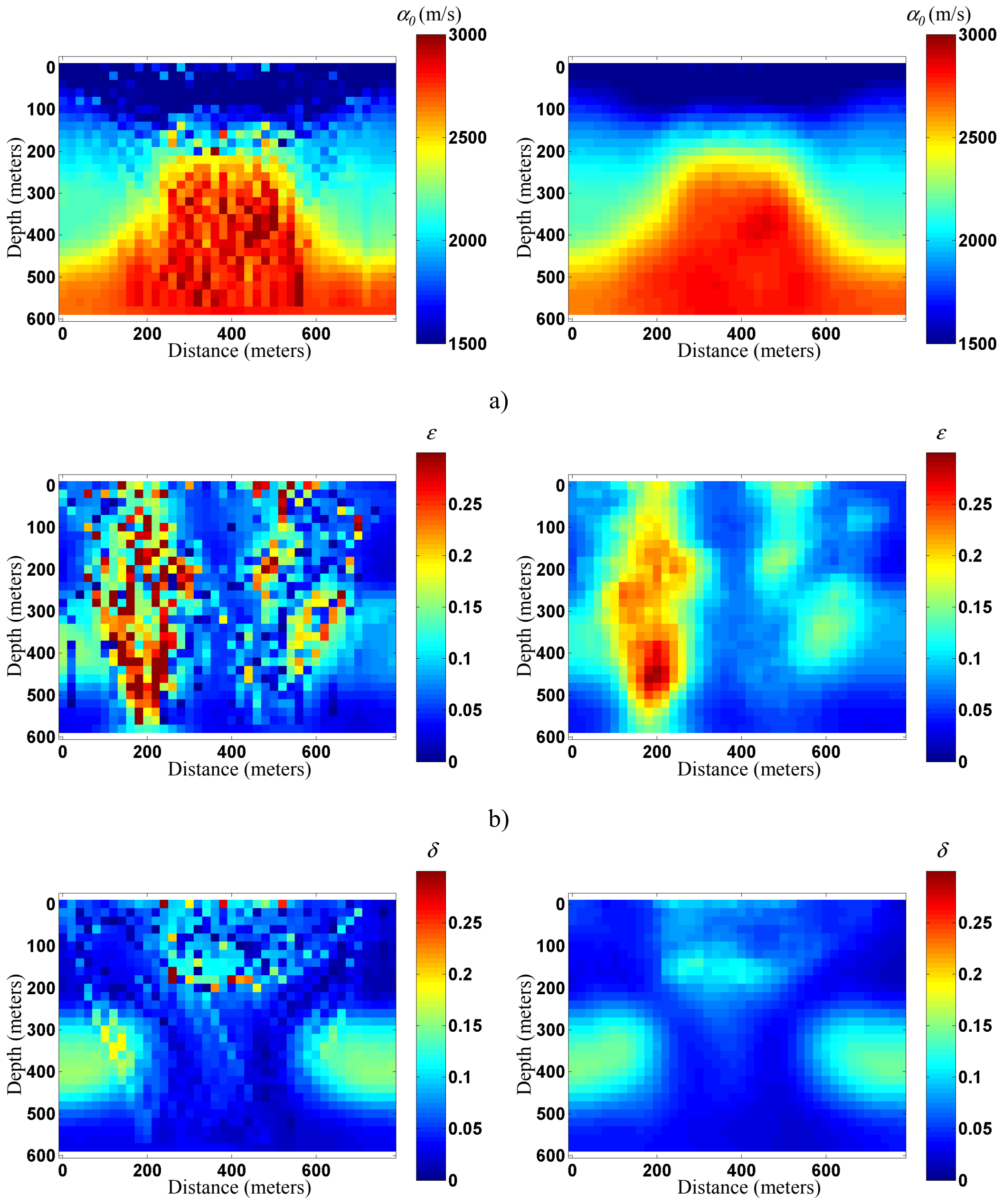

a)

b)

c)

Figure 5.91 Third iteration surface tomography results using initial model estimate with 25 percent random error added (left) no post processing, (right) 5 by 5 cell smoother applied; (a) α_0 (b) ε (c) δ.

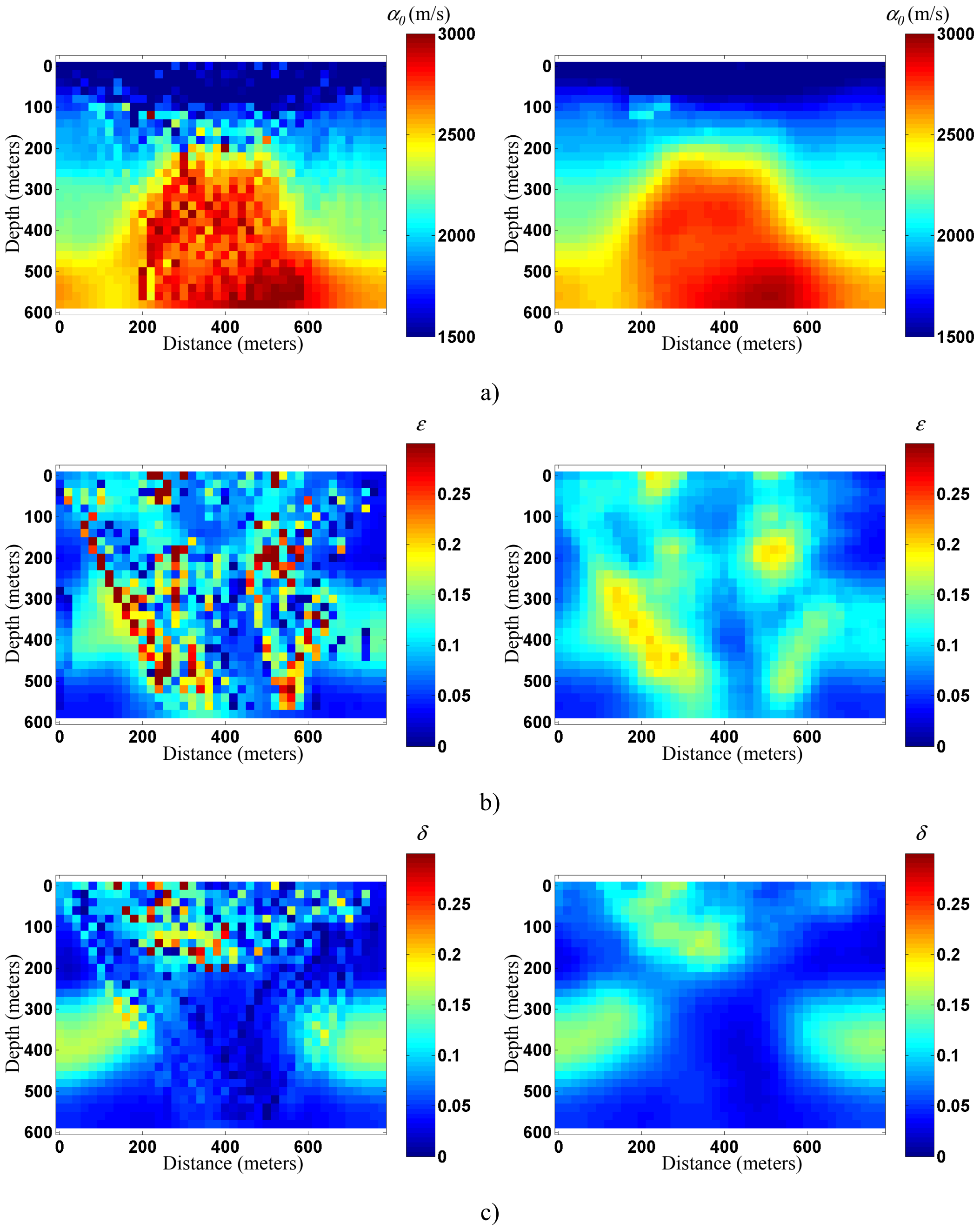

Figure 5.92 Third iteration surface tomography results using initial model estimate with 50 percent random error added (left) no post processing, (right) 5 by 5 cell smoother applied; (a) α_0 (b) ε (c) δ.

These results show the same trend seen in complex model 1. The tomogram for α_0 is quite reasonable given the lack of vertical velocity detection in surface tomography. The tomogram for ε is increasingly unstable with more random noise added while the δ tomogram is relatively stable except for the shallowest of cells. These shallow cells with an increase in δ are accounted for by the residual traveltime errors being minimized by δ due to amount of ray paths near 45 degrees.

5.2.4 Quasi-null space analysis – complex anisotropic models

The next set of tests show the results of applying the quasi-null space stabilization techniques on the complex anisotropic models. The quasi-null space techniques are applied to all six initial model estimates and provide similar results to those seen in the simple models. It is determined that the quasi-null space can only provide so much in terms of resolution and stabilization given that they are post inversion processes.

5.2.4.1 Dynamic filtering: complex model 1

5.2.4.1.1 Initial model estimate α_0=2500, m/s ε=δ=0

Figure 5.93 shows the results of dynamic smoothing applied to complex model 1 using for crosswell and surface tomography and using an initial model estimate of α_0=2500 m/s and where isotropy is assumed.

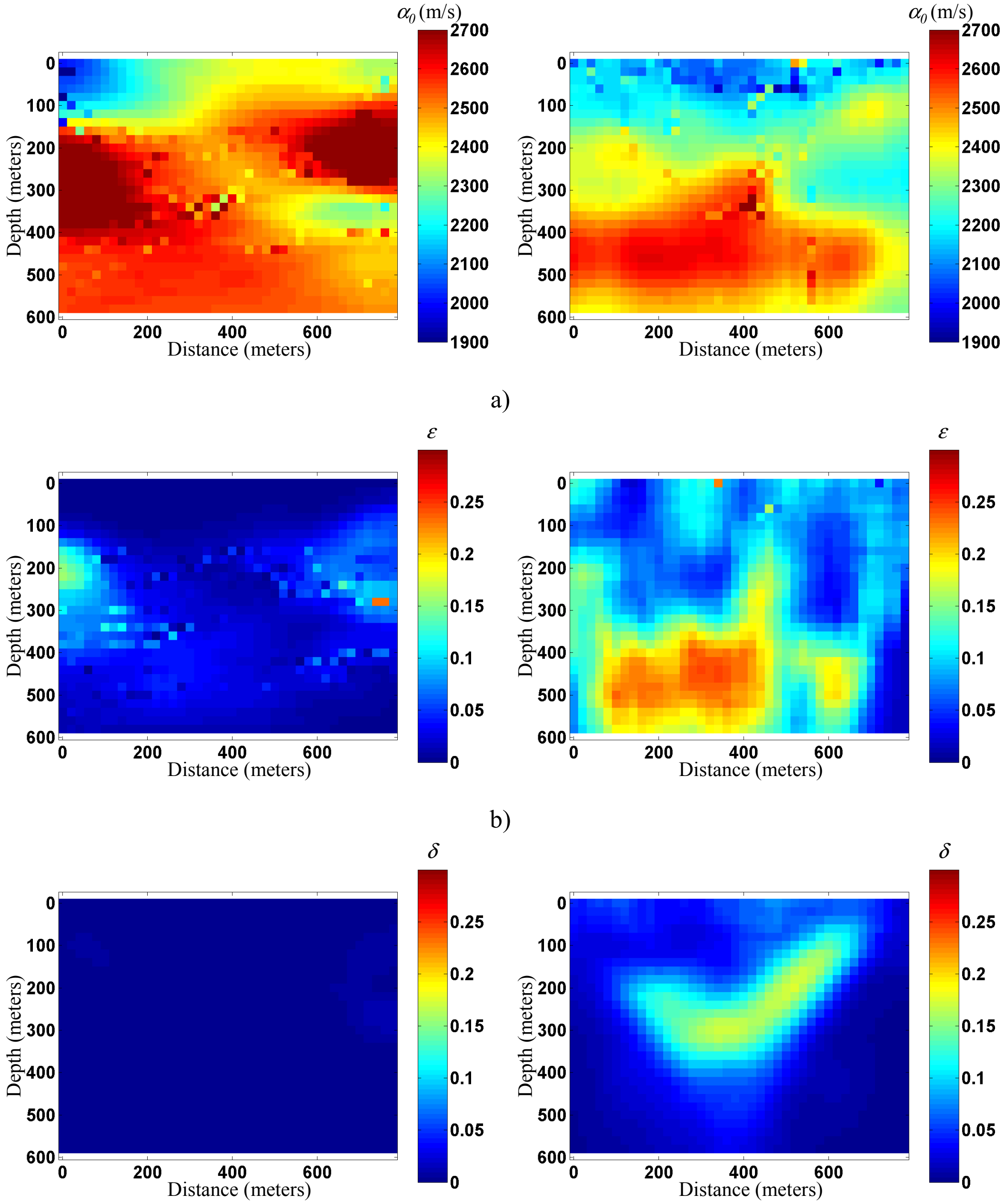

a)

b)

c)

Figure 5.93 Quasi-null space dynamic smoothing results using an initial model estimate of a constant vertical P-wave velocity and no anisotropy; crosswell (left) and surface (right): α_0 (a) ε (b) and δ (c).

The tomographic results show the basic trends that have been in the previous test results shown. The basic trends are:

- Crosswell tomography detects vertical velocity variation well and horizontal velocity variations poorly.
- Surface tomography detects horizontal velocity variations well and vertical velocity variations poorly.
- Crosswell tomography has a better chance to invert for ε than does surface tomography.
- Surface tomography has a better chance to invert for δ than does crosswell tomography.

5.2.4.1.2 Initial model estimate α_0=2500 m/s, ε=δ=known

Figure 5.94 shows the result of dynamic smoothing applied on the resulting tomogram assuming an initial model where the anisotropy is known completely and an initial P-wave velocity estimate of 2500 m/s.

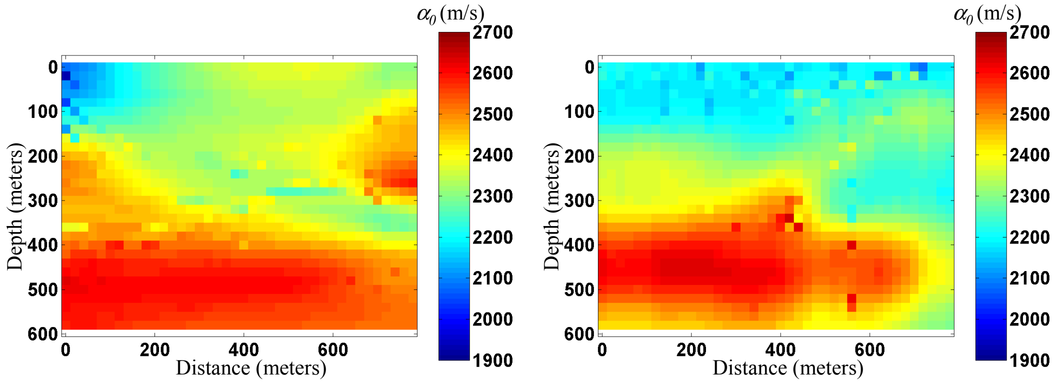

a) b)

Figure 5.94 Quasi-null space dynamic smoothing results using an initial model estimate which anisotropy is known; crosswell (left) and surface (right).

These results are similar to the isotropic results. These figures show that tomography, can in the best of situations, give results that are biased by the acquisition geometry and a function of the underlying velocity structure, even when the anisotropy is known completely.

5.2.4.1.3 Initial model estimate α_0=known, $\varepsilon=\delta=0$

Figure 5.95 shows the results of dynamic smoothing applied to tomograms that used as an initial model estimate in which the vertical P-wave velocity is known completely.

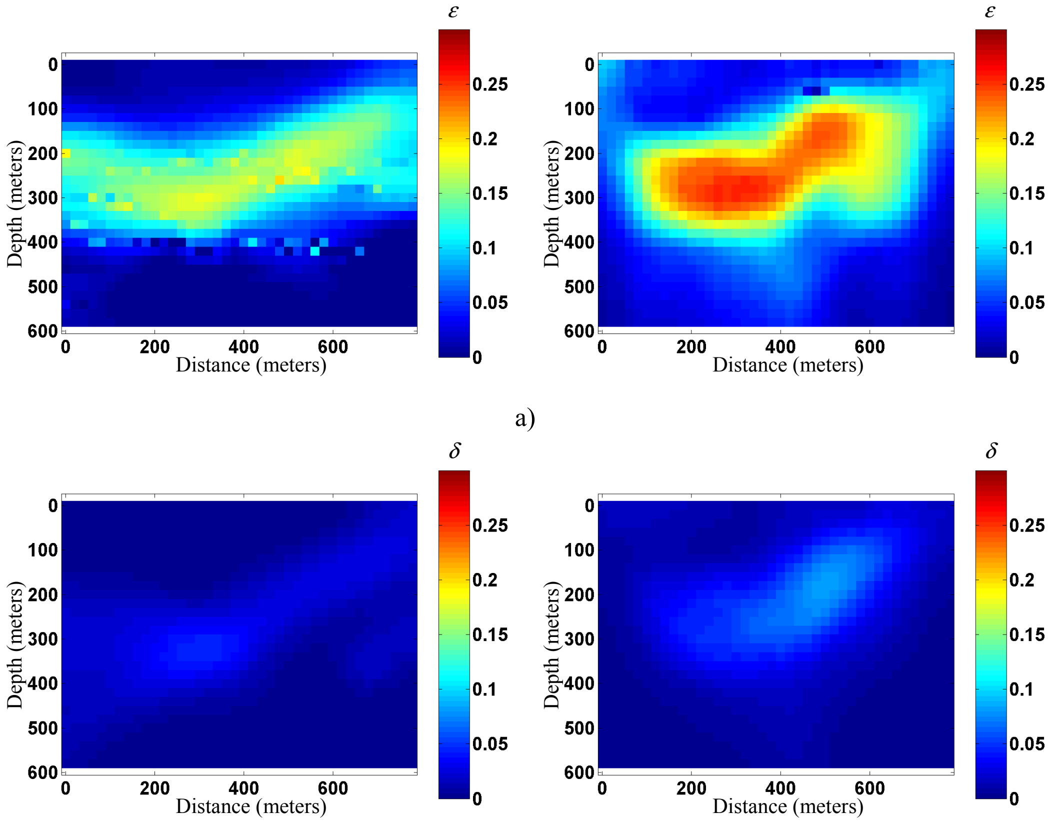

a)

b)

Figure 5.95 Quasi-null space dynamic smoothing results using an initial model estimate which α_0 is known completely; crosswell (left) and surface (right): ε (a) and δ (b).

These results show the best case scenario for attempting to invert for ε and δ. Important things to note are:

- The crosswell tomography estimate for ε has the anisotropic layer extend across the entire model as it should. The surface tomography estimate for ε has lateral extent. This is a function of the lack of horizontal raypaths near the edge of the survey.
- Crosswell tomography can give the best estimate for ε while surface tomography gives the best estimate for δ.

- The δ tomogram estimate is smoothed much more than the ε tomogram. This is a function of the general trend that ε is a more reliable inversion estimate than δ.

5.2.4.1.4 Initial model estimate α_0, ε, δ with random error

Figure 5.96 through 5.98 are the results of quasi-null space dynamic smoothing on tomograms resulting from initial model estimates that contained 10, 25 and 50 percent random error.

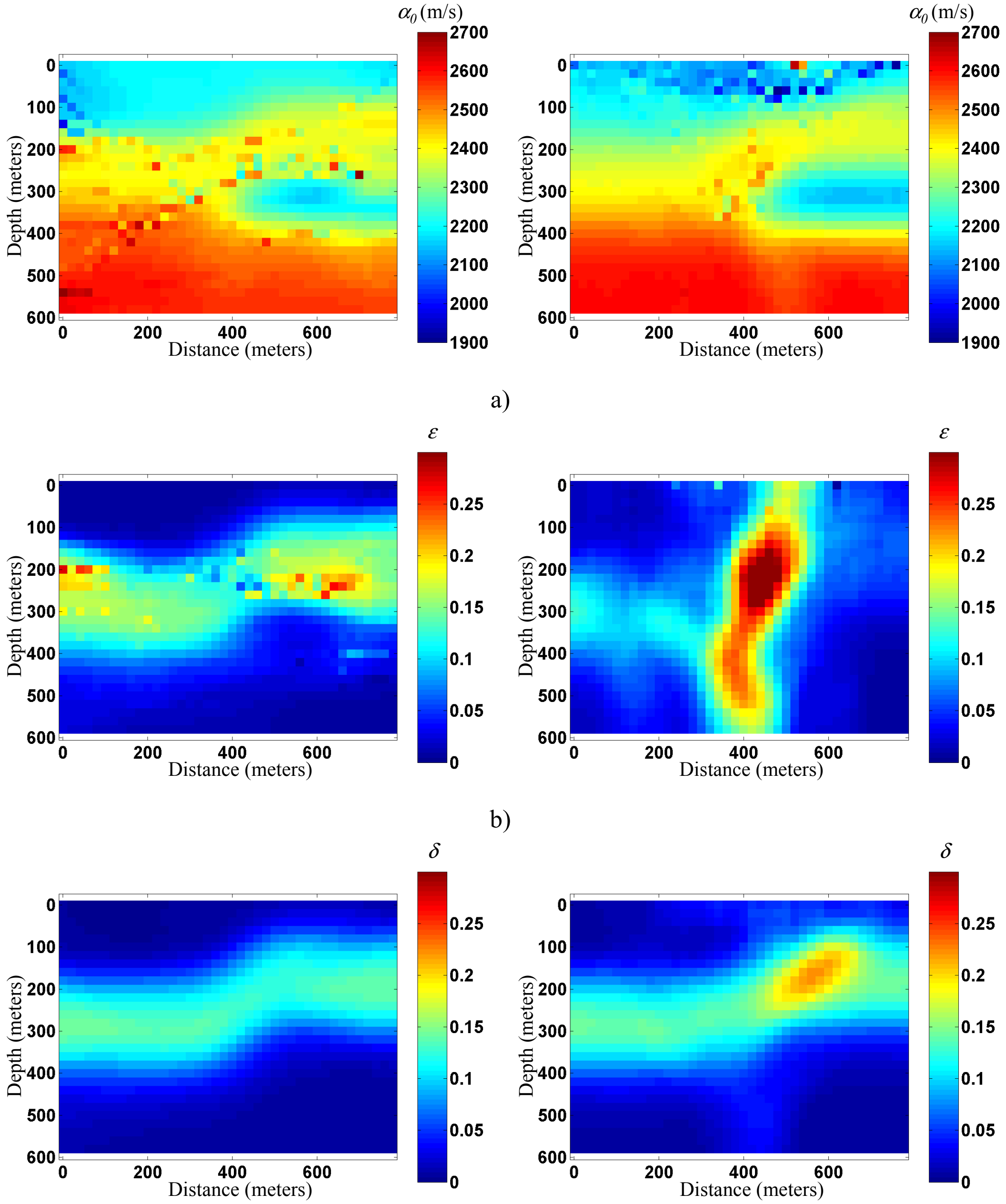

a)

b)

c)

Figure 5.96 Quasi-null space dynamic smoothing results using an initial model estimate which has random 10 percent model error; crosswell (left) and surface (right): α_0 (a) ε (b) and δ (c).

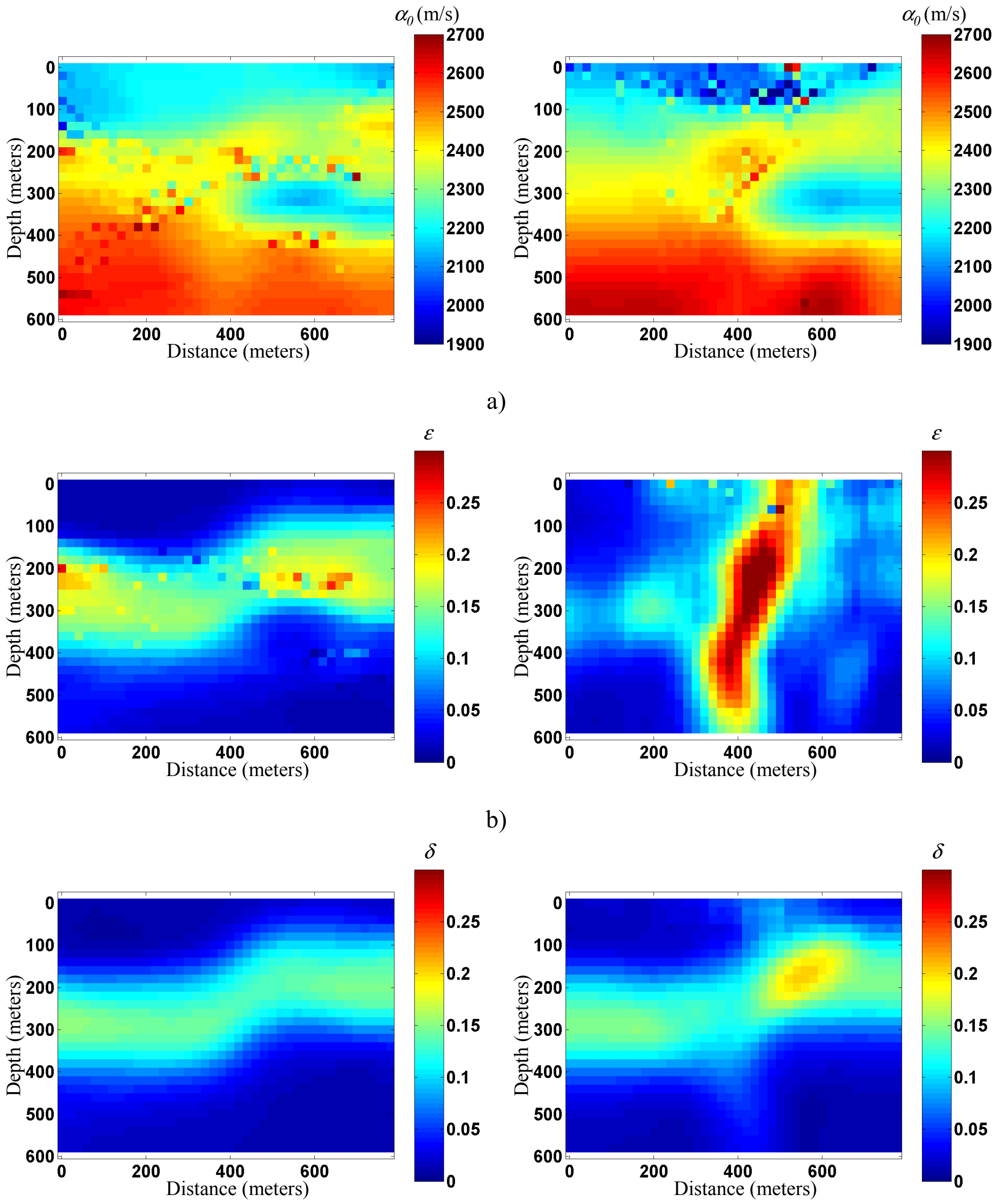

a)

b)

c)

Figure 5.97 Quasi-null space dynamic smoothing results using an initial model estimate which has random 25 percent model error; crosswell (left) and surface (right): α_0 (a) ε (b) and δ (c).

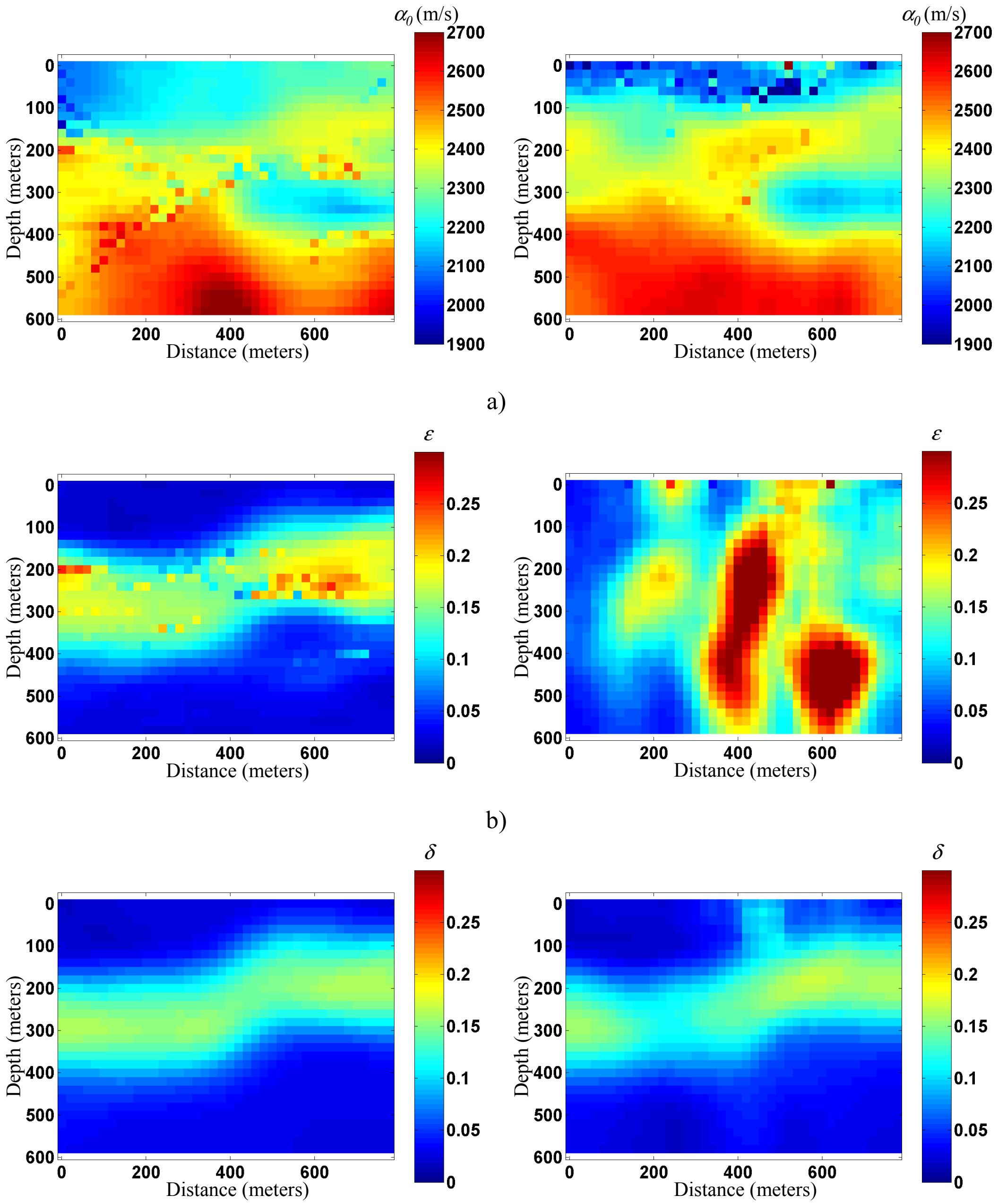

a)

b)

c)

Figure 5.98 Quasi-null space dynamic smoothing results using an initial model estimate which has random 50 percent model error; crosswell (left) and surface (right): α_0 (a) ε (b) and δ (c).

Figures 5.96 through 5.98 show the relative stability of the α_0 and δ inversions in contrast to the relative instability of the surface ε inversion. The α_0 tomogram in general degraded in solution quality with the increase in random model noise. This is reflected in the amount of smoothing present. The less error added to the model resulted in less smoothing. In general all the solutions are such that the output model is realistic, that it is geologically plausible.

The ε solution is quite stable for crosswell tomography, yet quite unstable for surface tomography. The smoothing does not reflect this as the presence of the highly anisotropic anomaly would normally indicate that the solution is in fact unstable. This result has not been smoothed because the rays have focused in that location of the anisotropic anomaly and as a consequence has a large number of linearly independent rays, making those cells reliable. In this instance the dynamic smoothing algorithm has functioned as intended, but it cannot discern between geologically plausible solutions and apparent inversion artefacts.

The δ tomograms are quite stable. The initial model estimate contained the correct model in addition to the random model error. These results show that the dynamic smoother recognizes that the δ parameter contributes the least to the velocity perturbation and as such is deemed unreliable. Given that the tomogram is entirely unreliable, it was smoothed completely. In this case, the smoothing worked out fortuitously as the random noise was suppressed by the high-cut filter applied revealing a very good estimate for δ.

5.2.4.2 Dynamic filtering: complex model 2

For completeness, the next set of tests is to perform quasi-null space analysis on the second complex velocity anomaly. The results seen are similar to those of complex model 1 and show the basic trends already discussed. They are however some differences in the results and they are based solely on the differences in the underlying structure. How the underlying structure interacts with the acquisition geometry will ultimately determine the capability of tomography.

5.2.4.2.1 Initial model estimate α_0=2500 m/s, ε=δ=0

Figure 5.99 shows the results of applying dynamic smoothing on the results of crosswell and surface for complex model 2. The initial model estimate used has α_0=2500 m/s and isotropy is assumed.

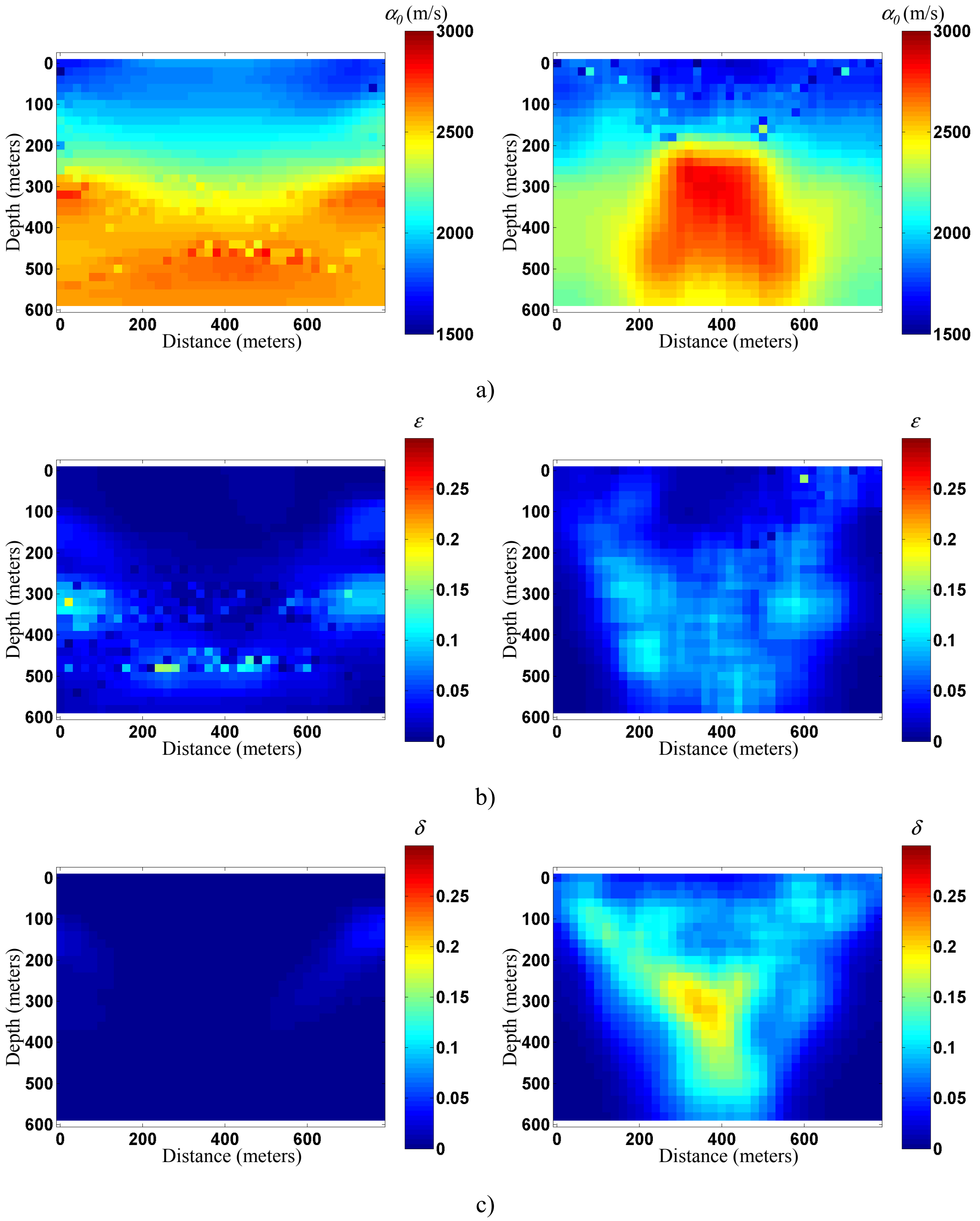

a)

b)

c)

Figure 5.99 Quasi-null space dynamic smoothing results using an initial model estimate of α_0=2500 m/s and no anisotropy; crosswell (left) and surface (right): α_0 (a) ε (b) and δ (c).

The α_0 tomogram is a result that is expected. The crosswell tomogram result detects vertical velocity variations while the surface tomogram detects horizontal velocity variations. The zone of tomographic interest is detectable by the crosswell result, although smeared laterally, and not detected at all by surface tomography. The ε tomograms show that the crosswell result is more reliable than the surface results, based on the amount of smoothing present. The crosswell result is far superior in estimating ε. The δ tomograms are equally unreliable. As mentioned previously, the crosswell tomogram, appears to do a better job in estimating is δ, primarily because of the underlying velocity model. In general, the dynamic smoothing adds value only for the tomograms which contain cells that are deemed reliable. These tomograms are limited to both α_0 tomograms and the crosswell ε tomogram.

5.2.4.2.2 Initial model estimate α_0=2500 m/s, ε=δ=known

Figure 5.100 shows the results of dynamic smoothing applied to the tomographic results when using an initial model estimate where the amount of anisotropy is known.

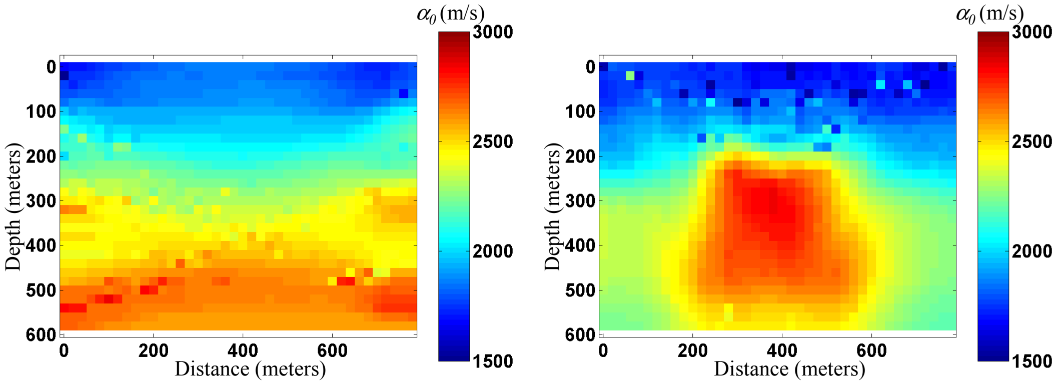

a) b)

Figure 5.100 Quasi-null space dynamic smoothing results using an initial model estimate in which the anisotropy present is known completely; crosswell (a) and surface (b).

The dynamic smoothing results show a crosswell result that has had a majority of the cells smoothed and a surface tomography result with a minimal amount of cells smoothed. The lack of lateral velocity detection is evident to the quasi-null space analysis and as such has smoothed the crosswell tomogram. In contrast the surface tomography result has conserved the model edges while smoothing areas where the reliability is not as high as is the case near the edges of the tomogram. In general, the dynamic smoothing is a consequence not only of the acquisition geometry but also the underlying velocity structure and whether horizontal or vertical velocity variations exist.

5.2.4.2.3 Initial model estimate α_0=known, $\varepsilon=\delta=0$

Figure 5.101 shows the results of dynamic smoothing applied to the tomographic results when using an initial model estimate where α_0 is known.

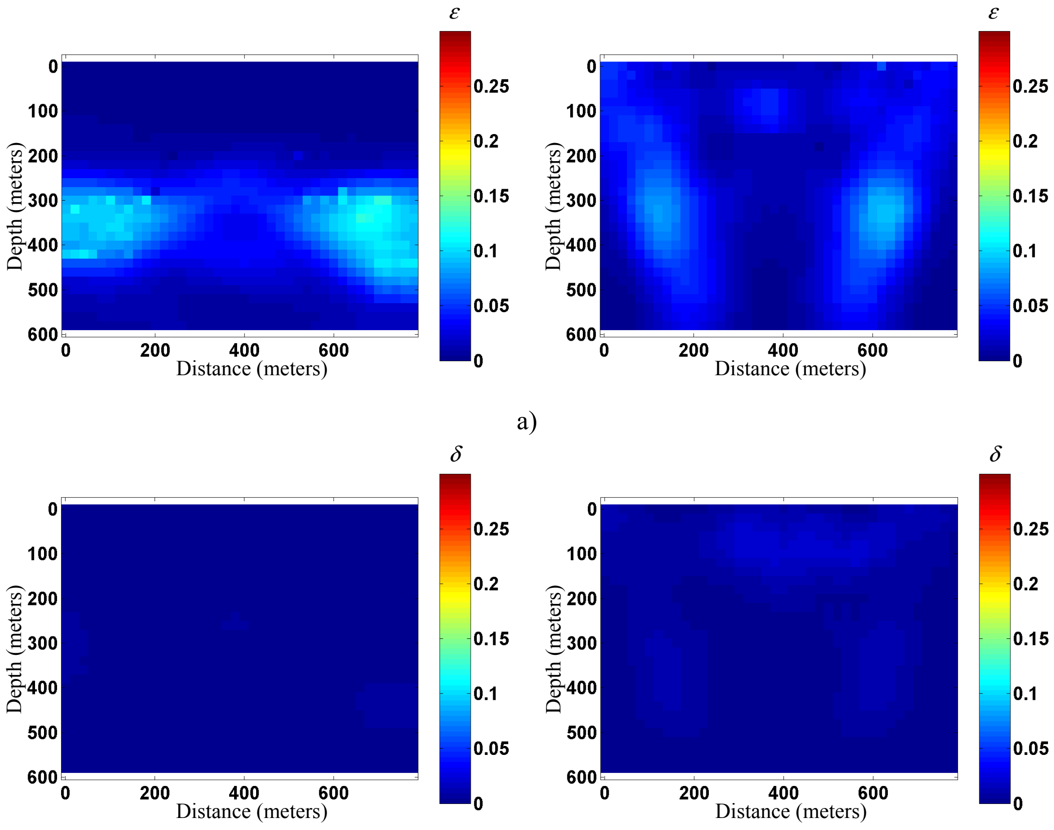

a)

b)

Figure 5.101 Quasi-null space dynamic smoothing results using an initial model estimate in which α_0 is known completely; crosswell (left) and surface (right): ε (a) and δ (b).

This result shows a smoothed ε surface tomography result and a relatively unsmoothed ε crosswell tomography result. As expected the δ tomograms are both smoothed as they were deemed unreliable solutions predominantly due to the lack of near 45 degree rays.

5.2.4.2.4 Initial model estimate α_0, ε, δ with random error

Figures 102 through 104 show the results of quasi-null space dynamic smoothing applied to the crosswell and surface tomography results that used initial models with 10, 25 and 50 percent model error added to the correct model.

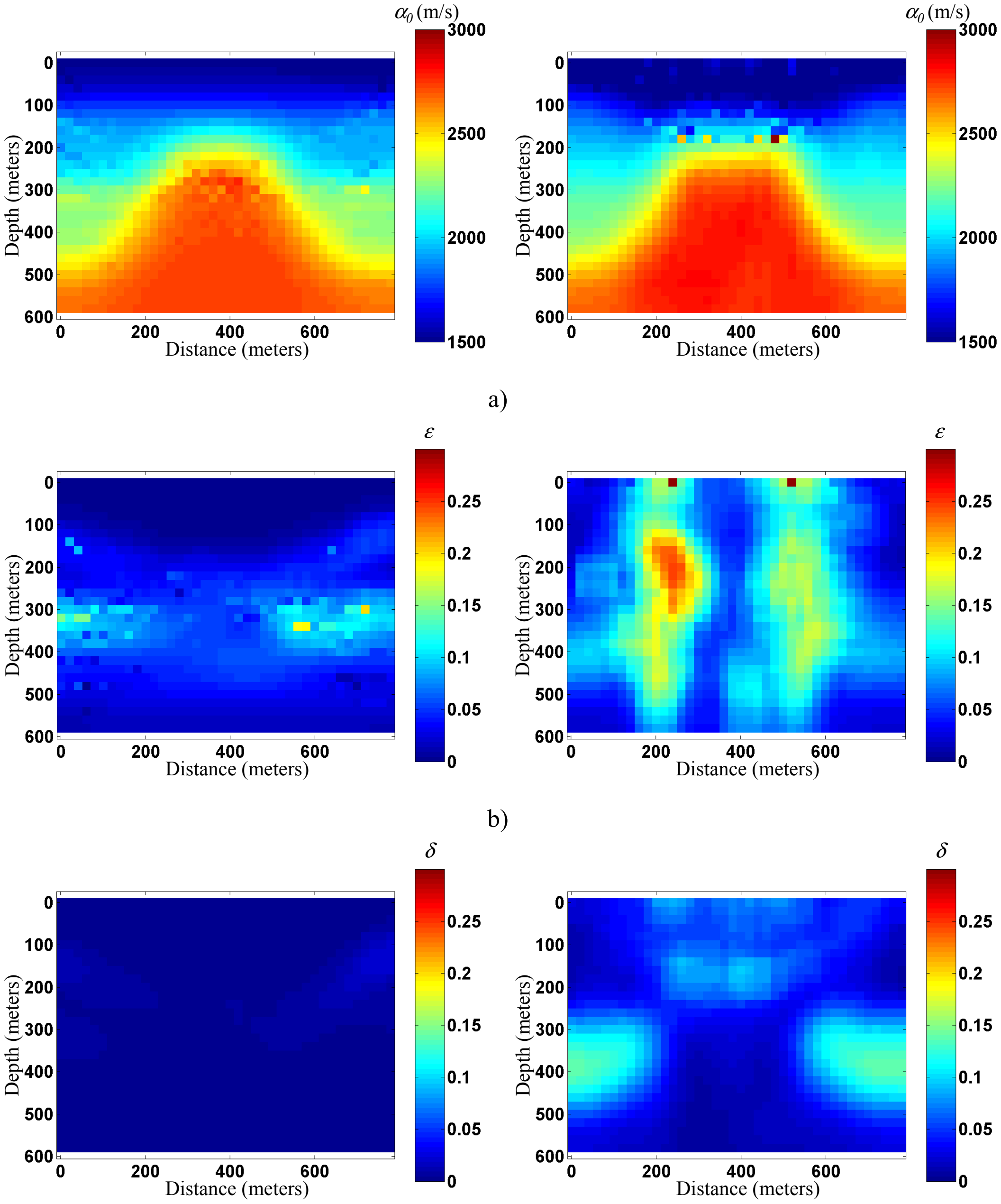

a)

b)

c)

Figure 5.102 Quasi-null space dynamic smoothing results using an initial model estimate which has 10 percent model error; crosswell (left) and surface (right): α_0 (a) ε (b) and δ (c).

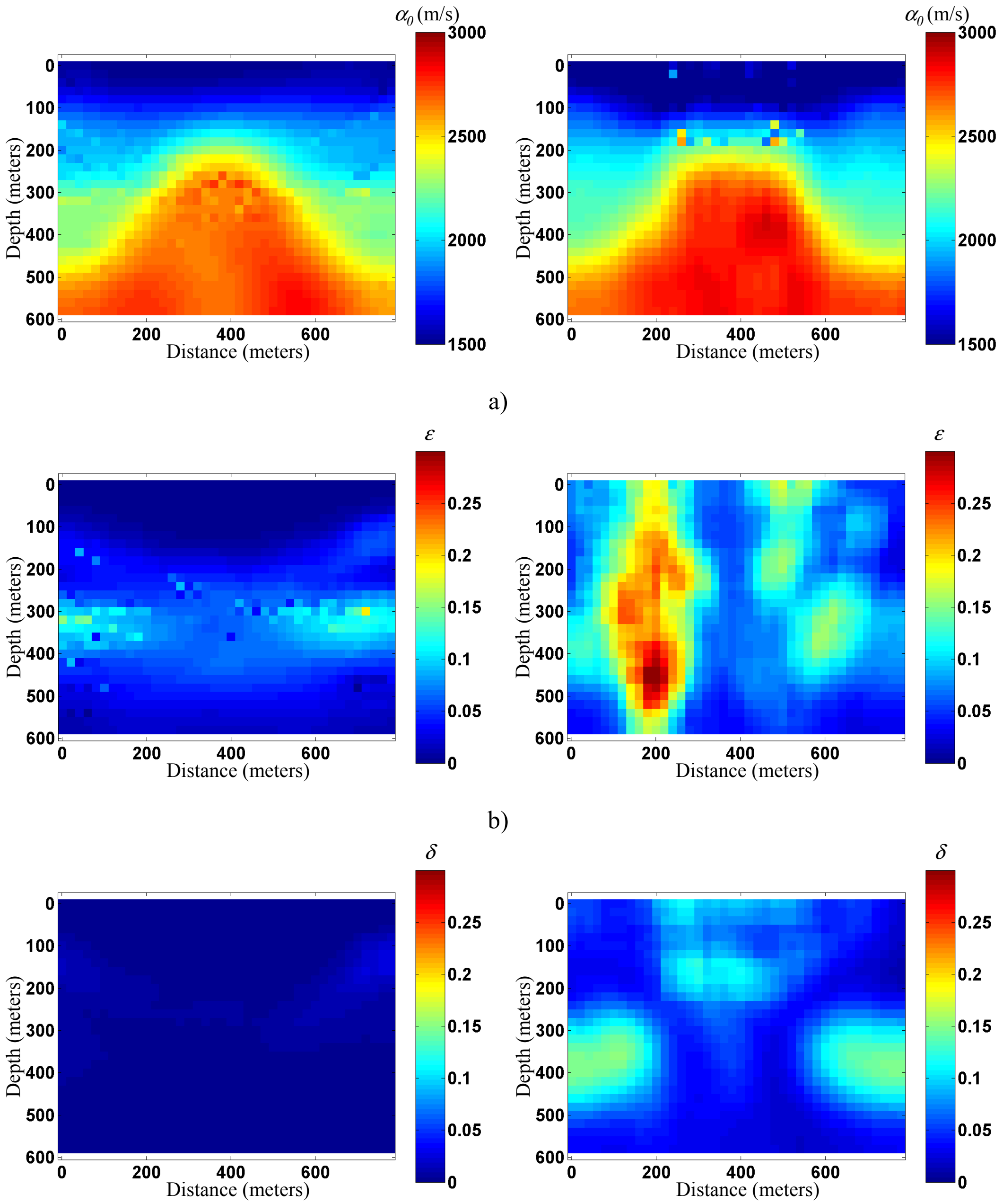

a)

b)

c)

Figure 5.103 Quasi-null space dynamic smoothing results using an initial model estimate which has 25 percent model error; crosswell (left) and surface (right): α_0 (a) ε (b) and δ (c).

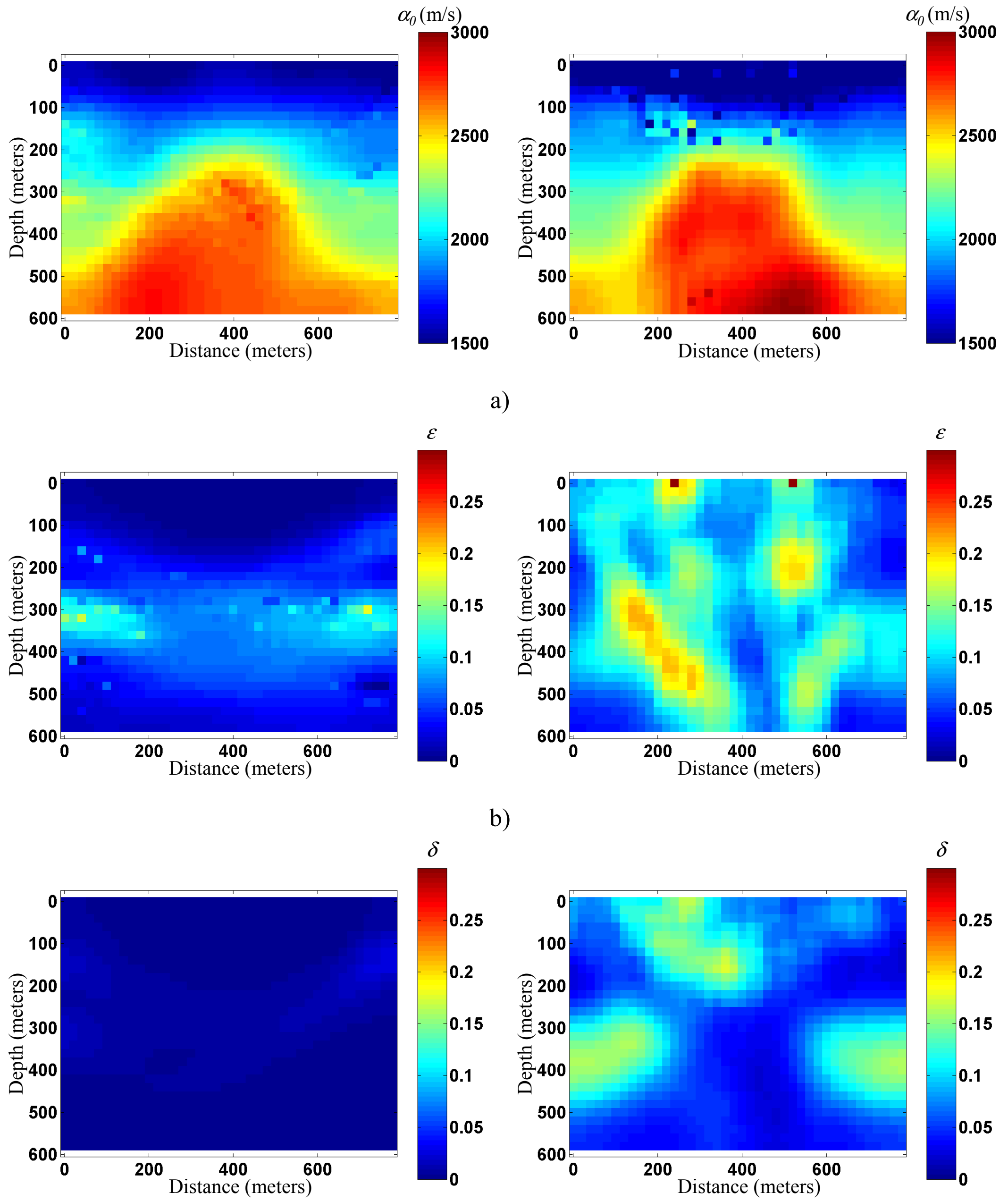

a)

b)

c)

Figure 5.104 Quasi-null space dynamic smoothing results using an initial model estimate which has 50 percent model error; crosswell (left) and surface (right): α_0 (a) ε (b) and δ (c).

The results seen in the previous figures are similar, qualitatively, to those of complex model 1. The α_0 tomogram shows that the crosswell result is more smoothed than the surface result. Also, the surface ε tomogram is more smoothed than the crosswell result while the crosswell δ tomogram is more smoothed than the surface results. As discussed previously, this is all a function of the acquisition geometry and the underlying model structure and the roles they play in determining the rays present for inversion.

5.2.4.3 Integration: complex model 1

5.2.4.3.1 Initial model estimate α_0=2500 m/s, $\varepsilon=\delta=0$

Figure 5.105 shows the quasi-null space integration result when using an initial model estimate where α_0=2500 m/s and assuming isotropy.

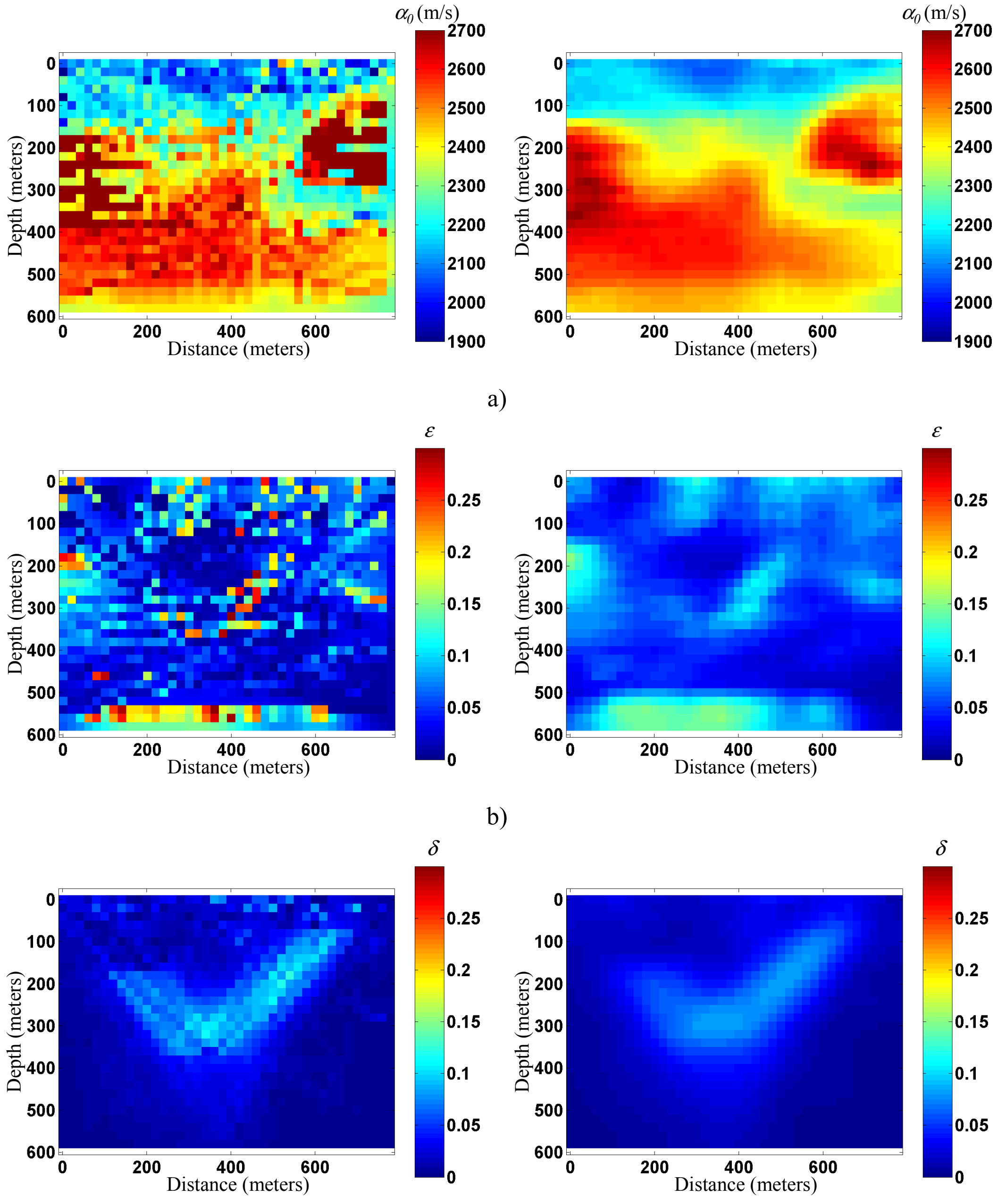

a)

b)

c)

Figure 5.105 Quasi-null space integration results using an initial model estimate which has as an initial model estimate of constant α_0=2500 m/s and assuming isotropy; unsmoothed (left) and smoothed (right): α_0 (a) ε (b) and δ (c).

The resulting tomograms show the complimentary nature of crosswell and surface tomography. Crosswell tomography highlights the vertical velocity variation and surface tomography highlights the lateral velocity variations. The low-velocity zone of interest is clearly detected in α_0, although the structure of the model is inaccurate. The ε tomogram is mostly dominated by crosswell solution through the anisotropic layer and dominated by the surface result near the surface and the bottom of the model. The ε tomogram shows the downfall of the technique in that the most reliable cell may still not actually provide an accurate solution. If both crosswell and surface tomography both produce bad results for one cell, quasi-nulls space integration will take the more reliable solution, but it does not change the fact that both solutions are inaccurate. The δ tomogram is clearly dominated by the surface tomography result, primarily a function of the raypath angles.

5.2.4.3.2 Initial model estimate α_0=2500 m/s, ε=δ=known

Figure 5.106 shows the results when using an initial model estimate where α_0=2500 m/s and the anisotropy of the model is known.

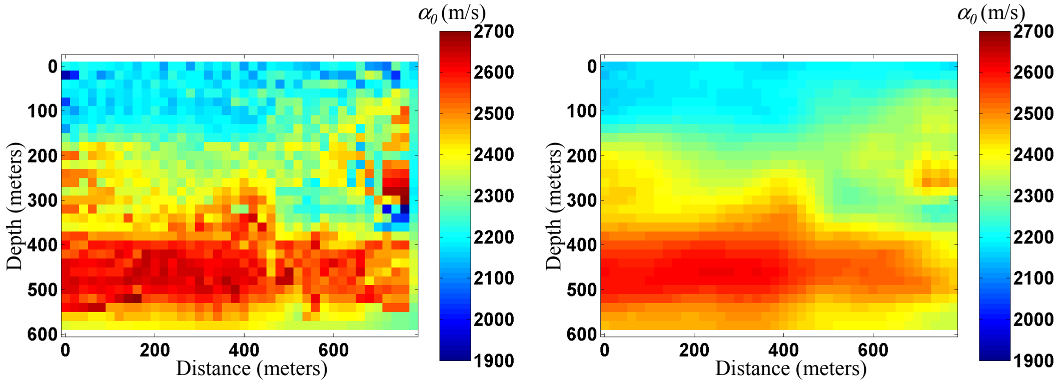

a) b)

Figure 5.106 Quasi-null space integration results using an initial model estimate which ε and δ are known; unsmoothed (a) and smoothed (b).

This integration result shows the low-velocity anomaly of interest resolved quite clearly. The structure and the velocity values are accurate. This result is about the best that one can hope.

5.2.4.3.3 Initial model estimate α_0=known, $\varepsilon=\delta=0$

Figure 5.107 shows the quasi-null space integration result when using an initial model estimate where α_0 is known and isotropy is assumed.

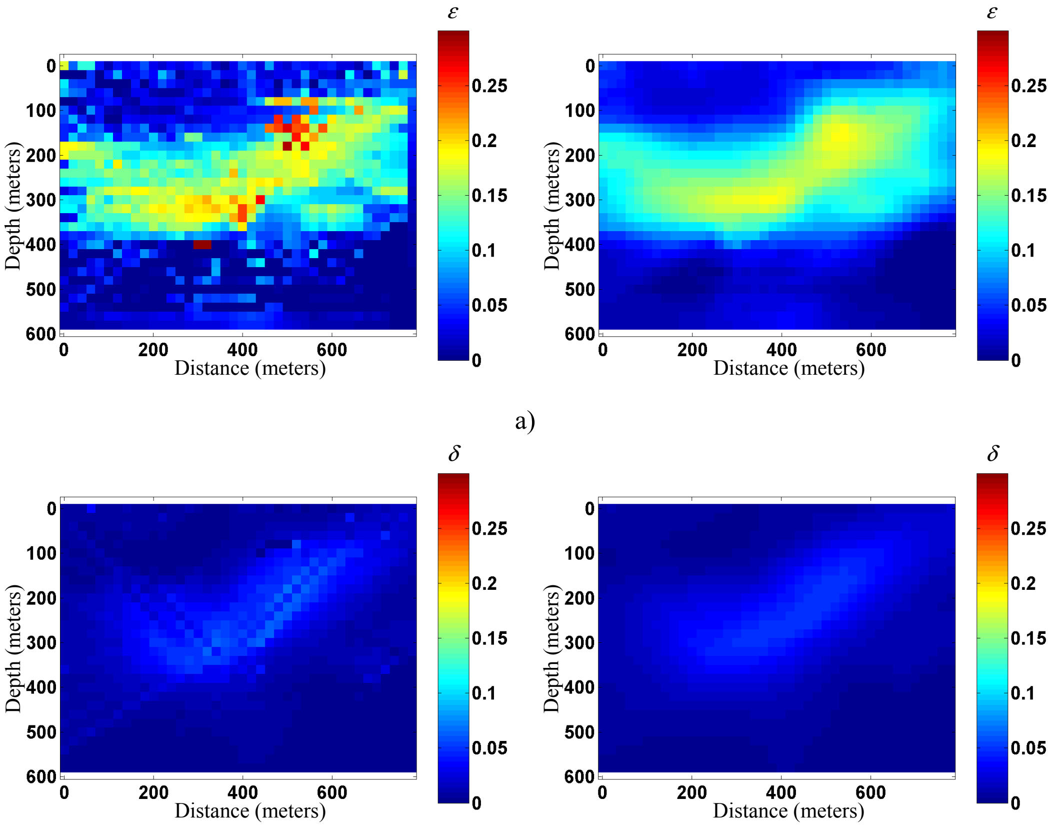

a)

b)

Figure 5.107 Quasi-null space integration results using an initial model estimate in which α_0 is known completely; unsmoothed (left) and smoothed (right): ε (a) and δ (b).

The ε and δ tomograms are quite accurate. In general, when α_0 is known leads to the best estimate of the anisotropic parameters. As a consequence the integrated result produces the most accurate results. When both the surface and crosswell tomography results are good, the integration output will be comprised of the best possible solutions. This is the opposite of the results of Figure 5.105b.

5.2.4.3.4 Initial model estimate α_0, ε, δ with random error

Figures 5.108 through 5.110 shows the results when using an initial model estimate which contains 10, 25 and 50 percent random model error added respectively.

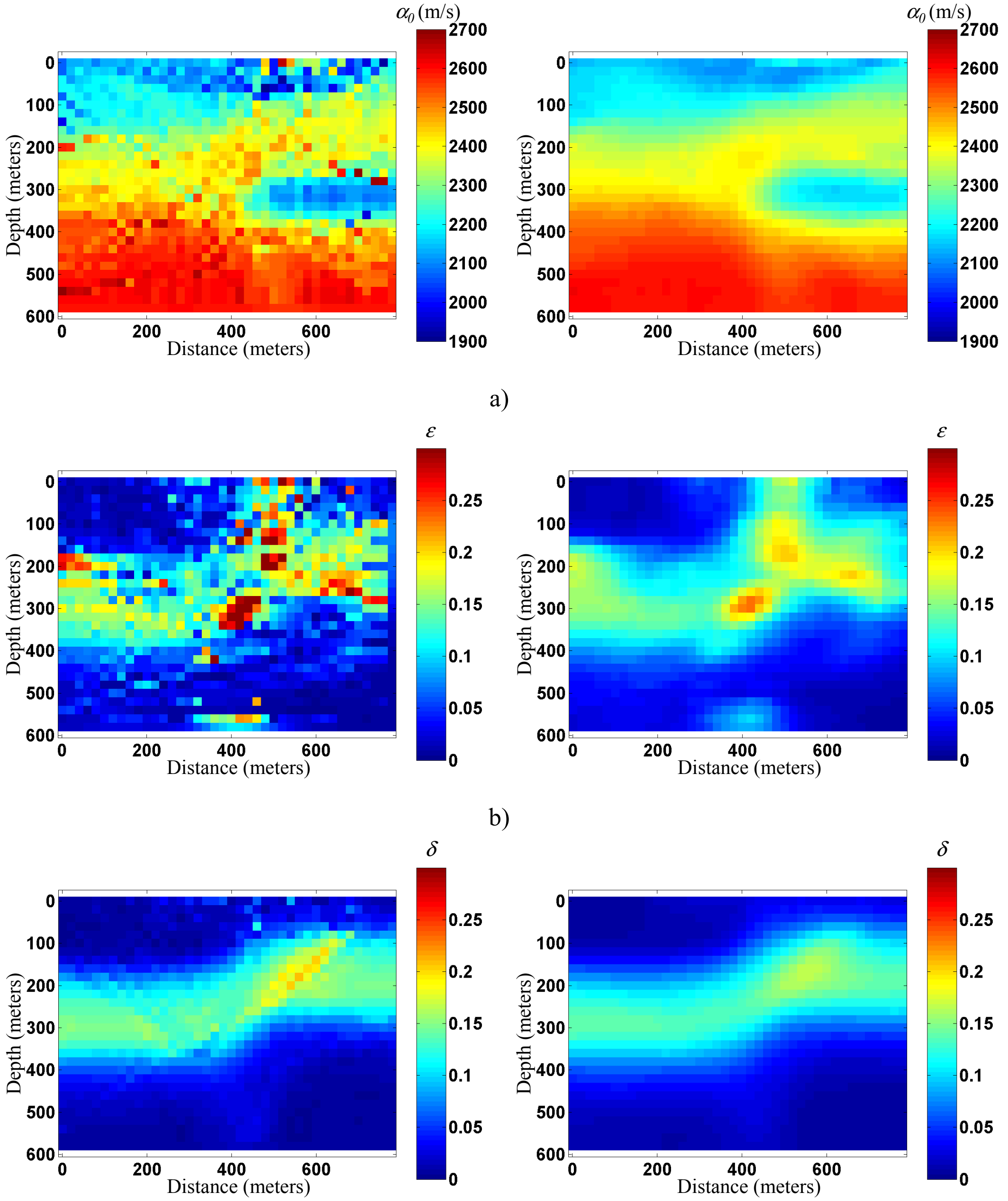

a)

b)

c)

Figure 5.108 Quasi-null space integration results using an initial model estimate which has random 10 percent model error; unsmoothed (left) and smoothed (right): α_0 (a) ε (b) and δ (c).

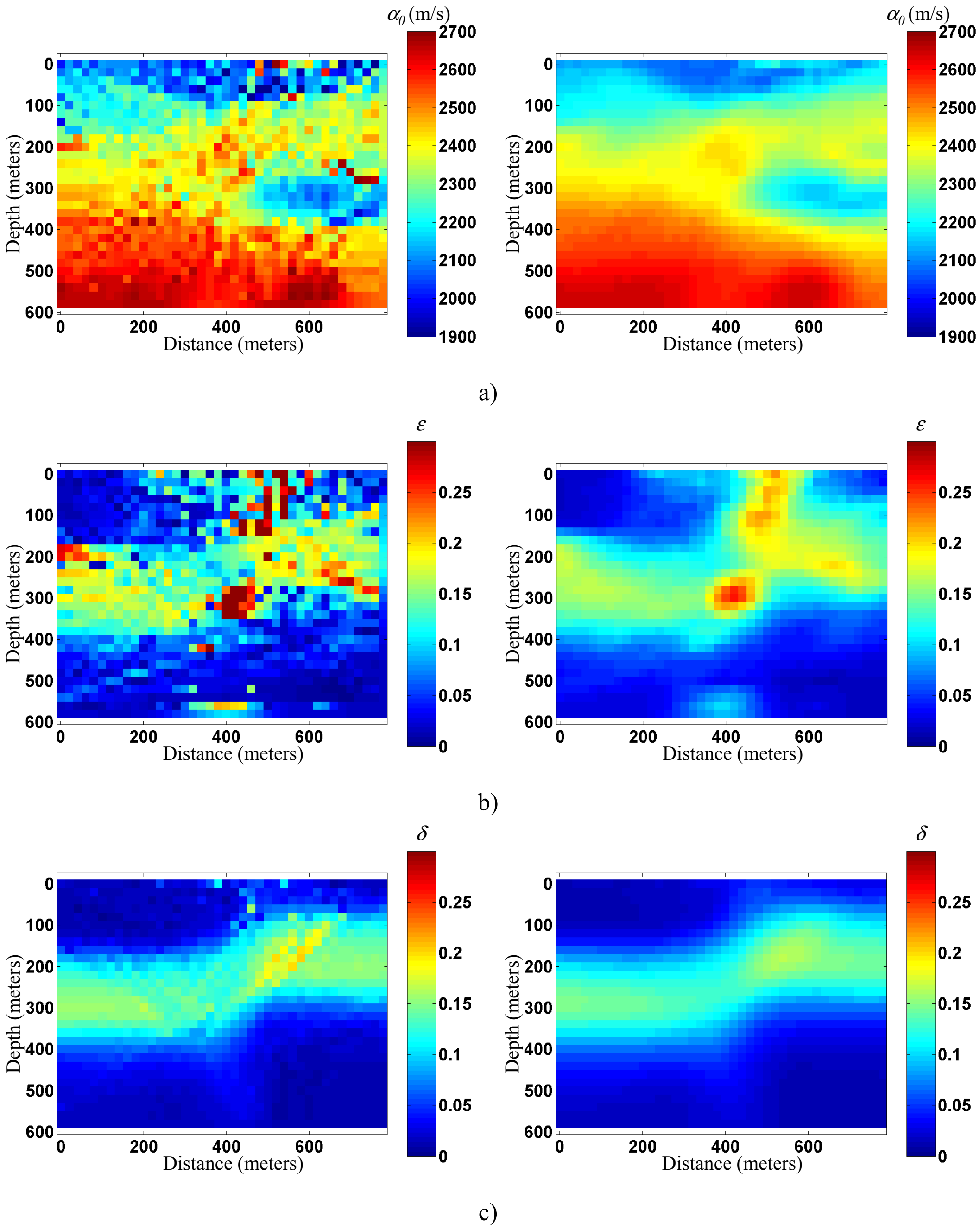

Figure 5.109 Quasi-null space integration results using an initial model estimate which has random 25 percent model error; unsmoothed (left) and smoothed (right): α_0 (a) ε (b) and δ (c).

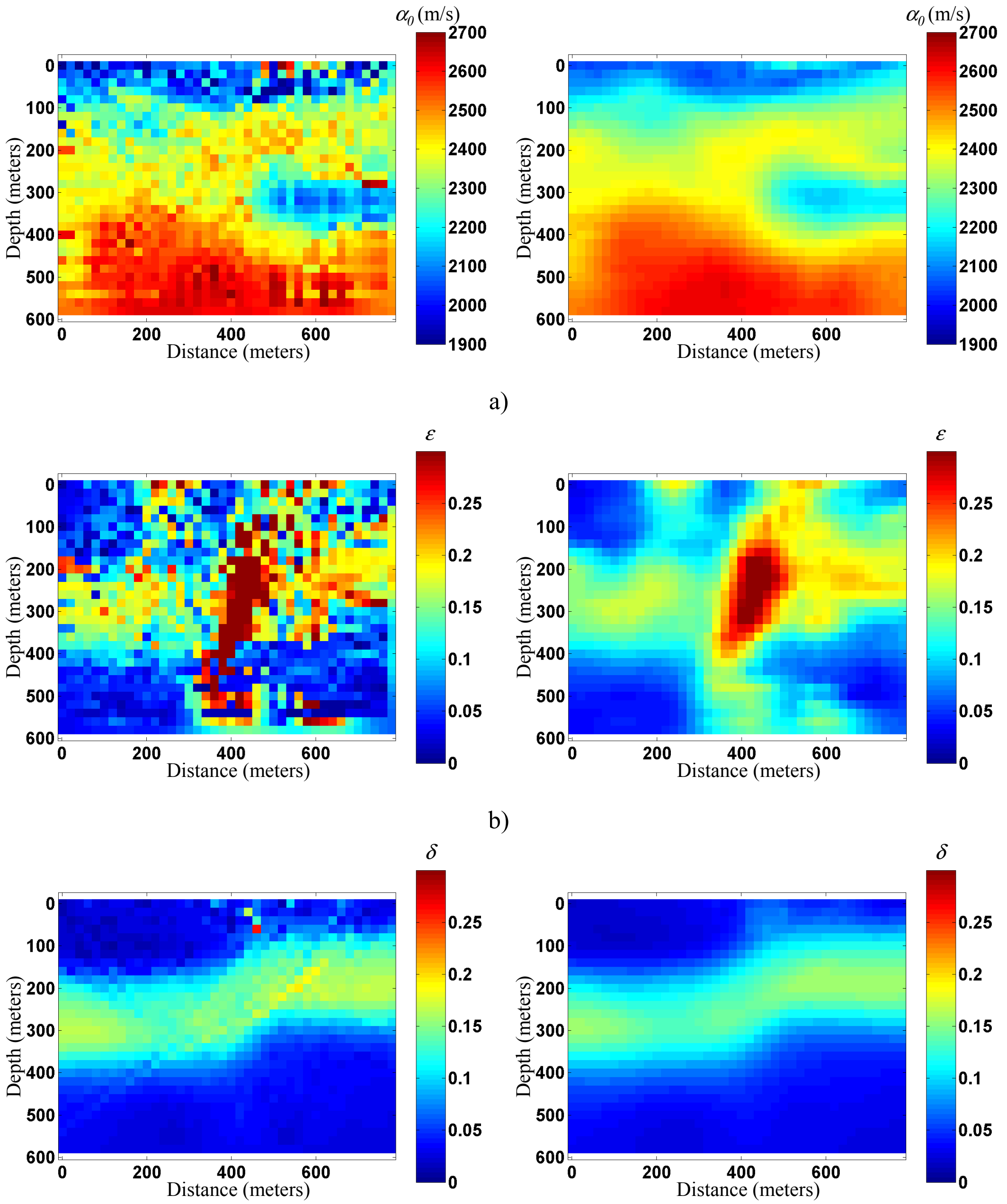

a)

b)

c)

Figure 5.110 Quasi-null space integration results using an initial model estimate which has random 50 percent model error; unsmoothed (left) and smoothed (right): α_0 (a) ε (b) and δ (c).

This set of three figures, shows the worst integration results. Figure 5.108 shows quite stable results. The α_0 and δ tomogram show very good results while the ε tomogram shows hints of the surface tomography instability. Figure 5.109 shows an increasing amount of ε tomogram instability where Figure 5.110 shows the greatest amount of instability. The question is, how can the unstable component of the ε surface tomography solution be a part of the integrated solution? The integrated solutions actually reflect the dominant raypaths and the acquisition geometry. In particular, Figure 5.110b, shows the correct lateral extent of the anisotropic layer via crosswell tomography, while the inaccurate ε values near the top and bottom of the model are a result of surface tomography. The largest ε values are positioned correctly and come from the surface result. The surface result had a large concentration of rays at this location and as a result was deemed quite reliable. The integration technique shows promise as the integration technique correctly chooses only the correct portion of the surface tomography result and allows the ε tomogram to be filled in by the more stable crosswell solution.

5.2.4.4 Integration: complex model 2

For completeness Figures 5.111 through 5.116 show the results of the quasi-null space integration technique on complex model 2.

5.2.4.4.1 Initial model estimate α_0=2500 m/s, $\varepsilon=\delta=0$

Figure 5.111 shows the results of quasi-null space integration, for complex model 2 when using an initial model estimate of α_0=2500 m/s and assuming isotropy.

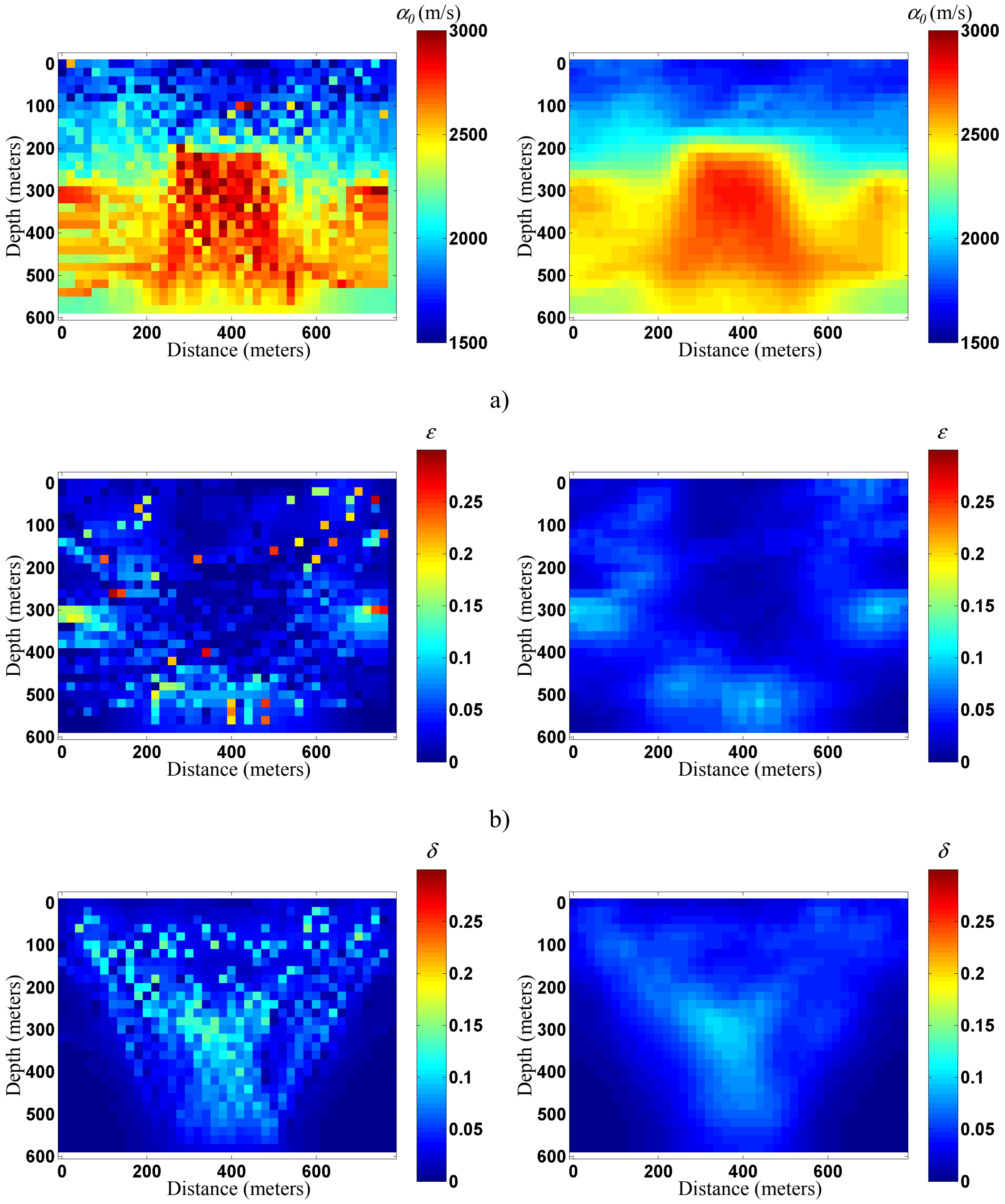

a)

b)

c)

Figure 5.111 Quasi-null space integration results using an initial model estimate of constant α_0 of 2500 m/s; unsmoothed (left) and smoothed (right): α_0 (a) ε (b) and δ (c).

The results for α_0 and ε tomograms are very good. The α_0 tomogram reveals the dome-like structure has been detected and produced the best image of the velocity structure. The ε tomogram correctly detects the anisotropic layers, albeit with additional errors in the estimate because of the inclusion of the surface result. As discussed previously, the increased ray coverage of surface tomography makes the integrated result acquisition geometry dependent. The δ tomogram is inaccurate and is mostly a consequence of the dominant raypath angle.

5.2.4.4.2 Initial model estimate α_0=2500 m/s, ε=δ=known

Figure 5.112 shows the integrated result using an initial model estimate where α_0=2500 m/s and the anisotropy is known.

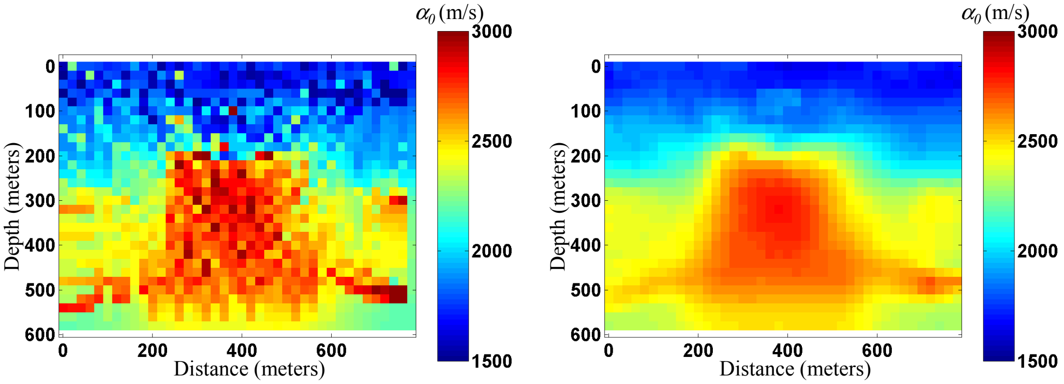

a) b)

Figure 5.112 Quasi-null space integration results using an initial model estimate which has anisotropy known completely; unsmoothed (left) and smoothed (right).

This is the best result for complex model 2. The dome-like structure is imaged quite well and the magnitudes of α_0 are quite accurate as well. This result is the reason why the integration technique should be tested when crosswell and surface experiments are available.

5.2.4.4.3 Initial model estimate α_0=known, ε=δ=0

Figure 5.113 shows the results of quasi-null space integration when using an initial model estimate where α_0 is known and isotropy is assumed.

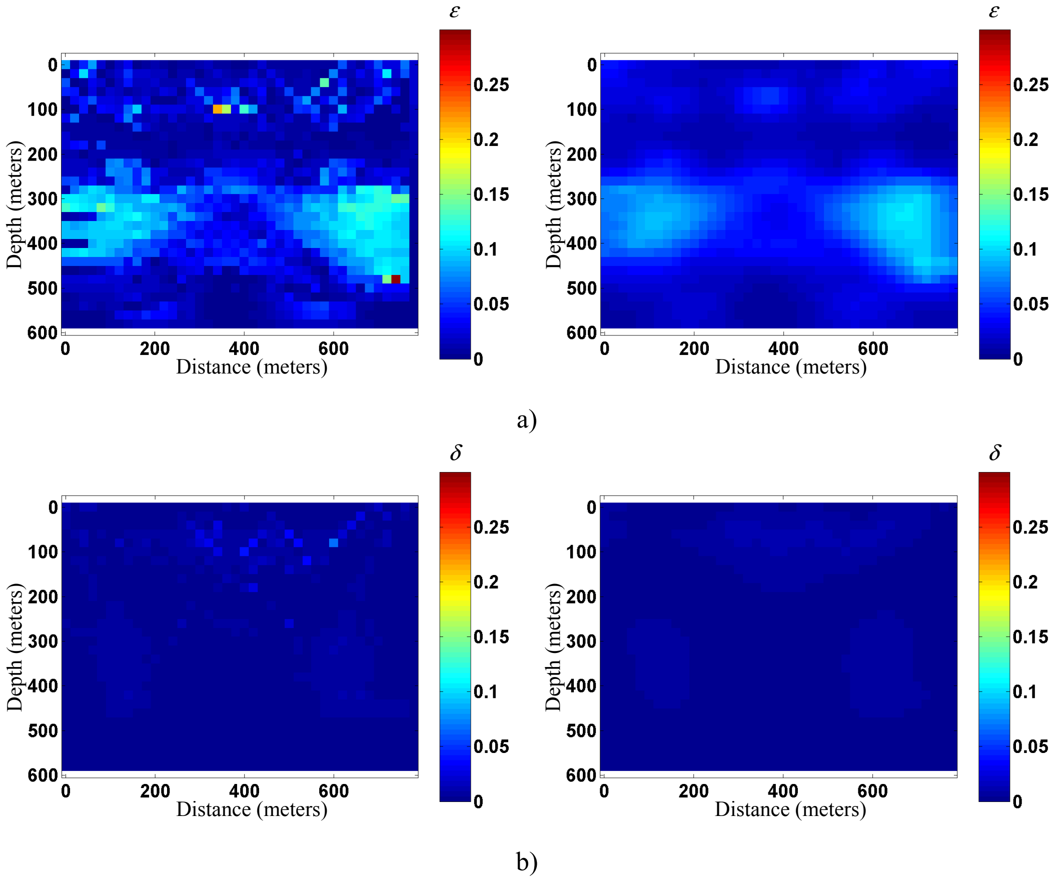

Figure 5.113 Quasi-null space integration results using an initial model estimate which has α_0 known exactly; unsmoothed (left) and smoothed (right): ε (a) and δ (b).

This result shows a very accurate representation of ε. The anisotropic anomaly has been smeared laterally, a consequence of the crosswell result, and there are estimate errors near the top and bottom of the model, a consequence of the surface result. That being said the largest errors have been eliminated by correctly choosing the more reliable cells leading to the best estimate of ε in complex model 2. The result for δ detects the anomaly however the estimates for the structure and magnitude of the anomaly are quite poor. This is a consequence of the limited rays present mostly a consequence of the underlying velocity structure.

5.2.4.4.4 Initial model estimate α_0, ε, δ with random error

Figures 5.114 through 5.116 show the integration results when using initial model estimate where 10, 25 and 50 percent random model error has been added.

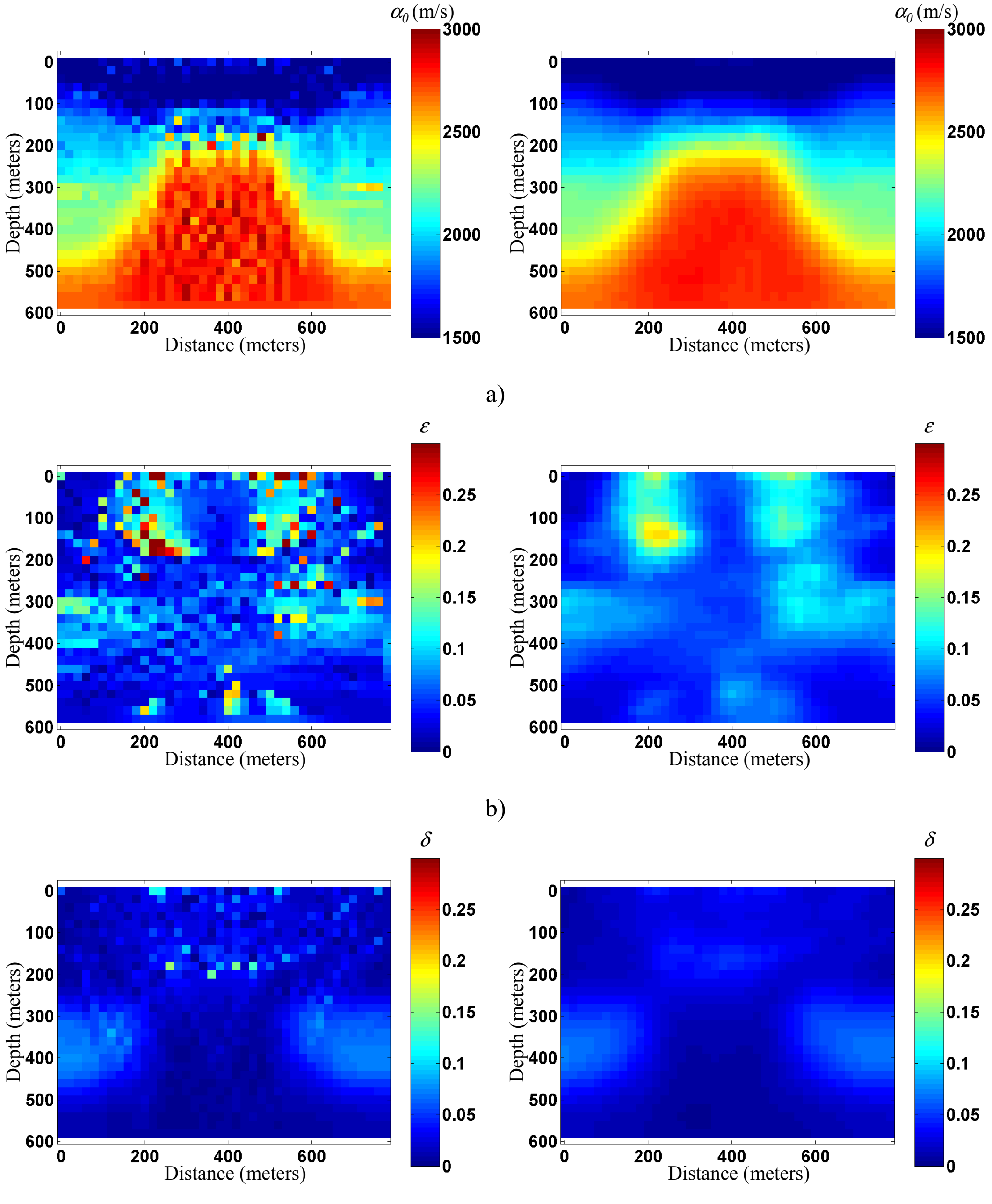

a)

b)

c)

Figure 5.114 Quasi-null space integration results using an initial model estimate which has random 10 percent model error; unsmoothed (left) and smoothed (right): α_0 (a) ε (b) and δ (c).

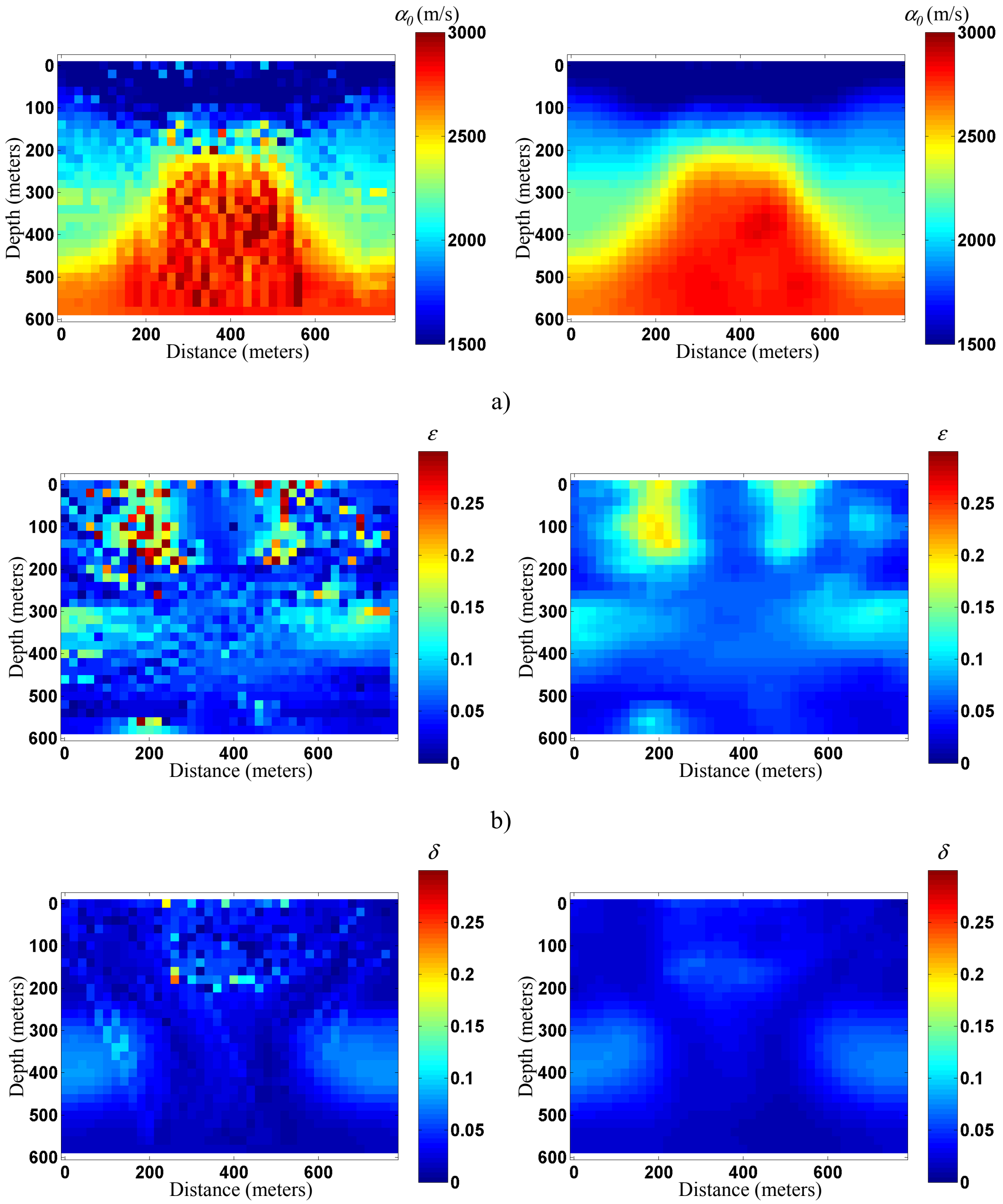

a)

b)

c)

Figure 5.115 Quasi-null space integration results using an initial model estimate which has random 25 percent model error; unsmoothed (left) and smoothed (right): α_0 (a) ε (b) and δ (c).

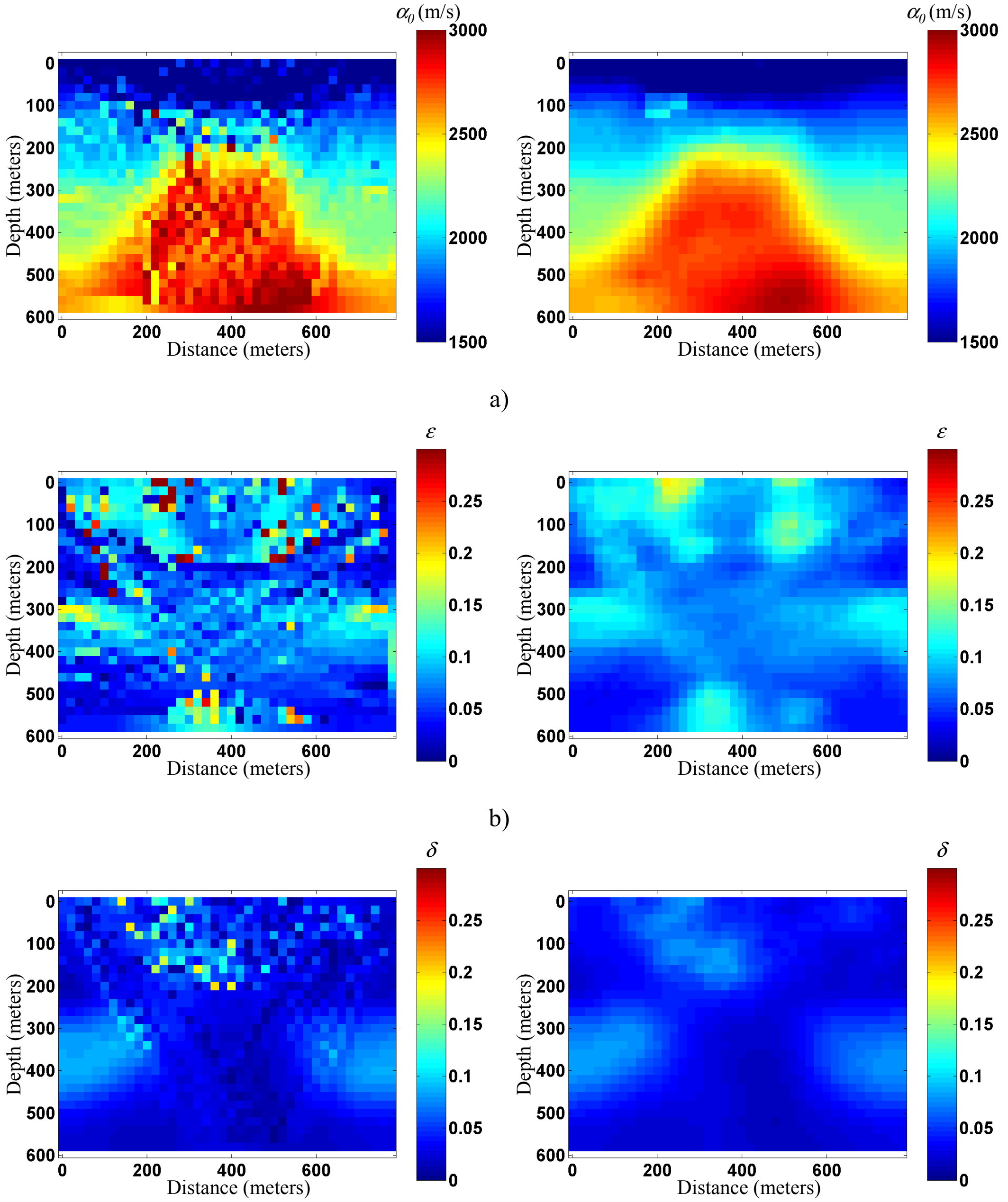

a)

b)

c)

Figure 5.116 Quasi-null space integration results using an initial model estimate which has random 50 percent model error; unsmoothed (left) and smoothed (right): α_0 (a) ε (b) and δ (c).

These results show the following general trends:

- The α_0 tomogram is quite stable.
- The ε tomogram correctly detects the anomaly of interest but also includes the surface tomography errors at the top and bottom of the model.

- The δ tomogram is mostly a function of the smoother and the errors surface tomography errors near the top of the model.

In general the following can be said of the integration results:

1. The α_0 integrated tomogram is based primarily on which of crosswell or surface tomography best resolves the anomaly.
2. The integrated ε tomogram is primarily biased toward crosswell geometry as it is best suited to estimate the horizontal velocity component of anisotropy.
3. The integrated tomogram of δ is the most unreliable of the inversion process. Often the reliability is so low that the average of the two survey results is used.

5.3 Summary

The results of the isotropic and anisotropic tomography for crosswell and surface geometries can be summarized by the following points:

1. Tomography attempts to minimize traveltime errors but is biased by the acquisition geometry and the underlying velocity structure.
2. Crosswell tomography detects vertical velocity variations while surface tomography detects lateral velocity variations.
3. Crosswell and surface tomography compliment each other well and when integrated produce superior tomograms.
4. Data driven quasi-null space techniques provide superior stabilization to low-pass filtering and the integration technique provides the most reliable tomograms.
5. Anisotropic tomography is highly dependent on the angle distribution of the data; horizontal rays are required for ε and 45 degree rays for δ.

6. Anisotropic tomography is in general unreliable for structured areas if an accurate initial estimate for α_0 is not given.
7. The quasi-null spaces for α_0, ε and δ are different because of the physics governing wave propagation. Both ε and δ are angle dependent ($\sin^2\theta\cos^2\theta$ and $\sin^4\theta$ respectively) where as α_0 is only dependent on distance.
8. The quasi-null space is useful when used as a basis for dynamic smoothing and integration techniques introduced in this thesis. The quasi-null space determines general solution reliability and gives insight into what cells contribute to the solution.

CHAPTER 6. CONCLUSIONS

The tomographic workflow presented in the thesis is founded on two main principles: isotropic and transversely isotropic wave propagation and stable inversions. Each step is important in achieving accurate traveltime inversion results.

The modelling methods presented assume planewave propagation and first arrival traveltimes. Traveltimes are computed via a first order finite-difference solution to the eikonal equation and are calculated along expanding wavefronts. Raypaths are traced by using the principle of reciprocity and Fermat's principle of least time. Angle dependent modifications are made to the isotropic modelling routine to include Thomsen's anisotropic parameters of ε and δ.

The inversion method chosen is Singular Value Decomposition. This technique solves over and underdetermined sets of equation in a manner similar to other conventional minimization techniques. The pseudo-inverse constructed from SVD is equivalent to the least squares solution as well as being the solution of minimum norm. However the greatest assets of SVD are the orthogonal data and model matrices that can be used to analyze the inversion solution. One such way to analyze the inversion solution is via the quasi-null space, as suggested by Bohm and Vesnaver (1996). The quasi-null space is a representation of solution reliability. This thesis uses the quasi-null space to stabilize the inversion solution in two different ways. The first smooths unreliable results while maintaining the high frequency data of reliable results. The second uses two different acquisition geometry tomography results and integrates them into one output tomogram. This output tomogram is constructed by using the more reliable inversion value from each experiment.

The results of applying the workflow to data is analysed in terms of model structure resolvability and stable parameter estimation. Two distinct sets of models were created: simple and complex. The simple velocity model tests are important as they give insight to the basic responses of tomography. Knowing this impulse response is useful in determining whether parameter estimates are real or simply tomography artefacts. The complex models were important in that they test the limitations and capabilities of the algorithm.

In the isotropic regime, the inversion results are quite good and the quasi-null space stabilization techniques work well. Analysing the results shows that surface and crosswell tomography compliment each other. Surface tomography resolves lateral velocity variations while crosswell tomography resolves vertical variations. Surface tomography is at an advantage in that additional information is added in the form of reflecting interfaces and thus has the possibility of much more data than crosswell tomography. Testing also reveals that high-velocity zones are preferentially resolved. This is because the high-velocity zones act as ray attractors. The increase in ray density helps in resolving velocity structures. Implementing the quasi-null space techniques in isotropic regimes proved to be quite successful both in smoothing the unreliable results and integrating reliable cells to produce an optimal tomogram.

Anisotropic tomography results are mixed. The estimate for α_0 is in general similar to that of the isotropic velocity estimate. For the most part, it is difficult to obtain an accurate solution for Thomsen's anisotropic parameters of ε and δ as the number of unknowns triple yet the amount of data remains the same. The estimation for ε is optimized in crosswell tomography as the inversion process for the near horizontal rays is decreased to a two parameter estimation as for near horizontal rays the impact of δ is approximately zero. It is especially difficult to determine an accurate solution for δ as it has the least of amount of effect on traveltime when compared to α_0 and ε. The optimal raypath for determining δ is one which travels at an angle of 45 degrees. This can only be accommodated amongst the shallower reflectors of the surface tomography experiments.

The greatest source of ambiguity in anisotropic tomography is the initial model estimate used. Changing the initial model estimate can drive tomographic inversions to different solutions. Reasons for this are the tomographic workflow used and the dependence of velocity to first order on α_0 and to second order on ε and δ. Anisotropic tomography begins by modelling traveltimes of initial model estimate and correcting residual traveltime errors, to first order, by perturbing α_0. Any remaining traveltime errors are then corrected for by ε and δ. As shown in Chapter 5, estimates for ε and δ are dependent on the predominant raypath angle which depends nonlinearly on α_0, ε and δ. Thus assuming that second order traveltime residuals derive from perturbations to ε and δ the first iteration solution for α_0 will directly affect the solution for ε and δ. Solutions for ε and δ are unstable, biased heavily on the initial model estimate. It is important to start the anisotropic inversion process with as close to a correct velocity model as possible to remove as much of the uncertainty as possible. Isotropic tomography is also biased by the initial model estimate but not nearly to the extent that the anisotropic case is.

The inherent nonlinearity of the tomographic process, especially in the underdetermined anisotropic regimes, makes it difficult to converge to the correct solution. The quasi-null space adapts itself to the data after each iteration adapting itself to the acquisition geometry and the velocity structure. A lowpass filter was designed to eliminate random noise and was shown to provide significant improvement. However it does not filter points in a manner which maintains resolution and solution integrity.

The quasi-null space for α_0, δ and ε are distinct. Each null space arises from the first order dependency of each parameter on time. It turns out that α_0 depends on the distance traversed through a cell while δ and ε depend not only on distance but also the angle of propagation.

The quasi-null space dynamic smoothing and integration techniques are useful in discerning the more reliable solution. It also has the ability to discern which initial model estimate is best to use. It has been shown in the anisotropic tests that the overall reliability for α_0, ε and δ are dependent upon the initial model estimate used. The relative reliability of the parameter estimate is an indication of which initial model estimate is best represents the actual model. In general if the initial model estimate is close to the actual model tomography will converge to the correct solution.

Future research in this area of study can focus on different least-squares optimization techniques. There are a number of different constraints that can be applied to further decrease the size of the solution space. The constraints can be defined so as to include realistic geologic geometry, such as lateral continuity, or include well data. Further research can also be directed to including both crosswell and surface seismic data into a single inversion problem. In such a problem, a single model would solve for both geometries simultaneously, as opposed to methods presented in this thesis. Additional data can also consist of using not only the compressional waves but also the shear modes. This can be especially useful for constraining the anisotropic inversion. A proposed method to increase anisotropic solution stability is to decrease the number of cells in the model so that the problem is less overdetermined or perhaps assume a more restricted nature of anisotropic propagation by assuming elliptical anisotropy. In this scenario only two parameters would have to be estimated, horizontal and vertical velocity.

Perhaps the most important conclusion to be drawn from all the testing performed is that each tomographic result is highly dependent upon the acquisition geometry and the underlying structure of the model. Acquisition geomteries can be modified to help in determining Thomsen's anisotropic parameters by acquiring longer offsets to better identify δ, but the underlying velocity structure is fixed and the inherent problems that come with it cannot be overcome. Making too many generalizations about tomography can lead to incorrect assumptions and misinterpretation of the results. That being said working in the depth domain allows for interpretation of the tomogram. The resulting tomogram which exhibits a more geologic type structure is more likely to represent the best solution.

BIBLIOGRAPHY

Asakawa, E. and Kawanaka, T. 1993. Seismic raytracing using linear traveltime interpolation: Geophysical Prospecting, **41**, 99-111.

Alkhalifah, T. and Tsvankin, I., 1995, Velocity analysis for transversely isotropic media: Geophysics, **60,** 1550-1566.

Backus, G. E., 1962, Long-wave elastic anisotropy produced by horizontal layering: Journal of Geophysical Research, **67**, 4427-4440.

Bishop, T. N., Bube, K. P., Cutler, R. T., Langan, R. T., Love, P. L., Resnick, J. R., Shuey, R. T., Spindler, D. A. and Wyld, H. W., 1985. Tomographic determination of velocity and depth in laterally varying media: Geophysics, **50**, 903-923.

Bohm, R. P., and Vesnaver, A. L., 1996. In quest of the grid: Geophysics, **64,** 1116-1125.

Bording, R. P., Gersztenkorn, A., Lines, L. R., Scales, J. A., and Treitel, S., 1987, Applications of traveltime tomography: Geophysics Journal Research astr Soc, **90**, 285-303.

Brown, R. J., Lawton, D. C., and Cheadle, S. P., 1991. Scaled physical modeling of anisotropic wave propagation: multioffset profiles: Geophysical Journal International, **107**.

Carrion, P., 1991, Dual tomography for imaging complex structures: Geophysics, **56,** 1395-1404.

Chapman C. H., and Pratt, R. G., 1992, Traveltime tomography in anisotropic media-I. Theory: Geophysics Journal International, **109**, 1-19.

Dellinger, J., 1991, Anisotropic finite-difference traveltimes, 61st Ann. Internat. Mtg: Soc. of Expl. Geophys., 1530-1533.

Eaton, D. W. S., 1993, Finite-difference traveltime calculation in anisotropic media: Geophysics Journal International, **114**, 273-280.

Gerszkenstorn, A and Scales, J. A., 1988, Smoothing seismic tomograms with alpha-trimmed means, Geophysical Journal, **92**, 67-72.

Lines, L. R. and LaFehr, E. D., 1989, Tomographic modeling of a cross-borehole data set: Geophysics, **54,** 1249-1257.

Marsden, J. E. and Tromba, A.J., 1996, Vector Calculus: W. H. Freeman and Company
.

Matsuoka, T. and Ezaka, T., 1992. Raytracing using reciprocity: Geophysics **57**, 326-333.

Musgrave, M. J. P., 1970, Crystal acoustics: Introduction to the study of elastic waves and vibrations in crystals: Holden Day.

Postma, G. W., 1955, Wave propagation in a stratified medium: Geophysics, **20**, 780-806.

Pratt, R. G., and Chapman, C. H., 1992, Traveltime tomography in anisotropic media-II. Application: Geophysics Journal International, **109**, 20-37.

Qin, F., Luo, Y., Olsen, K. B., Cai, W., and Schuster, G. T., 1992. Finite-difference solution of the eikonal equation along expanding wavefronts: Geophysics **57**, 478-487.

Robinson, E. and Clark, D., 1987, Fermat and the principle of least time: The Leading Edge, **06,** 34-37.

Scales, J.A., Smith, M. Treitel, S, 2001, Geophysical Inverse Theory: Samizdat Press.

Sheriff, 1999, Encyclopedic Dictionary of Exploration Geophysics: Soc. Expl. Geoph.

Slawinski, M.A. (2002) Seismic waves and rays in elastic media: Elsevier Science (draft)

Slawinski, M. A., Slawinski, R. A., Brown, R. J. and Parkin, J. M., 2000, A generalized form of Snell's law in anisotropic media: Geophysics, **65,** 632-637.

Stewart, R. R., 1988, An algebraic reconstruction technique for weakly anisotropic velocity (short note): Geophysics, **53,** 1613-1615.

Stork, C. and Clayton, R. W., 1985, Iterative tomographic and migration reconstruction of seismic images, 55th Ann. Internat. Mtg: Soc. of Expl. Geophys.

Thomsen, L. 1986. Weak elastic anisotropy: Geophysics, **51**, 1954-1966.

Van Trier, J., and Symes, W. W., 1991, Upwind finite-difference calculation of traveltimes: Geophysics, **56**, 812-821.

Vesnaver, A. L., 1996. The contribution of reflected, refracted and transmitted waves to seismic tomography: A tutorial: First Break, **14**, 159-168.

Vidale, J., 1988, *Finite*-difference calculation of traveltimes: Bulletin of the Seismological Society of America, **78,** 2062-2076.

Whitmore, N., and Lines, L., 1986, VSP depth migration of a salt dome flank: Geophysics, **51**, 1087-1109.

Zhou, H., 1993. Traveltime tomography with a spatial-coherency filter: Geophysics, **58**, 720-726.